UNIVERSITÀ DEGLI STUDI DI PALERMO

Dottorato in Ingegneria dell’Innovazione Tecnologica

Dipartimento di Ingegneria
Settore Scientifico Disciplinare (ING-IND/26)

MODELLING OF MEMBRANE PROCESSES: FROM CFD TO PROCESS OPTIMIZATION

IL DOTTORE
Ing. Mariagiorgia Floriana La Cerva

IL COORDINATORE
Prof. Salvatore Gaglio

IL TUTOR
Prof. Giorgio Micale

CO TUTOR
Prof. Michele Ciofalo
Prof. Andrea Cipollina

CICLO XXXII
ANNO CONSEGUIMENTO TITOLO 2020

Acknowledgements

Here, then, these three wonderful years of PhD are concluded...

Going back to the early days, I remember the thousand doubts and fears of starting this PhD on topics quite far from my master's degree. However, I have always had the sure support of a professor who has been much more than a simple tutor since my Bachelor’s thesis. Dear *Professor Ciofalo*, I thank you for your help, your advices, for the knowledge you gave me, for your time, for the laughter and your trust. The results achieved, this thesis, the person I am today, I owe all this to you. Thank you!

A special thanks also to *Professor Cipollina* who believed in me and gave me the opportunity to learn so much. Your passion for research, your critical point of view, your ethics, have been an inspiration to me. Thank you!

Thank you, too, *Professor Micale*, for always having time to ask me for updates, to cheer me up and support me.

Thanks also to *Alessandro Tamburini*, *Luigi Gurreri*, *Michele Tedesco* and *Massimiliano Di Liberto* who do not appear as tutor or co-tutor but have always helped me during my PhD and contributed to the work that led to this thesis.

I have to thank all my colleagues who welcomed me into an already cohesive group but made me feel immediately part of the "family". *Francesco*, *Rosa*, *Serena Lima*, *Giuseppe*, *Maurizio*, *Javier*, *Alessandro Cosenza*, *Mimma*, *Daniele*, *Fabrizio*, *Andrea Culcasi*, *Nunzio*, *Valentina*, thanks for everything!

I’m sure that now you will think that I have forgotten you but obviously it is not so! *Antonino* you deserve a special thanks! We have shared so much, in the *REvivED* project, at Wetsus, in London and after everything we have experienced I can say that I owe you so much! At the end of this journey I can say that you are my best friend!

During my PhD I was very lucky to supervise two special students, who learned a lot and gave a great contribution to this work. Thanks so much *Serena Bellia* and *Antonella Filingeri*.

I would also like to thank the amazing people I met at Wetsus and the people involved in the *REvivED* project with whom I have carried out a wonderful job and shared wonderful experiences.

I thank all my "colleagues" of the choir, especially *Antonella* and *Peppino* with whom I share the love for music that will always be my refuge from the world.

Thanks to *Federica* and *Chiara* who shared with me the years of university and now are two special friends who are always close to me.

A huge thank you to *Ilenia*, the older sister I chose, with whom I share everything for 23 years. Without the tragic/comic moments we had together, I would never have been able to finish this thesis in good health.

Last but not least, I thank my parents *Giuseppe* and *Rossana*, my sister *Angela* and my brother *Salvatore*. Despite the difficult moments we had to overcome, you always supported me and always believed in me.

Thank you all!

Mariagiorgia Floriana La Cerva

Table of content

List of Figures

List of Tables

Nomenclature

Symbol	**Quantity**
A	Cross-sectional area
A_p	Water permeability constant
B	Salt permeability constant
C	Concentration of salt
C^{SOL}	Bulk solution concentration
C_{IEM}^{SOL}	Solution concentration at the generic IEM
C_w	Concentration at a wall
$CONC$	Concentrate solution
c_p	Specific heat at constant pressure
D	Diffusivity
D^{SOL}	Salt diffusivity in solution
D_{IEM}	Salt diffusive permeability in membrane
DIL	Diluate solution
d_{eq}	Equivalent diameter
d_f	Spacer filament diameter
d_h	Hydraulic diameter
E	Nernst electric potential
E_i	Electric field
F	Faraday's constant
f	Friction factor
G_S	Mass flow rate of salt
G_{SOL}	Mass flow rate of solution
G_W	Mass flow rate of water
Gz	Greatz number
H	Thickness
h	Heat transfer coefficient
i	Electrical current density

i_{lim}	Diffusion limited current density
i_{SC}	Short-circuit current density
I	Electrical current
J_W	Water Flux
$J_{W,OSM}$	Osmotic water Flux
$J_{W,E.OSM}$	Electro-osmotic water Flux
K^{SOL}	Singular pressure loss coefficient
k	Mass transfer coefficient
L	Length
$L_{p,IEM}$	Osmotic permeability of the generic membrane
l	Pitch of spacers
M_S	Molar mass of salt
M_W	Molar mass of water
N_S	Salt molar flux
N_S^{COUL}	Coulombic salt molar flux
N_S^{DIF}	Diffusive salt molar flux
Nu	Nusselt number
n_{CP}	Number of cell pairs
n_H	Hydration number
P	Pressure
p	Pillar side
Q	Volume flow rate
q	Total thermal power
q_w''	Thermal flux at a wall
R_{blank}	Ohmic resistance of electrodes
Re	Reynolds number
R_G	Gas constant
R_T	Dimensionless thermal resistance
r_{blank}	Ohmic resistance of electrodes per cell pair

r_{ext}	External load
r_{IEM}	Membrane areal electric resistance
r_{SOL}	Solution areal electric resistance
$r_{T,ext}$	External thermal resistance
r_w	External resistance to mass transport
S	Area
Sc	Schmidt number
Sh	Sherwood number
T	Absolute temperature
T_b	Bulk temperature
T_{ext}	External temperature
T_w	Wall temperature
Tr	Transport number
t	Time
U	Superficial velocity
u_m	Interstitial velocity
u_{void}	Void velocity
V_f	Volume of fluid
V_T	Thermal voltage
V_{TOT}	Total volume
v_{LOAD}	Voltage at the external load per cell pair
W	Width
y	Co-ordinate along the flow direction

Greek symbols

α	Intrinsic angle between filaments
α_{IEM}	Membrane permselectivity
β	Shadow factor
Γ	Diffusivity

γ	Flow attack angle
γ_{SOL}	Activity coefficient
δ	Diffusion boundary layer thickness
δ_c	Half channel thickness
ΔP	Pressure gradient
ΔV	External voltage
Δv_{ext}	External voltage per cell pair
ε	Spacer porosity
ε_d	Dielectric permittivity
η_{BL}	Polarization voltage drop per cell pair
$\eta_{\Delta C}$	Voltage drop per cell pair related to axial concentration variation
η_{Ω}	Ohmic voltage drop per cell pair
θ	Independent time
θ_{IEM}^{SOL}	Polarization coefficient
λ	Current efficiency
λ_f	Fluid thermal conductivity
λ_{spa}	Spacer thermal conductivity
μ	Dynamic viscosity
ν	Kinematic viscosity
π^{SOL}	Osmotic pressure
ρ	Density
ρ_e	Space charge density
ρ_W	Water density
σ	Electrical conductivity
τ	Dimensionless time
Φ	Total flux of φ entering the unit cell
φ	Generic scalar
ϕ	Electric potential

Ψ	Optimization function
χ	Pump efficiency

Averages

$\{\cdot\}$	Average over one wall of a unit cell
$\tilde{\cdot}$	Average over both walls of a unit cell
$\langle\cdot\rangle$	Average over the whole stack area

Acronyms

AEM	Anion exchange membrane
ARED	Assisted reverse electrodialysis
BWRO	Brackish water reverse osmosis
CapC	Capital costs
CCD	Critical current density
CEM	Cation exchange membrane
CFD	Computational fluid dynamics
CS	Cost saving
DNS	Direct numerical simulation
ED	Electrodialysis
EDL	Electric double layer
ERD	Energy recovery device
GPD	Gross power density
IEM	Ion-exchange membrane (AEM/CEM)
LCD	Limiting current density
MD	Membrane distillation
NED	Net energy density
NPD	Net power density
NPP-NS	Nernst-Planck-Poisson Navier-Stokes equations
OCF	Overlapped Cross filaments

OCV	Open circuit voltage
OpC	Operating costs
PPD	Pumping power density
PV	Pressure vessel
RED	Reverse electrodialysis
RO	Reverse osmosis
SCR	Space charge region
SW	Seawater
SWRO	Seawater reverse osmosis
TLC	Thermochromic Liquid Cristals
TPC	Temperature polarization coefficient
TWW	Treated wastewater
UF	Ultrafiltration
UPC	Unit product cost

Part I: Membrane processes

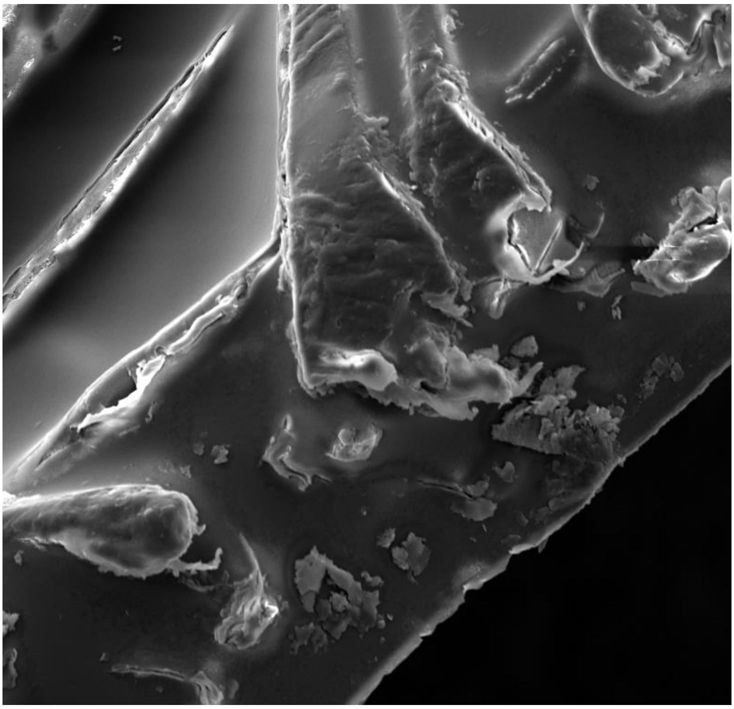

1. General overview

In recent years, membrane processes have been used in many fields (medicine, food industry, desalination, etc.), replacing largely traditional separation methods. The affirmation of these processes is related to their advantages: temperatures close to the environment, no need for chemical additives, a compact and modular design, the ability to selectively transfer specific components and the production of low pollutants and reusable waste [1]. A membrane separation process is driven by a force which activates the flow through the membrane only of some components of the mixture fed, obtaining the permeate (product) and the concentrated or retentate (waste). The primary role of a membrane is therefore to act as a selective barrier, which can allow the passage of some components of the mixture while retaining others. The driving force of the process can be a difference in pressure, concentration, electrical potential or temperature.

Among many existing membrane processes, three processes, which are attracting increasing interest, were deeply studied and investigated in this work: Reverse Electrodialysis (RED), Electrodialysis (ED) and Membrane Distillation (MD).

In the New Policies Scenario, rising incomes and the population increase of 1.7 billion people in developing urban areas, push up global energy demand by more than a quarter to 2040. An increase in electricity demand in developing economies requires strategies for economic development and emission reduction that look at the availability, convenience and clean production of electricity [2]. Research must push in the discovery of new processes for the sustainable production of electricity and in the development and advancement of existing ones. Among many renewable energies, recently the so-called “blue energy” has received renewed interest. This term refers to the possibility to exploit the free energy stored in the salinity difference between the fresh water and salt water as a completely renewable energy source [3] and RED is one of the emerging technology which can harvest the energy from salinity gradient, meeting the demand of new, clean and renewable power sources [4].

In a world scenario of scarcity of clean and potable water, worsened by population growth, intensive agriculture and industrialization [5], ED and MD offer the possibility of obtaining fresh water from brackish or sea waters under operating conditions much more advantageous than other purification or water desalination processes. In particular, ED can operate in atmospheric conditions and does not need intensive pre-treatment [6]. MD offers a theoretical 100% rejection of macromolecules and non-volatile compounds, it can operate at low temperature and pressure and it is insensitive to feed concentration [7]. Despite these important advantages, these two technologies are not yet established in the world desalination market especially of seawater, which is covered by Reverse Osmosis (RO) for 63% [8]. Even though being a process widely used, seawater desalination by RO (SWRO) is high energy demanding. Some new directions for process intensification look at the implementation of hybrid schemes for the combined production of water and energy [9,10] or for the pre-desalting of seawater aiming at the reduction of pumping power requirements [11,12].

2. Membrane Distillation

Membrane Distillation is a thermal separation process that uses a hydrophobic and microporous membrane to separate the vapour from the aqueous solution [13]. The thermal energy supplied to the solution involves the formation of water vapour that can passes through the pores of the membrane reaching a cold channel, the distillate channel, in which it condenses. MD is governed by the difference in temperature, and thus by the partial pressure difference, between the two sides of the membrane.

MD modules can be made in a *plate and frame* configuration (usually in laboratory scale) or according to the spiral wound module concept, which is illustrated in Figure 1: the feed and permeate channels, the membrane and the spacers are wrapped around the manifold in which the permeate is collected. The most studied configuration is the Direct Contact Membrane Distillation (DCMD), where the permeate is collected in a cold stream in direct contact with the membrane. This configuration is characterized by high driving force but also high heat losses.

MD is characterized by low operational pressure requirement as well as low working temperatures. The low temperatures make the MD interesting both in the medical field, where high temperatures would sterilize biological fluids [14], and in the food industry, for example to preserve the flavour and colour of concentrated fruit juices [15]. Moreover, it is also possible to associate alternative renewable energy sources such as geothermal energy, solar energy or to exploit waste heat with conventional MD systems, and boost its applicability in remote areas and small scale production [13,16,17]. The lower operating pressures involve lower equipment costs, greater process safety and reduce the stresses to which the membranes are subjected. For this reason, no particular mechanical characteristics of the membranes are required and their only function is that of maintaining the liquid / vapour interface. It is so necessary for the membrane to be hydrophobic and porous.

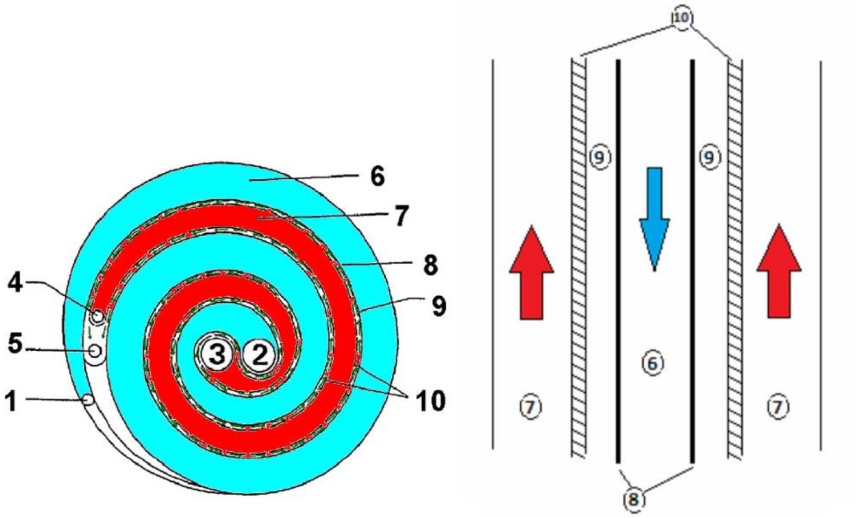

(a) (b)

Figure 1. Sketch of a Fraunhofer spirally wound MD module (adapted from [18]*). (a) Transverse cross section, showing (1) coolant inlet; (2) coolant outlet; (3) feed inlet, (4) feed outlet; (5) condensate outlet; (6) coolant; (7) feed; (8)-(9) membranes, (10) condensate channels. (b) radial cross section, showing (6) coolant, (7) feed, (8) dividing foils, (9) condensate channels, (10) membranes.*

Another important distinct feature of MD is its ability to desalinate highly saline brines and wastewater [19]. For this characteristic, MD is the most appropriate option to treat brines produced in reverse osmosis (RO) plants [20,21].

The interest in MD process development was demonstrated also by the European Commission who funded some projects as for example *Mediras* [22], which aimed at reducing the cost of produced water by MD technology. The overall objective was to optimize a solar driven MD desalination system, demonstrate its cost effectiveness and reliability and bring the technology to the market.

Despite the demonstrated advantages and the many experimental and theoretical studies conducted in recent years, MD is not yet fully developed from the commercial point of view. One of the main reason is the high energy consumption (typical thermal energy consumption ~100 kWh/m^3) compared, for example, to multiple effect distillation, or MED (thermal energy consumption ~40 kWh/m^3 for large plants) and reverse osmosis, or RO (mechanical energy consumption 2–4 kWh/m^3) [7,23,24]. Other reasons are related to the lack of commercially available high performance membranes, the low water flux. One of the main causes responsible for low water flux is the temperature polarization phenomenon, while the concentration polarization has a negligible effect on the permeate flow rate reduction [25].

Temperature polarization results in a temperature difference at the membrane interfaces smaller than the temperature difference between the bulk solutions (Figure 2) and it can lead to a dramatic reduction of the actual transmembrane temperature driving force [7,25].

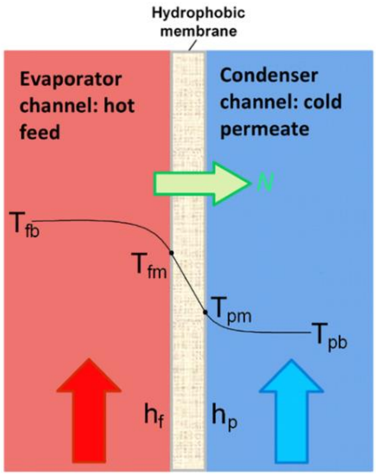

Figure 2. Sketch of the temperature polarization effect in Membrane Distillation.

3. Electromembrane processes

The term “electromembrane process” refers to a large family of processes quite different in their basic concept and/or application. However, they are all characterized by a mass transport coupled with an electrical current through ion-exchange membranes (IEMs) [26]. They can be classified according to their properties as cation exchange (CEM) and anion exchange membranes (AEM) or according their structure as homogeneous and heterogeneous membranes. Cation exchange membranes contain negatively charged groups fixed to the polymer matrix. Due to the exclusion of anions, i.e. the coions, a CEM is impermeable to anions while permeable to the mobile cations, i.e. the counterions. On the contrary, an AEM contains positively charged groups fixed to the polymer matrix and it is preferentially permeable to anions and impermeable to cations. The selectivity of the membrane to the passage of counterions is indicated by the permselectivity. The basic unit in electromembrane processes is called cell pair and consists of a CEM, a “diluate” compartment, an AEM and a “concentrate” compartment. The space between membranes is maintained by inserting polymeric spacers or profiled membranes. In regard to spacers, a net with overlapped or woven filaments is the most frequently used in membrane processes [27]. A number of cell pairs (from some units/dozens at laboratory scale [28,29] to some hundreds for prototypes and industrial units [30]) are piled in order to compose a stack.

The co-ion exclusion of the IEMs, also referred to as Donnan exclusion, gives rise to an electrical double layer at each IEM-solution interface, where the chemical potential gradient is counterbalanced by the electrical potential gradient (Donnan potential), so that the net flux would be nil for perfectly permselective membranes [31]. In other words, due to the electrochemical equilibrium of the solution-IEM-solution system, an electrical potential difference is generated over each membrane, referred to as Nernst potential. The sum of the contributions of all the IEMs of a stack is the open circuit voltage (OCV).

Electromembrane processes can be used in the desalination of salt solutions or in the conversion of chemical energy into electrical energy [26]. The two corresponding processes are Electrodialysis and Reverse Electrodialysis, respectively.

Electrodialysis

Electrodialysis (ED) is known since 1890, but applied for water desalination only since the 1950s [32–34], when the first suitable ion-exchange membranes were commercially available [35,36]. A schematic representation of ED process is reported in Figure 3a: when an aqueous salt solution is pumped through the compartments of the stack and an electrical potential is established between the anode and cathode, the ions are forced to move towards the opposite electrode, i.e. the cations migrate toward the cathode and the anions toward the anode. In this migration, the cations pass through CEMs, but are repulsed by AEMs. Similarly, the anions pass through the AEMs, and are retained by the CEMs. The overall result is the ion concentration increase in alternate compartments called concentrate compartments, while the others, named diluate compartments, become depleted [31]. In order to desalinate the diluate compartment, once a concentration gradient is created between the two channels, the external applied voltage must exceed the Nernst potential, the Ohmic voltage drops and the non-Ohmic voltage drops, related to water transport, back diffusion and mass transport phenomena. The end compartments in Figure 3a contain red-ox solutions which convert the electron flux into an ion flux, and are delimited by electrodes connected to an external power supply. In the past, NaCl has been used as the electrode rinse solution but this causes the production of active Cl_2 in the anodic compartment. Electrode rinse solutions containing SO_4^{2-} salts are now usually preferred in order to avoid damages to the anode [37].

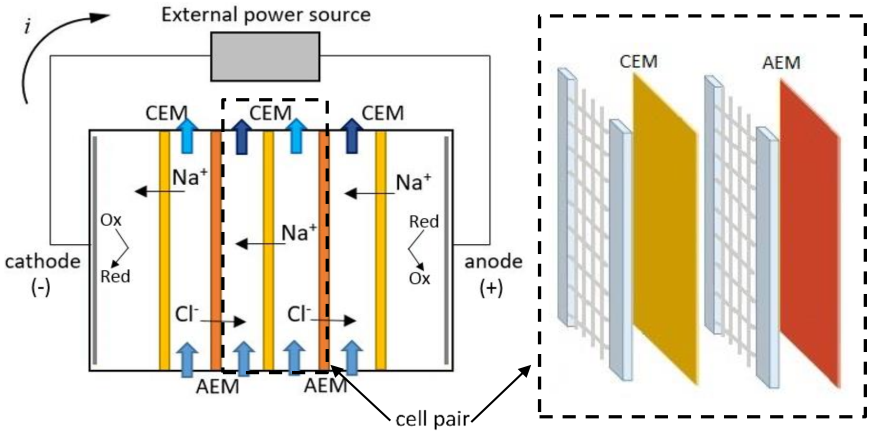

(a) (b)

Figure 3. Schematic representation of a) ED stack and b) cell pair in a parallel flow configuration.

Currently, the largest industrial-scale application of ED is brackish water desalination while in other applications, ED has become of increasing relevance in the last decade, e.g. in the production of high-quality industrial process water and the treatment of industrial effluents [37,38]. In seawater desalination, ED has not yet established at industrial-scale and this is mainly due to the relatively higher cost of ion-exchange membranes (IEMs) compared to RO membranes, and to the reduction of permselectivity when seawater is used as the feed solution [37]. However, possible applications of ED for seawater desalination are currently studied. A combination of ED and brackish water reverse osmosis (BWRO) was for example proposed by Galama *et al*. [39] as an alternative to seawater reverse osmosis (SWRO). In addition, the application of multistage ED to seawater desalination is also currently studied [31].

Contribute to establishing ED as the new standard for seawater desalination is also the aim of the *REvivED water* EU project [40]. In this project, 10 partners, including the University of Palermo, are currently studying multistage ED systems, RED-ED and ED-RO configurations but also ED coupled with photovoltaic panels for desalination in remote and developing countries. The final goal of this project, which will finish in 2020, will be to produce safe, affordable and cost-competitive drinking water, with significantly reduced energy consumption compared to state-of-the-art Reverse Osmosis (RO) technology.

It must be pointed out that, since the first ED experiment, the performance of the ED process has greatly improved due to the research efforts towards producing high-performing ion-exchange membranes [41]. However, real membrane properties still have an important role in limiting the performances, especially non-ideal permselectivity and water permeability. The minimum energy consumption, expected for seawater desalination, may increases by a factor of 3 if co-ions flux is considered and by about 10% when also the water flux is considered [42,43].

Performance of ED stacks are also determined by concentration polarization phenomena, which cause mass transfer limitations and the non-Ohmic voltage drop. According to the IUPAC Recommendations, concentration polarization is defined as "a concentration profile that has a higher (lower) level of solute nearest to the upstream membrane surface compared with the more-or-less well-mixed bulk fluid far from the membrane surface" [44]. An example of concentration profiles close to a cation exchange membrane is reported in Figure 4.

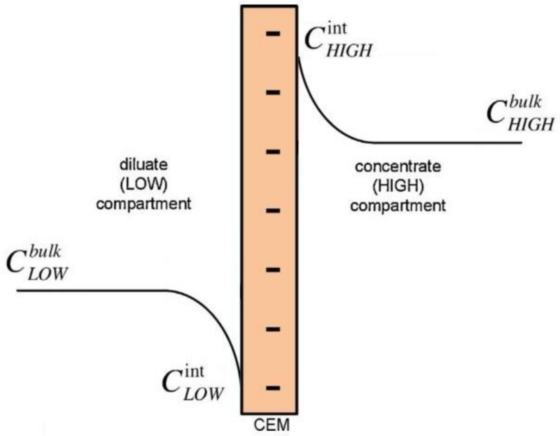

Figure 4. Concentration profiles in ED, in diluate and concentrate compartments, close to a CEM.

These profiles arise because the kinetics of transport in solutions and in membrane is different and this leads to the creation of enrichment and depletion layers next to the membrane. The concentration gradient at the membrane interfaces is larger than that one between the two bulk solutions and it leads to a larger Nernst potential that has to be exceeded, with a consequent increase in energy consumption. Concentration polarization has another serious effect in ED: in the diluate channel, the concentration at the membrane surface decreases with current density and, according to the classical theory, when becomes equal to zero, the limiting current density i_{lim} is reached. This is the maximum reachable current density according to this theory. However, in ED, it was observed that this limit does not exist. Beyond a certain current density, still named limiting current density (LCD, to distinguish from i_{lim}), the electrical resistance drastically increases due to the depletion of ions within the boundary layer [45]. Even if the mass transport keeps slowly growing as the current density exceeds the LCD because of the transport of H^+ and OH^-, produced by a water splitting reaction, and mainly because of the electroconvection [46], the overlimiting region is still a non-operating region so far and thus it is important to determine the LCD by studying the concentration polarization. However, several studies presented in the literature demonstrated that the LCD appearance in ED does not correspond to the zero concentration at the membrane interface, thus it cannot be explained by the classical theory of concentration polarization [47–49]. Therefore, the prediction and determination of LCD in ED is still an open and widely discussed issue.

Reverse Electrodialysis

RED is an electrochemical membrane-based process that directly converts the chemical energy associated with the salinity gradient between two solutions into electrical energy (Figure 5).

The end compartments are fed by the electrode rinse solution containing an ionic couple (for example, Fe^{3+}/Fe^{2+} if the end membranes are AEMs or $[Fe(CN)_6]^{3-}/[Fe(CN)_6]^{4-}$ if they are CEMs [50,51]) and are provided with electrodes which can be closed via an external circuit on an electrical load. When the circuit is closed the voltage at the electrodes triggers redox reactions, with release of electrons at the anode and consumption of electrons at the cathode, so that an electrical current flows through the load. As a consequence, the co-ion exclusion of the IEMs gives rise to selective ionic fluxes within the stack: cations move through CEMs and anions through AEMs, from each concentrate channel towards the two neighbouring diluate ones. The voltage over the stack, and thus over the external load, will be given by the OCV less the voltage losses due to different phenomena, collectively indicated as the internal resistance of the stack.

Applications of the RED process started to harvest the natural salinity gradient that can be found for example where river water is mixed with seawater, i.e. for the case of open-loop configuration systems. Several investigations have been performed to understand how operating conditions and membrane properties can affect the power density. Since the first experiment, carried out in 1954, which reported a power density of 0.05 W/m^2 [52], an increase of about 176% was achieved after 55 years with a power density of 0.93 W/m^2, reported by Veerman *et al*., when seawater-river water are used [28]. The obtainable power density can further increase if high salinity solutions and/or high temperatures are adopted. For example, Daniilidis *et al*. [53] obtained a power density of 6.7 W/m^2 using brines at 60 °C.

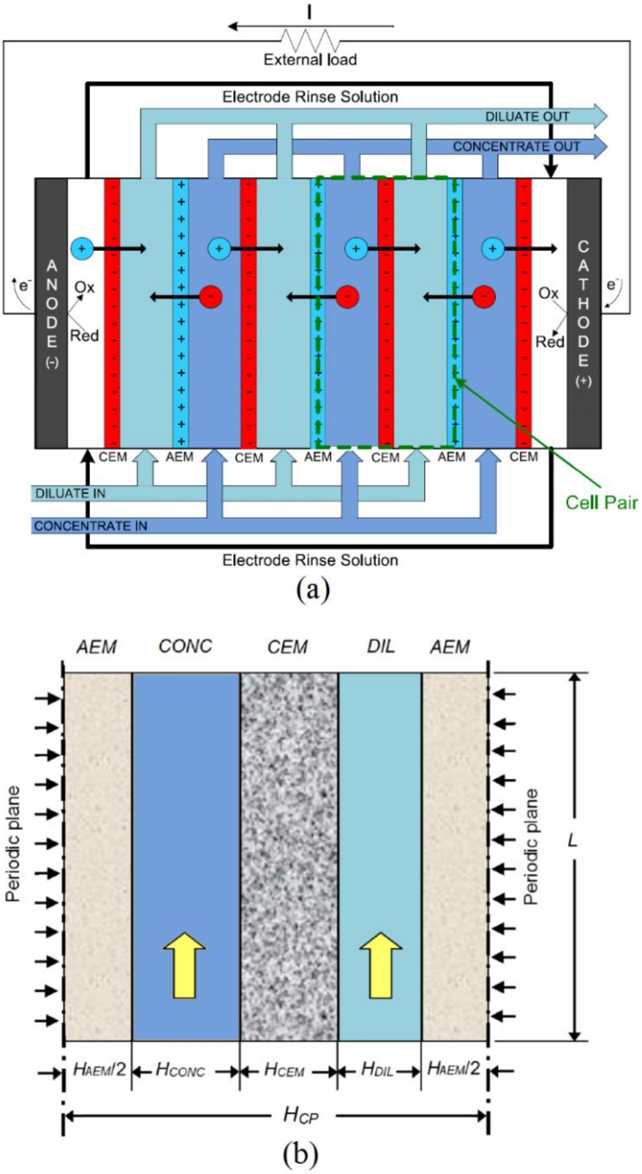

Figure 5. Schematic representation of a RED stack (a) and of an individual cell pair (b).

These approaches were studied at University of Palermo within the activities of *REAPower* EU project [54], which led to the successful design and operation of the first pilot scale prototype, installed in real environment and fed with natural seawater and brine from the saltworks [30,55].

RED technology has been investigated also in a closed-loop configuration within the *RED-Heat to Power* EU project [56], with the aim to convert low-grade waste heat into electricity. In this case, it is possible to talk of a Reverse Electrodialysis-Heat Engine (RED-HE) in which a traditional RED unit is coupled with a Thermal Regeneration Unit (TRU) [57]. The latter can restore the initial concentrations of the solutions exiting from the RED unit, closing the loop.

Even though these improvements, RED is still characterized by small net power density values, limiting the applicability of this process. The net power density which can be provided by a RED stack is determined by the following main aspects: (i) theoretical (maximum) electromotive force, or OCV; (ii) Ohmic losses; (iii) pumping power consumption; and (iv) non-Ohmic losses [58]. OCV depends mostly on the ratio between the ion activities of the two solutions, but also on the membranes permselectivity which can undergo a non-negligible reduction when concentrated solutions are adopted [53,59]. Ohmic losses are due to the stack elements such as membranes, diluate channels, concentrate channels and electrode compartments. When the diluate compartments are fed by a low concentration solution as river water, often they give the main contribution to the Ohmic resistance [60–62]. On the contrary, when more concentrated solutions are used, the membranes' resistance is the dominant contribution [53]. Moreover, non-conductive spacers may cause a significant increase of the compartment's Ohmic resistance [53,60–63]. Profiled membranes offer a path for the ionic flow through the conducting profiles, so that the electrical resistance may remain unchanged or even decrease, depending on the relative electrical conductivity of membrane and solution. Vermaas *et al.* [64] reported a reduction of 30% of the Ohmic resistance in a stack using profiled membranes with respect to a stack provided with non-conducting spacers; similar findings emerged from a subsequent study [65].

The obtainable net power may be significantly reduced by the energy consumption for pumping the feed solutions. At the flow rate that maximizes the net power this reduction is typically ~10-20% [28,60,64–66]. The total pressure drop through the stack is due to (i) the distribution/collection system (manifolds) and (ii) the channels [66]. A properly designed geometry of the manifolds can reduce drastically their contribution to the hydraulic loss [65,67]; on the other hand, the channel features (inter-membrane distance and shape) may have a weighty effect on the net power. In regards to the channel shape, traditional net spacers may lead to a pressure drop much higher than in the empty channel [65,68,69], while profiled membranes may have simpler geometries able to increase only slightly the hydraulic friction [64,65,70].

The ion transport across IEMs from the concentrate channel to the diluate one causes non-Ohmic phenomena of concentration changes that result in a reduction of driving force and thus in a further voltage drop. This voltage loss is usually quantified as non-Ohmic loss, by analogy with the Ohmic one, and is due to two contributions caused by: (i) the streamwise concentration change in the bulk of the solution, and (ii) the concentration polarization in the diffusion boundary layers [58].

When an electrical current passes through a RED stack, a concentration boundary layer (Figure 6) develops between each membrane surface and the fluid bulk [31]. The increased salt concentration at the membrane surface in the diluate channel and, conversely, the decreased salt concentration at the membrane surface in the concentrate channel reduce the actual electromotive force [60]. By using the couple seawater – river water, the contribution of concentration polarization to the stack resistance is significant [60,62,64,71].

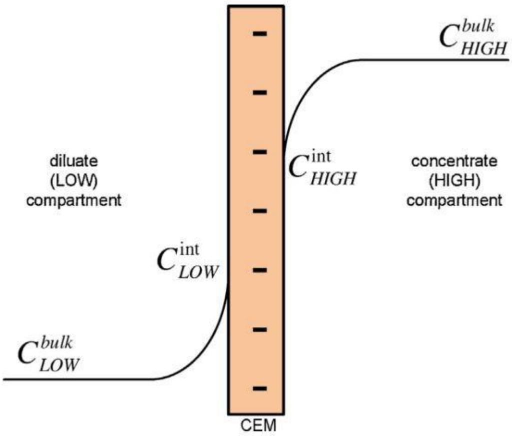

Figure 6. Concentration profiles in RED [59]*, in diluate and concentrate compartments, close to a CEM.*

4. RO and hybrid systems

Among membrane processes for water desalination, reverse osmosis (RO) has become the dominant technology [72,73], covering 63% of the world desalination market [8]. In RO plants, high pressure seawater feed pumps supply the pressure necessary to generate a positive flux of fresh water through the membrane [74].

Energy consumption is the largest operational cost of seawater reverse osmosis (SWRO) [11]. As in all separation processes, a thermodynamic lower constraint to the energy required for the separation of a feed *(f)* of given salinity into a diluate *(d)* and a concentrate *(c)* is the difference in Gibbs free energy between feed and products, $G_f-(G_d+G_c)$. The issue is analysed, for example, by Post *et al.* [6]. In the limit of an infinite amount of feed, the minimum energy per unit volume of the diluate coincides with the osmotic pressure difference existing between feed and diluate (~2.8 MPa, or 0.78 kWh/m^3, if the feed is seawater at 32 g/l NaCl). The minimum energy increases significantly as the d/f volume ratio (water recovery ratio) increases; for example, obtaining 1 m^3 of freshwater from 2 m^3 of seawater requires ~1 kWh.

However, the above values hold only in the limit of reversible separation processes, characterized by vanishing flow rates. If a significant flow rate of diluate is required, irreversible phenomena become important and the energy required for separation increases.

In SWRO plants, specific energy consumption has declined dramatically in the past 40 years: better membranes, improvements in pump efficiency and the use of energy recovery devices (ERD) have allowed values of 3–4 kWh/m^3 or even lower to be obtained [75].

In order to enhance process performance and reduce energy consumption, researchers are studying new nanotube and nanocomposite membranes [17] and new designs of the pressure vessels [76], though this cannot overtake the thermodynamic constraint related to the need of exceeding the osmotic pressure of the stream flowing in the feed channel to obtain a permeate. Some new directions for process intensification look at the implementation of hybrid schemes for the combined production of water and energy [9,10] or for the pre-desalting of seawater aiming at the reduction of pumping power requirements [11,12].

Under this respect, two different approaches have been proposed. The first requires a low-salinity sink stream, such as reclaimed water from a waste water treatment plant. Pre-desalting is obtained by the transport of water from the sink stream into the feed seawater, when osmotic membranes are adopted (e.g. Pressure Retarded Osmosis, Forward Osmosis and Pressure Assisted Osmosis [77–79], see

Figure 7a), or, *vice versa*, by the transport of salt from the feed seawater into the sink stream, when ion-exchange membranes are used (e.g. Reverse Electrodialysis, short-circuit Reverse Electrodialysis and Assisted Reverse Electrodialysis [80–82], see Figure 7b).

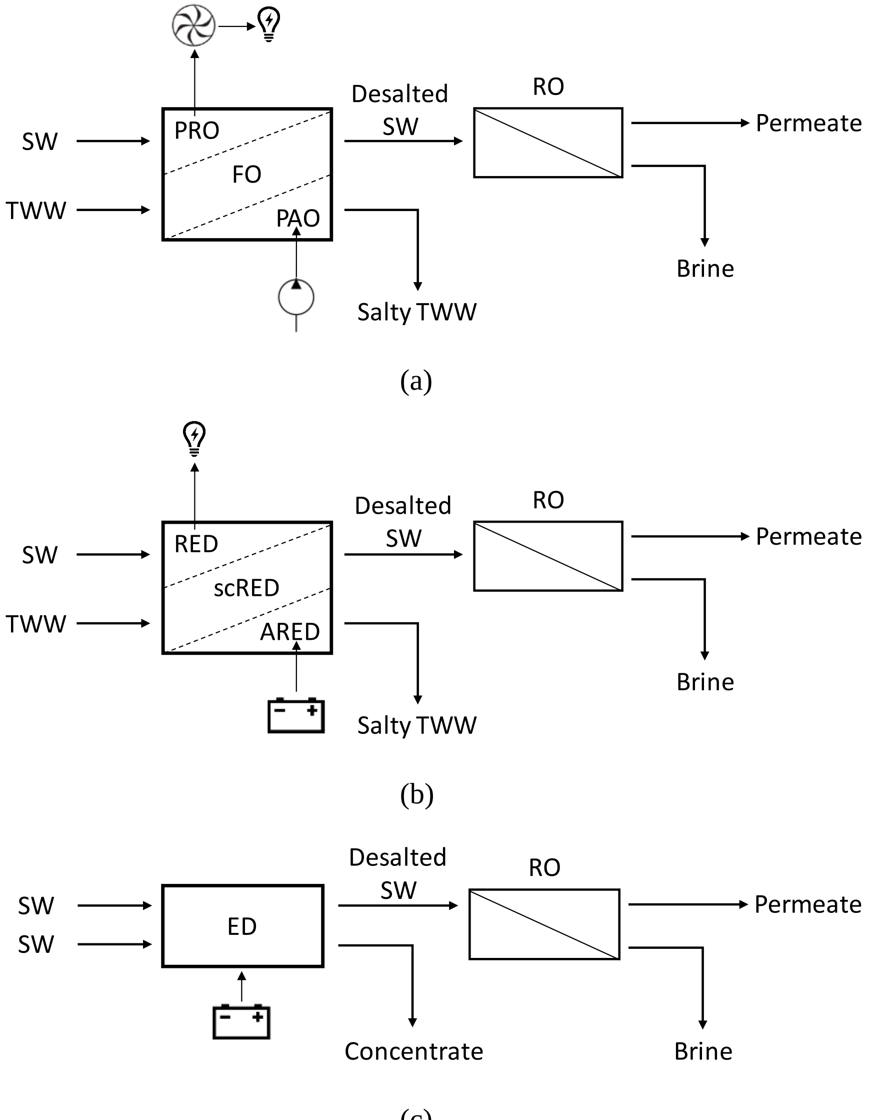

(a)

(b)

(c)

Figure 7. Schematic diagrams of the possible hybrid system configurations where Reverse Osmosis is coupled with a) Pressure Retarded Osmosis (PRO), Forward Osmosis (FO) or Pressure Assisted Osmosis (PAO); b) Reverse Electrodialysis (RED), short-circuit Reverse Electrodialysis (scRED) or Assisted Reverse Electrodialysis (ARED); c) Electrodialysis (ED).

With the second approach, pre-desalting is obtained by transport of salt from the feed stream into a higher salinity sink stream (Electrodialysis, see Figure 7c).

Hybrid configurations where electromembrane processes are coupled with RO are currently studied at University of Palermo within the activities of the *REvivED water* project, which include the construction of a pilot prototype. Experimental tests will demonstrate the energy savings and advantages, bringing the integrated ED/RED-RO system in desalination market.

5. Scope and outline of the thesis

The scope of the thesis is to study membrane processes that can have an important role in the world energy/water market but still are not at an industrial scale. These processes, i.e. MD and electromembrane processes, can be improved, developed and optimized studying each phenomena involved in the process, from the microscopic scale to the process scale. A validated simulation tool is the more powerful, easy and fast way to understand where the process can be improved and if new solutions (e.g. hybrid systems involving RO) can be implemented in order to produce more energy/drinking water with a lower cost, becoming in this way competitive with respect to other standard processes.

The membrane processes described in the previous sections, are inherently affected by polarization phenomena, which cause always a decrease of the driving forces and thus a loss of efficiency. The negative effects of polarization phenomena can be counteracted improving convective motions, which affect mixing and thus the temperature/concentration field within the channel. Therefore, polarization phenomena depend strongly on the channel geometry (size and shape) and the flow rate [68–70,83]. Spacers, usually made up of a network of overlapped or woven filaments (see Figure 8), can act as mixing promoters. They are also essential as they mechanically support the membranes. In ED and RED, profiled membranes (Figure 9) can be used instead of spacers: profiles allow to support the membranes, as the spacers do, but without their disadvantages (cost, increased Ohmic resistance of the channels) [64].

In such systems, understanding the fluid dynamics in the channels is crucial for enhancing mixing in order to reduce undesirable polarization effects but also for limiting pressure drop. Spacers or profiled membranes indeed are obstacles that cause an increase of the friction factor with respect to the empty channel case.

In order to study how the presence of spacers or profiled membranes reduces polarization effects, mass transport or heat transport in the channels can be studied by means of 3-D Computational Fluid Dynamics simulations. Local temperature or concentration distributions and flow field can be visualized and simulation results are post-processed in order to obtain the Nusselt number, the Sherwood number and the friction factor. These dimensionless numbers can give a qualitative information about the spacer/profiled membrane performance given from the balance of the polarization phenomena reduction and the pressure drop increase.

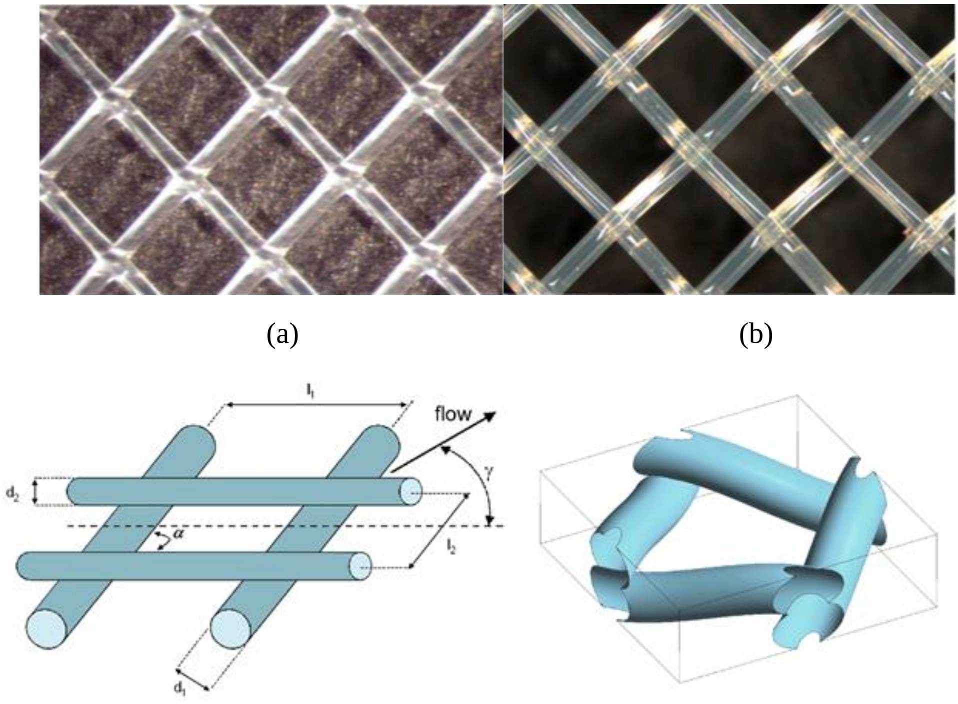

(a) (b)

(c) (d)

Figure 8. Pictures of net spacers with (a) overlapped crossing filaments and (b) woven filaments. (c) General overlapped spacer geometry, formed by stacking two arrays of cylindrical rods, or filaments: the most general case is characterized by diameters d1, d2, pitches l1, l2, included angle α and flow attack angle γ. (d) Woven geometry: a unit cell is shown for the case d1= d2, l1= l2=6 d, α=90°.

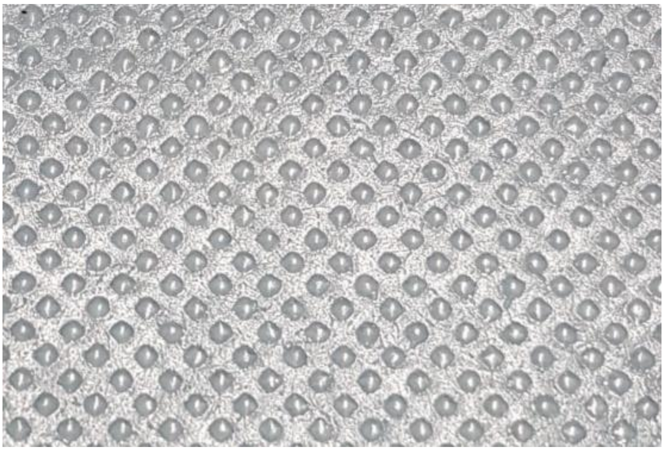

Figure 9. Top view of a profiled membrane with pillars profiles.

In electromembrane processes, mass transport (of salt and water) is not the only phenomenon involved. Ohmic phenomena, related to the resistance offered by aqueous salt solutions, membranes and spacers, have to be considered. In complex shape channels, which can also include conductive membrane profiles, determining the Ohmic resistance can be tricky and CFD simulations can be helpful.

Another phenomenon observed in ED is the electroconvection, i.e. the appearance of electrokinetic eddies at current density values higher than the Limiting Current Density (LCD). CFD simulations can study the formation and the growth of these eddies.

Because of the complexity and the different phenomena involved in electromembrane processes, purely empirical methods, based on experimental tests and on a trial-and-error approach, are not practical for design and performance prediction, thus mathematical models appear to be mandatory. A complete, albeit simple, model of electromembrane processes can be coupled with CFD, implementing correlations of the dimensionless numbers in order to estimate polarization phenomena and pressure drops. This approach gives a quantitative appreciation of the relative importance of fluid dynamics-dependent quantities in affecting performance parameters (e.g. the maximum obtainable net power density in RED or the minimum energy consumption in ED). The model, provided it is tuned and validated against experiments, can be used for optimization purposes. However, while in RED operations the optimization to maximise the net power density can be performed without any limitation, in ED operations, the current density should not overcome the Limiting Current Density. The model should then provide an estimation of this important parameter so that it can be used to design ED units that work far from the LCD.

As already observed, the Limiting Current Density issue in ED it is not yet fully clarified, as well as its determination and it requires further and deep investigations, even based on carefully designed experimental campaign.

Such a complete model can still be implemented in user-friendly platforms such as Excel™ or in more advanced Fortran codes and can be used for process design and development of electromembrane processes.

In previous sections, electromembrane processes were also presented as pre-desalination methods in hybrid configurations with Reverse Osmosis. These systems can be designed and optimized by using a hybrid model where, the previous validated model for electromembrane processes can be coupled with a model for RO.

In **Part II**, CFD models for heat and mass transfer investigations in complex channels filled either by spacer either by profiled membranes are presented. Some aspects related for example to the proper choice of boundary conditions or the definition of dimensionless numbers are critically discussed. The results are presented in more detail for Membrane Distillation in Section 3 and for electromembrane processes in Section 4. In this section, CFD approaches to simulate Ohmic phenomena and electroconvection are also presented and discussed. Moreover, the results about pressure drops, which is a common aspect for all membrane processes investigated, are presented in Section 5.

In **Part III**, the one-dimensional model for electromembrane processes is presented. A model validation in ARED and RED operation modes and model predictions with different spacers and profiled membranes are reported in Section 3. In this chapter, it is presented also the RED optimization, aiming at maximizing the net power density. In Section 4, the model is validated also in ED mode. Moreover, the LCD issue is deeply investigated: the influence of operating conditions, spacers or profiled membranes, and membrane properties is discussed.

In **Part IV**, a simulation tool for hybrid system is presented. The pilot prototype, installed in Spain within the activities of the REvivED project, is described. Experimental results from the pilot plant are used to validate the hybrid model that is used then to perform a sensitivity analysis.

The summary of the main results is presented in the **Conclusions** chapter, as well as possible improvements and future outlook.

Part II: CFD in membrane processes

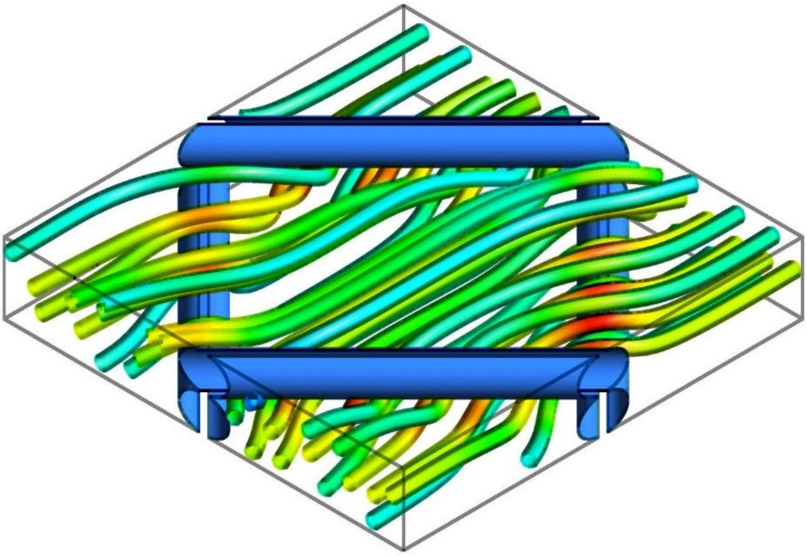

The following results have partially been published in:

La Cerva *et al*., *Desalination*, vol. 411, 2017.

Ciofalo *et al*., *Journal of Physics: Conference Series*, vol 923, 2017.

Ciofalo *et al*., *International Journal of Thermal Science*, vol. 145, 2019.

La Cerva *et al*., *Journal of Membrane Science*, vol. 541, 2017.

1. Literature review

Applications of Computational Fluid Dynamics to the characterization of spacer-filled channels for membrane processes started to appear in the literature with some consistency in the 1990s. In the following literature review, the main works about CFD simulations of heat and/or mass transfer in spacer-filled channels will be summarized and divided between 2-D and 3-D cases. For each main group, the literature will be presented in chronological order.

Some of the published studies regarded simplified, two-dimensional geometries (e.g. cylindrical obstacles placed in a plane channel). Thus, in 2001 Cao *et al.* [84] conducted two-dimensional simulations with the Ansys-Fluent™ code for a plane channel provided with filaments of circular cross section placed orthogonally with respect to the flow. They investigated the influence of the filament arrangement (adjacent to one wall, staggered, floating) on velocity distribution, wall shear stress, turbulence. Convective transport was not explicitly simulated but mass transfer coefficients were estimated from the hydrodynamic quantities (boundary layer thickness, wall shear stress). The simulations showed that transverse spacer cylinders floating in the channel may be more desirable then filaments touching the walls. They also showed that reducing the distance between transverse spacer cylinders can reduce shear stress peaks and produce more active eddies, which may improve mass transfer at the membrane surfaces. However, it was demonstrated that the reduction in the transverse cylinder distance could also significantly increase the channel pressure drop and thus the operating costs.

In 2013 Qureshi and Shakaib [85] considered developing flow in a multi-cell geometry, consisting of a flat two-dimensional channel with transverse cylindrical filaments, half the channel height in diameter and longitudinally spaced by 3 or 4 times the channel height (spacers s3 and s4). Steady-state (laminar), 2-D simulations were conducted by Ansys-Fluent™. The authors used velocity inlet and pressure outlet conditions at the opposite vertical faces and assumed the membrane surfaces to be impermeable and no-slip walls. Furthermore, they imposed a constant heat flux at the top and bottom walls. They found that shear, heat and mass transfer rates were 10-20% higher in spacer s3. They compared CFD predictions with empirical correlations proposed in 1987 by Schock and Miquel [86] and obtained a satisfactory agreement in the Sherwood number, while the Nusselt number was underpredicted by CFD.

In 2012 Shakaib *et al.* [87] studied the effect of spacer arrangement on both sides of the membrane in MD by conducting two-dimensional simulations with Ansys-Fluent™ for a multi-cell geometry including a hot (feed) channel, a thermally conductive membrane, and a cold (permeate) channel. The hot and cold channels were of the same height and each was provided with its own spacer. As in the previous studies, spacers were modelled as simple arrays of filaments of circular cross section placed orthogonally with respect to the flow and occupying half the channel height. The authors imposed a constant thermal conductivity for the membrane and a variable inlet velocity for the feed and permeate channels (Re≈100-700 by the present definitions). Laminar flow was assumed for Re<~300 and two different turbulence models (Spalart-Allmaras and *k*-*ω*) were used for larger Re. CFD results were compared with the experimental correlation proposed by Phattaranawik *et al*. [88] in 2003 for the Nusselt number and a satisfactory agreement was reported. The authors found that recirculation and stagnant zones are created near the contact points between the spacer filaments and the membrane surface; the recirculation regions reduce temperature polarization while the stagnant zones produce the opposite effect. In agreement with Cao *et al*. [84], they observed that heat transfer rates increase when the spacer filaments are not in contact with the membrane and that staggered filament arrangements are preferable.

Although they may provide valuable insight into the basic mechanisms of flow separation and drag, 2-D studies can only deal with transverse filaments and are not adequate to predict the complex mixing and heat / mass transfer enhancement caused by real 3-D spacers.

In 2001 Karode and Kumar [89] presented purely hydrodynamic CFD simulations for a multi-cell model of the ultrafiltration spacer-filled channels investigated experimentally by Da Costa *et al*. [90]. The authors considered overlapped spacers in which the pitch (inter-filament distance) to channel height ratio ranged between 1 and 4 and the Reynolds number between ~500 and ~5000. Steady-state flow was assumed in all cases. The PHOENICS™ CFD code was used. The main factors influencing the effectiveness of a spacer were found to be the pitch to channel height ratio and the angle between the spacer filaments. For the highest inlet flow rates, simulations overestimated the pressure drop compared to that measured experimentally; Karode and Kumar attributed this discrepancy to the non-ideality of the actual spacers that could allow some fluid flow between the filaments and the membrane.

Li *et al*. [27] used the CFX-4.3™ code to study, for a non-woven geometry, the influence on mass transfer of pitch (distance between parallel filaments) l, angle α between filaments and flow attack angle γ. They carried out direct numerical simulations (DNS) for Reynolds numbers of ~200-1000, a range in which spiral wound membrane modules may actually operate. The authors defined the average mass transfer coefficient as the area average of the local mass transfer coefficient.

The results, in terms of Sherwood number in function of Power number (Pn), showed the spacer geometry to be optimal for l/H=4, α=120° and γ=30°.

Koutsou *et al*. [91] performed DNS at Re<800 using Fluent™. The computational domain was a periodic unit cell. The authors highlighted that a transition to unsteady flow occurs at Reynolds numbers of 140–180 for the parameter range examined. They also found the presence of closed recirculation zones attached to the spacer filaments, presumably detrimental for concentration polarization and fouling. In a later paper, Koutsou *et al*. [92] investigated Reynolds and Schmidt number effects on the time-mean local and spatially-averaged Sherwood number, taking into consideration various realistic spacer geometries. They carried out 3-D DNS with the same Reynolds number range as in [91] and Schmidt numbers in the range 1-100. A local time-mean value of the mass transfer coefficient (k) at the channel walls was defined on the basis of the local time-mean value of the wall mass flux and of the local time-mean concentration at the channel symmetry plane. In order to calculate the overall mean Sherwood number, the authors used the spatially averaged value of k. They found that the distributions of the local time-mean Sherwood number at the top and bottom walls were symmetrical with respect to the channel diagonal, which was also the direction of the mean flow.

Koutsou *et al*. [93] developed a novel spacer geometry consisting of spheres of diameter equal to the channel height H connected by cylindrical segments of diameter H/2. They considered the periodic unit cell formed by four neighbouring spherical nodes and connecting segments and performed DNS using Fluent™. The main advantage of this novel geometry is that the contact of the spherical spacer nodes with the membrane surfaces occurs pointwise, unlike in conventional geometries characterized by contact lines that create "dead" zones associated with reduced mass transfer rates. The authors observed the same general trends of results obtained with conventional spacers, but, regarding the local shear stresses and mass transfer coefficients on the membrane surface, they found that the novel geometry exhibits higher values and a more uniform spatial distribution of these parameters.

Cipollina *et al*. [94] studied spiral wound MD channels with double layer filament spacers using either DNS or steady state simulations. The computational domain included 5-6 unit cells both streamwise and spanwise and was meshed by a tetrahedral unstructured finite volume grid. The code used was Ansys-CFX™. The authors imposed Re ≈ 400, developing flow and thermal fields along the unit cells starting from uniform inlet velocity and temperature (i.e., inlet-outlet conditions with no periodicity), and a uniform heat flux on both walls. They concluded that higher velocities reduce temperature polarisation while filaments transverse to the flow increase polarisation. In a further paper [95], the authors extended the study to a larger variety of non-woven spacers. The results confirmed that filaments mainly parallel to the fluid flow direction are to be preferred, and showed that 3- and 4-layer spacers provide a better compromise between low ΔP and low temperature polarization than diamond or oblique 2-layer spacers.

Al-Sharif *et al*. [96] studied the effect of three different overlapped spacers on fluid dynamic, heat transfer and temperature polarization using OpenFOAM®. Like Cipollina *et al*. [94,95], they adopted a developing flow approach, i.e. they considered a certain number of unit cells in the axial direction and applied uniform profiles for velocity and temperature at the inlet of the domain and zero gradient conditions at the outlet. A uniform heat flux boundary condition was imposed on both walls. From the results of simulations for Re ≈ 300-1200, the authors stated that spacers characterized by 3 layers of orthogonal cylindrical filaments placed at 0° (filaments touching the walls) and 90° (central filaments) with respect to the flow (type 3) caused the lowest pressure drop, symmetrical temperature profile and high velocities near the membrane walls. Spacers with two layers of orthogonal cylindrical filaments placed at 0°-90° with respect to the flow (type 2) were the least desirable as they produced asymmetric temperature and velocity profiles and high pressure drops. An intermediate behaviour was reported for spacers with a flow attack angle of 45° (type 1).

Also Mojab *et al*. [97] used OpenFOAM® to investigate by DNS laminar to turbulent flow regimes in a channel provided with an overlapped spacer, which consisted of two layers of mutually orthogonal rods, or filaments, placed at 45° with respect to the flow direction. The filament spacing was just 1.085 times the channel height, equal in its turn to twice the rod diameter. This configuration was identical to the commercial spacer CONWED-1™. The authors used the periodic unit cell approach with no-slip conditions at the spacer and membrane surfaces. They found that the main flow splits into two streams which move parallel to the filaments with 90° direction difference to each other. At the cell midplane these streams interact and exchange momentum. The 90° angle between the flow streams produces tangential forces which cause secondary swirling motions in the main flow streams. The authors found four different flow regimes: laminar-steady (Re<480), laminar-unsteady-periodic (Re=480-720), fully unsteady (Re>720) and turbulent flow proper (Re>2400).

Saeed *et al*. [98] used Fluent™ to investigate the impact of dimensionless filament mesh spacing on wall shear stress and mass transfer coefficients for the two membrane walls. They employed steady state and laminar flow conditions and considered as the computational domain a strip of unit cells including six bottom filaments and one top filament. The average mass transfer coefficient was defined as the area average of the local mass transfer coefficient. The authors compared different spacers with pitch to channel height ratios (*l*/*H*) varying between 2 and 6; cases with different values of *l*/*H* for the top and bottom layer of filaments were also considered. The Reynolds number (based, in this case, on hydraulic diameter and mean interstitial velocity) ranged between 75 and 200 (when computed on the basis of the present definition, Re varies as a function of the pitch to channel height ratios of each filament layer). In all simulations the flow direction was parallel to the top filaments. The authors observed closed flow recirculation near the bottom membrane surface for spacer geometries characterized by $l/H \leq 3$. For spacers with $l/H \geq 4$ they observed reattachment and separation regions, with a reattachment point location that shifted downstream with an increase in Re, until it met the next bottom filament. Finally, they found that the spacer arrangement with l/H=4 on both walls provides moderate pressure drops and the highest Spacer Configuration Efficacy (defined as the ratio of the Sherwood number to the power number).

With the aim of characterizing water flow in a spacer filled channel, Bucs *et al.* [99] performed Particle Image Velocimetry (PIV) in a transparent test section provided with a commercial non-woven Toray™ spacer with a thickness of 0.787 mm, l/H=5.56, a flow attack angle of 45° and filaments of diameter varying along their axis. They also simulated the unit cell of the experimental geometry, reconstructed from computerized tomography (CT) scans. The authors assumed steady laminar flow and Re≈112, 256 and 480. The measured flow was laminar with only a slight unsteadiness in the upper velocity limit, and CFD simulations were in good agreement with the measured flow fields.

Tamburini *et al.* [100] studied the effects of spacer orientation on heat transfer in MD channels provided with non-woven spacers using DNS, the unit cell approach and the Ansys-CFX™ code. In order to reproduce their own experimental measurements as faithfully as possible, the authors considered only one of the walls (top wall) to be thermally active (i.e., representing a membrane) and imposed on it a third-type (mixed) boundary condition with an outer temperature of 19°C and an interposed thermal resistance $r_{T,ext}$ of $6.25 \cdot 10^{-3}$ m^{2}K/W. The opposite (bottom) wall and the filament surfaces were assumed to be adiabatic. The average Nusselt number {Nu} was defined as the area average of the local Nu on the active wall. The authors found that, when the fluid moves at a 45° angle with respect to the filaments adjacent to the top wall, {Nu} is higher than in the 0° and 90° orientations. They also compared CFD predictions with their own experimental results, obtained by Liquid Crystal Thermography, and found a good agreement in the time averages of both local and surface-averaged Nusselt numbers.

Gurreri *et al*. [69] used Ansys-CFX™ to simulate woven (w) and overlapped (o) spacers with three pitch to height ratios (l/H=2, 3, 4), two different flow directions (either parallel to a filament, γ=0, or bisecting the angle formed by the filaments, γ=45°) and four Reynolds numbers (1, 4, 16, 64). Such low Re are representative of flow in Reverse Electrodialysis (RED) stacks. They found that the filament spacing has a clear effect on Sh for all Re only in woven spacers with γ=45° (in the range investigated, Sh decreases as l/H increases), while for the overlapped arrangement the dependence of Sh on l/H is not as significant. The authors stated that the woven arrangement establishes different flow fields than those typical of overlapped spacers, raising pressure drop but favouring mixing, especially for higher Reynolds numbers and γ=45°. Finally, they found that the woven spacer with γ=45° is the most promising configuration for mixing; it yields higher values of Sh than the case γ=0° for all Re and l/H, although the improvements are lower at high Re.

As the above review shows, CFD simulations of spacer-filled channels for membrane processes started to appear in the literature since the year 2001 and have been presented at an increasing rate since then. They have been based, in most cases, on a small number of open source or commercial codes (OpenFOAM®, Ansys-CFX™, Ansys-Fluent™ and, in one case, PHOENICS™), since in-house codes are poorly suitable for the complex geometry of spacer-filled channels. Published studies are almost evenly divided between those using the Periodic Unit Cell approach [27,69,91–93,97,99,100] and those simulating multi-cell, developing flow configurations [85,87,89,94–96,98]. Further distinctions can be drawn according to the 2-D [84,85,87] versus 3-D [27,69,89,91–100] dimensionality of the simulations and to the flow regimes investigated: thus, some authors carried out only steady-state, laminar simulations [69,85,87,95,97,99]; others dealt with unsteady and early turbulent regimes by Direct Numerical Simulation [27,91,92,94,100]; and others yet [84,87] used turbulence models (RNG k-ε in the former case, Spalart-Allmaras and k-ω in the latter). In regard to the phenomena modelled, some papers [89,91,97,99] simulated only the fluid flow, while others considered also heat transfer [85,87,94–96,100] or mass transfer [69,92,93,98].

Schwinge *et al*. [101], Ghidossi *et al*. [102], Hitsov *et al*. [103], Karabelas *et al*. [104] and other authors have presented reviews addressing a number of issues in the modeling of spacer-filled channels. Fimbres-Weihs and Wiley [105] examined problems concerning the definition of the dimensionless numbers that characterize the phenomenon, the use of periodic conditions, and the comparison of 3-D vs. 2-D and steady-state vs. transient simulations.

2. Modelling complex channels: general aspects and approaches

In this chapter, the "unit cell approach", adopted in all the simulations performed will be presented. Moreover, a number of aspects not sufficiently clarified so far will be discussed before reporting the results of a computational simulation campaign that aims to study transport phenomena in the typical channels of the membrane processes here investigated. The main issues addressed in the following sections are:

- definition of dimensionless numbers;
- influence of boundary conditions;
- complex influence of the parameters l/H, γ, Re.

Most of the results that follow were obtained for the spacer geometry consisting of identical overlapping cylindrical filaments (Figure 8c) with d_f=$H/2$ and an intrinsic angle α=90°, under steady-state (laminar) flow assumptions. All simulations were conducted by the finite volume code Ansys-CFX™. Numerical methods and computational details will be discussed in the following sections.

2.1 Unit cell approach

The problem is described by the continuity, Navier-Stokes and scalar transport equations for a constant-property fluid. In the following the transported scalar will be assumed to be a generic scalar φ.

In order to simulate fully developed flow and scalar fields by simply applying periodicity conditions at the opposite faces [69,100], "true" pressure P^* and scalar φ^* are replaced by their periodic components P, φ such that

$$P^* = P + P_s s \tag{1}$$

$$\varphi^* = \varphi + \varphi_s s \tag{2}$$

in which s is the distance along the streamwise (main flow) direction while P_s and φ_s are the large-scale gradients of pressure and scalar, respectively, in the same direction. Note that P_s is always negative while φ_s is positive for flux entering the fluid and negative in the opposite case.

In the simulations, the pressure gradient P_s is imposed while the flow rate and thus the bulk flow Reynolds number Re follow as results of the simulation.

As regards the large-scale scalar gradient, a balance yields $\varphi_s = (\Phi_{in}/V_f)/(\rho u_{void})$ in which u_{void} is the mean “void channel” velocity in the direction s and Φ_{in} is the total flux of φ entering the unit cell from the walls:

$$\Phi_{in} = \int_S \Gamma \nabla\varphi \cdot \mathbf{n}\, dS \tag{3}$$

where Γ is the diffusivity and S is the total wall surface area in the unit cell. Both the flux and u_{void} are evaluated as parts of the solution during the course of the simulation.

Substituting Eqs. (1)-(2) for P^* and φ^* in the standard momentum and scalar transport equations, after some manipulation one obtains the following governing equations (written in Cartesian tensor notation):

$$\frac{\partial \rho}{\partial t} + \frac{\partial \rho u_j}{\partial x_j} = 0 \tag{4}$$

$$\frac{\partial \rho u_i}{\partial t} + \frac{\partial \rho u_i u_j}{\partial x_j} = -\frac{\partial P}{\partial x_i} + \frac{\partial}{\partial x_j}\mu\frac{\partial u_i}{\partial x_j} - P_s\frac{\partial x_i}{\partial s} \tag{5}$$

$$\frac{\partial \rho\varphi}{\partial t} = -\frac{\partial}{\partial x_j}\left(-\Gamma\frac{\partial \varphi}{\partial x_j} + \rho u_j \varphi\right) - \frac{\Phi_{in}}{V_f}\cdot\frac{u_s}{u_{void}} \tag{6}$$

in which u_s is the component of the local velocity along the direction s.

Translational periodic boundary conditions were now adopted for all variables at the opposite faces of the computational domain.

2.2 Definition of dimensionless numbers

Reynolds number

In regard to the Reynolds number, several definitions can be found in the literature, differing in the choice of the length and velocity scales. The length scale has been variously identified with the filament diameter d_f, the channel height H, or the hydraulic diameter $d_h=4V_f/S_{wet}$, in which V_f is the volume of fluid and S_{wet} the wetted surface (including both the filaments and the membrane walls). A further alternative consists in using the hydraulic diameter of the void channel, which can be identified with twice its height (2H) in the limit of laterally infinite plane channel. As to the velocity scale, some authors prefer the volume-averaged velocity u_m along the main flow direction s, which coincides with the area average of u_s on any arbitrary cross section orthogonal to the flow and is sometimes called the interstitial velocity:

$$u_m = \frac{1}{V_f} \int_{V_f} u_s dV \tag{7}$$

An alternative velocity scale is the void channel velocity u_{void}, i.e. the velocity which would yield the given flow rate if the channel were void of any spacer; u_{void} is sometimes called the inlet, approach or superficial velocity. The two quantities u_m and u_{void} are related by

$$u_{void} = u_m \varepsilon \tag{8}$$

where ε is the porosity, or void ratio, V_f/V_{tot}.

Thus, at least the following quantities (covering seven out of a total of eight possible combinations!) have been called the “Reynolds number” in the literature:

- $Re_{(1)} = u_m\, d_h/\nu$ [87,89,94,95,97–99]
- $Re_{(2)} = u_{void}\, d_h/\nu$ [96]
- $Re_{(3)} = u_{void}\, H/\nu$ [96]
- $Re_{(4)} = u_{void}\, 2H/\nu$ [69,100,106]
- $Re_{(5)} = u_m\, H/\nu$ [27]
- $Re_{(6)} = u_{void}\, d_f/\nu$ [91–93]
- $Re_{(7)} = u_m\, 2H/\nu$ [107]

In particular, in a spacer with overlapped filaments of diameter d_f, distance between the filaments l and channel height H=2d_f, one has

$$\varepsilon = \frac{l/H - \pi/8}{l/H} \tag{9}$$

$$d_h = 2H\varepsilon \frac{l/H}{l/H + \pi/2} \tag{10}$$

(independent of the angle formed by the filaments with each other and with the main flow), so that between the above definitions of the Reynolds number the following relations apply:

$$Re_{(1)} = \frac{1}{\varepsilon} Re_{(2)} = 2ZRe_{(3)} = ZRe_{(4)} = 2\varepsilon ZRe_{(5)} = 4ZRe_{(6)} = \varepsilon ZRe_{(7)} \tag{11}$$

in which $Z=(l/H)/(l/H+\pi/2)$. Similar formulae can be written for spacers characterized by woven filaments or by more complex configurations. Definition $\mathrm{Re}_{(1)}$ is by far the most popular. Definitions $\mathrm{Re}_{(3)}$ and $\mathrm{Re}_{(4)}$, differing only by a factor 2, are based on velocity and length scales that do not depend on the spacer and are proportional to the flow rate through the channel, which may allow a more direct performance comparison between different spacers (including the "null" case of a void, i.e. spacerless, channel). Note that, for $l/H\rightarrow\infty$, one has $Z\rightarrow 1$ and $\mathrm{Re}_{(4)}\rightarrow \mathrm{Re}_{(1)}$.

Friction factor

With some exceptions [84,85,94,95,97,99], most of the literature on spacer-filled channels deals to some extent with measured or predicted pressure drops. Some authors [87,96] choose to report this quantity in dimensioned form (i.e., in Pa or Pa m^{-1}), or use the dimensioned or dimensionless wall shear stress [91,92] or the power number, related to the pumping power consumption per unit volume [27]. However, the commonest choice [69,89,98,100] is to make the pressure drop ΔP dimensionless as a Darcy friction coefficient f on the basis of the usual relation

$$f=\frac{\Delta P}{\Delta s}\frac{2L_{ref}}{\rho U_{ref}^{2}} \tag{12}$$

in which Δs is the distance travelled along the main flow direction s, while L_{ref} and U_{ref} are the reference length and velocity, respectively. Note that f is four times the Fanning coefficient. The reported values of f depend sensitively on the choice of L_{ref} and U_{ref}. Normally, they are the same used to define the Reynolds number, but this is not always true; for example, Saeed *et al*. [98] evaluate Re from u_m and d_h but compute f from u_m and $2H$. The definitions adopted have an even larger influence on f than they have on Re, due to the U-square term in Eq. (12). For example, adopting $L_{ref}=d_h$, $U_{ref}=u_m$ to compute $f_{(1)}$ and $L_{ref}=2H$, $U_{ref}=u_{void}$ to compute $f_{(4)}$, from the above formulae for overlapped spacers it follows that $f_{(1)}/f_{(4)}=0.291$ for $l/H=2$, 0.527 for $l/H=4$, and 0.8 (still far from 1) for $l/H=12$. One also has $\mathrm{Re}_{(1)}/\mathrm{Re}_{(4)}=0.560$ for $l/H=2$, 0.718 for $l/H=4$, and 0.884 for $l/H=12$. Since $f_{(1)}<f_{(4)}$ and simultaneously $\mathrm{Re}_{(1)}<\mathrm{Re}_{(4)}$, while f is normally a decreasing function of Re, plotting $f_{(1)}$ against $\mathrm{Re}_{(1)}$ yields a curve far below the corresponding plot of $f_{(4)}$ against $\mathrm{Re}_{(4)}$. These differences should be kept in mind when comparing results from different literature sources.

Nusselt and Sherwood number

With a few exceptions [94–96], most of the studies dealing with heat/mass transfer in spacer-filled channels express the relevant results in dimensionless form by introducing a Nusselt or a Sherwood number. Considering, for example, heat transfer, one has:

$$Nu = \frac{hL_{ref}}{\lambda_f} \tag{13}$$

in which h is the heat transfer coefficient (ratio of a heat flux to a temperature difference), L_{ref} is the reference length scale, and λ_f is the fluid's thermal conductivity. For mass transfer, Nu is replaced by Sh, h is replaced by the mass transfer coefficient k (ratio of amass flux to a concentration difference), and λ_f is replaced by the kinematic diffusivity D. If, coherently, one defines Nu on the basis of the same length scale used for the definition of Re and f, then different Nusselt numbers are obtained, which, following the above nomenclature for Re, may be classified as

- $Nu_{(1)} = Nu_{(2)} = h\,d_h/\lambda_f$ [85,87,98,105]
- $Nu_{(3)} = Nu_{(5)} = h\,H/\lambda_f$ [27]
- $Nu_{(4)} = h\,2H/\lambda_f$ [69,100]
- $Nu_{(6)} = h\,d_f/\lambda_f$ [92,93]

(with obvious changes when mass transfer is considered). Also in this case, the different definitions should be carefully considered when comparing results from different literature sources.

Making reference to heat transfer, and assuming the heat flux to be positive if it exits the channels (cooled fluid), the most common definition of the local heat transfer coefficient is:

$$h = \frac{q_w^{"}}{T_b - T_w} \tag{14}$$

In Eq. (14), $q_w^{"}$ is the local heat flux, T_w is the local wall temperature and T_b is the bulk temperature, usually defined as:

$$T_b = \frac{\int_A \rho c_p T u_s dA}{\int_A \rho c_p u_s dA} \tag{15}$$

A being the area of a generic cross section of the channel and u_s the velocity component along the main flow direction s. Often ρ and c_p can be treated as constant properties. Note that T_b remains a function of s. In some circumstances, notably involving complex three-dimensional geometries, the association of the wall temperature at a given point on the surface with the bulk temperature at a specific abscissa s is rather arbitrary. Moreover, in many simulations adopting the unit cell approach, only the periodic component of the bulk temperature, not varying from cell to cell, is simulated. In these cases, it may be preferable to define the bulk temperature by replacing the area integrals in Eq. (15) with volume integrals taken over the whole unit cell. Yet another alternative is to replace the bulk temperature in the definition (14) of h with a different reference value, e.g. the fluid's temperature at the channel midplane [91] or the fluid's inlet temperature [87]. In the case of mass transfer, temperature is replaced by concentration and h is replaced by a mass transfer coefficient k.

The problem with the above definition of h or k is that, in complex geometries involving flow recirculation, these coefficients may easily become singular or negative in some regions of the wall. This occurs whenever the isosurface $T=T_b$ (or $C=C_b$) touches the wall; h (k) diverges on the line $T_b=T_w$ ($C_b=C_w$) and becomes negative inside this line. Even in the absence of singularities, the simple fact that the isosurface $T=T_b$ (or $C=C_b$) approaches the wall closely may give rise to abnormal and unphysically large values of h or k. This kind of distribution is rather common, especially for imposed flux (Neumann) or mixed (third-type) boundary conditions, two-side heat/mass transfer, high Reynolds numbers and high Prandtl/Schmidt numbers. The only situation in which singularities cannot occur are those characterized by imposed wall temperature or concentration (Dirichlet boundary conditions).

Several computational studies dealing with heat or mass transfer prefer to avoid the complications related to the definition of h or k and mention only temperatures or concentrations and heat/mass fluxes.

In most papers dealing with heat or mass transfer in spacer-filled channels [27,85,92,93,98], the average coefficient is simply defined as the area average

$$h^{(1)} = \{h\} = \frac{1}{S}\int_S h\,dS = \frac{1}{S}\int_S \frac{q_w''}{T_b - T_w}\,dS \tag{16}$$

where S may be the whole active transfer surface or a sub-region of it (e.g., one of two active channel walls). Obvious modifications apply if mass transfer is considered. The problem with this definition is that, if the local h (or k) is singular or attains unphysically very high or negative values (for the reasons discussed in the previous section), also its average $\{h\}$ (or $\{k\}$) will be affected by this behaviour and will attain anomalous values. A definition of the averages that does not suffer from this problem is [69,100]:

$$h^{(2)} = \frac{\{q_w^{"}\}}{T_b - \{T_w\}} \tag{17}$$

in which $\{q_w^{"}\}$ and $\{T_w\}$ are surface averages of $q_w^{"}$ or T_w over the surface of interest (e.g., one of the walls or both walls). The usual obvious modifications apply in the case of mass transfer. Corresponding dimensionless numbers Nu$^{(1)}$, Nu$^{(2)}$ or Sh$^{(1)}$, Sh$^{(2)}$ can be obtained from the above definitions by using Eq. (13) or its mass transfer equivalent, provided a length scale has been chosen. Nu$^{(1)}$ and Nu$^{(2)}$ coincide when a uniform wall temperature is imposed, while they are different when a uniform wall heat flux or a wall thermal resistance are imposed. In fact, one can write:

$$Nu^{(1)} = constant \times \left\{\frac{q_w^{"}}{\Delta T_{bw}}\right\}, \qquad Nu^{(2)} = constant \times \frac{\{q_w^{"}\}}{\{\Delta T_{bw}\}} \tag{18}$$

in which $\Delta T_{bw}=T_b-T_w$. When T_w is imposed, ΔT_{bw} is a constant (say, ΔT_{bw}^0) and one has

$$Nu^{(1)} = Nu^{(2)} = constant \times \frac{\{q_w^{"}\}}{\Delta T_{bw}^0} \tag{19}$$

On the contrary, when a uniform heat flux is imposed, $q_w^{"}$ is a constant (say, $q_w^{"0}$) and one has

$$Nu^{(1)} = constant \times q_w^{"0}\left\{\frac{1}{\Delta T_{bw}}\right\} \neq Nu^{(2)} = constant \times q_w^{"0}\frac{1}{\{\Delta T_{bw}\}} \tag{20}$$

since the average of the reciprocal is not the reciprocal of the average.

The difference between the two definitions is illustrated in Figure 10, which reports average Nusselt and Sherwood numbers, computed by definitions (1) and (2), as functions of the Reynolds number for an overlapped spacer with l/H=4, a flow attack angle γ=45° and two-side heat/mass transfer. The values 4 and 600 were assumed for the Prandtl and Schmidt numbers, respectively. Third type boundary conditions were imposed at the walls. It can be observed that Nu$^{(2)}$ and Sh$^{(2)}$ are always lower than Nu$^{(1)}$ and Sh$^{(1)}$, and that the difference increases with Re. It can also be observed that the difference between $Sh^{(1)}$ and $Sh^{(2)}$ (Sc=600) is larger than that between $Nu^{(1)}$ and $Nu^{(2)}$ (Pr=4).

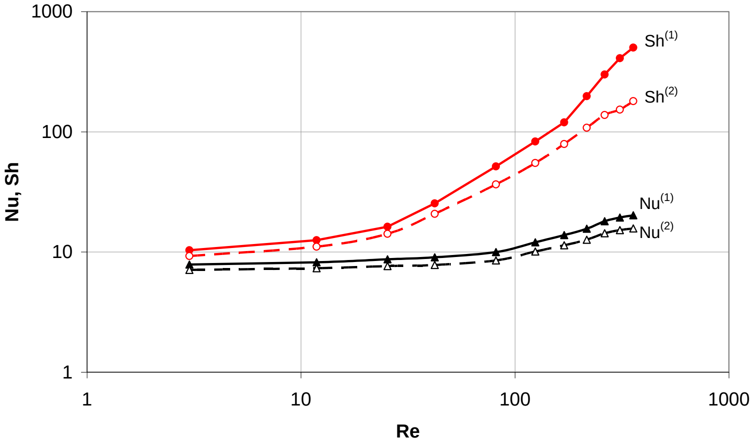

Figure 10. Average Nusselt and Sherwood numbers, computed by definitions (1) and (2), as functions of the Reynolds number for an overlapped spacer with l/H=4, flow attack angle γ=45°, two-side heat / mass transfer and third-type boundary conditions (Prandtl number Pr=4, Schmidt number Sc=600).

2.3 One side against two side heat transfer

A fluid-filled channel can be subjected to different types of heat or mass transfer on the two sides, as sketched in Figure 11 for the case of heat transfer.

Case (a) is heat transfer from one-side with the opposite side wall adiabatic. Case (b) is two-side asymmetric heat transfer with heat inflow from one side and outflow from the opposite side. Finally, case (c) is two-side symmetric heat transfer with heat inflow or outflow from both sides. Indicative bulk and wall temperatures are also shown in the figures; of course, in all cases the sign of T_w-T_b is arbitrary.

In the case of MD, case (a) (one-side heat transfer) is usually realized in laboratory-scale experimental rigs [100,106–109] or small-scale, *plate and frame*, MD equipment [110–112] because it is simpler to build and allows an easier experimental characterization of temperatures and heat fluxes. In electromembrane processes, this case is not feasible, as two opposite ion-exchange membranes (CEM and AEM) are needed to realize the process (ED or RED).

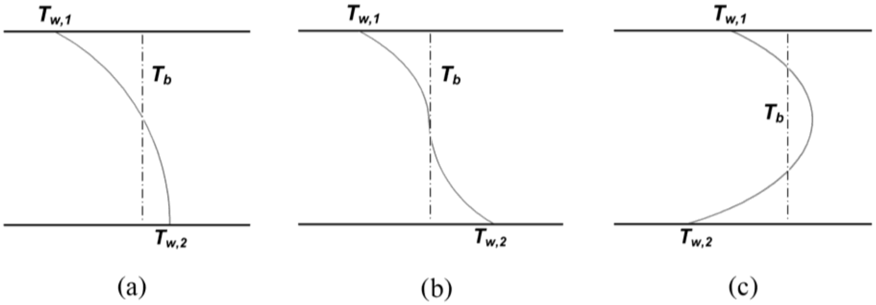

Figure 11. Sketch of possible heat transfer arrangements in membrane processes. (a) one-side heat transfer with one adiabatic wall; (b) two-side asymmetric heat transfer with heat inflow from one side and outflow from the opposite side; (c) two-side symmetric heat transfer with heat inflow or outflow from both sides. Bulk and wall temperatures are shown.

Case (b) (heat / mass inflow from one side of the channel, outflow from the opposite side) is found, for example, in the Memsys™ modules adopted in Vacuum Multi Effect Membrane Distillation (V-MEMD) [113], in which the generic stage is powered by the condensation heat from a previous stage, thus saving the thermal energy that otherwise should be provided from the outside. Only one side of each channel is provided with a microporous membrane that allows the passage of vapour, while the other side is a thin polypropylene sheet, on the outside of which the vapour from the previous stage condenses.

Asymmetric mass transfer conditions can be also observed in electromembrane processes, as in the Blue Acid-Base Battery currently studied within the activities of the *BAoBaB* EU project [114]. The BAoBaB technology uses bipolar membranes and monopolar ion-exchange membranes to obtain electrical energy from water volumes with different pH and salinity, which are stored externally. One channel is in between an IEM and a bipolar membrane, thus yielding to asymmetric fluxes of ions and water, which is produced or dissociated in the bipolar membrane.

The case (c) can be observed in most of the commercially adopted MD plant. An example are the spiral wound modules developed at the Fraunhofer Institute [115], schematically depicted in Figure 1: the hot (feed) channel is placed between two membranes followed by two condensate channels, two conductive walls and two cooling channels, and the whole arrangement is then spirally wound to achieve compactness and reduce heat losses. The feed channel is usually provided with a spacer (not shown).

A two-side symmetric mass transfer is the commonly observed in electromembrane processes as ED or RED.

Among computational studies of membrane processes, both the one-side configuration (a) [87,94,95,100,116,117] and the two-side, symmetric configuration (c) [27,69,92,98] have been considered.

In the case of heat transfer, for a spacerless plane channel subjected to hydrodynamically and thermally fully developed flow, the difference in the Nusselt numbers for one-side and two-side heat transfer is illustrated in Figure A.1. It can be observed that two-side heat transfer yields Nusselt numbers higher by a factor ~1.5 with respect to one-side transfer for any given dimensionless thermal resistance R_T. Therefore, switching from one-side to two-side heat transfer causes an increase of the total heat exchanged by about three times. The physical interpretation of the increase in the Nusselt number on a given wall (say, the top wall) caused by the occurrence of symmetric heat transfer also on the opposite wall (say, the bottom wall) rests on the observation that switching from one-side to two-side heat transfer moves the adiabatic condition $\partial T/\partial y=0$ at the bottom wall to a formally identical symmetry condition $\partial T/\partial y=0$ at the midplane, thus halving the actual distance between bulk fluid and wall. Since velocity profiles are not affected by the thermal boundary conditions, the increase in Nu is not twofold but smaller (~1.5 times).

For spacer-filled channels, the behaviour of the Nusselt number is more complex but follows the same general trend. For example, Figure 12 compares $Nu^{(2)}$ on both walls in two-side heat transfer with $Nu^{(2)}$ on the single active (top) wall in one-side heat transfer for an overlapped spacer having $l/H=2$ and $\gamma=0°$ (a) or 45° (b).

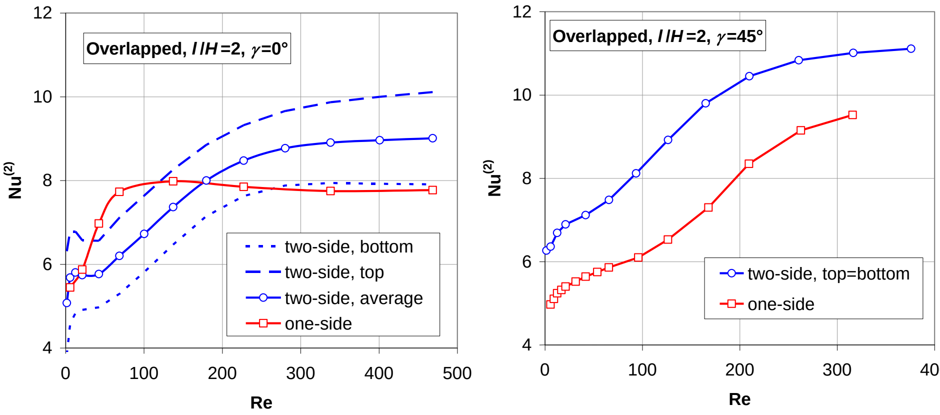

(a) (b)

Figure 12. Comparison of one- and two-side heat transfer in an overlapped spacer filled channel for l/H=2. The values of $Nu^{(2)}$ *on the top and bottom walls and of their average in two-side heat transfer are reported as functions of the Reynolds number along with the values of* $Nu^{(2)}$ *on the only active wall (top wall) in one-side heat transfer. (a)* $\gamma=0°$*; (b)* $\gamma=45°$*. Note that in this latter case one has* $Nu^{(2)}_{top} = Nu^{(2)}_{bottom}$.

Note that the second definition of the average Nusselt number was used in order to obtain more regular and meaningful results. Note also that for γ=45°, graph (b), the values of $Nu^{(2)}$ on the two walls are identical for symmetry reasons (see also subsection 2.4) and, of course, coincide also with their average. It can be observed that, for γ=0° (main flow aligned with the spacer filaments adjacent to the top wall), the Nusselt number in the case of heat transfer from the top wall only exhibits a completely different behaviour than either the top- or the bottom-wall Nu in two-side heat transfer; in particular, it exhibits a large plateau which shrinks considerably in the case of two-side transfer.

Once averaged between top and bottom walls, the two-side Nusselt number is lower than the single $Nu^{(2)}$ obtained in one-side transfer for Re<~180, but becomes up to 15% higher for larger values of the Reynolds number. For the flow attack angle of 45°, the trends of the two curves are similar but the two-side Nusselt number is 1.15-1.35 times higher than the one-side Nusselt number at all Re, so that the overall thermal power exchanged for any bulk to wall temperature difference is from 2.3 to 2.7 times larger (of course, the heat transferred per unit membrane surface area is only 1.15-1.35 times larger).

Figure 13 reports corresponding results for l/H=4. In this case, it can be observed that for both orientations the Nusselt number in two-side heat transfer, once averaged between top and bottom walls, is systematically higher than the single $Nu^{(2)}$ obtained in one-side transfer. Their ratio is lower than that (~1.5) observed in the spacerless channel (Figure A.1), decreases with Re, and is higher for γ=45° than for γ=0° (1.37-1.16 against 1.21-1.07).

From these results (obviously valid also for mass transfer), it can be concluded that:

- In MD, where both one-side and two-side are practically feasible, two-side heat transfer should be preferred as it generally provides larger heat transfer rates per unit membrane surface area at the Reynolds numbers (>200) expected in practical applications;
- Experimental and computational results obtained for one-side transfer cannot be extended to two-side transfer, because not only the absolute values of the average Nusselt (Sherwood) number, but also its trend with Re and other parameters, may differ significantly, and the relative performance ranking of the various configurations examined may be altered.

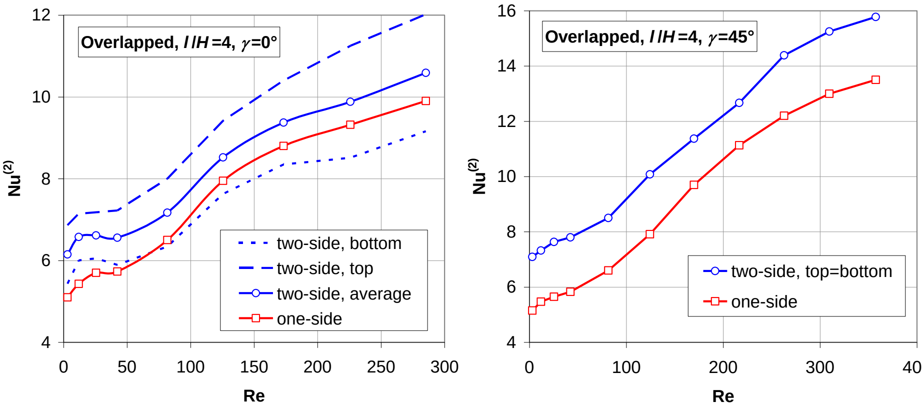

(a) (b)

Figure 13. Comparison of one- and two-side heat transfer in an overlapped spacer filled channel for l/H=4. The values of $Nu^{(2)}$ *on the top and bottom walls and of their average in two-side heat transfer are reported as functions of the Reynolds number along with the values of* $Nu^{(2)}$ *on the only active wall (top wall) in one-side heat transfer. (a) γ=0°; (b) γ= 45°. Note that in this latter case one has* $Nu^{(2)}_{top} = Nu^{(2)}_{bottom}$.

2.4 Influence of boundary conditions

The different boundary conditions that can be imposed at a wall for a scalar transport equation are schematically illustrated in Figure 14. For the purpose of clarity, reference is made to temperature and heat transfer; obvious modifications apply if concentration and mass transfer are considered instead.

The different BC's can be regarded as particular cases of the most general 3rd type condition:

$$T_w - T_{ext} = r_{T,ext} q_w^{"} \tag{21}$$

in which T_w is the wall temperature; T_{ext} is the temperature of some external medium; $r_{T,ext}$ is the interposed thermal resistance per unit wall area, inclusive of the conductive resistance of the membrane and (if appropriate) of the convective resistance on the opposite fluid flow; and $q_w^{"}$ is the wall heat flux. This is made clear by writing:

$$q_w^{"} = \frac{T_b - T_{ext}}{r_{T,ext} + 1/h} \tag{22}$$

in which h is the convective heat transfer coefficient. Case (a) is obtained for $r_{T,ext}$«$1/h$ and approaches uniform wall temperature (1st type, or Dirichlet) conditions; case (b) applies to a generic condition; case (c) is obtained for $r_{T,ext}$»$1/h$, and approaches uniform heat flux (2nd type, or Neumann) conditions.

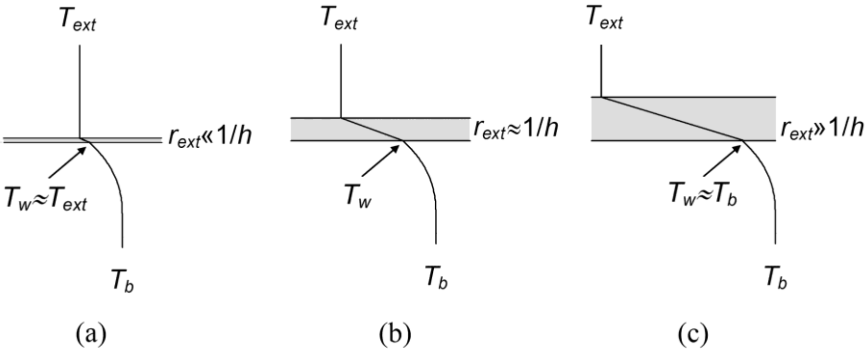

Figure 14. Thermal boundary conditions at a wall obtained as particular cases of the general 3rd type condition for different values of the ratio between the wall thermal resistance $r_{T,ext}$ and the convective heat transfer resistance 1/h. (a) Case $r_{T,ext}$«1/h, approaching uniform wall temperature (1st type, or Dirichlet) conditions; (b) generic case ($r_{T,ext}\approx 1/h$); (c) case $r_{T,ext}$»1/h, approaching uniform heat flux (2nd type, or Neumann) conditions.

The thermal resistance $r_{T,ext}$ can be made dimensionless as $R_T = r_{T,ext}\, \lambda_f/\delta_c$, in which λ_f is the thermal conductivity of the fluid and δ_c is the channel's half-height (other choices of the reference length are, of course, possible).

Accurate solutions for the Nusselt number under any prescribed value of R_T can be obtained for the case of a (void, or spacerless) plane channel, as described in detail in the Appendix A. Figure A.1 therein reports the Nusselt number (based on the hydraulic diameter $2H$ of the void channel) as a function of R_T both for two-side and one-side heat transfer. The limiting conditions $R_T \to 0$ (uniform wall temperature) and $R_T \to \infty$ (uniform wall heat flux) are also reported. It can be observed that thermal boundary conditions affect the Nusselt number to a significant extent, and that Nu is always increasing with R_T both for one-side and for two-side transfer.

In a real spacer-filled channel for membrane processes, the actual boundary conditions will be, in general, of some intermediate type, with an external resistance $r_{T,ext}$ and an external temperature T_{ext} that will depend on the specific process. For example, in Direct Contact Membrane Distillation $r_{T,ext}$ may represent the thermal resistance of the membrane itself in series with the condensation thermal resistance on the permeate side, and T_{ext} will be the condensing temperature. In numerical simulations, most authors imposed at the walls either a uniform temperature / concentration [27] or a uniform heat / mass flux [85,95,96]. Tamburini *et al*. [100] simulated their own experiments on Membrane Distillation, conducted under one-sided heat transfer (see Section 3), by imposing the mixed (3rd type) boundary condition of Eq. (13) with $r_{T,ext}$=0.00625 m^{2}K/W (corresponding to R_T=0.75 for the geometry investigated) at one of the walls (active, top wall), the opposite wall being adiabatic. Only Shakaib *et al*. [87] explicitly simulated both the hot and the cold fluid, thermally coupled through a membrane of prescribed thickness and thermal conductivity.

In the following, in order to study how the Nusselt number in a spacer-filled channel is affected by the thermal resistance, simulations were repeated for different geometric configurations and Reynolds numbers letting R_T vary between 0 and 100. Figure 15 shows the behaviour of the averages Nu$^{(1)}$ and Nu$^{(2)}$ as functions of R_T for one-side heat transfer, γ=45° and l/H=4, Re≈42 (graph a) or l/H =2, Re≈126 (graph b).

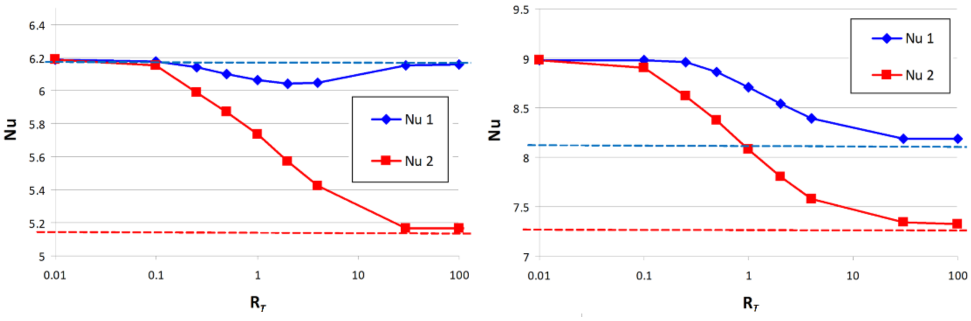

(a) (b)

Figure 15. Dependence of the average Nusselt numbers Nu$^{(1)}$ and Nu$^{(2)}$ on the dimensionless wall resistance R_T for one-side heat transfer in a spacer-filled channel (overlapped, γ=45°). (a) l/H=4, Re≈42; (b) l/H=2, Re≈126. Broken lines are the theoretical values of Nu in a plane (spacerless) channel for $R_T \to 0$ (red) and $R_T \to \infty$(blue).

The more reliable of the two averages, i.e., Nu$^{(2)}$, decreases monotonically with R_T in both cases; the highest values of Nu$^{(2)}$ are attained for R_T=0 (isothermal wall conditions) and the lowest for $R_T \to \infty$. Note that this behaviour is opposite to that reported in the Appendix for the case of a spacerless channel, where Nu increases monotonically with R_T and thus is larger for an imposed uniform wall heat flux than for an imposed uniform wall temperature. This is not surprising since spacer-filled channels exhibit a strong and complex non-uniformity of heat transfer rates over the active wall surface of each unit cell, whereas a spacerless plane channel exhibits only a large-scale longitudinal variation of wall temperature and/or heat flux.

For l/H=4, γ=0°, Re≈42 and one-side heat transfer, Figure 16 shows the influence of thermal boundary conditions on the local distributions of wall temperature (top row), local Nusselt number (middle row) and heat flux (bottom row). The left column is for R_T =0 (uniform wall temperature); the central column is for R_T=0.75 (mixed, or 3rd type boundary condition); finally, the right column is for $R_T \to \infty$ (uniform wall heat flux).

Figure 16 shows that the choice of the thermal boundary conditions at the wall affects the local distributions of thermal quantities even more than it affects average quantities such as $\mathrm{Nu}^{(2)}$. Therefore, in studies discussing the wall distributions of thermal quantities, and even more so in studies comparing experimental and predicted results for the same quantities, a realistic choice of the thermal boundary conditions appears to be crucial.

Needless to say, the above considerations can be adapted to mass transfer by a suitable change of notation, provided realistic values are adopted for the membrane resistance to mass transfer.

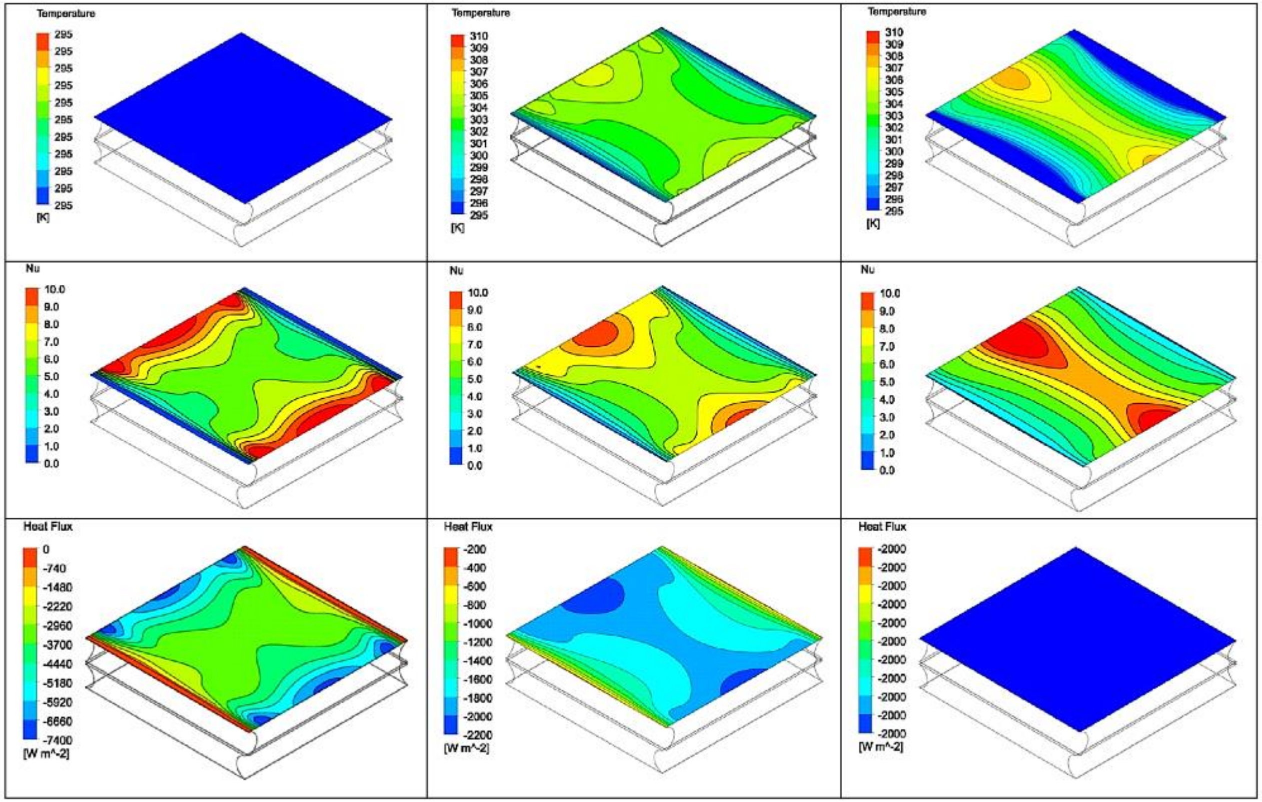

Figure 16. Computed top wall distributions for l/H=4, γ=0°, Re≈42, one-side heat transfer and different thermal boundary conditions: R_T=0, or uniform wall temperature (left), R_T=0.75, or general 3rd type boundary conditions (centre), and $R_T \rightarrow \infty$, or uniform wall heat flux (right). Top row: temperature; middle row: heat transfer coefficient; bottom row: heat flux.

2.5 Complex influence of the parameters l/H, γ, Re

In this Section, some considerations will be presented concerning the individual influence of the main spacer parameters that affect heat / mass transfer in membrane processes. The objective is to clarify to what extent this influence can be represented by simple correlations suitable for design purposes, especially by separated-effect power-law correlations of the kind commonly used in engineering [86,88]. In particular, the quantities l/H (spacer pitch to channel height ratio), γ (flow attack angle) and Re (Reynolds number) will be considered.

Simulations were carried out for overlapped non-conducting spacers with orthogonal filaments (intrinsic angle α=90°), two-side heat transfer, and Cauchy thermal boundary conditions at both walls, with a dimensionless thermal resistance R_T=0.75. One parameter at a time among l/H, γ and Re was made to vary. In order to avoid unnecessary complications, simulations were extended only to the largest Reynolds number still yielding a steady-state solution; a further increase in Re leads to the appearance of oscillations, suggestive of unsteadiness and of flow regimes which ought to be investigated by a more powerful, time-dependent approach [27,91,92,94,97,100] or by the use of turbulence models [84,87].

Influence of the Reynolds number

In regard to the influence of the Reynolds number, Figure 17a reports the average Nusselt number $\mathrm{Nu}^{(2)}$ at both walls as a function of Re for l/H=4 and three values of the flow attack angle γ (0°, 20° and 45°). Note that, for γ=45°, $\mathrm{Nu}^{(2)}_{\mathrm{top}}=\mathrm{Nu}^{(2)}_{\mathrm{bottom}}$. On the whole, a monotonic increase of $\mathrm{Nu}^{(2)}$ with Re can be observed, with some reservations concerning the bottom-wall value for γ=0° at low Reynolds numbers; however, the rate of variation of $\mathrm{Nu}^{(2)}$ with Re is not uniform, but depends on the flow attack angle and on the wall considered; this suggests that separated-effect correlations would perform poorly. The situation is even worse for the smaller aspect ratio l/H=2.5 (Figure 17b). Here, $\mathrm{Nu}^{(2)}$ is far from monotonic, but rather exhibits a *plateau* on either wall and at all attack angles; however, the level attained and the Reynolds number range in which $\mathrm{Nu}^{(2)}$ remains approximately constant depend on the specific wall and angle γ considered, and a simple fit of the results appears prohibitive. Results of comparable complexity are obtained by considering other aspect ratios and flow attack angles. Note that a *plateau* or even a decrease in Nu when expressed as a function of Re is not surprising since, as the fluid's velocity varies, the length of the wake and recirculation regions created downstream of each obstacle also varies, so that the flow interaction with the subsequent obstacles and with the walls changes in a complex way, and may either promote or impair heat / mass transfer.

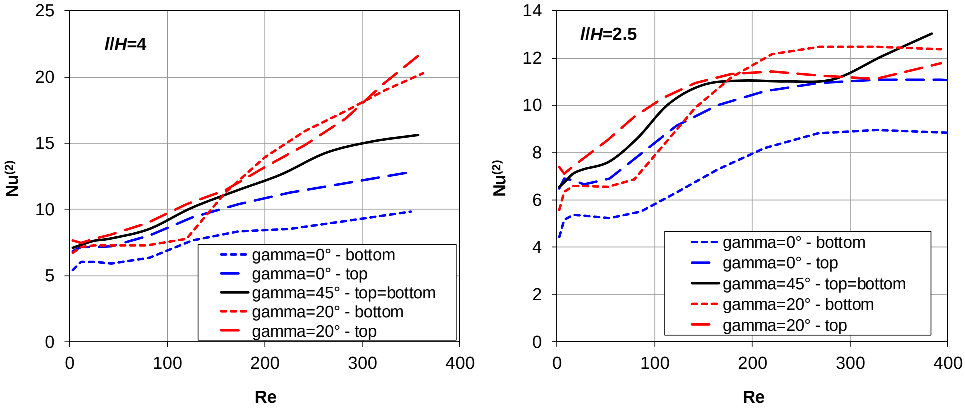

(a) (b)

Figure 17. Influence of the Reynolds number on heat transfer: average Nusselt numbers Nu$^{(2)}$ on top and bottom walls as functions of Re for overlapped spacers, two-side heat transfer and different flow attack angles γ. (a) l/H=4; (b) l/H=2.5.

Influence of the spacer pitch to channel height ratio l/H

In regard to the influence of the spacer pitch to channel height ratio *l*/*H* (aspect ratio) on pressure drop, Figure 18 reports the friction coefficient *f* (normalized by the friction coefficient in the corresponding spacerless channel, 96/Re) as a function of *l*/*H* in overlapped spacers for two different values of the flow attack angle *γ* (0° and 45°) and two different values of the Reynolds number Re (20 and 300). Note that *f* does not change if *γ* varies from 0° to 90°. The figure shows that *f* decreases markedly with *l*/*H* (of course, one expects $f/(96/\mathrm{Re}) \rightarrow 1$ for $l/H \rightarrow \infty$); it also shows that the influence of the flow attack angle *γ* (better discussed in the following Section) is negligible for the lower Reynolds number (20), while it is significant at Re=300, when inertial effects become important.

In order to illustrate the influence of *l*/*H* on heat / mass transfer, the behaviour of the average Nusselt number Nu$^{(2)}$ as a function of *l*/*H* for two values of Re (20 and 300) and *γ*=45° is reported in Figure 19a. The choice of this flow attack angle makes the values of Nu$^{(2)}$ on the two walls identical, so that a single value needs to be reported. It can be observed that, for the larger Reynolds number of 300, close to those expected in MD applications, Nu$^{(2)}$ possesses a marked maximum at $l/H \approx 3.5$, in accordance with most of the literature.

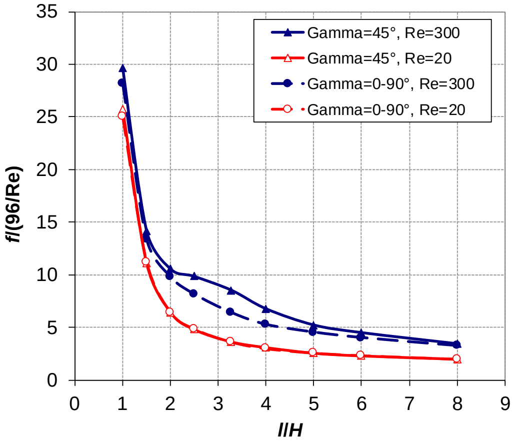

Figure 18. Influence of the spacer pitch to channel height ratio on pressure drop: friction coefficient f (normalized by 96/Re) as a function of l/H in overlapped spacers for two different values of the flow attack angle γ (0° and 45°) and two different values of the Reynolds number Re (20 and 300). Note that identical values of f are obtained for γ=0° and 90°.

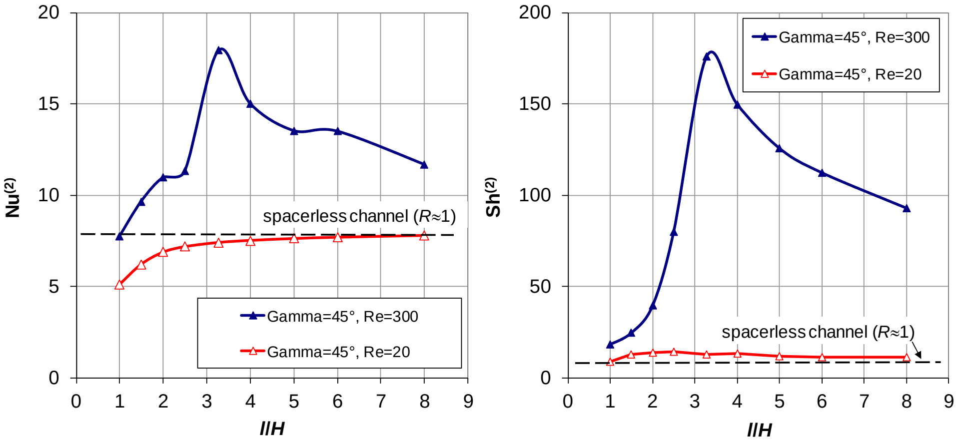

(a) (b)

Figure 19. Influence of the spacer pitch to channel height ratio on heat transfer: average Nusselt number $Nu^{(2)}$ (a) and Sherwood number $Sh^{(2)}$ (b) as functions of l/H for overlapped spacers, two-side heat transfer, γ=45° and two different values of Re (20 and 300). The dashed lines indicate the values of Nusselt and Sherwood for a fully developed spacerless channel.

A second noteworthy feature of the results is that, for *l*/*H*>4, $Nu^{(2)}$ decreases slowly with *l*/*H*, and still exhibits values only ~25% lower than the maximum for *l*/*H*=6. Taking account of the strong reduction in the friction coefficient associated with an increase in l/H, see Figure 18, high aspect ratio spacers are potentially attractive candidates in an optimization perspective. In regard to the viability of simple correlations, the complex dependence of $\mathrm{Nu}^{(2)}$ upon l/H shown by Figure 19a for Re=300 makes this possibility rather unlikely. At the lower Reynolds number, corresponding basically to creeping flow, $\mathrm{Nu}^{(2)}$ is always lower than the value (~8) obtained in a spacerless plane channel under comparable thermal boundary conditions (dimensionless thermal resistance $R_T\approx 1$), and increases with Re tending to this spacerless value for $l/H\rightarrow\infty$ (as it must be at any Re for physical consistency). This means that at very low Re, in the absence of significant secondary flow, the spacer acts mainly as an obstacle to heat transfer rather than as a promoter.

Figure 19b reports the corresponding behaviour of the average Sherwood number $\mathrm{Sh}^{(2)}$, computed under comparable boundary conditions for a Schmidt number of 600 (chosen as representative of sodium chloride in Direct or Reverse Electrodialysis) and a bulk concentration of ~0.5M. For Re=300, the behaviour of $\mathrm{Sh}^{(2)}$ is similar to that of $\mathrm{Nu}^{(2)}$ and exhibits its maximum at the same l/H ratio (~3.5). As a difference, for the lower Reynolds number (close to expected values in electromembrane processes) $\mathrm{Sh}^{(2)}$ remains slightly higher than the spacerless plane channel value of ~8 (which, in laminar flow, is independent of the Schmidt number and thus is identical to $\mathrm{Nu}^{(2)}$, see Appendix A), and exhibits an asymptotic approach from above to this value for $l/H\rightarrow\infty$.

Influence of the flow attack angle

In regard to the variation of the Nusselt (Sherwood) number with the attack angle γ, most of the experimental and fully three-dimensional computational studies presented so far consider only a few orientations, with the main flow parallel or orthogonal to the filaments, or bisecting the angle formed by these latter [69,89,91–93,95–97,99,100]. Note that an orientation cannot even be defined in the case of two-dimensional numerical simulations [84,87]. Yet, the few studies considering different attack angles [27], as well as physical intuition, suggest that orientations other than the basic ones mentioned above may offer advantages in terms of heat / mass transfer and frictional pressure drop, and thus are worth investigating.

Preliminarily it should be observed that, for each spacer configuration, symmetries exist such that the influence of γ needs not to be studied in the whole interval 0-2π, but in a narrower range. Consider, for example, the overlapped geometry sketched in Figure 20, in which the two arrays of wires are assumed to be mutually orthogonal and to have the same diameters and pitches. The flow attack angle γ can be conventionally defined as the angle formed by the main flow direction with the filaments touching the top wall (reference direction *x*). Alternative definitions have also been used in the literature.

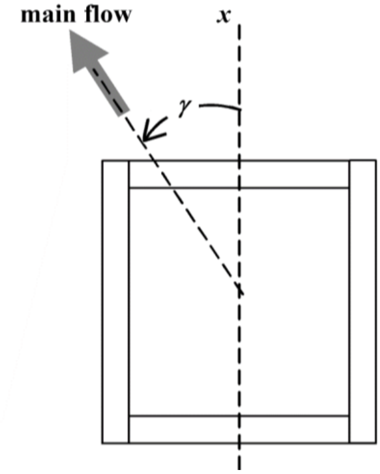

Figure 20. Sketch of the unit cell of an overlapped spacer-filled channel, showing the reference filament direction and the flow attack angle γ.

A moment's reflection shows that, for symmetry considerations, the following properties hold for any quantity φ that can be defined as an average over either the top or the bottom wall (e.g. pressure, shear stress, temperature, concentration, heat or mass flux, heat or mass transfer coefficient, Nusselt or Sherwood number):

$$\varphi_{wall}(\gamma) = \varphi_{wall}(\gamma + k\pi) \qquad (23)$$

("*wall*"="*top*" or "*bottom*"; $k = 0, \pm 1, \pm 2, \ldots$)

$$\varphi_{wall}(\gamma) = \varphi_{wall}(\pi - \gamma) \quad \text{("}\textit{wall}\text{"="}\textit{top}\text{" or "}\textit{bottom}\text{")} \qquad (24)$$

and, provided the same boundary conditions apply on the top and bottom wall,

$$\varphi_{top}(\gamma) = \varphi_{top}\left(\frac{\pi}{2} - \gamma\right) \qquad (25)$$

Thanks to the above properties, a knowledge of the behaviour of both top- and bottom-wall average quantities in the interval γ=0-π/4 (obtained either experimentally or computationally) is sufficient for the whole curves in 0-2π and for both walls to be built. Note that two consequences of Eqs. (23)−(25) are:

$$\frac{\partial \varphi_{wall}}{\partial y} = 0 \; for \; \gamma = k\frac{\pi}{2} \tag{26}$$

(“*wall*”=“*top*” or “*bottom*”; $k = 0, \pm 1, \pm 2, \ldots$)

$$\varphi_{top}\left(\frac{\pi}{4}\right) = \varphi_{bottom}\left(\frac{\pi}{4}\right) \tag{27}$$

If a quantity $\tilde{\varphi}$ is obtained by averaging over the whole (top+bottom) wall surface, then, as a consequence of the above symmetry properties, its dependence on γ is periodic with period $\pi/2$ and satisfies the following properties:

$$\frac{\partial \tilde{\varphi}}{\partial y} = 0 \; for \; \gamma = k\frac{\pi}{4} \quad (k = 0, \pm 1, \pm 2, \ldots) \tag{28}$$

$$\tilde{\varphi}(\gamma) = \tilde{\varphi}\left(\frac{\pi}{2} - \gamma\right) \tag{29}$$

Examples are the overall average Nusselt number, $\mathrm{Nu}^{(2)}_{avg}=[\mathrm{Nu}^{(2)}_{top}+\mathrm{Nu}^{(2)}_{bottom}]/2$ and the corresponding average Sherwood number $\mathrm{Sh}^{(2)}_{avg}$. Properties (28)-(29) hold also for the friction coefficient f.

For example, Figure 21 reports the behaviour of the average Nusselt number $\mathrm{Nu}^{(2)}$ as a function of γ for the top and the bottom walls of an overlapped spacer-filled channel characterized by $l/H=2$, Re≈130. The top-bottom average is also reported. Graph (a) shows in detail the interval $\gamma=0\text{-}\pi/4$, whereas graph (b) (built from graph (a) using the above symmetry properties) spans the whole interval $\gamma=0\text{-}2\pi$. It can be observed that both the individual top and bottom wall averages, and the overall average, exhibit a complex behaviour and are not monotonic functions of γ in the base interval $0\text{-}\pi/4$ (0-45°).

In particular, in the present case the overall average is minimum (~7.4) for $\gamma=0$, due to the deep minimum exhibited by the average Nu on the bottom-wall, where the flow is orthogonal to the filaments, and is maximum (~9.4) for $\gamma\approx 15°$, mainly due to the high heat transfer rates attained, again on the bottom wall, for this flow orientation. The variance of the overall (top-bottom) average with γ is necessarily lower than that exhibited by each wall average, but is still quite significant.

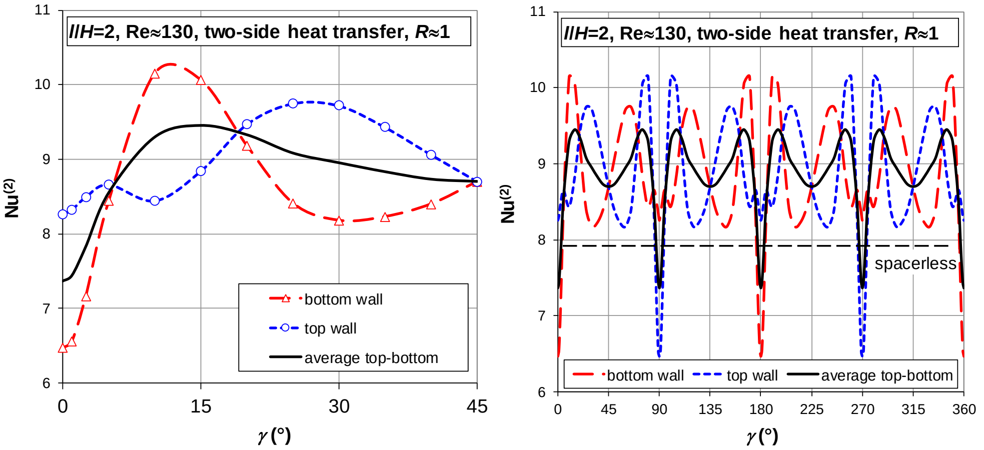

(a) (b)

Figure 21. Influence of the flow attack angle on the average Nusselt number $Nu^{(2)}$ *on the top and bottom walls for an overlapped spacer filled channel with* $l/H=2$*,* $Re\approx130$*, two-side heat transfer,* $R_T\approx1$*. (a) Detail of* $Nu^{(2)}_{top}$*,* $Nu^{(2)}_{bottom}$*, and top-bottom average for* $\gamma=0\text{-}\pi/4$*; (b) overall behaviour for* $\gamma=0\text{-}2\pi$*.*

Figure 22 reports the friction coefficient f (based on the hydraulic diameter of the spacerless channel, $2H$, and on the corresponding velocity u_{void}) as a function of γ for the same configuration in Figure 21, i.e. $l/H=2$, Re≈130 (in this case thermal boundary conditions are irrelevant). It can be observed that f attains a maximum for $\gamma\approx15°$, in approximate correspondence with the heat transfer maximum. Obviously no simple correlation, let alone a power-law one, can capture the complex behaviour of either Nu or f as functions of γ.

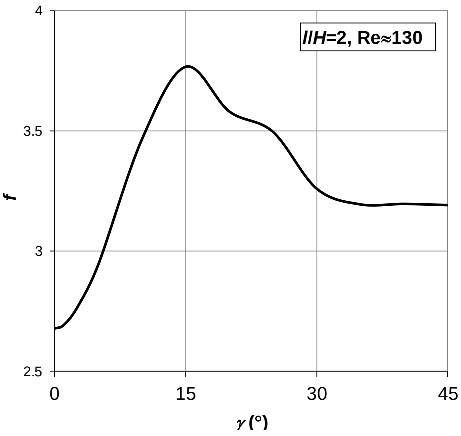

Figure 22. Influence of the flow attack angle on the friction coefficient f for an overlapped spacer filled channel with $l/H=2$*,* $Re\approx130$*.*

3. Membrane Distillation

Figure 23 reports examples of the computational domain in the two cases of overlapped filaments (a) and woven filaments (b). In all cases, the channel configuration is completely specified by the pitch-to-channel height ratio l/H and by the flow attack angle γ, defined as the angle formed by the main flow direction with one (arbitrarily chosen) array of filaments.

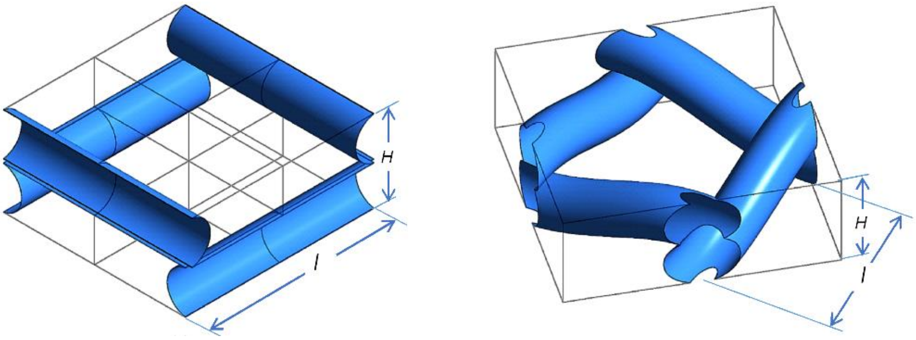

(a) (b)

Figure 23. Unit cell (computational domain) used for spacer-filled channels. (a) overlapped filaments; (b) woven filaments.

In MD, the transferred species is water vapour and the driving force is the temperature difference between feed and permeate, of the order of 5 to 50 K. The feed channel thickness usually ranges from 2 to 5 mm and the cross flow velocity from 5 to 20 cm/s, yielding Reynolds numbers (based on the hydraulic diameter of the channels) ranging from 200 to 2000. MD has been the subject of several computational studies carried out at the University of Palermo in the context of international research programs [94,95,100,106,107]. Moreover, an experimental technique, based on Liquid Crystal Thermography, was developed by Ciofalo *et al.* and adopted at the University of Palermo to visualize the temperature distribution on the active thermal wall of a hot channel in contact with a cold channel. The experimental set-up mimics a Direct Contact Membrane Distillation module and is described in Appendix B. Several experiments demonstrated the effect of spacers on the temperature distribution and on the thermal flux [100,106,107,118].

Usually, separation membrane processes exhibit concentration polarization. In Membrane Distillation, the effects of concentration polarization are usually negligible compared to that of temperature polarization: this phenomenon results in a temperature difference at the membrane interfaces smaller than the temperature difference between the bulk solutions. The loss of efficiency in the process is often quantified by introducing a temperature polarization coefficient (TPC), defined as:

$$TPC = \frac{T_{fm} - T_{pm}}{T_{fb} - T_{pb}} \tag{30}$$

in which "f" and "p" refer to feed and permeate while "m" and "b" refer to membrane surface and fluid bulk, respectively. This coefficient increases with the Reynolds number, especially for low Re, and decreases with the heat flux [108].

Mixing promoters are adopted to counteract this phenomenon. There are many studies in the literature on the characterization of spacer-filled channels, mostly focused on the investigation of the effect of spacer geometry (filament diameter, filament arrangement, filament spacing, angle between crossing filaments, flow attack angle) on fluid dynamics features such as recirculation, flow regime, flow pattern, shear rate distribution, mass and heat transport phenomena, and pressure drops.

Mathematically, the problem is described by the continuity, Navier-Stokes and energy equations for a constant-property fluid. The energy equation is a special form of the scalar transport equation, Eq. (6), written by substituting the specific enthalpy c_pT for φ, the total thermal power entering a unit cell, q for Φ_{in} and the thermal diffusivity, λ_f/c_p for Γ. Assuming also a constant property fluid in steady-state conditions, one has:

$$\frac{\partial \rho u_j c_p T}{\partial x_j} = \frac{\partial}{\partial x_j} \lambda_f \frac{\partial T}{\partial x_j} - \frac{q}{V_f} \frac{u_s}{u_{void}} \tag{31}$$

Periodicity conditions were imposed to all variables at the opposite faces of the computational domain.

The bulk temperature T_b is computed as the mass flow-weighted average of T on the inlet openings of the unit cell. The wall temperature T_w is directly provided by the CFX code as part of the solution. The wall heat flux q''_w is also provided by the code, or can be computed from T_w using Eq. (21).

The fluid was assumed to be water at 39°C with physical properties ρ=992.5 kg/m^3, c_p=4179 J/(kgK), λ_f=0.63 W/(mK), μ=6.67×10^{-4} Pa·s, yielding a Prandtl number of 4.42.

The computational tool used was the Ansys-CFX™ finite volume code, Releases 17 and 18.

3.1 Influence of the thermal conductivity of the spacer

In MD, spacer filaments are usually made of some polymeric material whose thermal conductivity (λ_{spa}≈0.12-0.20 W·m^{-1}K^{-1}), albeit low, is not negligible with respect to the thermal conductivity of water (λ_f≈0.6 W·m^{-1}K^{-1}). Therefore, conduction through the spacer is expected to have some influence on heat transfer and thus on the Nusselt number. These effects are implicitly taken into account in experimental work (provided the same spacer material is adopted as in real applications), but in computational work the issue is generally neglected: spacers are simulated as non-conducting regions or even as non-gridded regions external to the computational domain, and zero heat flux conditions are imposed at the fluid-spacer interfaces.

Some simulations were run with the spacer filaments included in the computational domain and gridded with finite volumes, and continuity of temperature and normal heat flux imposed at the fluid-spacer interface. The conductivity ratio λ_{spa}/λ_f was made to vary between 0.01 (equivalent to non-conducting filaments, and chosen only as a consistency test) and 4 (realizable, for example, by using plastics charged with a suitable filler). Note that common practical applications correspond to $\lambda_{spa}/\lambda_f \approx 0.25$.

Figure 24 shows the average Nusselt number Nu$^{(2)}$ as a function of the ratio λ_{spa}/λ_f for two values of the Reynolds number and for l/H=2, two-side heat transfer, γ=45° (note that $\mathrm{Nu}^{(2)}_{top}=\mathrm{Nu}^{(2)}_{bottom}$ for this flow attack angle). The Nusselt number increases considerably with the conductivity ratio: even for a realistic spacer conductivity (λ_{spa}/λ_f =0.25), Nu$^{(2)}$ values are some 7% higher than in the non-conductive case, and the increment rises to ~50% in the case of high-conductivity filaments (λ_{spa}/λ_f =4). Interestingly, the relative increment of Nu$^{(2)}$ depends little on the Reynolds number.

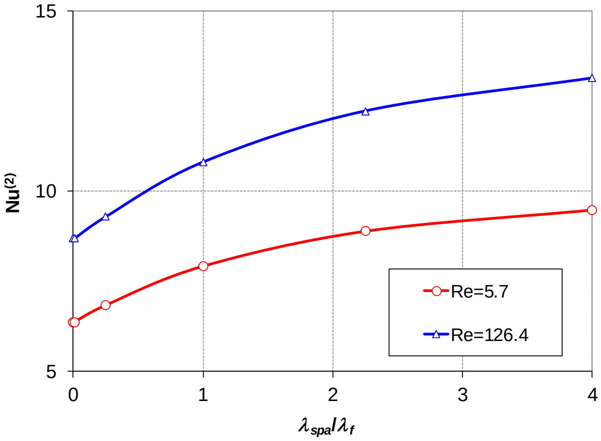

Figure 24. Influence of the thermal conductivity of the spacer: Nusselt number $Nu^{(2)}$ *as a function of the conductivity ratio* λ_{spa}/λ_f *for an overlapped configuration with* $l/H=2$, $\gamma=45°$, *two-side heat transfer. Note that* $Nu^{(2)}_{top}=Nu^{(2)}_{bottom}$ *for this flow attack angle.*

Figure 25 and Figure 26 report maps of the local Nusselt number Nu on the top and bottom walls corresponding to four different values of the conductivity ratio (0.01, 0.25, 1 and 4) for the same configuration ($l/H=2$, $\gamma=45°$, two-side heat transfer) and Re=5.7 and 126.4, respectively. They show that the presence of the conductive filaments not only leads to an increase of the local and average Nu values but also produces a profound change in the distribution of Nu; in particular, as expected, the low values of Nu in correspondence with the wall-spacer contact areas increase considerably with λ_{spa}/λ_f, while maxima are less affected.

At least two conclusions can be drawn from the above results:

I) In comparative studies between experimental results and CFD predictions, these latter should include the simulation of conduction in the spacer filaments since it is typically responsible for 5-10% of the overall heat flow.

II) Leaving cost considerations apart, the use of conductive spacers might be beneficial in MD. Of course, not all of the thermal power transferred from the hot bulk fluid to the conducting spacer can be regarded as “useful”. In fact, only the fraction transferred back to the near-wall, colder fluid results in an increased vapor mass flux through the membrane, whereas the fraction that is directly transferred from the spacer to the membrane by conduction through the contact spots can actually be detrimental, as it increments the conductive losses that reduce the feed temperature without producing any permeate. Therefore, the net effect of the spacer conductivity depends on the exact geometry of the spacer and of the spacer-membrane contact areas, and some considerable CFD and experimental work is required before definite conclusions on this issue can be drawn.

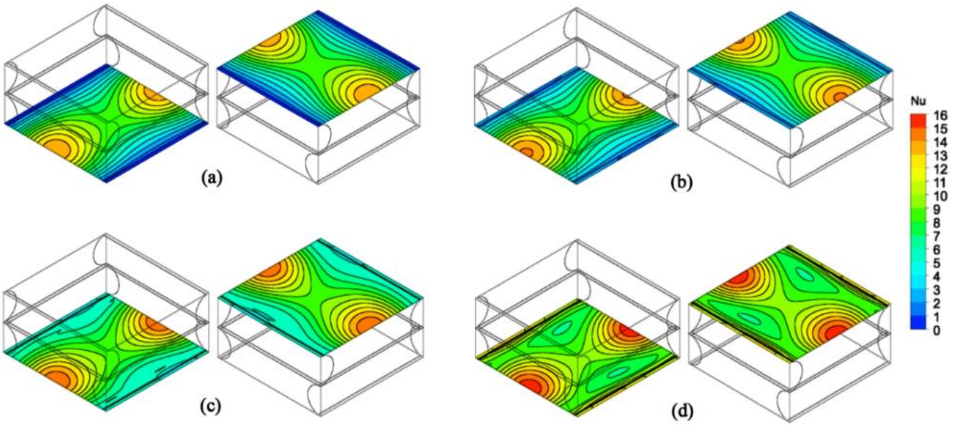

Figure 25. Top and bottom wall distributions of the local Nusselt number for an overlapped spacer with l/H=2, γ=45°, Re=5.7, two-side heat transfer and different values of the thermal conductivity of the spacer filaments. (a) λ_{spa}/λ_f =0.01; (b) λ_{spa}/λ_f =0.25; (c) λ_{spa}/λ_f =1; (d) λ_{spa}/λ_f =4.

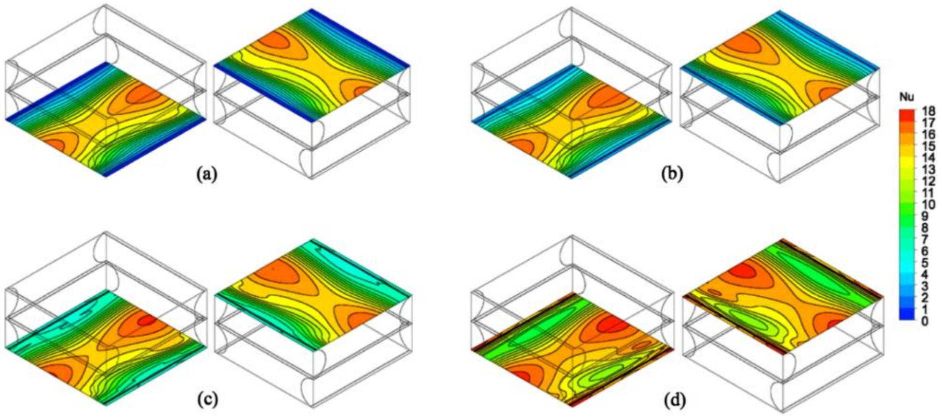

Figure 26. Top and bottom wall distributions of the local Nusselt number for an overlapped spacer with l/H=2, γ=45°, Re=126.4, two-side heat transfer and different values of the thermal conductivity of the spacer filaments. (a) λ_{spa}/λ_f =0.01; (b) λ_{spa}/λ_f =0.25; (c) λ_{spa}/λ_f =1; (d) λ_{spa}/λ_f =4.

3.2 Selection of turbulence models

In MD [13], feedwater channels are usually 2-5 mm thick and velocities may reach 0.2 m/s, so that the Reynolds number may range up to ~2000 yielding (in the tortuous geometry created by the spacers) turbulent flow conditions.

Some authors studied turbulent and unsteady regimes by Direct Numerical Simulation (DNS) [27,91,92,94,100]. However, at high Reynolds number, DNS becomes too computationally expensive, and the use of a turbulence model may be more suitable. In the literature, there are some papers, as for example [84,87], in which turbulence models (RNG k-ε in the former case, Spalart-Allmaras and k-ω in the latter) are adopted.

In this section, all the turbulence models available in Ansys-CFX™ were used and compared in transitional and turbulence regimes. The results were also compared with experimental results obtained at the University of Palermo by Liquid Crystal Thermography [100,107,118]. The technique and the results used to validate the computational results are summarized in Appendix B.

The spacer geometry considered is sketched in Figure 23a. It consists of two overlapped layers of cylindrical rods arranged at 90°, with a pitch to channel height ratio l/H=2. Both in the experiments and in the numerical simulations, heat transfer occurred only from the top wall, representing the fluid-membrane interface, while the opposite bottom wall was adiabatic. Three values of γ were considered here: 0°, 45° and 90°.

In order to define dimensionless quantities, reference was made to the corresponding "void" configuration, i.e. to a spacerless, laterally indefinite, plane channel of height H and hydraulic diameter $2H$. Thus, the definition of the bulk Reynolds number was $\mathrm{Re}_{(4)}$ reported in Part II, Section 2.2, which can be written as:

$$Re = \frac{u_{void} 2H}{\nu} = \frac{2Q}{W \cdot \nu} \tag{32}$$

where $u_{void} = Q/(W \cdot H)$ is the mean "void channel" streamwise velocity, Q the volume flow rate and W the channel's lateral dimension.

3.2.1 Computational methods and turbulence models

In regard to the thermal boundary conditions, the bottom wall and the rods were assumed to be adiabatic (q''_w=0), while at the top wall a third type (Robin) boundary condition was imposed (Eq. (21)) mimicking the actual boundary condition holding in the experiments, and with the same values for the outer temperature T_{ext} (19°C) and for the thermal resistance $r_{T,ext}$ (~$6.5\cdot10^{-3}$ m^{2}K/W).

The amplitude of the driving pressure gradient, imposed as source term in the Navier-Stokes equations, is dynamically adjusted so that u_{void} matches the experimental value.

Following a careful grid dependence study, conducted by using the SST k-ω turbulence model, a very fine block-structured finite volume grid of 4.2 million cells, all hexahedral, was chosen. The dimensionless distance y^+ of the first near-wall grid point (centre of a control volume) from the wall varied from ~1 to ~2 in the range of conditions investigated in the present study.

The turbulence models which were compared are summarized in Table 1, where they are grouped into four families according to two criteria. The former criterion distinguishes first order eddy viscosity / eddy diffusivity models (k-ε, RNG k-ε, k-ω, BSL k-ω, SST k-ω) from second order Reynolds stress / Reynolds flux models (LRR RS, SSG RS, ω RS, BSL RS). The latter criterion distinguishes ω-based models, in which the viscous / conductive sublayer is explicitly resolved by the computational grid (k-ω, BSL k-ω, SST k-ω, ω RS, BSL RS) from k-based models, in which the sublayer is not explicitly resolved and wall functions are used (k-ε, RNG k-ε, LRR RS, SSG RS).

Table 1. Turbulence models tested.

	***k*-based (wall functions)**	***ω*-based (no wall functions)**
First order (eddy viscosity / diffusivity)	k-ε, RNG k-ε	k-ω, BSL k-ω, SST k-ω
Second order (Reynolds stress / flux)	LRR RS, SSG RS	ω RS, BSL RS

Note that the same computational grid, which does resolve the sublayer, is used in all cases, but the adoption of the “scalable wall functions” option in Ansys-CFX™ forces the program to ignore all control volumes placed inside the sublayer and to bridge the first volumes lying outside this region with wall values through the wall function approach.

A brief description of the governing equations characterizing all models, which includes relevant references, can be given as follows.

- The k-ε model [119] solves two transport equations for the turbulence energy k and its dissipation rate ε; the turbulent viscosity is then obtained as $\mu_t=\rho C_\mu k^2/\varepsilon$. It is the industry standard model and is described in detail in all textbooks on turbulence.

- The RNG k-ε model is based on the renormalization group analysis of the Navier-Stokes equations [120]. The resulting transport equations for turbulence energy and dissipation resemble those in the standard k-ε model, but the model constants differ, and the constant $C_{\varepsilon 1}$ in the production term for ε becomes a function $C_{\varepsilon 1}$, RNG of k, ε, and the k-production term.

- The k-ω model [121] solves transport equations for the turbulence energy k and its relative dissipation rate (turbulence frequency) $\omega= \varepsilon/k$. The turbulent viscosity is obtained as $\mu_t=\rho k/\omega$.

- The BSL (baseline) k-ω model [122] is a blending between the k-ω model near the walls and the k-ε model in the outer region. It was developed to overcome a well known problem presented by the k-ω model, i. e. a strong sensitivity to freestream conditions.

- The SST k-ω model [121,123] differs from the BSL k-ω for the presence of a limiter to the eddy-viscosity, accounting for the transport of the turbulent shear stresses. It is believed to give highly accurate predictions of the onset and amount of flow separation under adverse pressure gradients and is currently adopted as default turbulence model in most CFD codes.

- k-based Reynolds stress models do not use the eddy viscosity hypothesis, but solve transport equations for all six components of the Reynolds stress tensor, the dissipation rate ε, and the three components of the turbulent heat flux (if present). The two versions LRR RS, from Launder, Reece and Rodi [124], and SSG RS, from Speziale, Sarkar and Gatski [125], are similar to each other and differ only in the values of some of the model constants.

- ω-based Reynolds stress models differ from k-based Reynolds stress models in that the transport equation for dissipation ε is replaced by one for the turbulence frequency ω. Ansys-CFX™ provides two variants, the ω RS and the BSL (baseline) RS models. The two models relate to each other in a similar way as the two equation k-ω and BSL k-ω models and are expected to provide similar results.

3.2.2 Results

Table 2 and Table 3 summarize computational results, respectively obtained for moderate Re (~600-750) and for high Re (~1820-1850). Experimental results (see Appendix B) are also reported for validation purposes. For each flow attack angle γ and Reynolds number Re, the surface-averaged wall heat transfer coefficient $\{h\}$ is reported. Results will be discussed in detail in the following, focussing not only on average values but also on the corresponding spatial distributions of the local heat transfer coefficient h.

The following Figure 27, Figure 28 and Figure 29 report the distributions of h on the top (thermally active) wall of the unit cell as predicted by all turbulence models for moderate Reynolds numbers (~600-750) and flow attack angles γ=0°, 45° and 90°, respectively. Surface averages $\{h\}$ are also indicated. The corresponding experimental distributions, reported in Appendix B in Figure B. 3 (a-c), are replicated for comparison purposes in the last map.

For Re=596 and a flow attack angle γ=0°, Figure 27, h exhibits an experimental surface-averaged value $\{h\}$ of 491. Distributions and average values in good agreement with the experimental results are provided only by the eddy viscosity ω-based models (k-ω, BSL k-ω, SST k-ω). In particular, the closest average value is provided by the SST k-ω model. Second order ω-based models (ω RS, BSL RS) yield unphysical distributions of h, with multiple maxima along the spanwise direction (horizontal in the figures). The ω RS model met also convergence difficulties, yielding oscillatory solutions and a heavy underprediction of $\{h\}$. k-based models using wall functions, both of the first order (k-ε, RNG k-ε) and of the second order (LRR RS, SSG RS), yield flat distributions of h, with the absence of values below 3-400 $\mathrm{Wm^{-2}K^{-1}}$, which made it advisable to use a different colour key in the maps. These models yield also a heavy overprediction of $\{h\}$ and unphysical distributions of h, exhibiting a strong asymmetry about the main flow direction.

It should be observed that, in the present simulations, for γ=0° and 90° symmetry of the computed flow and thermal fields about the main flow direction is expected as a consequence of the geometric symmetry, but is not explicitly enforced: in fact, the side boundaries are defined as periodicity planes and not as symmetry planes. Therefore, a simulation's ability to reproduce the expected solution symmetries is itself a bonus, independent of the quantitative agreement on h or other quantities. Of course, symmetry could be enforced by defining the side boundaries as symmetry, and not periodicity, planes, but a moment's reflection shows that this approach, besides being somewhat artificial, would not be applicable to flow attack angles other than 0° or 90°.

Table 2. Summary results of $\{h\}$ *for moderate Reynolds number.*

	γ=0° (Re=596)	γ=45° (Re=690)	γ=90° (Re=745)
EXP	**491**	**904**	**669**
k-ω	456	786	577
BSL k-ω	509	710	748
SST k-ω	487	779	695
ω RS	377	676	479
BSL RS	466	752	621
k-ε	604	613	627
RNG k-ε	616	600	713
LRR RS	694	544	730
SSG RS	653	543	730

Table 3. Summary results of $\{h\}$ *for high Reynolds number.*

	γ=0° (Re=1840)	γ=45° (Re=1850)	γ=90° (Re=1820)
EXP	**1038**	**1498**	**1112**
k-ω	1160	1354	1196
BSL k-ω	1189	1391	1343
SST k-ω	1142	1416	1219
ω RS	1228	1327	1137
BSL RS	1254	1298	1295
k-ε	1630	1201	1390
RNG k-ε	1674	1123	1414
LRR RS	1805	1068	1550
SSG RS	1818	1040	1428

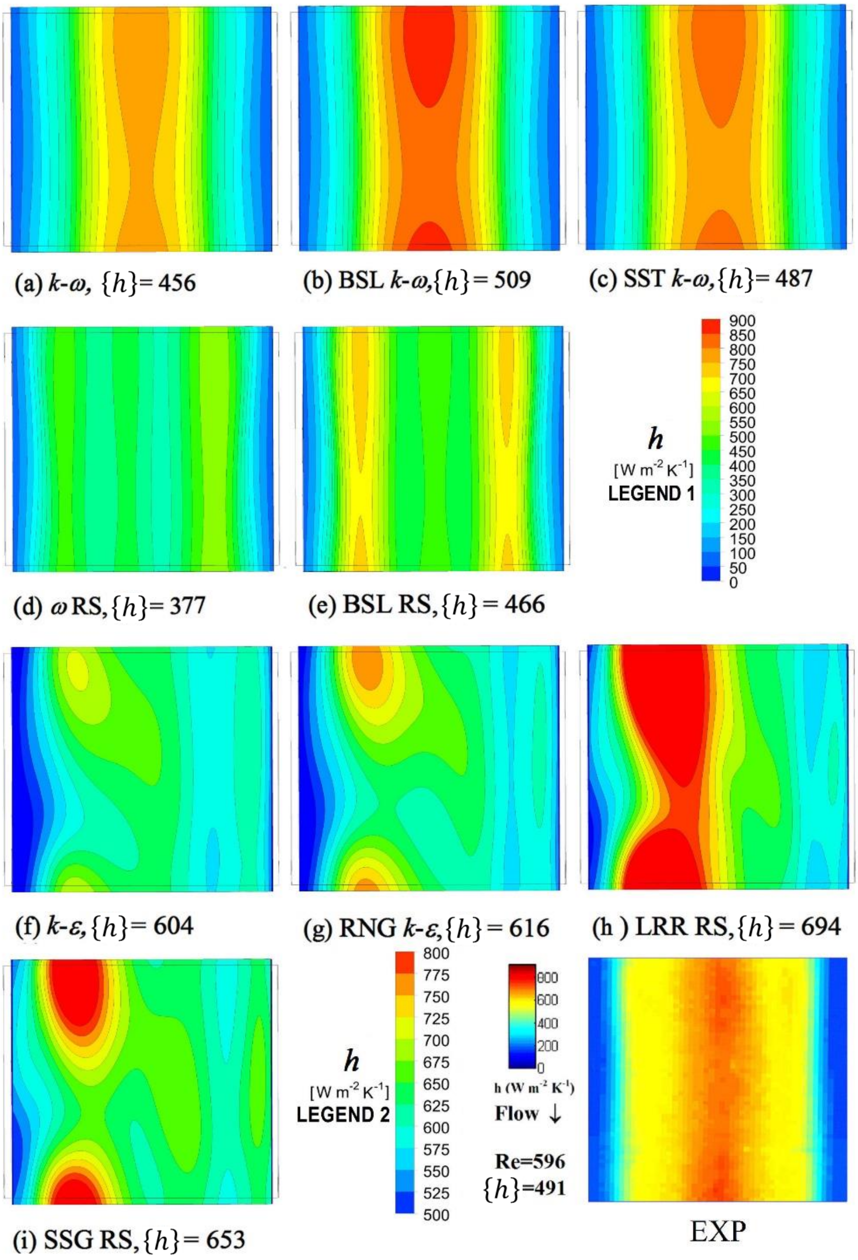
(a) k-ω, $\{h\}$= 456 (b) BSL k-ω,$\{h\}$= 509 (c) SST k-ω,$\{h\}$= 487

(d) ω RS,$\{h\}$= 377 (e) BSL RS,$\{h\}$ = 466

(f) k-ε,$\{h\}$= 604 (g) RNG k-ε,$\{h\}$ = 616 (h) LRR RS,$\{h\}$ = 694

(i) SSG RS,$\{h\}$= 653 EXP

Figure 27. Distributions of the local heat transfer coefficient h on the top (thermally active) wall predicted by alternative turbulence models for Re=596 and a flow attack angle γ=0°. Surface-averaged values $\{h\}$ are also reported. Legend 1 is for maps a-e (ω-based models), legend 2 for maps f-i (k-based models). The corresponding experimental distribution is reported in the last map and exhibits an average value of 491 Wm^{-2}K^{-1}.

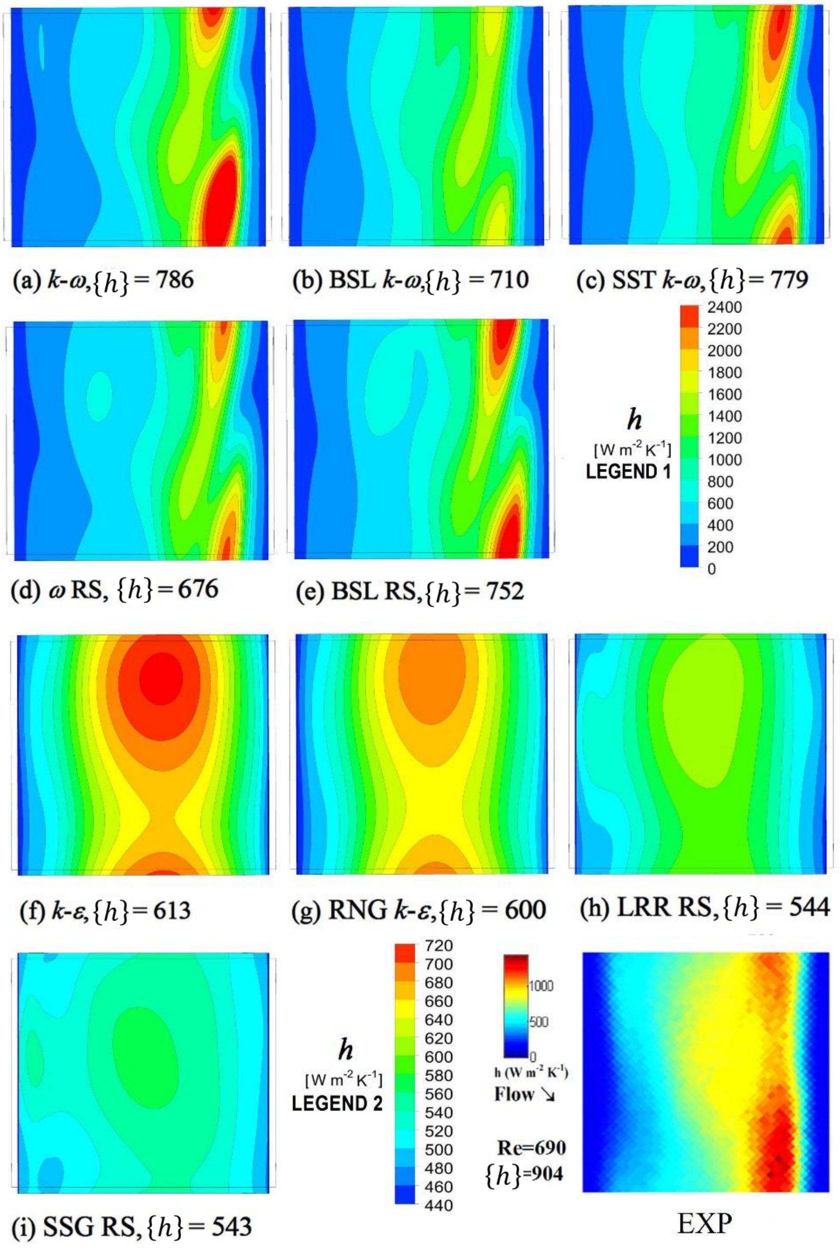

(a) k-ω, $\{h\} = 786$ (b) BSL k-ω, $\{h\} = 710$ (c) SST k-ω, $\{h\} = 779$

(d) ω RS, $\{h\} = 676$ (e) BSL RS, $\{h\} = 752$

(f) k-ε, $\{h\} = 613$ (g) RNG k-ε, $\{h\} = 600$ (h) LRR RS, $\{h\} = 544$

(i) SSG RS, $\{h\} = 543$ EXP

Figure 28. Distributions of the local heat transfer coefficient h on the top (thermally active) wall predicted by alternative turbulence models for Re=690 and a flow attack angle γ=45°. Surface-averaged values $\{h\}$ are also reported. Legend 1 is for maps a-e (ω-based models), legend 2 for maps f-i (k-based models). The corresponding experimental distribution is reported in the last map and exhibits an average value of 904 Wm^{-2}K^{-1}.

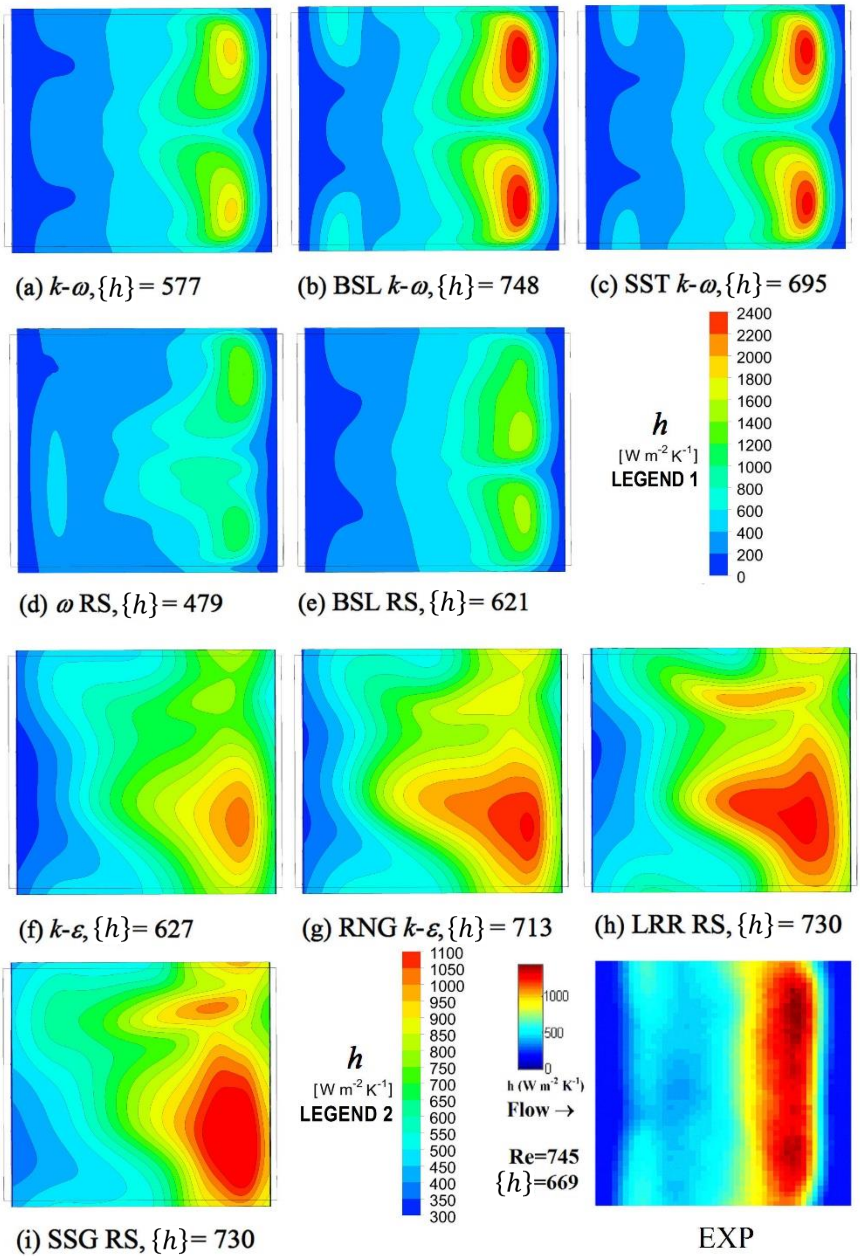

(a) k-ω, $\{h\}=577$ (b) BSL k-ω, $\{h\}=748$ (c) SST k-ω, $\{h\}=695$

(d) ω RS, $\{h\}=479$ (e) BSL RS, $\{h\}=621$

(f) k-ε, $\{h\}=627$ (g) RNG k-ε, $\{h\}=713$ (h) LRR RS, $\{h\}=730$

(i) SSG RS, $\{h\}=730$ EXP

Figure 29. Distributions of the local heat transfer coefficient h on the top (thermally active) wall predicted by alternative turbulence models for Re=745 and a flow attack angle γ=90°. Surface-averaged values $\{h\}$ *are also reported. Legend 1 is for maps a-e (ω-based models), legend 2 for maps f-i (k-based models). The corresponding experimental distribution is reported in the last map and exhibits an average value of 669 Wm*$^{-2}$*K*$^{-1}$.

Figure 28 reports computed distributions of *h* on the top wall for Re=690 and a flow attack angle *γ*=45°. Surface averages {*h*} are also shown. The corresponding experimental distribution exhibits a surface-averaged value {*h*} of 904. In this case, *h* distributions in qualitative agreement with the experimental results are provided by all *ω*-based models (*k-ω*, BSL *k-ω*, SST *k-ω*, *ω* RS and BSL RS), which, however, all underpredict {*h*}. The average value of {*h*} closest to the experimental one (786 against 904 $Wm^{-2}K^{-1}$) is provided by the *k-ω* model. All *k*-based models using wall functions, both of the first order (*k-ε*, RNG *k-ε*) and of the second order (LRR RS, SSG RS) yield (i) a very heavy underprediction of {*h*} and (ii), as in the case *γ*=0°, flat spatial distributions of *h*, in which both the highest and the lowest values are absent. Again, this made it advisable to use a different colour key than for the *ω*-based models.

Finally, Figure 29 reports computed distributions of *h* on the top wall for Re=745 and a flow attack angle *γ*=90°. Surface averages {*h*} are also shown. The corresponding experimental distribution exhibits a surface-averaged value {*h*} of 669. For this flow attack angle, *h* distributions in qualitative agreement with the experimental results are provided by first-order *ω*-based models (*k-ω*, BSL *k-ω*, SST *k-ω*); the best agreement on {*h*} is provided by the SST *k-ω* model, which overpredicts it by ~4%. Second-order *ω*-based models (*ω* RS, BSL RS) yield excessively flat distributions of *h* and some unphysical asymmetry about the flow direction; the *ω* RS model, in particular, gives also a strong underprediction of {*h*}. Note that, despite their similarity, the *k-ω* model underpredicts {*h*} by ~14% while the BSL *k-ω* model overpredicts it by ~12%.

All *k*-based models using wall functions, both of the first order (*k-ε*, RNG *k-ε*) and of the second order (LRR RS, SSG RS), yield wrong spatial distributions of *h*, with excessively uniform values over the active wall and a strong unphysical asymmetry about the flow direction. Among them, the *k-ε* model underpredicts {*h*} by ~4% while all others (RNG *k-ε*, LRR RS, SSG RS) overpredict {*h*} by 7-9%.

In the light of the above results, it is clear that for Reynolds numbers between ~600 and ~750 acceptable predictions of the mean value and the overall distribution of the local heat transfer coefficient *h* can only be obtained by using *ω*-based models, which explicitly resolve the near-wall layer.

The following Figure 30, Figure 31 and Figure 32 concern test cases at higher Reynolds number (~1800). They are organized as Figure 27, Figure 28 and Figure 29 and regard the same three flow attack angles (*γ*=0°, 45° and *γ*=90°, respectively). The corresponding experimental distributions of *h* are reported in Appendix B in Figure B. 4 (a-c) and are repeated for ease of comparison in the last map of each figure.

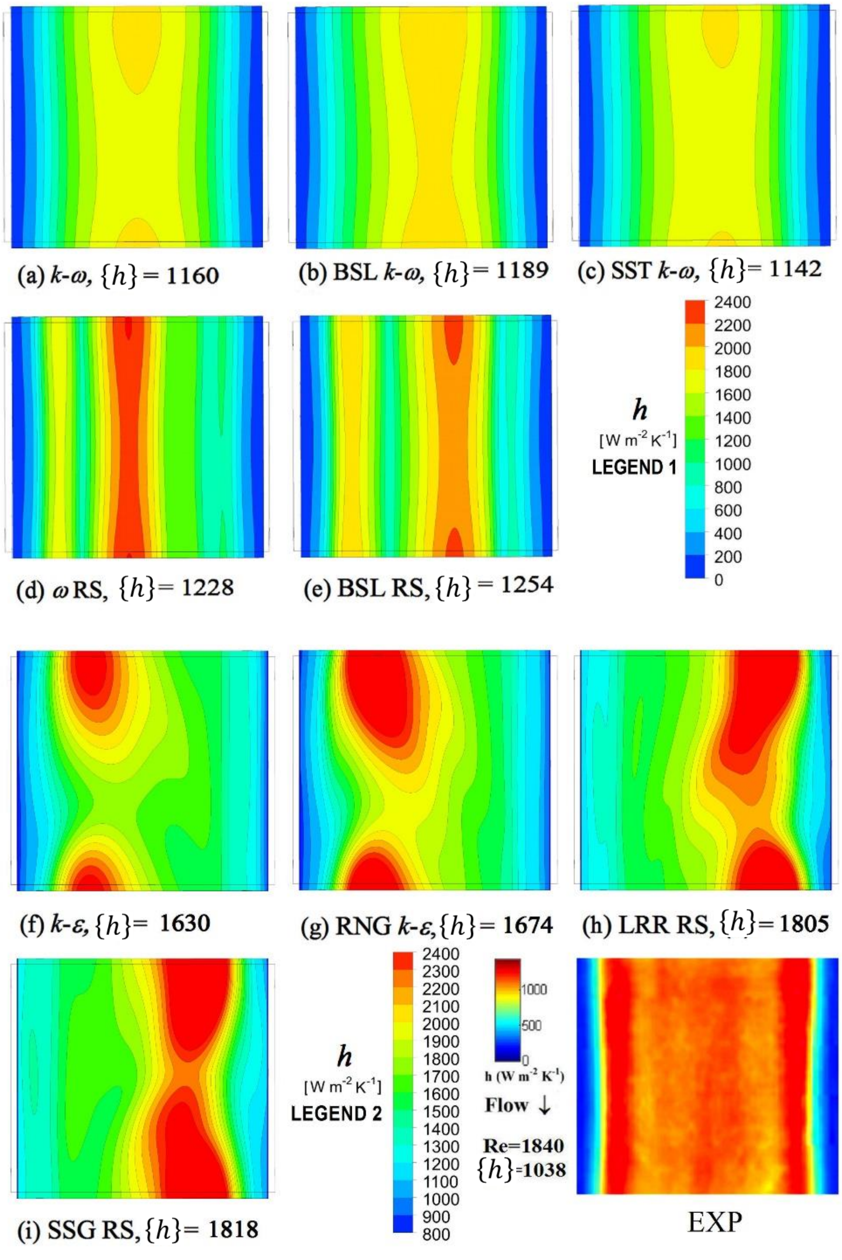

(a) k-ω, $\{h\} = 1160$ (b) BSL k-ω, $\{h\} = 1189$ (c) SST k-ω, $\{h\} = 1142$

(d) ω RS, $\{h\} = 1228$ (e) BSL RS, $\{h\} = 1254$

(f) k-ε, $\{h\} = 1630$ (g) RNG k-ε, $\{h\} = 1674$ (h) LRR RS, $\{h\} = 1805$

(i) SSG RS, $\{h\} = 1818$

EXP

Figure 30. Distributions of the local heat transfer coefficient h on the top (thermally active) wall predicted by alternative turbulence models for Re=1840 and a flow attack angle γ=0°. Surface-averaged values $\{h\}$ are also reported. Legend 1 is for maps a-e (ω-based models), legend 2 for maps f-i (k-based models). The corresponding experimental distribution is reported in the last map and exhibits an average value of 1038 Wm^{-2}K^{-1}.

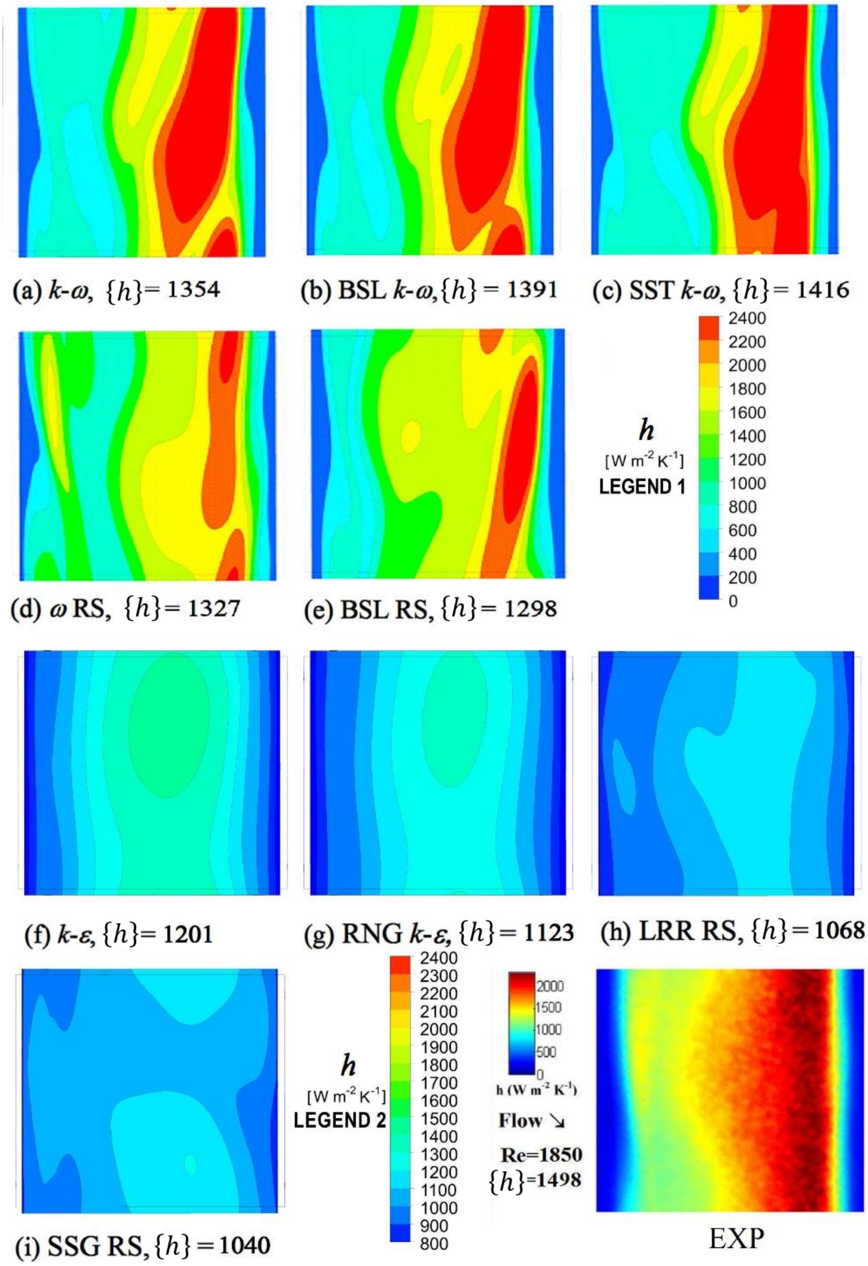
(a) k-ω, $\{h\}$= 1354

(b) BSL k-ω,$\{h\}$ = 1391

(c) SST k-ω, $\{h\}$= 1416

(d) ω RS, $\{h\}$= 1327

(e) BSL RS, $\{h\}$= 1298

(f) k-ε, $\{h\}$= 1201

(g) RNG k-ε, $\{h\}$= 1123

(h) LRR RS, $\{h\}$ = 1068

(i) SSG RS, $\{h\}$ = 1040

EXP

Figure 31. Distributions of the local heat transfer coefficient h on the top (thermally active) wall predicted by alternative turbulence models for Re=1850 and a flow attack angle γ=45°. Surface-averaged values $\{h\}$ are also reported. Legend 1 is for maps a-e (ω-based models), legend 2 for maps f-i (k-based models). The corresponding experimental distribution is reported in the last map and exhibits an average value of 1498 $Wm^{-2}K^{-1}$.

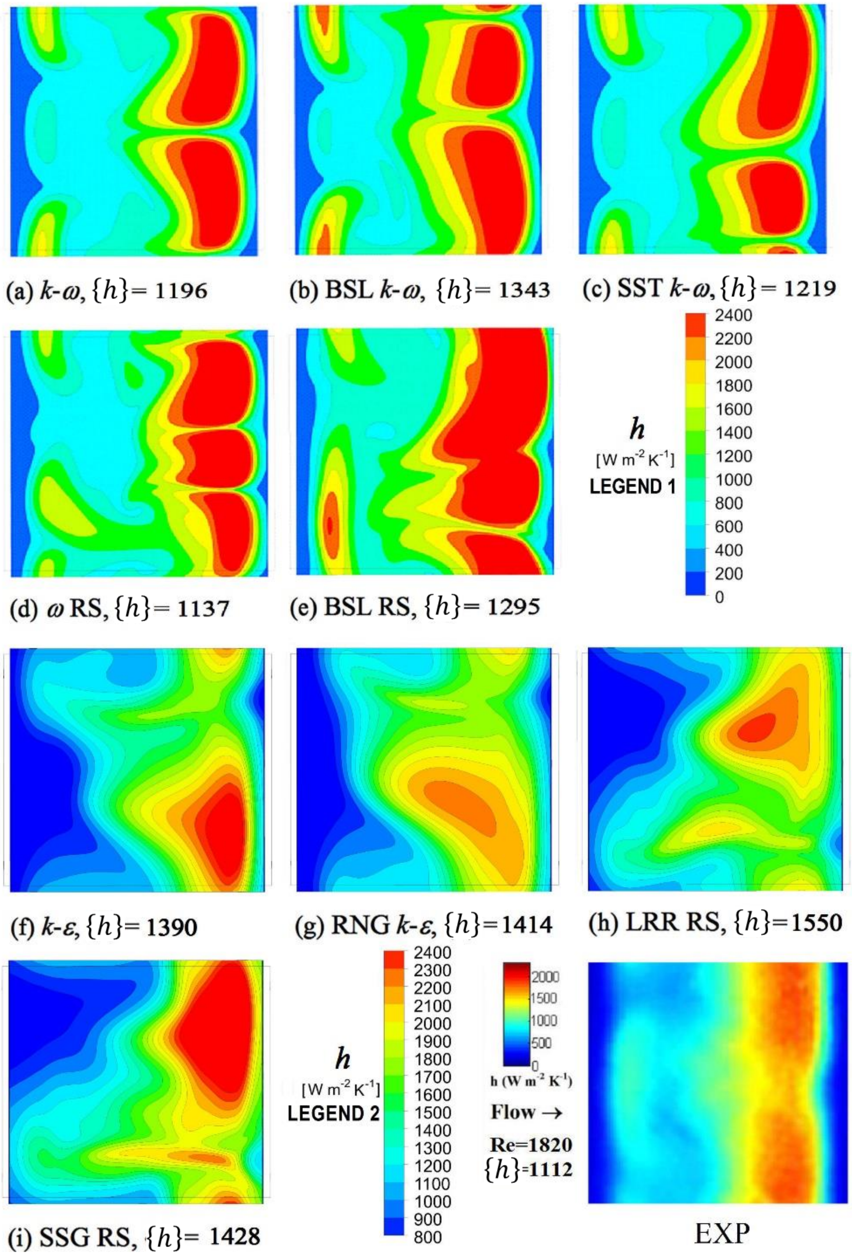

(a) k-ω, $\{h\}$= 1196

(b) BSL k-ω, $\{h\}$= 1343

(c) SST k-ω, $\{h\}$= 1219

(d) ω RS, $\{h\}$= 1137

(e) BSL RS, $\{h\}$= 1295

(f) k-ε, $\{h\}$= 1390

(g) RNG k-ε, $\{h\}$=1414

(h) LRR RS, $\{h\}$=1550

(i) SSG RS, $\{h\}$= 1428

EXP

Figure 32. Distributions of the local heat transfer coefficient h on the top (thermally active) wall predicted by alternative turbulence models for Re=1820 and a flow attack angle γ=90°. Surface-averaged values $\{h\}$ are also reported. Legend 1 is for maps a-e (ω-based models), legend 2 for maps f-i (k-based models). The corresponding experimental distribution is reported in the last map and exhibits an average value of 1112 Wm^{-2}K^{-1}.

For γ=0° and Re=1840, Figure 30, first-order ω-based models (a-c) yield acceptable results, with mean values of h overpredicted by ~10-15%. The least discrepancy on $\{h\}$ is provided by the SST model (c), while the most symmetric distribution is provided by the k-ω model (a). The second-order ω-based models ω RS and BSL-RS, maps (d) and (e), yield a larger overprediction of $\{h\}$ and a multi-modal distributions of h along the spanwise direction which, although vaguely reminiscent of the multi-modal distribution exhibited by the experiments, is asymmetric with respect to the main flow direction and shows wrongly located and excessively high maxima. The k-based models (f)-(i) all yield a strong overprediction of $\{h\}$ (60-75%) and distributions which are strongly asymmetric with respect to the main flow direction.

For γ=45° and Re=1850, Figure 31, ω-based models provide an acceptable agreement with the experiments both in the mean value and in the distribution of h. Values of $\{h\}$ are underpredicted by 5 to 13%, the best agreement being provided, as in most other cases, by the SST model. The k-based models using wall functions, graphs (f) to (i), yield unrealistically flat h distributions and a large underprediction of $\{h\}$ (20-30%).

Finally, for γ=90° and Re=1820, Figure 32, only the k-ω model (a) provides both the expected symmetry in the distribution of h and an acceptable agreement of $\{h\}$ with the experimental result (7% overprediction). The other two first order ω-based models BSL k-ω and SST k-ω, maps (b) and (c), and much more so the second-order ω-based models ω RS and BSL RS, maps (d) and (e), yield asymmetric distributions of h although mean values $\{h\}$ are still acceptable. The k-based models using wall functions, maps (f) to (i), provide strongly asymmetric and irregular distributions of h and a large (25-40%) overprediction of $\{h\}$.

Note that the experiments indicate that the orientation γ=45° provides the highest $\{h\}$, whereas k-based models predict that it provides the lowest. Note also that, at the present Reynolds numbers, all k-based models, with the exception of the simple k-ε, encountered convergence difficulties and provided oscillatory solutions (the results shown in Figure 27, Figure 28 and Figure 29 and in Table 3 are averages of these oscillatory solutions).

Figure 33 compares experimental and computational values of the surface-averaged heat transfer coefficient $\{h\}$ on the top (thermally active) wall in the range Re=100~2000 for all three attack angles (0°, 45° and 90°). Computational results were all obtained by the SST k-ω turbulence model, which provides the best results in agreement with the experiments. Circles denote the test cases for which experimental and predicted h distributions have been reported above. For the lowest Reynolds number cases (Re<~400), the SST model predicted laminarization and yielded results practically identical to those obtained by steady-state, laminar flow simulations (no turbulence model).

At all flow attack angles, predictions are satisfactory up to Re~500. For larger Re, a substantial underprediction is obtained for γ=45°, while results for γ=0° and 90° are generally overpredicted, especially at Re>1000.

On the whole, the influence of the flow attack angle is underpredicted; for example, at Re=1000 experimental results show that $\{h\}$ increases from ~760 to ~1150, i.e. by ~50%, when γ increases from 0° to 45°, whereas CFD results indicate only a ~30% increase (from ~760 to ~1000).

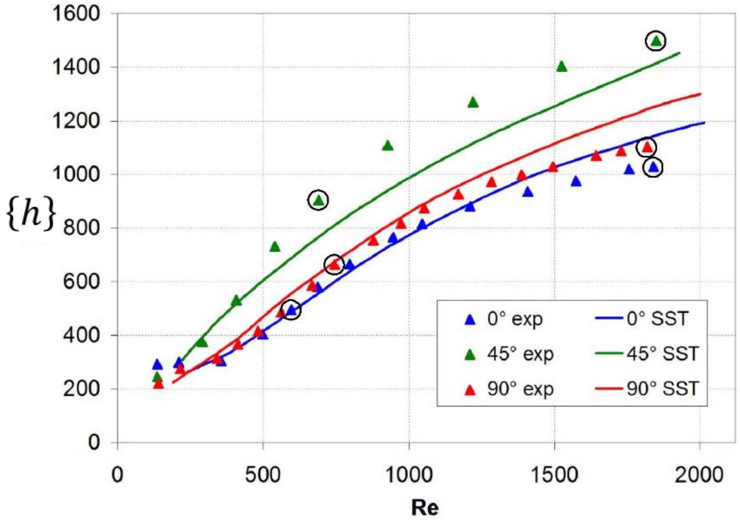

Figure 33. Comparison of experimental and computational (SST k-ω model) values of the surface-averaged heat transfer coefficient $\{h\}$ *(in* $Wm^{-2}K^{-1}$*) on the top (thermally active) wall for Re≈100-2000 and all three attack angles. Circles indicate the test cases for which h distributions were reported.*

3.3 Database of results for overlapped spacers

As observed in Section 2.5, the parameters Re, l/H and γ have a complex influence on the Nusselt number and friction factor that cannot be predicted by simple separated-effect correlations. When the parameters are made to vary in a wide range of values, as for example the Reynolds number in MD, ranging usually between 200 and 2000, interpolation from an adequately large database of Nusselt number and friction coefficients is probably to be preferred to the use of correlations, which instead can be used if small variation ranges are considered.

For this reason, a large number of CFD simulations (~1300) were performed for overlapped non-conductive spacers with intrinsic flow attack angle α=90°. The CFD model, already validated with experimental results (see Appendix B) for one-side heat transfer, was used to simulate two-side heat transfer, which is the most commonly adopted in commercial systems.

$Nu^{(2)}$ on both walls (top and bottom) was evaluated in the range 0°-45° for γ, from which the behaviour of Nu in the whole range 0-2π (as explained in Section 2.5) can be extrapolated, for six different values of l/H and in a wide range of Reynolds number, including turbulent regime. For this reason, SST k-ω turbulence model was used for Re>~300.

The results of this large database are reported in Appendix C. An analogous database for woven spacers is being built at University of Palermo.

4. Electromembrane processes

3-D CFD simulations were used in order to study the mass transfer and other phenomena typical of electromembrane processes (e.g. Ohmic phenomena and electroconvection) in the presence of geometrically complex configurations (spacer-filled channels and profiled membranes). Despite the different phenomena simulated and the lower range of Re, the modelling approach is the same as reported in the previous sections and the main general results (see Part II, Section 2) are still valid.

The convective-diffusive transport of salt, treated as a neutral species, was described by a scalar transport equation:

$$\frac{\partial c u_j}{\partial x_j} = \frac{\partial}{\partial x_j} D \frac{\partial c}{\partial x_j} + S_c \tag{33}$$

By analogy with the momentum equations, c represents the periodic component of salt concentration (expressed in mol/m^3), while the compensative term S_C is included at the right hand side in order to balance salt inflow or outflow through the walls representing fluid-membrane interfaces (note that it is positive for the concentrate channel and negative for the diluate one).

The bulk concentration C was defined in all cases as:

$$C = \frac{1}{Q} \int_A u_s c dA \tag{34}$$

in which A is the cross sectional area and $Q=u_{void}A$ is the volumetric flow rate. Due to the compensative sink term S_C, C is independent of the specific cross section chosen. The unit cell-averaged mass transfer coefficient k on each wall is defined as:

$$k = \frac{\{N_{s,w}\}}{\{c_w\} - C} \tag{35}$$

in which $\{c_w\}$ is the wall concentration and $\{N_{s,w}\}$ is the molar flux from the wall into the fluid, both averaged over a specific wall (solution-membrane interface) of the unit cell. This definition is preferable to the alternative one of computing a local transfer coefficient and then averaging it over a wall, since this latter is prone to singularities for complex geometric configurations, as explained in Section 2.2.

The cell average denoted by { } should not be confused with the overall average $\langle\cdot\rangle$, conducted over the whole stack projected surface and used in the model (Part III):

cell averages such as $\{c_w\}$ and $\{N_w\}$ are still, in general, functions of the axial location along the channels, y.

Finally, k is made dimensionless as a Sherwood number Sh=$k(2H)/D$. In the following, with Sh will be identified the Sh$^{(2)}$ (see Section 2.2).

The flow and transport equations were solved by a finite-volume method using the Ansys-CFX™ code.

4.1 Spacer-filled channels

In the case of spacer-filled channels, delimited by planar ion-exchange membranes, the CFD simulations were limited to the concentrate and dilute fluid compartments, considered one at a time. At both walls, simulating the solution-membrane interfaces, a third-type (Robin) boundary condition was imposed for the scalar c (concentration):

$$-D\left.\frac{\partial c}{\partial n}\right|_w = \frac{\{c_w\} - C_{ext}}{r_w} \tag{36}$$

in which D is the salt diffusivity in the solution, $\{c_w\}$ is the local concentration at the wall, C_{ext} is an arbitrary “external” concentration, whose value is irrelevant to the purpose of computing the Sherwood number, and r_w is a resistance to mass transfer which was set equal to the diffusive resistance of the channel, H/D. This choice provides Sherwood numbers intermediate between those that would be computed under conditions of uniform wall concentration ($r_w \to 0$) and uniform wall mass flux ($r_w \to \infty$); however, the dependence of Sh upon r_w is small.

Figure 34 shows two fluid compartments filled (by way of example) with identical woven filament spacers and sandwiched between ion-exchange membranes, to form a periodically repetitive unit of a whole cell pair. In the direction orthogonal to the membranes, periodic planes cut midway through one of the membranes as in Figure 5. Of course, in principle the concentrate and the diluate channels might have different heights and might be filled by different spacers.

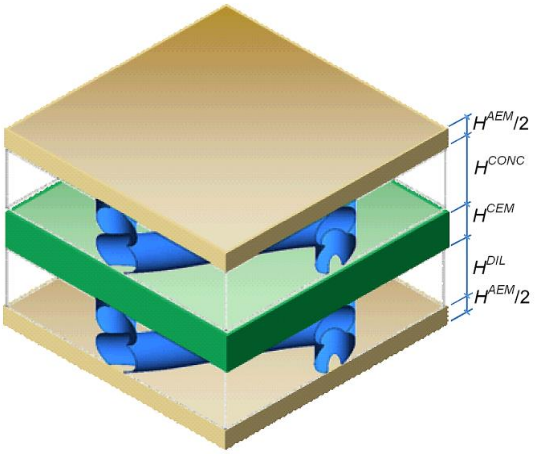

Figure 34. Concentrate and dilute fluid compartments filled by spacers and sandwiched between ion-exchange membranes, to form a periodically repetitive unit of a whole cell pair (the example shown refers to woven filaments).

The main results obtained by CFD for the mean Sherwood number Sh (i.e. the average of the Sh numbers obtained on each surface) for overlapped (graph a) and woven spacers (graph b) with l/H=2 (which is the standard commercial value) and flow incidence angles γ of 0°-90°, and 45° (0° and 90° are equivalent in the case of woven spacers) are shown in the range Re≤70 (that of the highest interest for electromembrane processes) in Figure 35. Best-fit polynomial correlations are also reported; these were used as a basis to evaluate Sh (on each of the four interfaces) in the context of the model described in Part III.

A strong influence of the flow attack angle on mass transfer can be observed in both graphs while a complex dependence upon Re is exhibited only with overlapped spacers by some of the curves (especially for γ=90°). At very low Re, most of the Sherwood number curves fall below the plane-channel value, which is ~8 under third-type boundary conditions; this means that spacers are actually impairing, rather than promoting, mass transfer because of shadow effects. At the Reynolds numbers typically expected in RED (e.g. 5-20), overlapped spacers (graph a) report the highest values of Sh for filaments orthogonal to the main flow direction (γ=90°), which, of course, may interest only one of the walls, while, at higher Re (20-70), they are obtained for γ=45°, symmetrically on both walls.

With woven spacers (graph b), the highest values of Sh are obtained for γ=45° (flow directed along the diagonal of the spacer diamonds) in the whole range of Re.

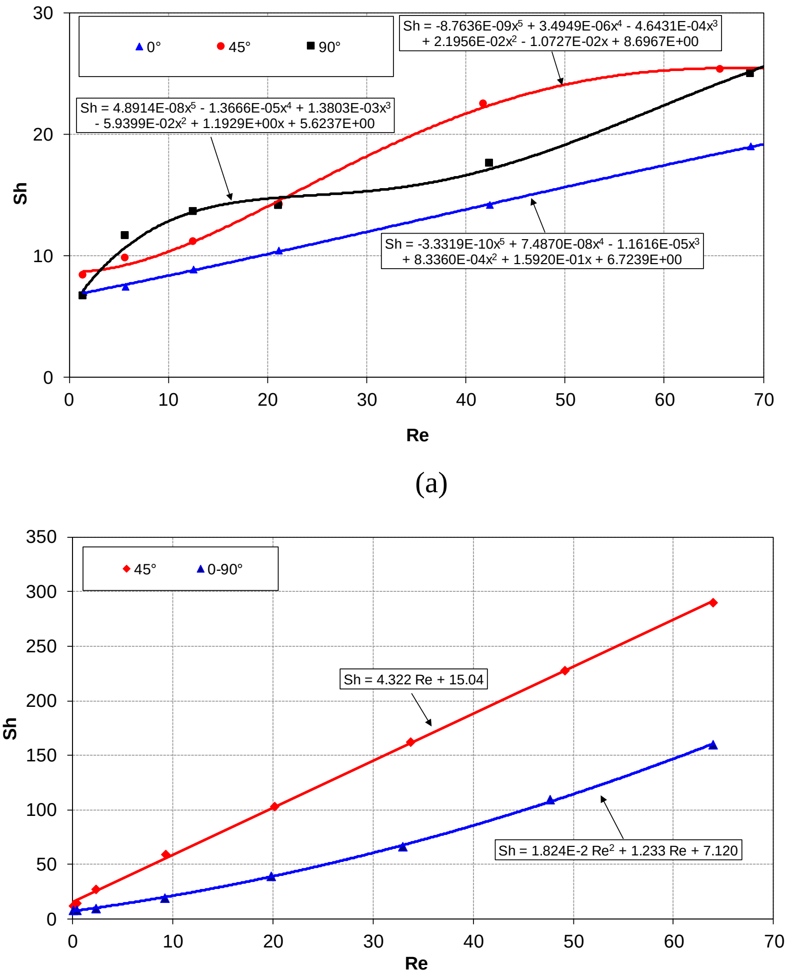

(a)

(b)

Figure 35. CFD results for Sh number (symbols) and best-fit polynomials (lines) for overlapped (a) and woven (b) spacers with l/H=2 and different flow attack angles. Results obtained considering Sc=600.

4.2 Profiled membranes

In the case of profiled membranes, the separate-channel approach adopted for the numerical simulation of spacer-filled channels does not seem adequate, mainly because concentration boundary conditions at the membrane walls are not known *a priori*. Therefore, flow and scalar (salt) transport simulations were performed for the cell pair as a whole. In the lateral and streamwise directions, the unit cell approach was retained and periodic boundary conditions were imposed. Figure 36 reports examples of the unit cell (computational domain) used for profiled membranes. Graph (a) refers to a configuration that called here "Overlapped Crossed Filaments" (OCF), case (b) to the more common case of pillars (in this case square in shape).

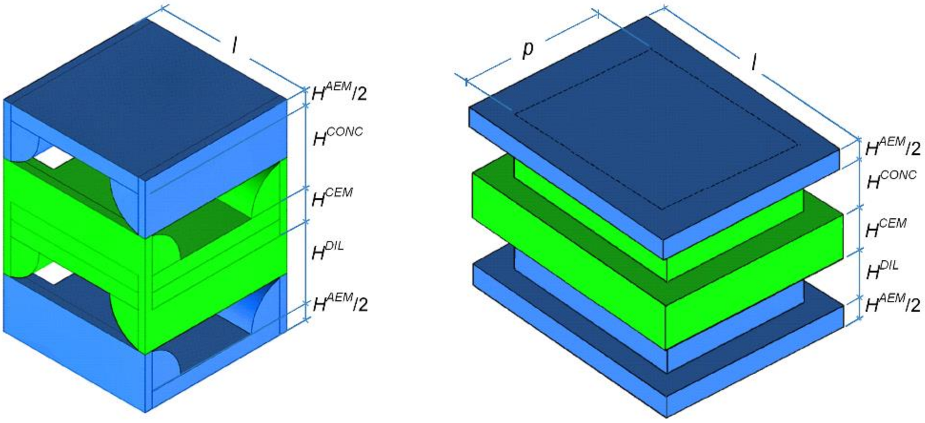

(a) (b)

Figure 36. Unit cell (computational domain) used for profiled membranes. (a) Overlapped Crossed Filaments (OCF); (b) Square pillars.

In the case of profiled membranes, a purely diffusive scalar transport equation was solved also in the solid regions (simulating the ion-exchange membranes):

$$\frac{\partial}{\partial x_j} D^* \frac{\partial c}{\partial x_j} = -S_C^* \tag{37}$$

(in which D^* is the diffusivity in the generic membrane and S_C^* is a suitably defined compensative source term, similar to its counterpart S_C adopted in the fluid compartments, Eq. (33)). Two different bulk concentrations were imposed in the two channels, and a single realistic value of the scalar diffusivity D^* (typically 10^{-11} m^2/s, much lower than the salt diffusivity in the solutions) was imposed in the membranes to allow a salt flux from the concentrate to the dilute solution. Since the Sherwood numbers depend only marginally on the specific distributions of concentration and molar flux over the walls, the exact choice of D^* is immaterial. By this method, at the solid-fluid (membrane-solution) interfaces general interface conditions (continuity of concentration and normal molar flux), and concentration boundary conditions did not need to be assigned.

Results obtained by CFD for the Sherwood number Sh (on each surface) in the range Re≤70 are shown in Figure 37 for OCF profiled membranes with l/H=2 (graph a) and pillars (graph b) with l/p=2 and p/H=6.66, where p is the width of the pillar profile (these values were chosen as they were the same of the first available profiled membrane provided by Fujifilm B.V.). Three flow attack angles (0°, 45° and 90°) are considered and best-fit polynomials are reported.

In graph (a), Sh is greatly enhanced by the OCF membrane profiles, attaining values even twice larger than those caused by the overlapped spacers (see Figure 35a), and the influence of the flow attack angle is small. In the Reynolds number range investigated, the configuration that provides the largest overall enhancement of mass transfer is that at γ=45°, which acts symmetrically on both walls.

In regard to pillars, as shown in Figure 36b, each channel confines with two membranes, one of which bears the square protrusion (filling the whole thickness H), inclusive of four thin rectangular sides, while the other is flat but lacks a central square in correspondence with the pillar. Therefore, the two Sherwood numbers are denoted here as “protrusion side” and “flat side”.

Note that the Sherwood number relevant to a given wall is the dimensionless counterpart of the mass transfer coefficient k defined by Eq. (35), in which both the wall molar flux N_w and the wall concentration c_w are averaged over the whole wall surface. It was observed by detailed maps of N_w obtained from CFD simulations that values of the molar flux on the lateral (side) walls of the pillars are very low, i.e., the relative contribution of these side walls to mass transfer is small. Therefore, average values of N_w and k (i.e., Sh) on the protrusion side of a channel, which includes the side walls, tend to be lower than on the flat side, although the corresponding overall molar flux (in mol/s) may be larger due to the larger total area of the solution-membrane interface.

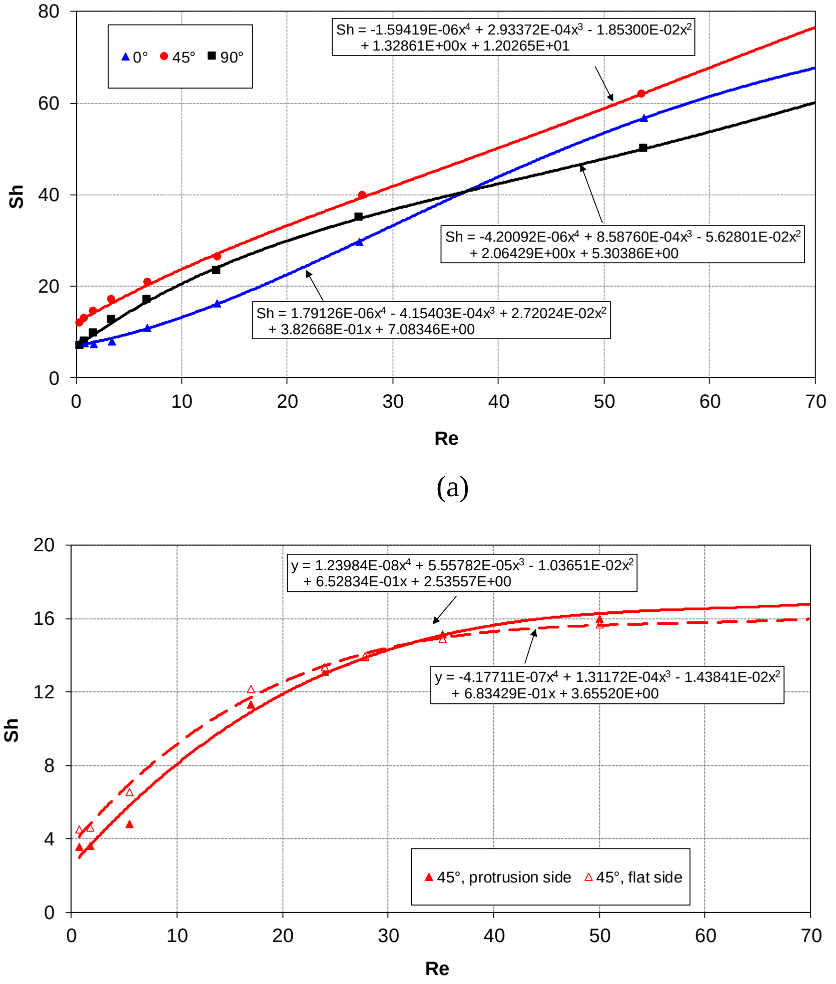

(a)

(b)

Figure 37. CFD results for Sh number (symbols) and best-fit polynomials (lines) for OCF (a) with l/H=2 and pillars (b) profiled membranes with l/p=2 and p/H=6.66 and different flow attack angles. Results obtained considering Sc=600.

4.3 Adjustments for concentration and entrance effects

All the Sherwood numbers reported in the previous sections were computed for a reference Schmidt number Sc_{ref}=600, roughly corresponding to solutions of intermediate dilution ($C\approx100$ mol/m^3). On the basis of a performed sensitivity study, the influence of Sc, and thus of the concentration C, can be taken into account by multiplying the reported values of Sh by $(Sc/Sc_{ref})^{1/2}$, a factor which becomes significant only for highly concentrated solutions. Only in the case of parallel, fully developed flow in a plane (spacerless) channel the Sherwood number is independent of the Schmidt number and thus does not require any concentration adjustment.

Moreover, all the values of Sh reported in the previous sections were computed for fully developed flow. It is well known that in a real, finite-length channel, the local Sherwood number decreases towards its fully developed value Sh_∞ as a function of the dimensionless distance from inlet, $y^*=(y/d_h)/Pe$, where d_h is the hydraulic diameter (=2H) and Pe=Re·Sc is the Peclet number [126]. The inverse of y^* is known as the Graetz number (Gz) and the problem of determining Sh in the entry region is known as the Graetz problem. As a rule of thumb, in laminar flow in spacerless channels the ratio Sh/Sh_∞ becomes negligibly different from unity (e.g., <1.05) for $y^*>0.02$ while it may be as high as 3-5 for $y^*=10^{-4}$. In RED and other mass transfer processes, due to the high value of Sc (e.g. ~600) and despite the low values of Re (e.g. 10), Pe may be quite high (e.g. 6000), so that the condition $y^*=0.02$ is attained for $(y/D_h)=120$. For channels with H=300 μm (d_h=600 μm), this value corresponds to a distance of 0.072 m, so that, in short stacks (e.g. L=0.1-0.2 m), entrance effects extend over a large portion of the stack and cannot be neglected.

Details of the behaviour of Sh in the entrance region depend on the inlet conditions and on the channel's geometry. For laminar flow in circular pipes with simultaneously developing flow and concentration fields, accurate correlations are provided by Gnielinsky [126]. For flat rectangular channels (which include the laterally indefinite plane channel as a limiting case), computational results have been collected by Lee *et al.* [127]. As an additional test, accurate numerical simulations were performed for varying Sc and Re in plane channels using Ansys-CFX™, confirming that the ratio Sh/Sh_∞ depends only on y^* (or Gz) and can be approximated by the simple correlation:

$$\frac{Sh}{Sh_\infty}=C_G\left[Gz+\left(\frac{1}{C_G}\right)^3\right]^{1/3} \tag{38}$$

with $C_G\approx0.18$. Figure 38 shows Eq. (38) along with results by Lee *et al.* [127] and CFD predictions.

Although not very accurate, Eq. (38) was chosen as the simplest correlation exhibiting the correct asymptotic behaviour both for $y^{*}\to 0$ and for $y^{*}\to\infty$. It also possesses the nice property that the average of Sh between the channel inlet and the generic axial location can be approximated by a correlation of the same form as the local one, Eq. (38), but with a different constant $C_G^{avg} = (3/2)C_G$ (~0.27). This is also reported in Figure 38 and shows that, as expected, entrance effects on the average Sh extend far downstream than local effects.

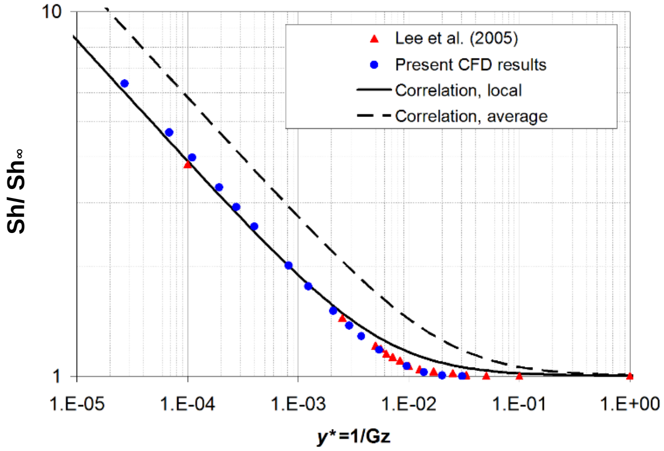

Figure 38. Entrance effects on the Sherwood number in plane channels. Results from the literature and from present CFD calculations are reported along with Eq. (38) (solid line). The broken line represents the correlation for the average Sherwood number in the interval 0 - y.*

Note that the local multiplier (Eq. (38) with C_G=0.18) should be used in conjunction with the one-dimensional stack model described in Part III, while the average multiplier (Eq. (38) with C_G^{avg}=0.27) is more suitable for lumped parameter models.

For more realistic channel configurations, involving spacers or profiled membranes, the literature reports few and unclear findings. For example, Shakaib *et al*. [128] conducted 3-D CFD simulations for developing flow in spacer-filled channels at Re>102, Sc≈650 and γ=0°/90°; they found that Sh differed significantly from its asymptotic value Sh_∞ only in the first 2 unit cells (see their Figure 3) and exhibited a non-monotonic behaviour on the face adjacent to the filaments at 90° incidence. In order to understand the entrance effects in the case of complex channels, simulations were performed considering an overlapped spacer with l/H=4, flow attack angle γ=0° (90°) and 45° and assuming two values for Re (5 and 25).

Results from these simulations, reported in Figure 39, show that both Re and γ have a complex influence on the trend of Sherwood from the inlet to the fully developed conditions. For this reason, it is not possible to find a simple correlation to estimate the entrance effects in the case of spacer-filled channels.

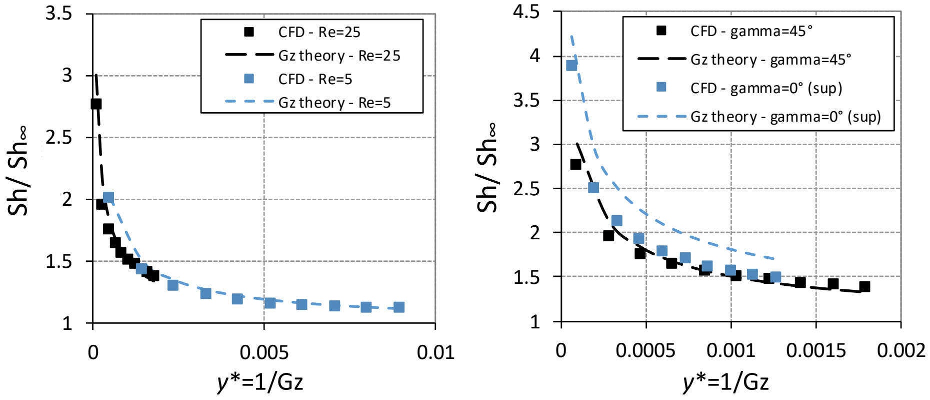

(a) (b)

Figure 39. Entrance effects on the Sherwood number in a channel consisting of 10 unit cells with overlapped spacer with l/H=4. Symbols are the CFD results in each cell. Dashed lines represent the Sherwood number estimated according to Graezt theory. a) results obtained for $\gamma=45°$ at Re=5 and 25. b) results at Re=5 for $\gamma=0°$ (only values at the top wall reported) and 45°.

The comparison of Figure 38 and Figure 39 shows that the entrance effects are less important in the case of spacer-filled channels, in which Sh/ Sh_∞ at the inlet is at most ~4 and after 8-10 cells is always lower than 1.5. In the case simulated, if the channel thickness *H* is for example 200 μm, *l* is 800 μm which means that after 8 mm from the inlet, Sh would be already 1.5 times higher than Sh_∞. This is really a small portion of the entire channel (length from 10 to 100 cm) where fully developed conditions can be observed.

As it is not possible to find a simple equation to estimate the entrance effects in channels with spacers or profiled membranes and their contribution is important only in a small portion of the channel, they were in this thesis neglected. It should be highlighted that neglecting the entrance effects lead to a conservative prediction. Indeed, entrance effects produce an increase of Sh in the first cells which corresponds to a decrease of concentration polarization phenomena. The latter are detrimental either in RED either in ED, thus their reduction is a beneficial effect. Neglecting the entrance effects will turn in an overestimation of concentration polarization phenomena and a conservative underestimation of generated voltage in RED or applied voltage in ED.

4.4 Ohmic behaviour

In electromembrane processes such as RED or ED, in addition to mass transport phenomena (ions and water), there are electrical phenomena which are mainly Ohmic phenomena.

With void (spacerless) channels and planar membranes, the Ohmic areal resistance of a cell pair can simply be computed as the series of four areal resistances:

$$r = r^{CONC} + r^{DIL} + r_{AEM} + r_{CEM} \tag{39}$$

Considering a spacerless channel of thickness H^{SOL}, filled by a solution of conductivity σ^{SOL}, the areal Ohmic resistance r^{SOL} is simply:

$$r^{SOL} = \frac{H^{SOL}}{\sigma^{SOL}} \tag{40}$$

The electrical conductivity σ of each solution is a function of its bulk concentration C and can be evaluated by Islam's correlations [129].

When spacers or profiled membranes are used, the resistance of the solution-filled channel cannot be estimated by Eq. (40). In the case of spacers, a portion of the channel is occupied by a polymeric material, which is not electrically conductive. This results in a resistance increase, known as shadow effect that can be considered by multiplying the resistance in Eq. (40) by a shadow factor $\beta \geq 1$. In the literature, there are several definitions of this shadow factor.

According to one of these definitions, the shadow effect acts on the channel resistance by reducing the effective area available for the transport of ions. For this reason, the shadow factor is equal to the reciprocal of the open area [59,130,131], i.e. the ratio of the *free* area, equal to the difference of the total area and the area covered by the mesh filaments, to the total area. In particular, Tedesco *et al*. [59] defined two different shadow factors because they observed that the open area of a specific spacer might be different in the direction perpendicular or parallel to the membrane.

Another possible definition links the increase in the channel resistance to the reduction of the volume of solution only. In this case, the shadow factor is defined as the reciprocal of the porosity, ε [132]. The latter is the ratio of the *free* volume, i.e.

the difference between the total volume and the volume occupied by the spacer, to the total volume.

Finally, also a third shadow factor which is the average of the two defined above is mentioned in the literature [133].

It is worthy to mention that in the literature there are works in which the shadow effect acts not only on the channel resistance but also on the membrane resistance [61,134].

In this thesis, only the effect on the channel resistance was considered and, in order to choose one definition to be adopted, CFD simulations were performed and new correlations were obtained in the case of profiled membranes.

The code Ansys-CFX™ was used to compute the Ohmic areal electric resistance r of the cell pair by solving the Laplace equation for the electrical potential, $\nabla^2\phi = 0$, on the basis of the concentration-dependent electric conductivities of solutions and membranes.

Simulations were performed considering 1, 10 and 30 g/l as concentration in both channels. Moreover, the cases with 1 g/l in the diluate and 1, 10 and 30 g/l in the concentrate were also simulated. The following geometries were simulated:

- Flat membrane and woven spacers with l/H=2 ($\varepsilon \approx 0.75$);
- OCF profiled membranes with l/H=2 ($\varepsilon \approx 0.6$);
- Pillars profiled membranes with l/p=2 and p/H=6.66 ($\varepsilon \approx 0.75$);

In regard to the areal Ohmic resistance of the membranes, recent measurements, presented by Galama *et al*. [135], suggest that for any given membrane it depends on the diluate concentration. Testing Fujifilm membranes (considered in this thesis), it was possible to observe that the Ohmic resistance of these membranes follows the same behaviour reported by Galama *et al*. [135] for Neosepta® membranes, which in both cases can be well approximated by the formula:

$$r_{IEM} = a + b(C^{DIL})^{-c} \tag{41}$$

where C^{DIL} is expressed in mol/m^3, b=7·10^{-3} and c=1.25 (for both Neosepta® and Fujifilm B.V. membranes); a is the asymptotic membrane areal resistance at high concentration in Ω·m^2.

In CFD simulations, membranes were treated as a homogeneous resistive material of electric conductivity σ_{IEM} which is obtained by the ratio of the nominal membrane thickness and the areal resistance computed by Eq. (41).

In Figure 40, CFD results (black symbols) for areal resistance of one cell pair with woven spacer (triangles), OCF (circles) and pillars (squares) profiled membranes are reported as functions of inlet concentrations. The areal resistance decreases when the inlet concentration increases, tending to an asymptotic value. This effect is less important in graph (b) in which the inlet concentration in the diluate is kept constant at 1 g/l and the inlet concentration in the concentrate compartment increases from 1 to 30 g/l. In all cases, cell pair areal resistance is higher when non-conductive polymeric spacers are considered while the lowest values are obtained with OCF membranes. This difference is larger at low inlet concentrations.

Areal resistance values obtained by appropriate correlations are compared with CFD results in Figure 40.

In particular, in the case of flat membranes and woven spacers, the areal resistance of the cell pair can be approximated by:

$$r = \frac{H^{CONC}}{\varepsilon^{CONC}\sigma^{CONC}} + \frac{H^{DIL}}{\varepsilon^{DIL}\sigma^{DIL}} + \frac{H_{AEM}}{\sigma_{AEM}} + \frac{H_{CEM}}{\sigma_{CEM}} \tag{42}$$

in which ε^{CONC} and ε^{DIL} are the porosity values of the spacer in the concentrate and diluate channels respectively. The above correlation slightly overestimates the areal resistance with a maximum error of ~10% at low inlet concentrations.

In regard to Ohmic losses in profiled membranes, in this case neither the membranes nor the channels possess a simple planar shape and thus, strictly speaking, the areal resistance r of a cell pair cannot be computed as the series of four resistances.

However, approximate but simple expressions for r, to be used in conjunction with simplified stack models, are desirable for parametrical design or optimization studies. For profiled membranes a reasonable approximation is to compute the areal resistance of the whole cell pair (see Figure 36) as:

$$r = \int_0^{H_{cp}} \frac{dx}{\langle\sigma\rangle} \tag{43}$$

i.e. as the series of the electrical resistances of infinitesimal layers of thickness dx, each characterized by an electrical conductivity $\langle\sigma\rangle = \sum_k \sigma_k (S_k/S)$, which is the area-weighted average of the electrical conductivities of the various materials present in the generic section.

The integral in Eq. (43) can be reduced to the sum of elementary algebraic expressions. In case of OCF membranes, the areal resistance of the cell pair can be approximated as:

$$\begin{aligned} r = {} & \frac{H^{CONC}}{2\sigma^{CONC} - (\sigma^{CONC} - \sigma_{CEM})\frac{\pi}{2}\frac{H}{l}} + \frac{H^{DIL}}{2\sigma^{DIL} - (\sigma_{CEM} - \sigma^{DIL})\frac{\pi}{2}\frac{H}{l}} \\ & + \frac{H^{DIL}}{2\sigma^{DIL} - (\sigma_{AEM} - \sigma^{DIL})\frac{\pi}{2}\frac{H}{l}} \\ & + \frac{H^{CONC}}{2\sigma^{CONC} - (\sigma^{CONC} - \sigma_{AEM})\frac{\pi}{2}\frac{H}{l}} + \frac{H_{AEM}}{\sigma_{AEM}} + \frac{H_{CEM}}{\sigma_{CEM}} \end{aligned} \tag{44}$$

As regards Ohmic losses in square-pillar profiled membranes, with reference to Figure 36b, it must be observed that no ionic current can flow through the contact area p^2 between a pillar belonging to one of the membranes (say, AEM) and the flat face of the opposite membrane (say, CEM): this occurs because anions can flow through AEM but not through CEM, and *vice versa* for cations. Thus, in each unit cell a given ionic species flows from a concentrate channel to an adjacent diluate channel mainly by crossing the appropriate membrane through a straight path of cross sectional area l^2-p^2. Alternative paths, involving ion flow through the small lateral surface of the pillars, exist, but they are associated with higher Ohmic resistances and depend on the shift between pillars of consecutive membranes (no shift was assumed in Figure 36b). If the contribution of these alternative paths is neglected, then the areal resistance of a cell pair can be estimated as:

$$r = \frac{l^2}{l^2 - p^2}\left(\frac{H^{CONC}}{\sigma^{CONC}} + \frac{H^{DIL}}{\sigma^{DIL}} + \frac{H_{AEM}}{\sigma_{AEM}} + \frac{H_{CEM}}{\sigma_{CEM}}\right) \tag{45}$$

Thus, the presence of square pillars enhances the Ohmic resistance of the cell pair by a factor $1/[1-(p/l)^2]$, i.e. $1/\varepsilon$ (for example, 1/0.75 if l/p=2).

The accuracy of the above approximations was verified *a posteriori* by comparing their predictions with accurate, 3-D numerical solutions for the electrical potential. Numerical simulations were conducted for the case of zero shift, assuming a uniform electrical conductivity in each membrane and insulating surfaces between each point touching the opposite membrane. The largest discrepancies (~14% at most) were obtained for low inlet concentrations (C^{CONC}=C^{DIL}=1 g/l), while they were much less (a few percent) in all other cases.

Note that even Eq. (42), proposed for spacer-filled channels, can be obtained as a special case of Eq. (43) in the limit of zero electrical conductivity of the filaments.

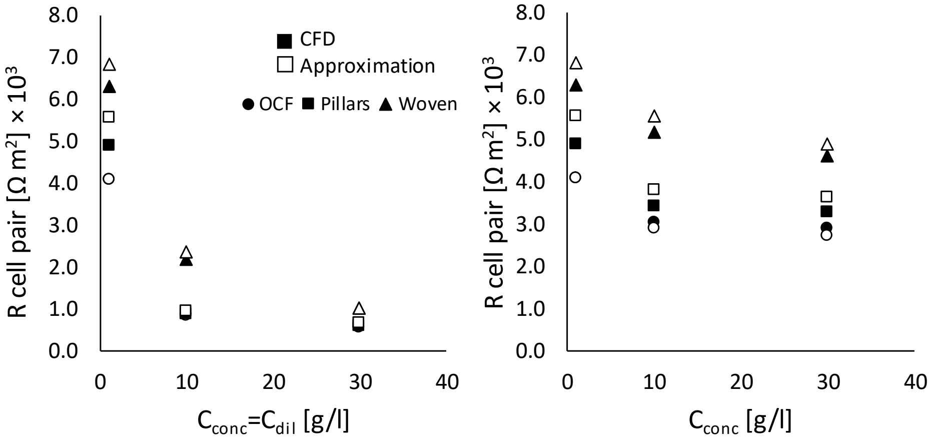

(a) (b)

Figure 40. CFD results for cell pair areal resistance in $\Omega \cdot m^2$ (black symbols) and values estimated by Eqs. (42), (44) and (45) (empty symbols) for (a) equal inlet concentrations and (b) $C^{DIL}=1$ g/l, $C^{CONC}=1$, 10 and 30 g/l.

4.5 Electroconvection

Since the first experiments with ion-exchange membranes, it was observed in the current-voltage curve the appearance of an overlimiting regime. This cannot be explained according to the classical diffusion theory which predict a maximum current, reached when the concentration at an interface is zero [136–138]. The first explanation for the overlimiting regime involved the contribution to charge transfer of new electric charge carriers (i.e. H^+ and OH^- ions generated at the depleted membrane surface in the water splitting reaction). However, it was soon demonstrated that water splitting gives only a minor contribution (~5%) to the current increase in the overlimiting region [139].

In 1978, Rubinstein and Shtilman [49], using a model without an imposed electroneutrality condition, showed for the first time that in the overlimiting regime an extended non-equilibrium space charge region (SCR) appears. In this region, adjacent to a ion-selective surface, if the applied potential exceeds a certain value, convective motions arise as the result of an electrokinetic instability due to the electric field acting on fluid regions with nonzero space charge density [140]. This phenomenon refers to as *electroconvection*.

The most recent state-of-the-art review of electroconvection has been presented by Nikonenko *et al*. [14]. It is now widely acknowledged that bulk electroconvection, arising in the quasi-electroneutral fluid bulk, does not exist [141], and that the first instability occurs either in the nanometer-thick region of high net space charge density (electric double layer, or EDL) adjacent to the surface, or in its micrometer-thick immediate neighbourhood (extended space charge region, or SCR) [142,143]. This kind of electroconvection is often called electroosmosis, although this term may be ambiguous since it is also used for water transport through a ion-selective membrane associated with ion hydration [37].

Since the earliest investigations, electroconvection was associated with membrane surface non-uniformity, either geometric (e.g. undulations and cavities) or electro-chemical (e.g. alternated spots of higher and lower electrical conductance). Several experimental [144–147], computational [148] and review [46,149] studies have been dedicated to the subject. Related studies have regarded the influence of various coatings on ion exchange membranes [150,151].

Most experimental work has relied on current-voltage curves, the features of electroconvection being only indirectly deduced. Kwak *et al*. [152] performed direct visualizations of electroconvective vortices using a fluorescent dye. De Valença [144] used PIV to visualize electroconvective flow in a cell filled with $CuSO_4$ solutions and bounded on one side by a CEM and on the opposite by an anode.

In recent years, experimental work on electroconvection has increasingly been accompanied by numerical simulations. Models in which electroneutrality is imposed cannot predict electroconvection. On the contrary, this phenomenon (and realistic current-voltage curves in the overlimiting current region) can only be predicted if the concentrations of anions and cations are separately assessed by solving the relevant transport equations (usually in the Nernst-Planck formulation), and the electroneutrality condition is replaced by the Poisson equation for the electrical potential having the space charge density as a source term. Finally, coupling the above equations with the Navier-Stokes and continuity equations for fluid motion gives the NPP-NS (Nernst-Planck/ Poisson – Navier Stokes) approach, which is by far that most commonly used in electroconvection simulations.

Actually, few papers adopt the full Navier-Stokes equations [153,154], as adopted in this thesis. Most authors prefer to use the simpler Stokes equations, i.e. to drop the inertial terms in the momentum equations in view of the small Reynolds numbers involved [155–157]. Also, most of the simulations presented are two-dimensional [153–156], while only a few are three-dimensional [157]. Luo *et al.* [158] used a 3-D Lattice-Boltzmann method to simulate the electrohydrodynamic motion caused in a fluid by the injection of free space charges from one of two plane-parallel electrodes, so that both problem and mathematical model are only partly related with the present ones.

4.5.1 Method

The governing equations solved in the present section are the following. They are written in tensor notation and for monovalent ions (z=1). Here, ρ, μ and ε_d are the density, viscosity and dielectric permittivity of the solution; D^+ and D^- are the diffusivities of cations and anions; and ϕ is the electric potential. Also, V_T is the thermal voltage $R_G T/F$, R_G being the gas constant and F the Faraday constant.

- Nernst-Planck transport equations for the concentrations of cations (c^+) and anions (c^-), in mol/m^3:

$$\frac{\partial c^+}{\partial t} = -\frac{\partial}{\partial x_j}\left(c^+ u_j - D^+ \frac{\partial c^+}{\partial x_j} - \frac{D^+}{V_T} c^+ \frac{\partial \phi}{\partial x_j}\right) \tag{46}$$

$$\frac{\partial c^-}{\partial t} = -\frac{\partial}{\partial x_j}\left(c^- u_j - D^- \frac{\partial c^-}{\partial x_j} - \frac{D^-}{V_T} c^- \frac{\partial \phi}{\partial x_j}\right) \tag{47}$$

in which the terms in parentheses represent advective, diffusive and migrative (Coulombic) ion fluxes;

- Poisson equation for the electric potential ϕ:

$$\frac{\partial}{\partial x_j}\frac{\partial \phi}{\partial x_j} = -\frac{\rho_e}{\varepsilon_d} \tag{48}$$

in which $\rho_e=F\,(c^+ - c^-)$ is the space charge density (in C/m^3);

- Navier-Stokes equations: continuity equation as reported in Eq. (4) and momentum equations for a constant-property fluid as:

$$\frac{\partial u_i}{\partial t} + \frac{\partial u_i u_j}{\partial x_j} = -\frac{1}{\rho}\frac{\partial P}{\partial x_i} + \frac{\partial}{\partial x_j}\nu\frac{\partial u_i}{\partial x_j} - \rho_e\frac{\partial \phi}{\partial x_i} \tag{49}$$

in which the last term is the electrophoretic force, product of the space charge density ρ_e by the electric field $E_i = -\partial\phi/\partial x_i$.

For 2-D simulations, the computational domain was that shown in Figure 41a, corresponding to a small region placed in the diluate channel near the CEM. It spanned L=20 μm in the x-direction by H=10 μm in the y-direction. These dimensions are the same used by Karatay *et al*. [31]. Following a grid-independence study, 200 × 400 (x×y) finite volumes were adopted, with a very strong refinement towards the lower wall (membrane) so that, for the first near-wall volumes, the grid size Δy was $0.13\cdot10^{-9}$ m. The electric double layer, a few nm thick, was thus resolved by several grid points.

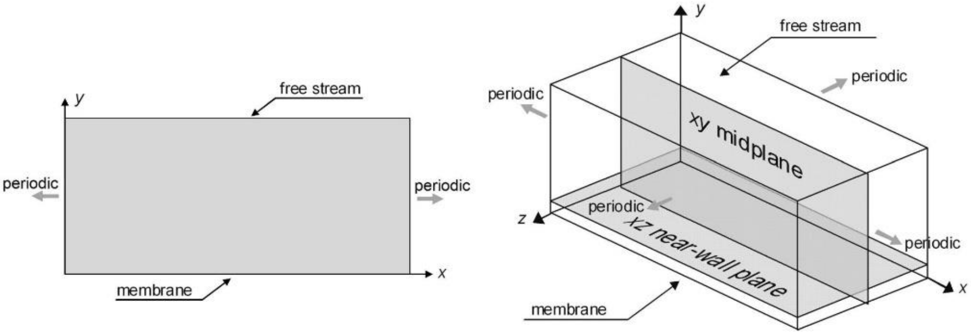

(a) (b)

Figure 41. Computational domains. (a): 2-D (L=20 μm, H=10 μm); (b): 3-D (L=20 μm, H=10 μm, W=10 μm).

The boundary conditions were as in [31]:

- on the lower side y=0, representing the interface with a cation exchange membrane, $\mathbf{u}$=0, ϕ=0, $\partial c^-/\partial y$=0 and c^+=2C, in which C is the bulk concentration (chosen equal to 10^{-3} mol/L);

- on the upper side y=H, representing the free-stream or bulk fluid, $\mathbf{u}$=0, ϕ=ΔV and c^+=c^-=C;

- on the left and right sides x=0, x=L, periodicity conditions for $\mathbf{u}$, ϕ and concentrations.

The initial conditions were $\mathbf{u}$=0 (still fluid), c^+=c^-=C and electric potential ϕ varying linearly between 0 and ΔV. Five different values of ΔV were simulated, namely, 1.1, 1.5, 2.1, 3 and 6 V.

For 3-D simulations, the computational domain was that shown in Figure 41b and was obtained extruding the 2-D domain of graph (a) by W=10 μm along the z direction. A grid of 160×250×80 (x×y×z) finite volumes was chosen, slightly coarser than the 2-D one in each x-y plane but with a comparable near-wall resolution. The total number of finite volumes was $3.2\cdot10^6$. Periodic boundary conditions were specified also along z.

All simulations were conducted using the Ansys-CFX™ code, based on a finite volume method, a strongly implicit coupling of the hydrodynamic variables, and implicit time stepping. The “high resolution” (second order upwind) interpolation scheme was used for the advection terms. Calculations were conducted in double precision. Either in 2-D or in 3-D, numerically stable results could only be obtained by using very short time steps, depending on the applied voltage ΔV and on the simulation stage. For example, for ΔV=3 V, Δt was kept at $1\cdot10^{-8}$ s during the first 10^4 time steps and was gradually increased up to $5\cdot10^{-8}$ s once the amplitude of fluctuations decreased and statistically steady conditions were attained. Slightly larger values of Δt could be used for lower ΔV, while the case ΔV=6 V required Δt to be kept at 10^{-8} s throughout. 3-D simulations were performed on a 128-core cluster, while 2-D simulations took little advantage of parallelism due to the small number of grid points (80,000), and ran in most cases on just 4 cores.

4.5.2 Results and discussion

Figure 4 shows 2-D results for the x-averaged current density $\{i\}$ as a function of time. $\{i\}$ is essentially independent of y, except in the space charge region, and thus can be evaluated at any distance > ~1 μm from the wall. Here it is made dimensionless as $\{I\}=\{i\}/i_{lim}$, in which the diffusion-limited current i_{lim} is estimated by the Peers equation [136]:

$$i_{lim} = \frac{FDC}{\delta(Tr_{IEM} - Tr_{SOL})} \tag{50}$$

assuming the diffusion boundary layer thickness $\delta=H$, the transport number $Tr_{IEM}=1$, $Tr_{SOL}=0.5$, in membrane and solution respectively. Time t is expressed in viscous units as $\tau=tD^+/H^2$. The present predictions are compared with results in [156]: a satisfactory agreement can be observed, especially in time-averages taken after the initial transient has died away. This occurs after a dimensionless time τ of ~0.06, corresponding (for the present case) to ~4.5 ms. The time average of $\{i\}$ tends to ~5 i_{lim}, well above the diffusion-limited current density.

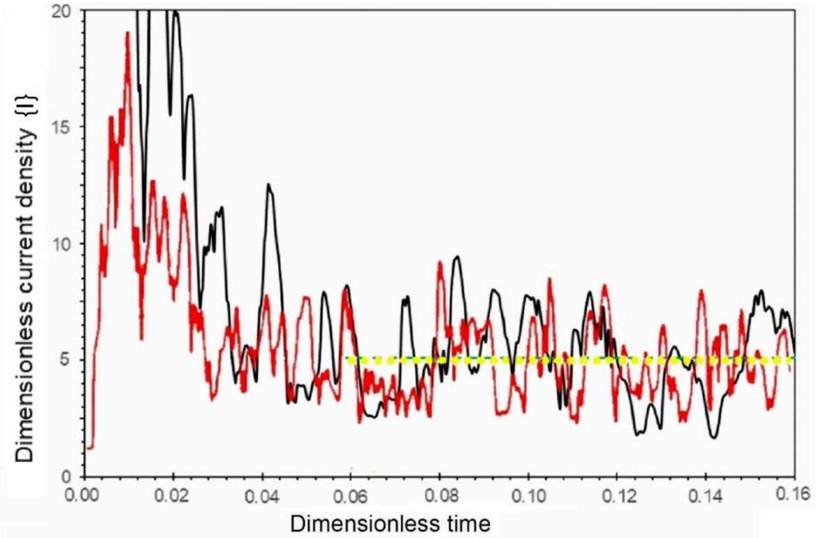

Figure 42. Time histories of the current density (averaged in the x direction) predicted for ΔV=3 V. Black line: present 2-D results, with the time average reported as a green-dashed line. Red line: 2-D results by Karatay et al. [156], *with the time average reported as a yellow-dotted line.*

The influence of the applied voltage ΔV is shown in Figure 43, which compares time histories of the x-averaged current density predicted by 2-D simulations for different values of ΔV. ΔV is normalized by the thermal voltage $V_T=R_G T/F$ (0.0252 V at T=300 K) while $\{i\}$ is normalized by i_{lim} as above. In order to make time-histories obtained for different values of ΔV more directly comparable, time is made dimensionless as $\theta=\tau\Delta V/V_T$, which can be called "independent time". The figure shows that, for $\Delta V<$ ~100 V_T, the current density tends to a constant value 2-4 times larger than i_{lim}, whereas, for larger ΔV, it exhibits strong fluctuations and a larger time-mean value. For all values of ΔV, $\{i\}$ attains its asymptotic behaviour for $\theta\approx 6$, which, however, corresponds to shorter and shorter real times as ΔV increases (from ~10 ms for ΔV=1.1 V to ~2 ms for ΔV=6 V).

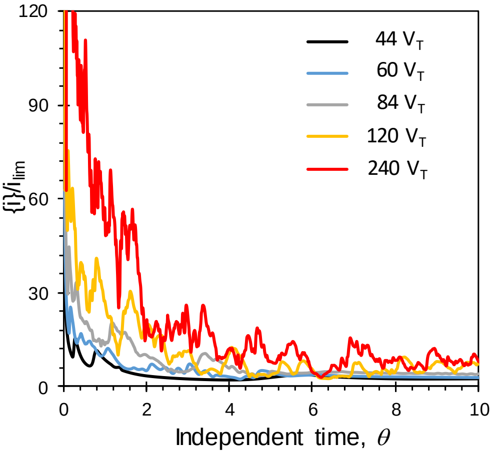

Figure 43. Time histories of the current density (averaged in the x direction) predicted for different values of the applied voltage. The abscissa is the "independent time" (defined in the text).

Figure 44 reports the near-wall profiles of c^+, c^- and net charge density ρ_e for ΔV =3 V. The results are from 3-D simulations, but similar profiles are given by 2-D ones. Note the double logarithmic scale. Three regions can be identified: a near-wall layer $y<10^{-8}$ m (10 nm), roughly corresponding to the electric double layer (EDL) proper, characterized by a large difference between cation and anion concentrations c^+, c^- and thus by a large space charge density ρ_e; an intermediate layer $10^{-8} < y < 3\times10^{-7}$ m (10~300 nm), which can be identified with the extended space charge region (SCR) discussed by Rubinstein and Zaltzman [143], in which ρ_e decreases by one order of magnitude but remains significant; and an outer region $y>3\times10^{-6}$ m in which the concentrations c^+, c^- become practically coincident and the space charge density negligible (electroneutral region).

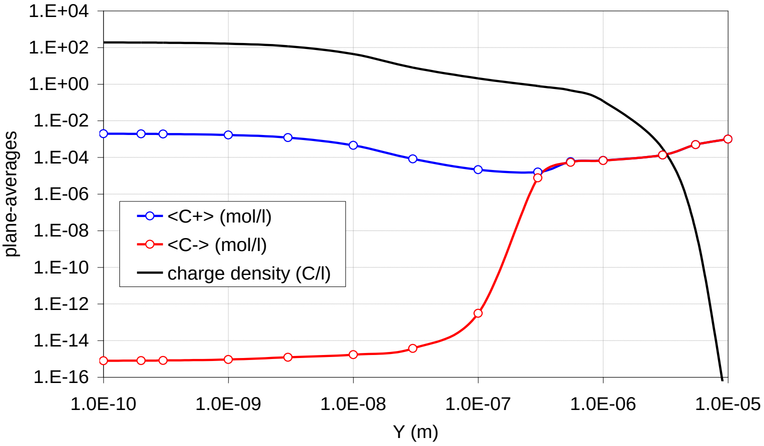

Figure 44. Horizontally-averaged ion concentrations and space charge density as functions of the distance y from the membrane (ΔV=3 V, 3-D simulation, t=1 ms). Note the double logarithmic scale.

Figure 45 compares 2-D and 3-D results obtained in a *x*-*y* plane for *ΔV*=3 V and different times. It reports vectors of current density superimposed on a false-colour map of the vertical velocity *v*.

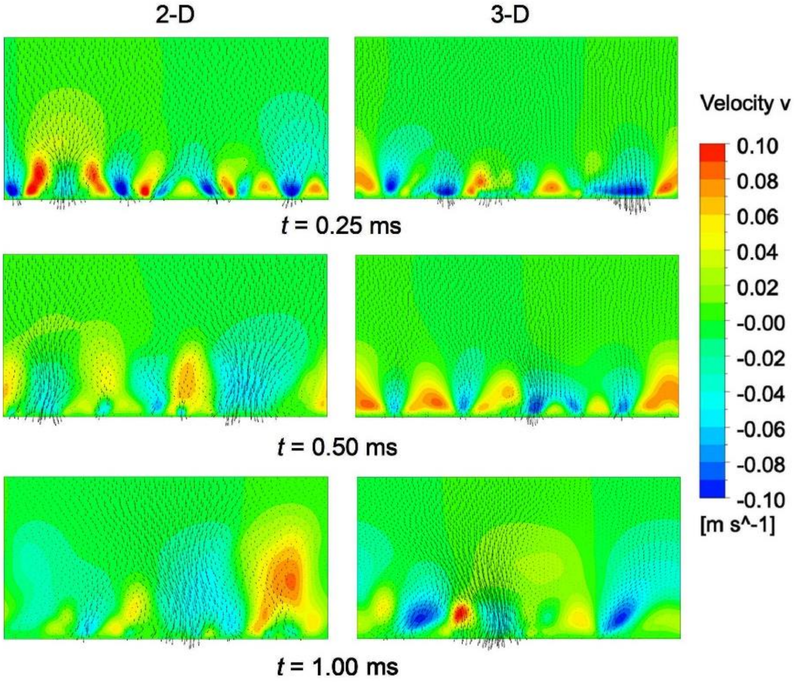

Figure 45. Velocity v and current density **j** *in a xy plane at various times. Left: 2-D; right: 3-D.*

Note that the current density is highly non-uniform and that it concentrates in regions of convective downdrafts (negative v) where convection, diffusion and migration terms in Eq. (47) are all directed towards the membrane, while it vanishes in updrafts (positive v) where convection opposes diffusion+migration. 2-D and 3-D results are comparable. Of course, the three-dimensional structure of electroconvection can only be revealed by 3-D simulations. An example is provided in Figure 46, which reports false colour maps of the vertical velocity v taken at different times on a y=constant plane located 0.6 μm away from the wall for the case ΔV =3 V (~119 V_T). Soon after the application of the electric field (t=0.25 ms), a roughly polygonal pattern of electroconvective cells develops, reminiscent of Rayleigh-Bénard convection and similar to the 3-D coherent structures predicted by Demekhin *et al*. [157]. As time progresses, the cells grow in size and decrease in intensity (t=0.50 ms), until they eventually become irregular and a statistically steady level of fluctuations is attained (t=1 ms). The final convection structure is in agreement with the predictions in [157] for ΔV >~60 V_T.

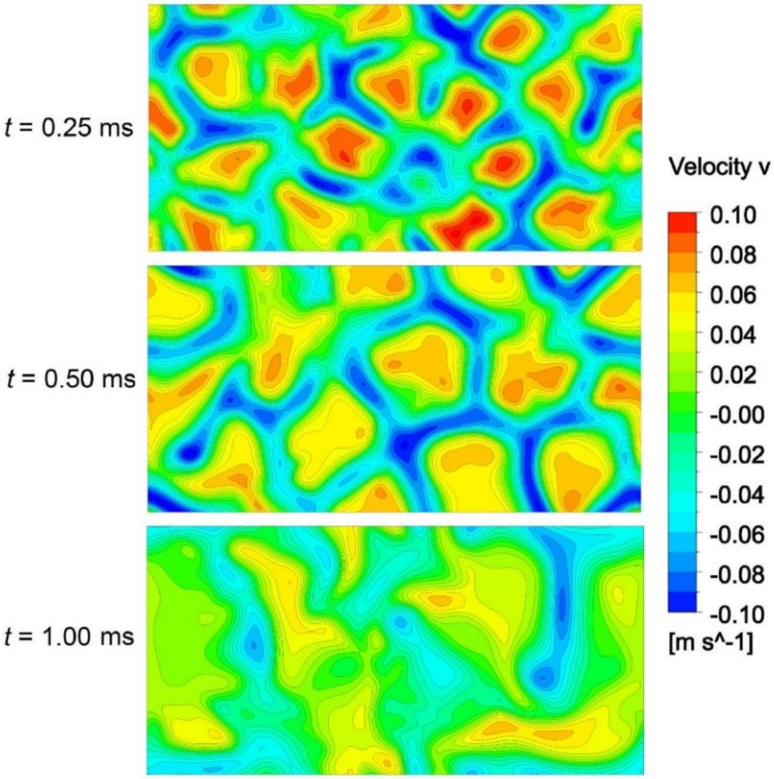

Figure 46. Velocity v in the xz plane y=0.6 μm at various times (3-D simulation).

5. Pressure drops

In membrane processes, spacers or profiled membranes are needed to create the space between the membranes and to enhance the mixing and reducing the polarization phenomena. However, they are obstacles to the fluid motion, thus the pressure drops distributed along the channels and, consequently, the pumping energy consumption increase.

The pumping energy consumption can play a different relative role depending on the membrane process considered.

In MD, pressure drops below 1 bar where experimentally measured in lab-scale modules [111] and, in a pilot scale, pumping energy consumption of 0.35 kWh/m^3 were observed [159]. The typical thermal energy required in membrane distillation is above ~100 kWh/m^3 [7,159], so the relative contribution of the pumping energy consumed is negligible. Note that the latter is an electric/mechanical energy and rigorously should not be directly compared with thermal energy. However, even converting the thermal energy in electric energy, in relative terms the pumping energy would still be a minor contribution.

In electromembrane processes, pressure drops from ~100 mbar in lab-scale systems [67], to ~1 bar in pilot installation [55] are reported in the literature. These pressure drops values and the corresponding pumping energy consumption are comparable to the values above reported for MD. However, they have a bigger impact in final performance of the process, especially in RED. In this case, indeed, the pumping energy consumption can be the 25% of the total generated electrical energy in the optimum condition [28] but, in other operating conditions, it can also bring the net produced energy to zero [28,160]. In ED, pumping power is usually negligible compared to electric power consumed directly by the stack, especially when high salinity feeds are treated [161]. Nevertheless, in large module, pumping energy consumption of ~23% of the total energy were reported in the literature [37].

It is worth to mention that asymmetric pressure drops in concentrate and diluate compartments can also lead to a membrane deformation, which affect the performance of the process. This effect is important especially when profiled membranes are adopted. Battaglia *et al*. [162,163] studied the influence of the transmembrane pressure on the ED/RED performance with profiled membranes by CFD simulations with fluid-structure interaction. They observed that, for a given transmembrane pressure, the distance between two profiles has a maximum beyond which the membranes touch and close the channels. They also reported an increase of Sh in the expanded channel (at high pressure) and an obvious increase of friction factor in the compressed channel (at low pressure). Moreover, membrane deformation can lead to flow misdistribution in the channels and poor performance of the process [164].

Therefore, it is clear that pressure drops must be taken into account especially in electromembrane processes.

In MD, in which the Reynolds number ranges from laminar to turbulent regime, due to complex dependence of the friction factor from the main parameters (see Part II, Section 2.5), simple correlation in this wide range cannot be obtained and a large database of results from which interpolate should be used. These results are reported in Appendix C for the overlapped spacer configuration, considering six values for *l*/*H*, the whole range of γ, and Re up to ~2600.

In electromembrane process, in which Re is usually lower than ~100, it is possible to obtain simple correlations of the friction factor as function of re. Moreover, in the following, only values of *l*/*H* and γ typically adopted in electromembrane processes will be considered, leading to a few correlations which then can be implemented in one-dimensional model of the process.

In all cases, the equation solved were the continuity and momentum (Navier-Stokes) equations (Eqs. (4)-(5)), for a Newtonian incompressible fluid, and considering steady-state conditions.

No-slip conditions were imposed at all solid walls. A “unit cell” treatment was adopted at the lateral boundaries with translational periodicity imposed at these faces. Note that, with this treatment, *P* represents the periodic component of pressure, while its large-scale streamwise gradient is $-P_s$. The pressure gradient (which depends on the flow attack angle γ) is imposed as a source term in the Navier-Stokes equations and the flow rate is computed as part of the solution. Actually what is imposed is Re_τ, that is the Reynolds number based on the friction velocity u_τ defined as:

$$u_\tau = Re_\tau \frac{\nu}{\delta_c} = \sqrt{\frac{\tau_w}{\rho}} \tag{51}$$

where ν is the kinematic viscosity and τ_w is the tangential shear stress. Once imposed Re_τ the solver calculates u_τ and then τ_w; from this it is then possible to calculate the pressure gradient in the generic direction *s* as τ_w/δ_c.

At each iteration of the numerical solver, the velocity component along the main flow direction is volume-averaged in the computational domain (unit cell) and is then multiplied by the porosity of the spacer (fluid volume/total volume) to obtain the superficial velocity u_{void}.

The main results obtained by CFD for the friction factor *f* for overlapped (graph a) and woven spacers (graph b) with *l*/*H*=2 and flow incidence angles *γ* of 45° and 0°-90° are shown in the range Re≤70 in Figure 47. The friction coefficient is normalized by the corresponding factor for parallel flow in an empty (spacerless) plane channel, 96/Re. Best-fit polynomial correlations are also reported; these were used as a basis to evaluate *f* in the context of the one-dimensional model described in Part III.

In graph (a) it can be observed that overlapped spacers enhance friction 5 to 8 times with respect to an empty (spacerless) channel, while the enhancement caused by woven spacers is much more important (from 14 to 20 times), as it can be observed in graph (b). The flow attack angle has no influence in the case of overlapped spacers at low Reynolds number. For Re>~30, *f* is slightly higher for *γ*=45°. Woven spacers show the opposite results, with a friction factor for *γ*=0°-90° which is always higher than in the case of *γ*=45°.

In regard to profiled membranes, results for the friction factor are reported in Figure 48 for OCF with *l*/*H*=2 (graph a) and pillars (graph b) profiled membranes with *l*/*p*=2 and *p*/*H*=6.66. As in the case of spacers, results are shown in the range Re≤70 for flow incidence angles *γ* of 45° and 0°-90°. In graph (a) it can be observed that OCF profiled membranes enhance friction even 10 times or more with respect to an empty (spacerless) channel, much more than corresponding overlapped spacers (see Figure 47a), even though with similar trends. The flow attack angle has, indeed, a small influence on the friction factor only at Reynolds number higher than ~30. Beyond this value, as for the overlapped spacers, the friction factor obtained for *γ*=45° is higher than the corresponding value for *γ*=0°-90°.

The lowest friction factor values were obtained in the case of pillars profiled membranes (Figure 48b). In this case, indeed, pillars enhance friction only 2 times with respect to a spacerless channel. Moreover, friction factor shows only a small influence of the Reynolds number, at least in the range investigated.

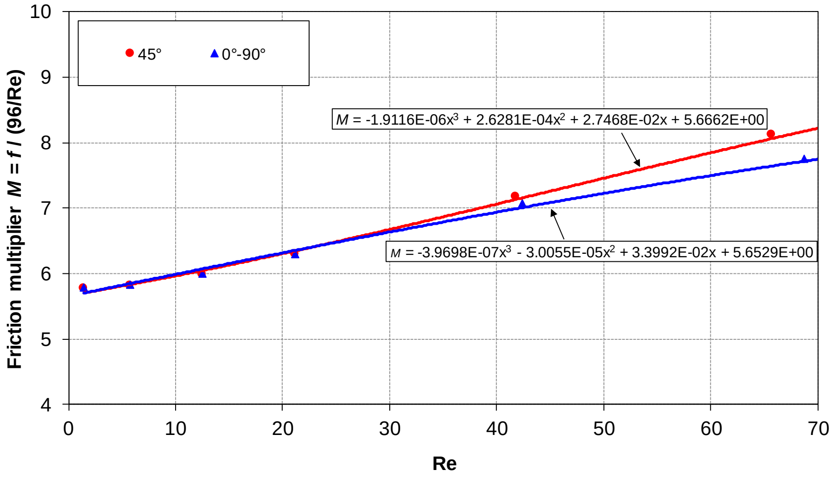

(a)

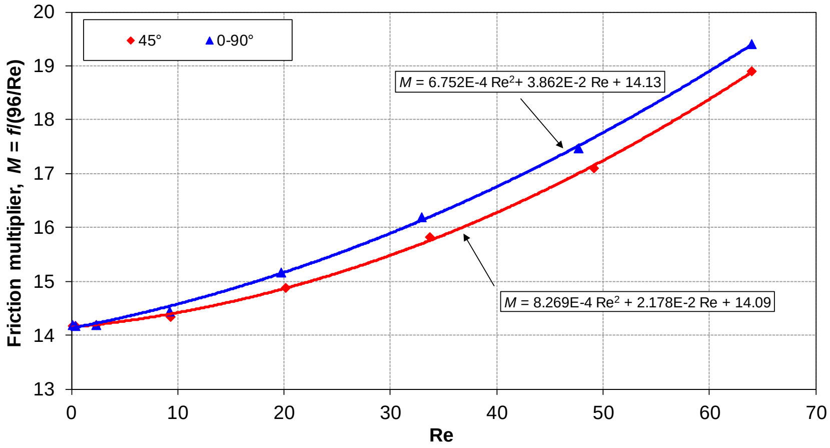

(b)

Figure 47. CFD results for friction factor f (symbols) and best-fit polynomials (lines) for (a) overlapped and (b) woven spacers with l/H=2 and different flow attack angles.

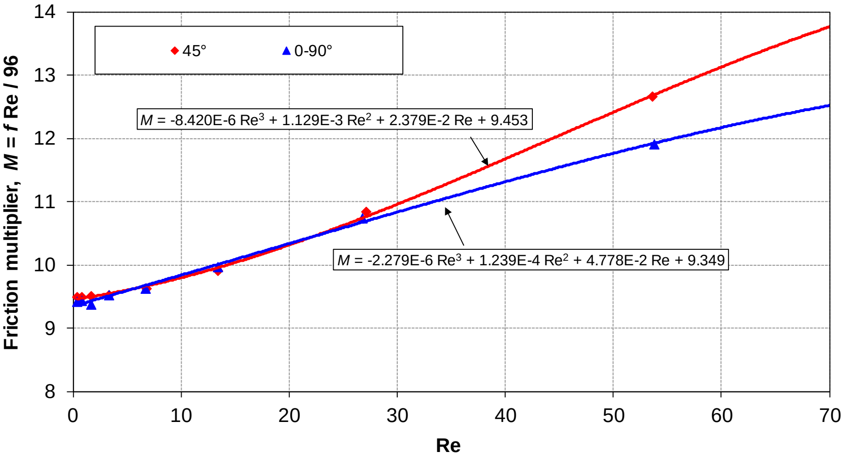

(a)

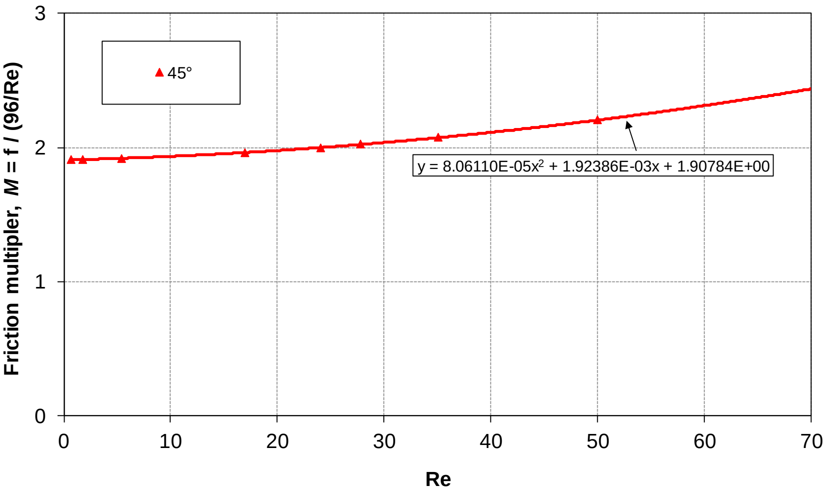

(b)

Figure 48. CFD results for friction factor f (symbols) and best-fit polynomials (lines) for (a) OCF with l/H=2 and (b) pillars profiled membranes with l/p=2 and p/H=6.66 and different flow attack angles.

Part III: Process modelling and characterisation of electromembrane systems

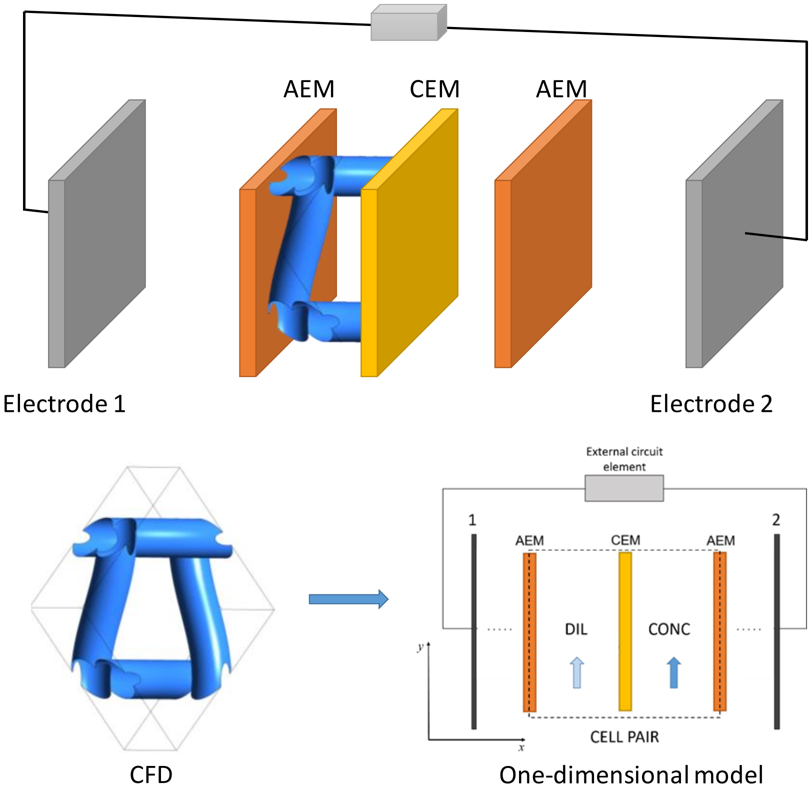

The following results have partially been published in:

La Cerva *et al.*, *Journal of Membrane Science*, vol. 541, 2017.

Ciofalo *et al.*, *Energy*, vol 181, 2019.

La Cerva *et al.*, *Desalination*, vol. 445, 2018.

1. Literature review

The mathematical modelling of a complex, multi-physics and multi-scale, process such as RED or ED involves to take into account all the relevant variables and phenomena and their interaction, including the geometric configuration of the stack, with a minimum of simplifying assumptions. Different modelling approaches have been proposed in the literature to describe ion transport in ED and RED, especially based on the Nernst–Planck equation or semi-empirical models that use experimentally established overall membrane properties. For example, Tedesco *et al.*[42,43] presented a simple 2-D model based on Nernst-Planck theory, in which the channels were supposed empty. The model equations were solved by using an algebraic equation solver, predicting process performance in terms of current efficiency for ED and salt flux efficiency for RED. The authors considered also non-ideal membranes and they quantify the effects of co-ion and water transport across the membrane.

Such a multi-physics approach can be implemented in advanced codes such as COMSOL™ that is indeed the most complete. Zourmand *et al.* [165] studied the mass transfer in ED by solving the model equations in COMSOL™. They neglected the co-ions and water transport and they also considered 2-D empty channels while corrugations over membrane surfaces were simulated by Tadimeti *et al.* [166] and Battaglia *et al* [167].

The drawback of using COMSOL™ is that each choice of the independent variables calls for a separate simulation, which may require hours of computing time; moreover, a fully 3-D simulation may require a large amount of memory and become computationally prohibitive. Therefore, this approach remains confined to the accurate simulation of few selected test cases, but is not suitable for parametrical and optimization studies, when a very large amount of different cases (ideally, a continuous configuration space) is to be considered.

An alternative approach, which offers great advantages in terms of computational speed at the price of some loss of accuracy, consists of using simplified overall semi-empirical models of the stack. These models are based on mass balance and transport equations for salt and water and require information about membrane properties empirically determined. They can be based on lumped parameters or distributed parameters. The latter should be preferred as they are more accurate and robust [161].

With this semi-empirical approach, a one-dimensional model can also incorporate local results (e.g. friction coefficients, mass transfer coefficients or polarization factors, and Ohmic resistances) computed by fully three-dimensional models.

In several studies [68–70,168] Computational Fluid Dynamics was applied to the prediction of concentration polarization and frictional pressure losses in channels for Reverse ElectroDialysis, identifying these phenomena as obviously detrimental to the performance of real RED stacks. In particular, refs. [68,69,168] concentrated on the influence of overlapped and woven spacers while ref. [70] considered profiled membranes, bearing pillar protrusions of either square or circular cross section.

However, CFD studies alone can only give qualitative indications on the relative merits and demerits of different configurations (e.g. net spacers versus profiled membranes). Coupling CFD results with a semi-empirical one-dimensional model, it is possible to understand quantitatively how polarization phenomena and pressure losses affect the performance of electromembrane processes.

This approach was used for example by Campione *et al.* [161,169] who presented a hierarchical model for ED and Capacitive Electrodialysis, implemented in gPROMS®, which use CFD results for Sh and f obtained for traditional woven spacers.

Pawlowski *et al.* [170] used the OpenFOAM® software package to predict pressure drop and concentration polarization in the presence of membranes with chevron corrugations and coupled these results with a one-dimensional model of RED process.

In this thesis, a unified one-dimensional model for electromembrane processes, valid for ED, RED and Assisted RED will be presented. Here, the 3-D finite volume code is used to predict not only pressure drop and mass transfer coefficients (Sherwood numbers) but also Ohmic resistances. Moreover, an empirical correlation is used to predict the LCD in ED.

2. One-dimensional model for electromembrane processes

This model combines a one-dimensional stack-level simulation with results (mass transfer coefficients, friction coefficients, Ohmic resistances) computed by 3-D simulations. The main assumptions are that the solutions contain only a binary electrolyte ("salt"), and that a stack consists of n_{CP} identical cell pairs (thus, flow misdistribution among the channels and parasitic currents through the manifolds are neglected).

In 3-D CFD simulations, the computational domain includes a single cell pair and is restricted to one repetitive unit of the lattice determined by spacers or profiled membranes. Streamwise and spanwise periodicity is imposed, while the "Unit Cell" approach described in Part II, Section 2.1 accounts for large-scale pressure and concentration gradients. Ionic transport is simulated by a convective-diffusive transport equation for the electrolyte, which can be obtained from the Nernst-Planck equations under the assumption of local electroneutrality [33,68,171,172]. Numerically solving the Laplace equation for the electric potential provides Ohmic resistances [160].

The one-dimensional stack-level model simulates a generic cell pair on the basis of water and electrolyte streamwise mass balances, accounting for the various contributions to the total fluxes of water (osmotic and electro-osmotic) and ions (Coulombic and diffusive) across the membranes. Both Ohmic and non-Ohmic contributions to the electric potential difference across a cell pair are accounted for. Experimental data or correlations are used for the properties of the membranes (e.g. salt and osmotic permeabilities, permselectivity, electrical resistance).

The model predicts streamwise distributions of local variables such as current density, concentrations and fluxes, and overall performance parameters such as total current and consumed/produced electric power. Parallel- or counter-flow arrangements can be simulated, while cross-flow layouts would require a 2-D approach. The model has been implemented on different platforms including Excel™ and G-95 Fortran.

For each channel *SOL* (either *CONC* or *DIL*), the quantity $U^{SOL}=Q^{SOL}/(W^{SOL}H^{SOL})$ (superficial velocity) is adopted as the reference velocity, independent of the presence of spacers or membrane profiles. Consistently, the hydraulic diameter of the generic channel is computed as $2H^{SOL}$, i.e. as the hydraulic diameter of a plane void (spacerless) channel of infinite spanwise extent, and the Reynolds number as $\mathrm{Re}^{SOL}=U^{SOL}\cdot 2H^{SOL}/\nu^{SOL}$. Note that stack width W and length L are the same for both solutions in parallel- or counter-flow.

The following sign conventions are adopted:

- the trans-membrane water flux J_W is positive if directed from diluate to concentrate;
- the trans-membrane salt flux N_S is positive if directed from concentrate to diluate.

With reference to Figure 49a, which shows a generic cell pair within a stack, the electric current density i is positive if directed from 1 to 2 through the stack (i.e. $i > 0$ for ED, $i < 0$ for RED and ARED); similarly, the external voltage Δv_{ext} (per cell pair) is positive if $V_1 > V_2$.

According to the process being simulated, either electrode (1 or 2) may be positive or negative and may play the role of anode (where oxidation reactions occur) or cathode (where reduction reactions occur). In particular (see Table 4 and Figure 49b and Figure 49c):

- the positive electrode is the anode in ED and ARED while it is the cathode in RED;
- the negative electrode is the cathode in ED and ARED, while it is the anode in RED.

Table 4. Signs of current and voltage and role of the electrodes in different working modes, with reference to the scheme of Figure 49.

Process	**Electrode 1**	ΔV_{ext}	***i* (direction)**	**Electrode 2**	**External circuit element**
ARED	Cathode (-)	< 0	< 0 (←)	Anode (+)	Generator
RED	Cathode (+)	> 0	< 0 (←)	Anode (-)	Resistance
ED	Anode (+)	> 0	> 0 (→)	Cathode (-)	Generator

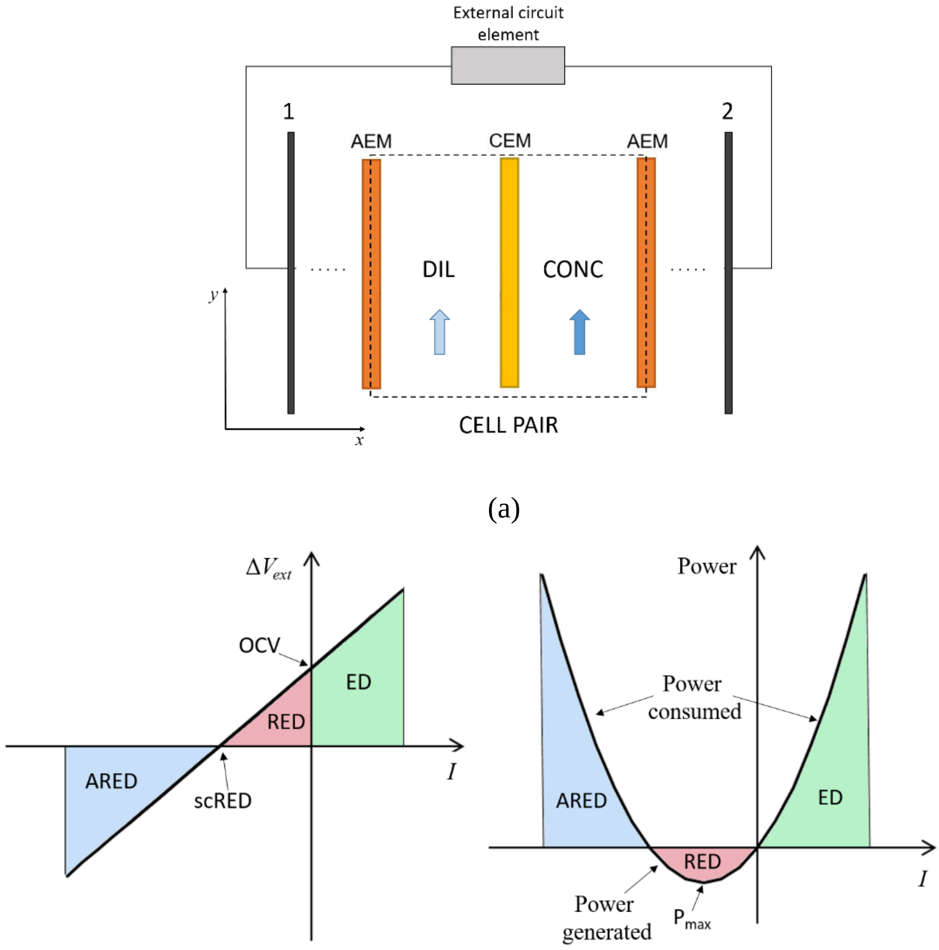

(a)

(b)

(c)

Figure 49. (a) Schematic representation of a cell pair; electrodes (1) and (2) are shown. The grey block indicates a passive or an active circuit element depending on the working mode. (b) Voltage-current curves; (c) power -current curves.

Using the above assumptions, the following governing equations may be expressed in a unified form for all working conditions (where fluxes are written for both membranes):

- Equations relating the mass flow rates of water and salt in the generic channel, G_W^{SOL} and G_S^{SOL} (in kg/s), varying along the axial coordinate y, with the volume flow rate of the solution Q^{SOL} (in m^3/s) and the bulk salt concentration C^{SOL} (in mol/m^3):

$$G_S^{SOL} = M_S C^{SOL} Q^{SOL}; \quad G_W^{SOL} = \rho^{SOL} Q^{SOL} - G_S^{SOL} \tag{52}$$

and their inverses:

$$C^{SOL} = \frac{G_S^{SOL} \rho^{SOL}}{M_S (G_W^{SOL} + G_S^{SOL})}; \quad Q^{SOL} = \frac{G_W^{SOL} + G_S^{SOL}}{\rho^{SOL}} \tag{53}$$

in which M_S is the molar mass of salt and ρ^{SOL} is the density of the solution, a function of concentration and temperature [173].

- Local mass balance of water and salt:

$$\frac{dG_W^{CONC}}{dy} = -\frac{dG_W^{DIL}}{dy} = \rho_W J_W W; \ \frac{dG_S^{CONC}}{dy} = -\frac{dG_S^{DIL}}{dy} = -M_S N_S W \tag{54}$$

in which ρ_W is the pure water density at the working temperature and J_W is the overall trans-membrane water flux in $m^3/(m^2s)$.

- Expression of J_W as made up of an osmotic and an electro-osmotic contribution:

$$J_W = J_{W,OSM} + J_{W,E.OSM} \tag{55}$$

- Expression of the osmotic flux:

$$J_{W,OSM} = L_{p,AEM}\left(\pi_{AEM}^{CONC} - \pi_{AEM}^{DIL}\right) + L_{p,CEM}\left(\pi_{CEM}^{CONC} - \pi_{CEM}^{DIL}\right) \tag{56}$$

in which $L_{p,IEM}$ is the osmotic permeability of the generic membrane IEM, while π_{IEM}^{SOL} is the osmotic pressure corresponding to the concentration C_{IEM}^{SOL} at the interface of the *SOL* channel with the IEM membrane (so that there are four such terms). Osmotic pressures can be computed as functions of the concentrations by Pitzer's formulae [174].

- Expression of the electro-osmotic flux:

$$J_{W,E.OSM} = -n_H N_S \frac{M_W}{\rho_W} \tag{57}$$

where n_H is the hydration number (~7 for NaCl) and N_S is the overall molar salt flux exchanged between the two solutions. Note that in RED and ARED the electro-osmotic water flux is always opposite to the osmotic one while in ED they are in the same direction.

- Expression of the total molar salt flux N_S (exiting or entering in a cell pair) as made up of a Coulombic and a diffusive component:

$$N_S = N_S^{COUL} + N_S^{DIF} \tag{58}$$

- Expression of the Coulombic salt flux N_S^{COUL} as proportional to the current density:

$$N_S^{COUL} = -[Tr_{CEM}^{+} - (1 - Tr_{AEM}^{-})]\frac{i}{F} \tag{59}$$

where F is the Faraday constant and $Tr_{IEM}^{\pm}$ is the transport number of counter-ions (either cations or anions) in the generic membrane IEM (either CEM or AEM). Monovalent ions are assumed here. Note that this definition is consistent with the sign conventions reported above.

- Expression of the diffusive salt flux:

$$N_S^{DIF} = N_{S,AEM}^{DIF} + N_{S,CEM}^{DIF} = \frac{D_{AEM}}{H_{AEM}}\left(C_{AEM}^{CONC} - C_{AEM}^{DIL}\right) + \frac{D_{CEM}}{H_{CEM}}\left(C_{CEM}^{CONC} - C_{CEM}^{DIL}\right) \tag{60}$$

where D_{IEM} is the salt diffusive permeability coefficient in the generic membrane. Note that one always has $N_S^{DIF} \geq 0$.

- Expression of the local Nernst potential E (per cell pair) as a function of the local solution concentrations:

$$E = (\alpha_{AEM} + \alpha_{CEM})\frac{R_G T}{F} ln\left(\frac{\gamma^{CONC} C^{CONC}}{\gamma^{DIL} C^{DIL}}\right) \tag{61}$$

in which α_{AEM}, α_{CEM} are the permselectivities of the anion and cation exchange membranes, C^{CONC} and C^{DIL} are the local bulk concentrations of concentrate and diluate, γ^{CONC} and γ^{DIL} are the corresponding activity coefficients, T is the absolute temperature and R_G is the gas constant. The activity coefficients γ can be estimated as functions of concentration by Pitzer's formulae [174]. Note that, by this definition, one always has $E \geq 0$. The Nernst potential assessed considering the inlet concentrations is called Open Circuit Voltage (OCV). The voltage drop $\eta_{\Delta C}$, associated to the concentration variation along the stack, can be computed as the difference between the OCV and the local Nernst potential E.

- Relation between the local current density i and the different potentials:

$$\Delta v_{ext} - E \pm \eta_{BL} = \eta_{\Omega}; \ \ i = \frac{\Delta v_{ext} - E \pm \eta_{BL}}{r + R_{blank}/n_{CP}} \tag{62}$$

in which η_{Ω} is the Ohmic voltage drop equal to the current density times the total areal Ohmic resistance. The latter is the sum of r is the areal Ohmic resistance of channels and membranes in a cell pair, and R_{blank} is the areal Ohmic resistance of the electrode compartments. η_{BL} is the non-Ohmic drop of E in a cell pair due to the presence of four concentration boundary layers; in the model, it is treated as intrinsically positive in all cases, but the "–" sign applies in the case of ED while the "+" sign applies in the case of (A)RED. Note that the presence of diffusion boundary layers always reduces the absolute value of the electric current. Note also that in ED one has $\Delta v_{ext}>E+\eta_{BL}$ and thus $i>0$, whereas in (A)RED one has $\Delta v_{ext}>E-\eta_{BL}$ and thus $i<0$.

- Expression of the non-Ohmic polarization voltage drop η_{BL} as the sum of four terms, one for each of the four solution-membrane interfaces in a cell pair:

$$\eta_{BL} = \eta_{AEM}^{CONC} + \eta_{CEM}^{CONC} + \eta_{AEM}^{DIL} + \eta_{CEM}^{DIL} \tag{63}$$

- Expression of the contribution η_{IEM}^{SOL} at the generic interface:

$$\eta_{IEM}^{SOL} = -\alpha_{IEM}\frac{R_G T}{F} ln\left(\theta_{IEM}^{SOL}\right) \tag{64}$$

in which θ_{IEM}^{SOL} is the polarization coefficient, defined as

$$\theta_{IEM}^{SOL} = min\left\{C_{IEM}^{SOL}/C^{SOL}, C^{SOL}/C_{IEM}^{SOL}\right\} \tag{65}$$

so that θ_{IEM}^{SOL} <1 in all cases. In the limit of perfect mixing, one has $\theta_{IEM}^{SOL}\rightarrow 1$ and $\eta_{IEM}^{SOL}\rightarrow 0$.

Each of the polarization coefficients θ is related to a Sherwood number

$$Sh_{IEM}^{SOL} = \left|\frac{N_{S,IEM}}{C^{SOL} - C_{IEM}^{SOL}}\right| \cdot \frac{2H^{SOL}}{D^{SOL}} \tag{66}$$

in which Sh_{IEM}^{SOL} is the Sherwood number at the generic solution-membrane interface, $2H^{SOL}$ is the hydraulic diameter of the channel occupied by the solution *SOL* and D^{SOL} is the salt diffusivity in solution *SOL* [175]. $N_{S,IEM}$ is the salt diffusive flux at the interface (solution side) between the generic membrane IEM and the generic solution *SOL*, identical on its two opposite IEM-*CONC* and IEM-*DIL* faces if the transport numbers in the two solutions are equal. $N_{S,IEM}$ can be written as:

$$N_{S,IEM} = N_{S,IEM}^{COUL} + N_{S,IEM}^{DIF} \tag{67}$$

in which the Coulombic contribution can be evaluated from the transport numbers of the counter-ion in the membrane IEM and in the adjacent solution *SOL*, $Tr_{IEM}^{counter}$, $Tr_{SOL}^{counter}$:

$$N_{S,IEM}^{COUL} = -(Tr_{IEM}^{counter} - Tr_{SOL}^{counter})\frac{i}{F} \tag{68}$$

and the diffusive contribution is

$$N_{S,IEM}^{DIF} = \frac{D_{IEM}}{H_{IEM}}\left(C_{IEM}^{CONC} - C_{IEM}^{DIL}\right) \tag{69}$$

Note that the total molar salt flux N_S exchanged between the two solutions, Eq. (58), is the sum of $N_{S,AEM}$ and $N_{S,CEM}$, as can be verified by using Eqs. (59) and (60). From the above definitions one has, after some manipulations:

$$\theta_{IEM}^{CONC} = min(X, 1/X) \;\; where \;\; X = 1 - \frac{N_{S,IEM}}{Sh_{IEM}^{CONC}} \frac{2H^{CONC}}{D^{CONC}C^{CONC}} \tag{70}$$

$$\theta_{IEM}^{DIL} = min(Y, 1/Y) \;\; where \;\; Y = 1 + \frac{N_{S,IEM}}{Sh_{IEM}^{DIL}} \frac{2H^{DIL}}{D^{DIL}C^{DIL}} \tag{71}$$

which hold for all operating conditions (ED, RED, ARED). The advantage of using the Sherwood number is that, unlike θ, Sh depends only on geometric configuration, Reynolds number and Schmidt number, but not on the specific values of the concentrations and of the current density. For complex geometries (e.g. spacer-filled channels), Sh is computed by fully 3-D simulations using the CFD code.

- Expressions for the Ohmic areal resistance r of a cell pair as reported in: Eq. (39) in the case of spacerless channels; Eq. (42) when spacer-filled channels and flat membranes are considered; Eq. (44) when OCF profiled membranes are adopted; Eq. (45) when membranes are profiled with pillars.

The above set of equations was cast into a finite difference algorithm providing either outlet concentrations and space-dependent current density for any given voltage at the electrodes, or outlet concentrations and voltage at the electrodes for any given (mean) current density. Current-voltage curves can thus be built and quantities such as current efficiency or power density can be computed.

In particular, for parallel flow, Eqs. (54) are integrated starting from known inlet concentrations. An iterative approach is required because η_{BL} depends on the salt fluxes $N_{S,IEM}$ via Eqs. (63)-(64) and (70)-(71), and thus on the current density i via Eq. (68), but in its turn i depends on η_{BL} via Eq. (62). The case of counter-current flow is treated by a further, “outer” iterative procedure between the inlet and outlet concentrations of the diluate channel.

3. (A)RED

3.1 Model validation

For a preliminary validation of the model in RED operations, here two sets of data obtained with a different number of cell pairs in the stack and different membranes were considered. In both cases, the relevant quantity is the Gross Power Density measured as a function of the flow velocity in the channels.

The gross power density GPD (per cell pair) is obtained as

$$GPD = v_{LOAD} \cdot \langle i \rangle \tag{72}$$

The current density $\langle i \rangle$ is obtained in the model integrating the local current density i and averaging on the active membrane surface.

The first set of data was presented by Veerman *et al*. [28], who used a stack with 50 cell pairs, 10×10 cm in size, equipped with Fumasep FAD/FKD membranes, and the standard river water / seawater solutions (C=500/17 mol/m^3). The height of both the concentrate and the diluate channels was 200 μm and the porosity of the woven spacer used was estimated to be 67%. The membrane properties, as reported by the authors on the basis of their own measurements either in the same paper [28] or in a parallel study [176], are summarized in Table 5.

Although the authors characterized osmotic fluxes through the membranes by reporting the water diffusivity, in order to facilitate comparisons this value was converted into an osmotic permeability, expressed in the usual units of ml/(m^2 h bar). In regard to quantities not explicitly reported by the authors, typical values, namely, $R_{blank}=10^{-2}$ Ω m^2 for the areal resistance of the electrodes and $n_H=7$ for the hydration number (necessary to compute electro-osmotic fluxes) were assumed.

Predictions obtained by the model are compared in Figure 50 with experimental results for different velocities of the solutions in the channels (Figure 6 of reference [28]). It can be observed that the model yields only a small overprediction of GPD by ~0.03 W/m^2, rather uniform in the velocity range considered. This small discrepancy is probably caused by non-ideal effects not considered in the model, such as parasitic currents or fouling.

Table 5. Membrane properties in seawater/river water as reported by Veerman et al. [28].

	AEM	**CEM**
Membrane type	Fumasep FAD (Fumatech)	Fumasep FKD (Fumatech)
Thickness [μm]	82	82
Permselectivity	0.95	0.95
Ohmic areal resistance [Ω m^2]	1.63×10^{-4}	5.9×10^{-4}
Salt diffusive permeability coefficient D_{IEM} [m^2/s]	1.3×10^{-11} [176]	1.3×10^{-11} [176]
Water diffusivity D_W [m^2/s]	1.3×10^{-9} [176]	1.3×10^{-9} [176]
Equivalent osmotic permeability $L_{p,IEM}$ [ml/m^2 h bar]	~22	~22

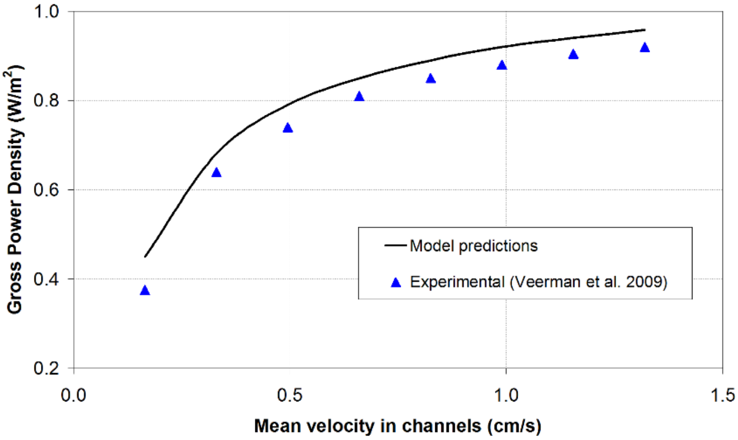

Figure 50. Comparison of the Gross Power Density (GPD) predicted by the presented model for different flow velocities with experimental results by Veerman et al. [28] *(Fumasep membranes).*

The second set of data was presented by Choi *et al*. [29], who used a small stack with only 1 cell pair, 5×5 cm in size, equipped with Selemion AMV / CMV membranes and Ti-wire woven spacers. Membrane properties are reported in Table 6. Salt diffusivity and water diffusivity (this latter roughly corresponding to an osmotic permeability) are not reported in [29] but were measured for these membranes by Veerman *et al*. [176]. As in Galama *et al*. [135], the overall Ohmic resistance of the membranes was found to be a function of the diluate concentration only. Assuming this resistance to be equally distributed among AEM and CEM, the authors' measurements (Figure 3 in [29]), once expressed as an areal resistance per single membrane, can be approximated by the simple formula r_{IEM}=0.0033+0.031/C^{DIL} (r_{IEM} in Ω m^2, C^{DIL} in mol/m^3), i.e. by a correlation of the same form as Eq. (41) but with different values of the constants *a*, *b* and *c*. The salt hydration number was assumed to be n_H=7. The height of concentrate and diluate channels was 200 μm as in the previous example.

The authors let the diluate concentration vary between ~0.85 and ~34 mol/m^3 (0.05-2 g/l), while the concentrate was seawater (C≈500 mol/m^3) in all cases. They let also the velocity in the channels vary between 0.42×10^{-2} and 2.5×10^{-2} m/s (flow rate 2.5 – 15 ml/min). The gross power density, GPD, was estimated from voltage measurements taken between reference points internal to the electrode compartments, so that it did not include the loss across the electrodes (which, in the case of a single cell pair, would be a considerable fraction of the electromotive force). The motion of the two solutions was in cross flow and followed the diagonals of the stack; however, for such short stack length (5 cm side), the difference from the present model's assumption of parallel flow can be considered negligible.

Table 6. Membrane properties as reported by Choi et al. [29].

	AEM	**CEM**
Membrane type	Selemion AMV	Selemion CMV
Thickness [μm]	120	120
Permselectivity	0.94	0.94
Areal resistance [Ω m^2]	0.0033+0.031/C^{DIL}	0.0033+0.031/C^{DIL}
Salt diffusive permeability coefficient D_{IEM} [m^2/s]	3.1×10^{-12} [176]	3.1×10^{-12} [176]
Water diffusivity D_W [m^2/s]	1.2×10^{-10} [176]	1.2×10^{-10} [176]
Equivalent osmotic permeability $L_{p,IEM}$ [ml/m^2 h bar]	~1.25	~1.47

Current density – gross power density curves obtained by the model are compared with experimental results of [29] in Figure 51, obtained for $U^{CONC}=U^{DIL}=0.42$ cm/s (flow rate 2.5 ml/min), $C^{CONC}=500$ mol/m^3 (seawater) and varying C^{DIL}, from 1.7 mol/m^3 to 34 mol/m^3. Maximum GPD values are predicted with fair accuracy; they first increase as C^{DIL} decreases from 34 to 8.5 mol/m^3, due to the increased C-ratio in the Nernst potential expression, Eq. (61); however, a further reduction of C^{DIL} causes GPD to decrease since the increase in the Ohmic resistance of the diluate channels overwhelms the Nernst effect. This non-monotonic trend is well reproduced by the model, although GPD is overestimated at the smallest diluate concentration (1.7 mol/m^3). Short circuit currents are overestimated at all concentrations, and particularly at low C^{DIL}, probably because parasitic current loops are present in the experiments but are not taken into account by the model.

Figure 51b is for $C^{CONC}=500$ mol/m^3, $C^{DIL}=17$ mol/m^3 and different values of the mean velocity U in both channels, from 0.42 to 2.5 cm/s. It can be observed that GPD increases with U, mainly because higher flow rates lead to smaller axial voltage drops $\eta_{\Delta C}$ (associated with the axial decrease of the concentration ratio); beyond a certain value of *U*, further increments fail to cause significant increases of GPD because axial effects become negligible with respect to other sources of voltage drop (Ohmic and non-Ohmic losses). This behaviour is correctly reproduced by the model, although it somewhat underestimates the influence of the flow rate.

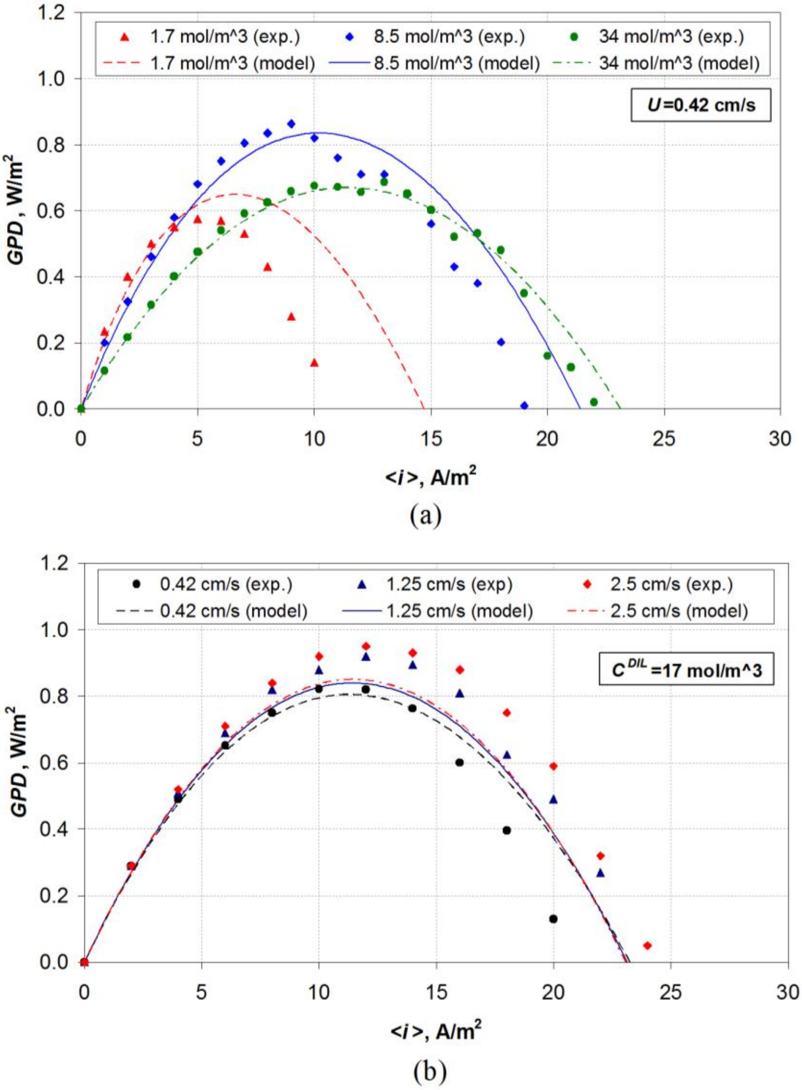

(a)

(b)

Figure 51. Comparison of the Gross Power Density (GPD) predicted by the presented model with experimental results by Choi et al. [29] *(Selemion membranes). (a)* $U^{CONC}=U^{DIL}=0.42\times10^{-2}$ *m/s,* $C^{CONC}=500$ *mol/m³ and varying* C^{DIL}*; (b)* $C^{CONC}=500$ *mol/m³,* $C^{DIL}=17$ *mol/m³ and varying velocity in the channels.*

In order to validate the model in ARED operations, an experimental campaign was performed. The experimental set-up and method are described in Appendix C. The stack was equipped with Type 10 membranes supplied by Fujifilm Manufacturing Europe BV (The Netherlands), whose properties are reported in Table 7, and woven spacers (Deukum GmbH, Germany), 270 μm thick, with pitch to height ratio $l/H = 2$ and a porosity of 75%.

Membranes were also experimentally characterized in terms of salt diffusion permeability and water permeability (see Appendix C). Feed solutions were prepared with deionised water and technical grade NaCl, with concentrations from 0.5 to 2 g/l for the dilute feed and 35 g/l for the concentrate. The same inlet fluid velocity of 0.5 cm/s was imposed in the concentrate and diluate compartment.

Table 7. Properties of the FUJIFILM Type 10 ion-exchange membranes (data provided by manufacturer).

	AEM	**CEM**
Permselectivity[a] [%]	97	98
Osmotic permeability $L_{p,IEM}$ [ml/m^{2}h·bar]	8.0	8.0
Salt diffusive permeability coefficient D_{IEM} [m^2/s]	4e-12	4e-12
Resistance[b] [Ω cm^2] (coefficient *a*) (Eq. (41))	1.77	1.89
Thickness (dry) [μm]	120	120
Thickness (wet) [μm]	130	130

[a] Based on electric potential measured over the membrane between 0.05 M and 0.5 M KCl solutions at 25°C.
[b] Measured in 2 M NaCl solution at 25°C.

A laboratory stabilized power supply (Elektro-Automatic GmbH, Germany) was used to apply the current under galvanostatic mode, allowing also the measurement of the stack voltage.

In Figure 52 experimental data and simulation results are reported for tests at: a) 35 – 0.5 g/l and b) 35 – 2 g/l. The external voltage and the outlet concentrations from the diluate and the concentrate compartments are plotted as a function of the mean current density. At $\langle i \rangle = 0$, the open circuit voltage is measured and this is higher when the ratio between the concentrations (35 and 0.5 g/l) is higher (Figure 52a). As shown in Figure 49b, when the current reaches the short-circuit value, the external voltage is zero. In ARED, in order to have currents higher than the short-circuit value, an external negative voltage must be applied. At increasing current densities, the external voltage increases (in absolute value) as well as the diluate outlet concentration, while the concentrate outlet salinity decreases.

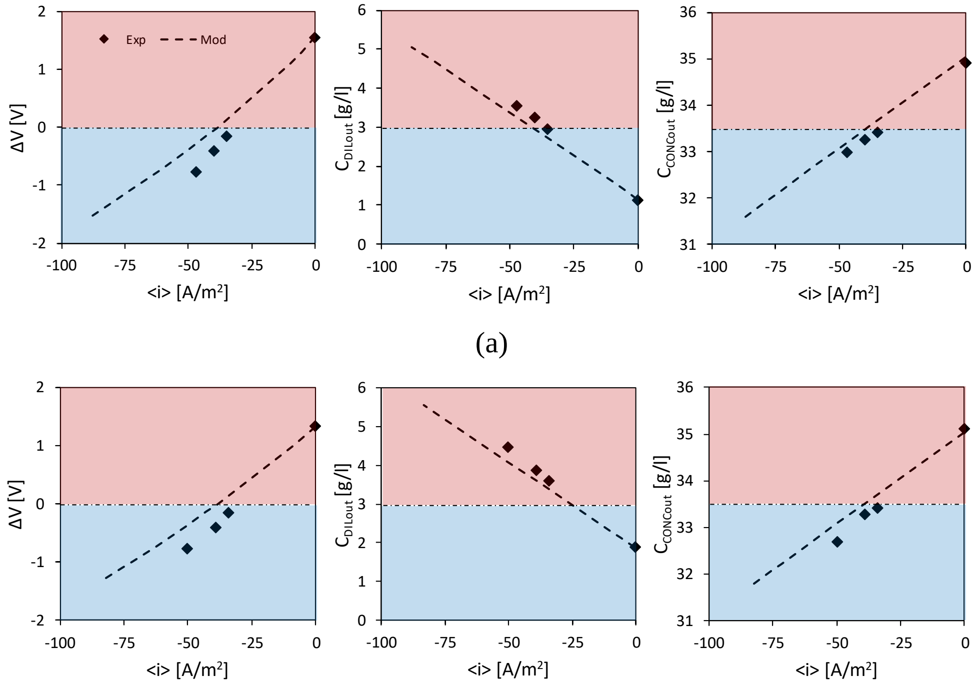

(a)

(b)

Figure 52. Comparison of experimental data (diamonds) and model predictions (dashed lines) for ARED operation. The external voltage (left column), the diluate (middle column) and concentrate (right column) outlet concentrations are reported as a function of the mean current density. a) 35 g/l and 0.5 g/l inlet feed concentrations. b) 35 g/l and 2 g/l inlet feed concentrations. Fluid velocity is 0.5 cm/s for both solutions.

Another set of experimental data is compared with model results in Figure 53. Here the inlet concentrations are 1 – 0.5 g/l and the fluid velocity is 1 cm/s. Due to the small concentration difference at the inlet, it is possible to observe at the outlet a higher concentration in the diluate channel than in the concentrate.

To further validate the model, a comparison with data from the literature is reported in Figure 54. In particular, the results reported by Vanoppen *et al.* in [81,177] are used and the simulation was carried out in the same conditions reported by the authors.

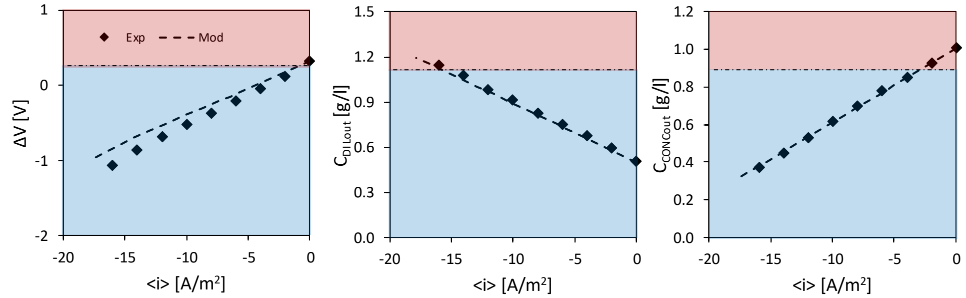

Figure 53. Comparison of experimental data (diamonds) and model predictions (dashed lines) for ARED operation. The external voltage (left column), the diluate (middle column) and concentrate (right column) outlet concentrations are reported as a function of the mean current density. 1 g/l and 0.5 g/l inlet feed concentrations. Fluid velocity is 1 cm/s for both solutions.

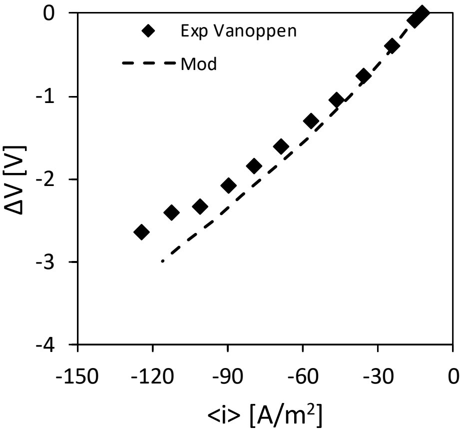

Figure 54. Comparison of experimental data (diamonds) and model predictions (dashed lines) for ARED operation. Experimental results are obtained by Vanoppen et al. [81,177].

In all cases, the model results, represented with dashed lines, are in good agreement with experiments. In Figure 52 and Figure 53, the model slightly overestimates the current density, likely due to some undersetting of the IEMs resistance values, while the salt fluxes are slightly underestimated. Such deviations are, however, acceptable and always in the conservative direction for the purposes of ARED process, which is considered as a pre-desalting step in hybrid schemes (see Part IV).

3.2 Comparison of geometries in RED

As a reference case, the empty channel, in which CFD results are not needed, is considered. Considering the conditions reported in Table 8, a stack length of 0.8 m, an areal blank resistance per cell pair r_{blank} equal to $5\cdot10^{-5}$ Ωm^2, and a potential difference across the external load per cell pair, v_{LOAD}, of 0.05 V, Figure 55a reports axial profiles of bulk concentrations. Note that, for an infinite stack length, these would tend asymptotically to two values such that the electromotive force, i.e. the Nernst potential E, Eq. (61), equals the imposed potential difference v_{LOAD} between the electrodes, so that both the local current density i and the local Ohmic losses η_Ω vanish. For realistic stack lengths, this condition is usually far from being reached.

Table 8. Conditions assumed in the reference case.

	CONC solution	**DIL solution**	**AEM membrane**	**CEM membrane**
Concentration C [mol/m^3]	500	17	-	-
Thickness [μm]	300	300	138	181
Inlet velocity [cm/s]	2	2	-	-
Osmotic permeability $L_{p,IEM}$ [ml/m^2 h bar]	-	-	5 [176]	5 [176]
Salt diffusive permeability coefficient D_{IEM} [m^2/s]	[175]	[175]	5.5×10^{-11} [176]	5.5×10^{-11} [176]
Hydration number n_H (-)	-	-	7	7
Permselectivity [%]	-	-	0.90 [176]	0.95 [176]
Ohmic areal resistance r [Ω m^2]	$\frac{H^{CONC}}{\varepsilon\sigma^{CONC}}$	$\frac{H^{DIL}}{\varepsilon\sigma^{DIL}}$	$a=2.8\cdot10^{-4}$ (Eq. (41) [135])	$a=2.5\cdot10^{-4}$ (Eq. (41) [135])

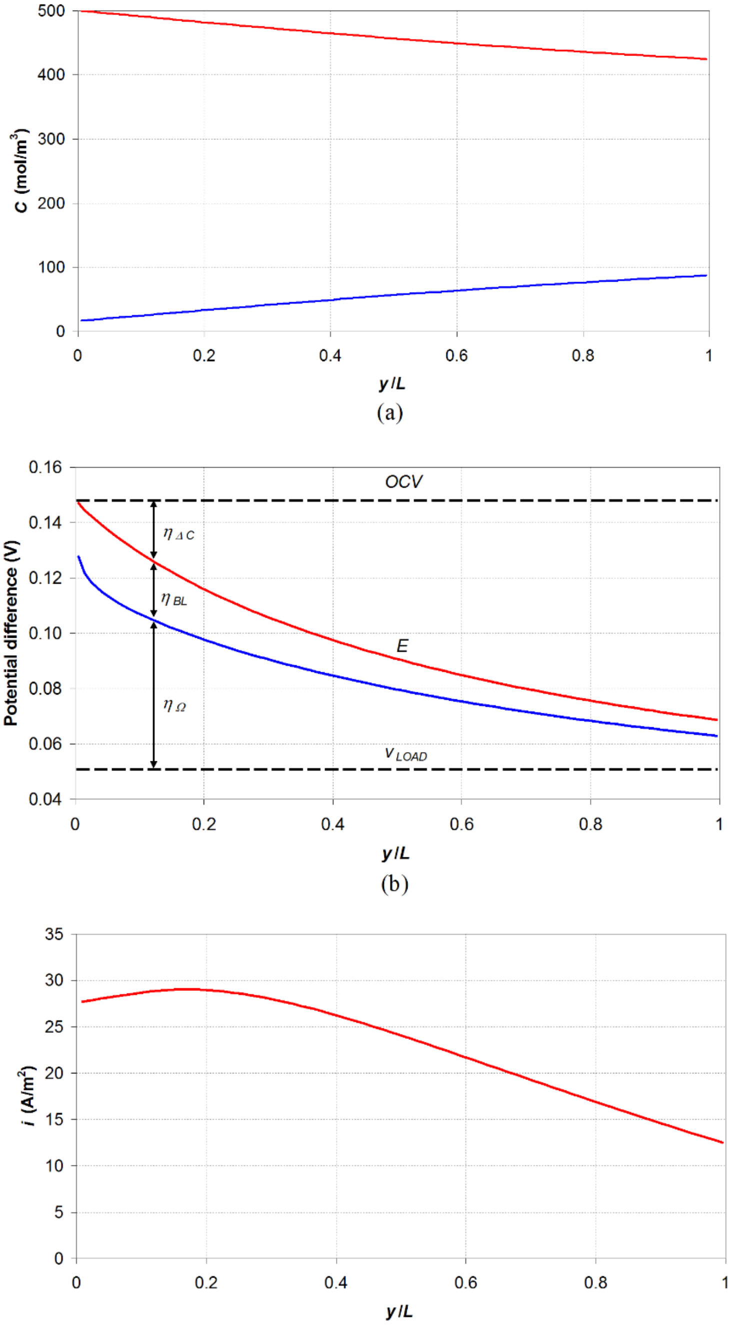

(a)

(b)

(c)

Figure 55. Axial profiles computed by the model for the conditions specified in Table 8. (a) concentrations; (b) electric potential differences; (c) current density.

Figure 55b reports axial profiles of the electric potential differences. Under the conditions considered here, most of the internal potential drop is associated with axial concentration variations ($\eta_{\Delta C}$) and with Ohmic losses (η_{Ω}). Note that, as one moves along y, $\eta_{\Delta C}$ increases while η_{Ω} decreases. Non-Ohmic losses associated with concentration changes in the direction orthogonal to the membranes (η_{BL}) are comparable with the other losses only in the first tract of the stack and play a secondary role elsewhere.

Finally, Figure 55c reports the axial variation of the electric current density i. Note that i initially increases due to the strong reduction of the Ohmic resistivity of the dilute solution. In the second half of the stack, i decreases exponentially with a large relaxation length.

If now v_{LOAD} is made to vary in small steps (e.g. 0.001 V) between 0 and OCV, current-voltage characteristic curves like those reported in Figure 56 are obtained.

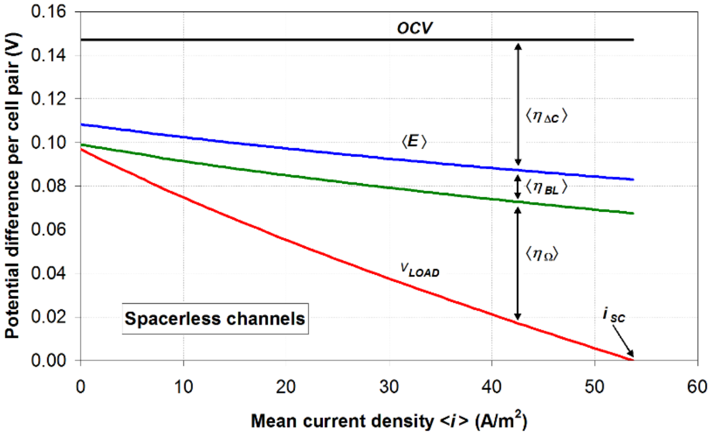

Figure 56. Current density-voltage characteristic curves computed by the model for the conditions specified in Table 8.

Here, voltage drops and current density ⟨i⟩ are mean values, obtained by averaging over the stack length L (or, equivalently, over the stack projected surface $S=L \cdot W$). Note that both the open circuit voltage OCV (~0.147 V here) and the potential difference v_{LOAD} across the external load r_{ext} are uniform along the stack and thus do not need averaging. i_{SC} is the short circuit current corresponding to $r_{ext}=0$ and $v_{LOAD}=0$ (~54 A/m^2 in the present reference case). It can be observed that the axial loss $\eta_{\Delta C}$ would be zero under open circuit conditions (⟨i⟩=0) in an ideal stack, i.e. in the absence of non-ideal effects (osmotic and electro-osmotic water flux and diffusive salt flux), but is significant even at zero current in the real stack considered here. Also polarization losses η_{BL} would vanish for $\langle i \rangle$=0 under ideal conditions, but are non-zero here due to the diffusive salt flux. As a consequence, the voltage across the load per cell pair (v_{LOAD}) under open circuit conditions (r_{ext}→∞), which would be equal to 0.147 V=OCV in an ideal stack, is only ~0.10 V in the present, real conditions. Only the Ohmic loss η_{Ω} vanishes for $\langle i \rangle$=0 both in an ideal and in a real stack.

The diagram in Figure 56, which is for a single cell pair and per unit area, can be turned into a *V-I* (total voltage – total current) plot by multiplying v_{LOAD} times n_{CP} (number of cell pairs in the stack) and $\langle i \rangle$ times $S=L\cdot W$ (projected surface area of the stack).

The net power density NPD is obtained by subtracting from GPD (Eq. (72)) the pumping power density PPD, associated with pressure losses in the concentrate and diluate channels. In its turn, PPD can be expressed as:

$$PPD = \frac{Q^{CONC}\Delta P^{CONC} + Q^{DIL}\Delta P^{DIL}}{S\chi} \tag{73}$$

in which $Q^{SOL}=U^{SOL}H^{SOL}W$ is the volume flow rate in each channel (*SOL*=either *CONC* or *DIL*), ΔP^{SOL} is the corresponding pressure loss, $S=LW$ is the (projected) surface area and χ is the efficiency of the pump.

The distributed pressure drop can be computed as

$$\Delta P^{SOL} = \int_0^L f^{SOL} \frac{1}{2H^{SOL}} \rho^{SOL} \frac{(U^{SOL})^2}{2} dy \tag{74}$$

in which f^{SOL} is the Darcy-Weisbach friction coefficient for channels filled with the SOL solution. Note that Eq. (74) allows for the streamwise variation of density and mean velocity of the solution to be taken into account, using the same axial discretization into *n* elements adopted for the calculation of electrical quantities and concentrations.

For plane channels / membranes in laminar flow, one has f=96/Re, while, for profiled membranes or spacer-filled channels, f is computed as a function of Re by CFD simulations of the unit cell for the appropriate geometry. As observed in Part II, Section 5, the presence of a spacer or of a profiled membrane may enhance the friction coefficients by several times with respect to a void (spacerless) plane channel.

For each channel, singular pressure drops can be collectively modeled as

$$\Delta P_{sing}^{SOL} = K^{SOL} \rho^{SOL} \frac{(U^{SOL})^2}{2} \tag{75}$$

in which the constant K^{SOL} (singular loss coefficient) accounts for area or direction changes both in the channels proper and in the relevant manifolds. Singular pressure losses in RED stacks may vary broadly according to the design chosen for the flow distribution system; it has been reported in the literature [67] that they may amount to a significant fraction of the overall pressure drop. Since, for f=50–500 and $L/d_{eq}=10^2$–10^3 (ranges of values typical of spacer-filled RED channels), the term fL/d_{eq} may vary between $5{\cdot}10^3$ and $5{\cdot}10^5$, values of K of 10^3–10^5 (or even larger) can be expected.

For the same reference case considered in the previous Figure 55 and Figure 56, Figure 57 reports the various computed power density terms (per cell pair) corresponding to the voltage terms in Figure 56 as functions of the average current density $\langle i \rangle$, together with the net power density (per cell pair) NPD= GPD-PPD computed by Eqs. (72)-(73) for $K^{CONC}=K^{DIL}=10^4$ and χ=0.7.

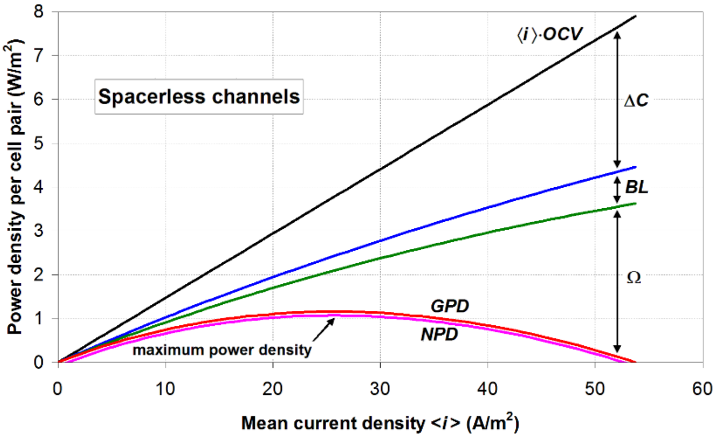

Figure 57. Current density-power density curves computed by the model for the same configuration as in Figure 56 and $K^{CONC}=K^{DIL}=10^4$, χ=0.7.

Note that, due to non-Ohmic effects, the maximum gross power density GPD is attained for a mean current density slightly less than one half the short-circuit value i_{SC}. The same value of $\langle i \rangle$ maximizes also the net power density NPD since the pumping power density PPD does not depend on $\langle i \rangle$. Note also that, under the present conditions, pumping losses are just a small fraction of the gross power density despite the high values chosen for the singular loss coefficients.

As an example of the influence of the channel configuration on the stack performance, Figure 58 reports voltage-current density characteristic curves computed by the model presented in Part III, Section 2 for the conditions reported in Table 8 for two different configurations: (a) woven spacers with l/H=2; (b) OCF profiled membranes with l/H=2. In both cases, the flow attack angle γ was 45°; the comparison with results for other values of γ (not reported here for the sake of brevity) shows that the influence of this parameter is only secondary at the present low Reynolds number.

These results should be compared with the corresponding predictions obtained by the same model for the ideal case of a void (spacerless) channel (Figure 56). The comparative examination of the current density- voltage (per cell pair) curves shows that the relative importance of different voltage losses is about the same in all cases: Ohmic and axial losses are of a similar magnitude, while boundary layer drops play only a secondary role. However, it can be observed that η_{BL} is utterly negligible in the case of woven spacers, which cause a very effective mixing, intermediate in the presence of OCF profiled membranes, and largest in the empty channel of Figure 56. Both woven spacers and OCF profiles yield a short-circuit current density slightly larger than the empty channel, showing that, in regard to mass transfer, they perform better than this latter.

Figure 59 reports power density-current density curves (load curves) for the same configurations as in Figure 58. These highlight the importance of frictional pressure drop: both woven spacers and OCF membranes cause much larger pumping losses than the empty channel, which significantly reduce the net power density.

An overall comparison between the three geometries examined is given in Figure 60. It reports the gross (a) and net (b) power density (per cell pair), GPD and NPD, as a function of the mean current density $\langle i \rangle$. Figure 60a shows that the highest gross power density and the highest short circuit current density are provided by OCF profiles, followed by woven spacers and then by the empty channel. On the other hand, as shown by Figure 60b, the highest net power density per cell pair is provided by empty channels, followed by OCF profiled membranes and then by woven spacers.

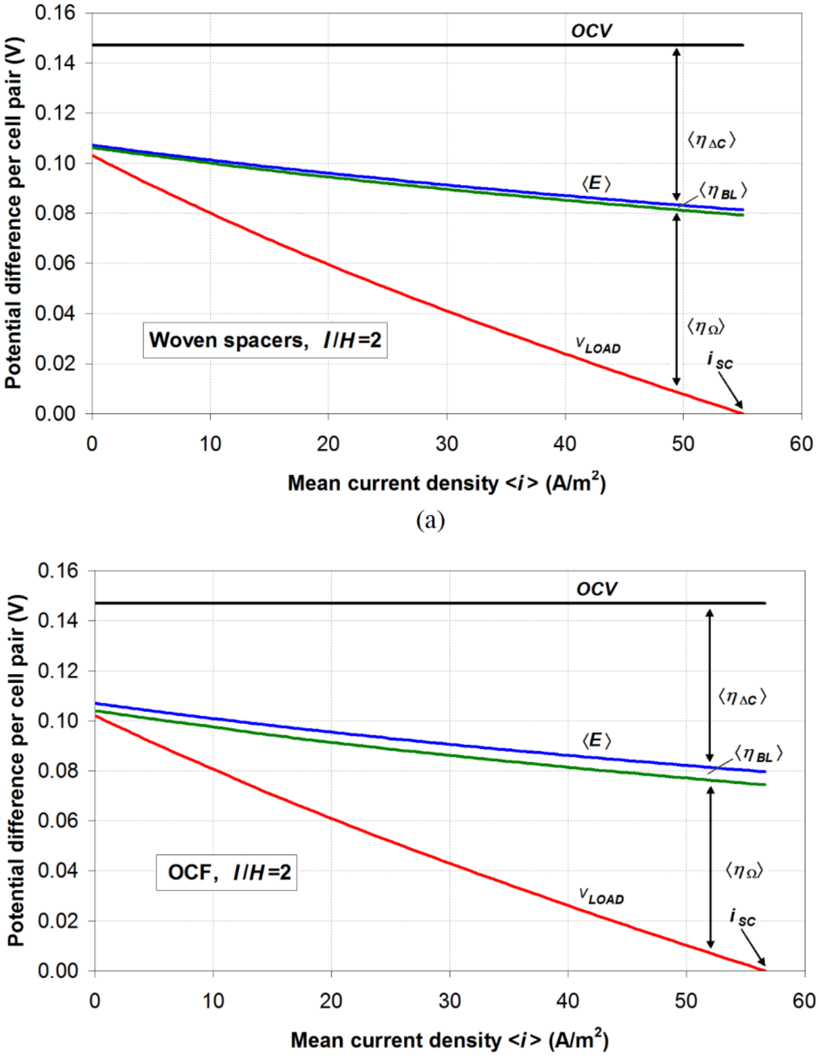

(a)

(b)

Figure 58. Current density-voltage curves computed by the model for the conditions specified in Table 8 and different configurations: (a) woven spacers with l/H=2; (b) OCF profiled membranes with l/H=2. The flow attack angle γ was 45° in both cases.

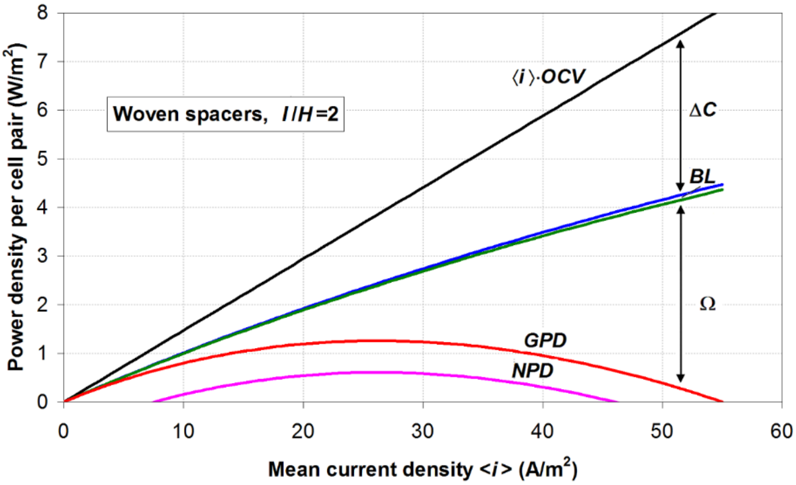

(a)

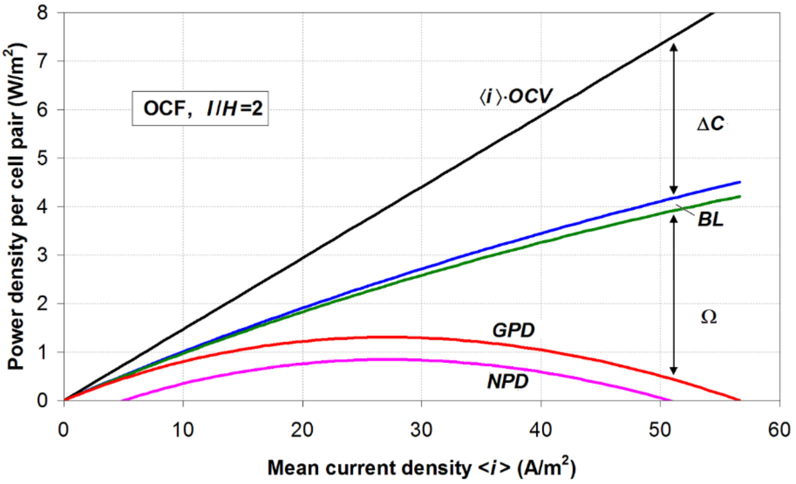

(b)

Figure 59. Current density-power density curves computed by the model for the conditions specified in Table 8 and different configurations: (a) woven spacers with l/H=2; (b) OCF profiled membranes with l/H=2. The flow attack angle γ was 45° in both cases.

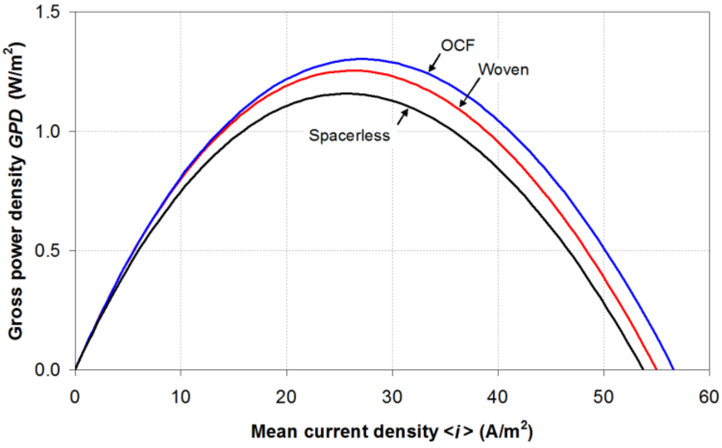

(a)

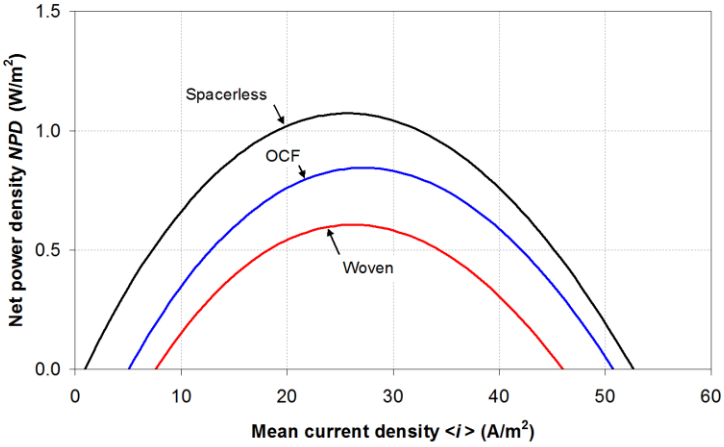

(b)

Figure 60. Summary results for the three geometries examined in the present study. (a) current density-gross power density curves; (b) current density-power density curves. See Table 8 for a description of the assumed conditions.

3.3 Optimization of RED

The optimization of RED systems is crucial for the promotion of the technology readiness level. However, only few studies have been carried out so far. Veerman *et al*. [178] developed for the first time a one-dimensional process model requiring empirical membrane properties. The model was based on some simplifying assumptions, e.g. independence of membranes' resistance on the solutions' concentrations and negligible concentration polarization effects. Moreover, pressure drops were calculated using experimental information. Channels' thicknesses and flow rates were optimized for different stack lengths in order to explore the different scenarios arising from three response parameters: the net power density, the net energy density and the quantity given by their product.

The same general approach of simulation was adopted in some recently published optimization studies [179–181], which include also other parameters in the objective functions, i.e. the lost work (with respect to the total energy from complete mixing) and the energy efficiency. Long *et al*. [180] simulated stacks with 50 cell pairs, 10×10 cm^2 active area and 200 μm thick channels, fed by seawater and river water solutions. Different membranes were simulated, thus finding the optimal flow velocities for each stack. The optimization was first conducted with the single objectives of maximum net power density and maximum energy efficiency. Then, a multi-objective optimization was performed taking into account both parameters and changing their weights. An algorithm selected the optimal point for each membrane stack. In another work [181], the same authors found optimal values of flow rates and channels' thicknesses in stacks of given sizes, including the total thickness, fed by seawater and river water solutions. Again, stacks made by different membranes were simulated. However, in this case, only the net power density was maximized.

Simulation results from the studies on RED optimization showed that optimal values may change significantly with the selected optimization criterion. Moreover, the above short review of pertinent literature shows that there is an intrinsic level of arbitrariness in the choice of the objective function, as well as in the assignment of the weights in the case of multi-objective analyses. Rather, the economic assessment is needed for a complete optimization study, i.e. aimed at finding the minimum cost of the energy produced. In this sense, given the high cost of the ion-exchange membranes, the maximization of the net power density can be regarded as a reliable optimization objective, which provides useful insights on system designs oriented to the cost reduction.

In this subsection, the one-dimensional model presented in Part III, Section 2 was used for an optimization study of broader range and from a different perspective with respect to the few examples available in the literature. The maximum net power density per cell pair has been searched for a single membrane type, analysing the effects of several operating and constructing parameters: inlet flow velocities and concentrations, channels' thicknesses, stack length, flow arrangement (parallel or counter-flow). Moreover, ideal spacer-less channels and channels filled by a woven net spacer were simulated.

3.3.1 Optimization and "scenario" variables

NPD and all other performance parameters of a given RED stack are functions of several variables. They have been listed in Table 9, grouped by type.

Note that Table 9 does not include either physical constants (e.g. the gas constant R_G or the Faraday constant F) or quantities that, at least under the present modelling assumptions, have no influence on the stack performance, such as the stack width W and the number of cell pairs n_{CP} (provided all quantities are referred to the single cell pair).

Now, some of the listed variables are not at the designer's disposal, but are imposed by availability considerations (e.g. electrolyte nature, T, C_i^{CONC} and C_i^{DIL}, at least in "open" RED in which concentrate and dilute solutions are naturally available). Others exert a monotonic influence, either beneficial or detrimental, on NPD: for example, singular pressure loss coefficients reduce NPD and should be made as low as possible; similarly, the blank resistance r_{blank} of the electrode compartments reduces NPD and should be kept to a minimum. The above quantities need not to be included in an optimization study, but can be regarded as "scenario" variables whose values are dictated by availability, design, economical or technological considerations other than the purpose of maximizing NPD.

On the other hand, some variables, namely, the thicknesses H^{CONC}, H^{DIL} and the inlet velocities U_i^{CONC}, U_i^{DIL} in the concentrate and diluate channels, are at the designer's disposal and exert contrasting effects, so that an NPD maximum is obtained for intermediate values of these parameters.

Table 9. Variables affecting the net power density (NPD) in Reverse Electrodialysis.

a) Design parameters and operating conditions

Quantity	*Symbol*	*Reference value or range*
Electrolyte nature (with associated physical properties and hydration number n_H)	-	NaCl (n_H=7)
Inlet concentrations	C_i^{CONC}, C_i^{DIL}	"Scenario" variables (500-5000 and 5-100 mol/m^3, respectively)
Channel thickness	H^{CONC}, H^{DIL}	Both 200 μm
Inlet velocities	U_i^{CONC}, U_i^{DIL}	Both 2 cm/s
Stack length	L	"Scenario variable (0.1-1 m)
Flow arrangement	-	"Scenario variable (parallel flow or counter flow)
Spacer type	-	"Scenario" variable (void, overlapped, woven)
Spacer pitch-to-height ratio	l/H	2 (if a spacer is present)
Flow attack angle	γ	45° (if a spacer is present)
Absolute temperature	T	298.15 K, or 25°C
Areal Ohmic resistance of electrodes (per cell pair)	r_{blank}	5×10^{-5} Ω m^2
Singular pressure loss coefficients in manifolds	K^{CONC}, K^{DIL} (with $\Delta p=K\rho U_i^2/2$)	Both 10^4

b) Membrane properties (AMX-CMX Neosepta®)

Quantity	*Symbol*	*Reference values*
Thicknesses	H_{AEM}, H_{CEM}	134 and 158 μm, respectively
Permselectivities	α_{AEM}, α_{CEM}	0.9 and 0.95, respectively
Diffusive permeabilities	D_{AEM}, D_{CEM}	Both 5.5×10^{-11} m^2/s
Osmotic permeabilities	$L_{p,AEM}$, $L_{p,CEM}$	Both 1.38×10^{-14} m/(s·Pa), or 5 ml/(m^2·h·bar)
Areal Ohmic resistances	r_{AEM}, r_{CEM}	Concentration-dependent (Eq. (41))

In the following, the maximum of NPD is sought in the four-dimensional parameter space of H^{CONC}, H^{DIL}, U_i^{CONC}, U_i^{DIL} for different combinations of the remaining ("scenario") variables. Among these latter, in this study the inlet concentrations C_i^{CONC} and C_i^{DIL} were made to vary between 500 and 5000 mol/m^3 and between 5 and 100 mol/m^3, respectively, while the stack length was made to vary between 0.1 and 1 m. Moreover, three distinct configurations were considered: void channels in parallel flow; woven spacer-filled channels in parallel flow; and woven spacer-filled channels in counter flow, so as to assess both the influence of spacers as opposed to the ideal case of void channels and the influence of counter- versus parallel-flow. On the whole, 6000 different combinations of "scenario" variables were examined.

3.3.2 Optimization algorithm

The gradient-ascent optimization algorithm adopted here is schematically illustrated in Figure 61 for the case of the search for the maximum of a function Ψ of two variables x_1, x_2. Starting from an arbitrary point A of coordinates x_i^A, the partial derivatives of Ψ (components of the gradient $\Delta\Psi$) are numerically approximated as:

$$\frac{\partial\Psi}{\partial x_i} \approx \frac{\Psi(\mathbf{x}_A + \Delta x_i \mathbf{e}_i) - \Psi(\mathbf{x}_A - \Delta x_i \mathbf{e}_i)}{2\Delta x_i} \tag{76}$$

(in which Δx_i are small increments of the x_i and $\mathbf{e}_i$ are the basis vectors). The point A is then moved in small steps ξ along the direction of the gradient:

$$\mathbf{x}_A \rightarrow \mathbf{x}_A + \xi\nabla\Psi \tag{77}$$

until Ψ ceases to increase (say, up to point B). The gradient in B is then re-computed and the process starts again with a new segment BC. The search terminates when no further displacement of the representative point leads to an appreciable increase in Ψ (point F). The step ξ was determined here as $C/||\nabla\Psi||$, in which $||\nabla\Psi||$ is the norm of the gradient:

$$||\nabla\Psi|| = \sum\left(\frac{\partial\Psi}{\partial x_i}\right)^2 \tag{78}$$

while C is a dimensionless parameter, initially of order 1 and then reduced by a factor <1 at each new segment. Note that the gradient is recomputed only at a few points (as Eq. (76) shows, the computation of the gradient requires the evaluation of Ψ at 2*n* points, *n* being the number of variables, and thus can be quite time-consuming). The above algorithm was implemented in G95 Fortran.

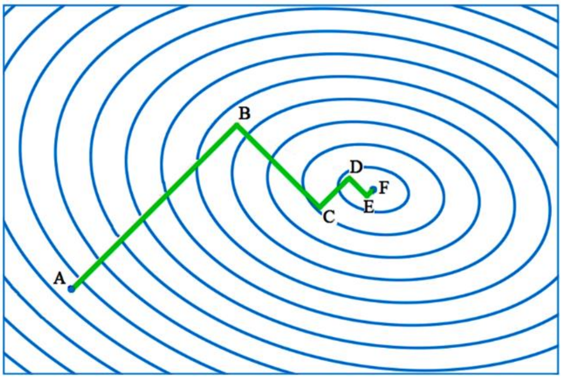

Figure 61. Illustration of the gradient-ascent optimization method for the case of 2 variables.

3.3.3 Results: spacerless channels in parallel flow

Figure 62 is for the ideal case of void (spacerless) channels in parallel flow. All quantities are reported as functions of the diluate concentration C_i^{DIL} for different concentrate concentrations C_i^{CONC} and a stack length L of 0.4 m.

Graphs (a) and (b) report the optimum channel thicknesses $H_{opt}^{CONC}$and H_{opt}^{DIL}, respectively. The optimum thickness of the concentrate channel, graph (a), increases monotonically both with C_i^{CONC} and with C_i^{DIL} and varies quite significantly, from ~240 μm (C_i^{CONC}=500 mol/m^3, C_i^{DIL}=5 mol/m^3) to ~400 μm (C_i^{CONC}=5000 mol/m^3, C_i^{DIL}=100 mol/m^3). On the other hand, the optimum thickness of the diluate channel, graph (b), increases monotonically with C_i^{DIL} but decreases monotonically with C_i^{CONC}, varying from ~100 μm (C_i^{CONC}=5000 mol/m^3, C_i^{DIL}=5 mol/m^3) to ~200 μm (C_i^{CONC}=500 mol/m^3, C_i^{DIL}=100 mol/m^3). The optimum thickness of the diluate channel is always much less than that of the concentrate channel.

Graphs (c) and (d) report the optimum superficial inlet velocities $U_{i,opt}^{CONC}$ and $U_{i,opt}^{DIL}$ $U_i^{DIL}{}_{opt}$, respectively. Both velocities increase monotonically with C_i^{CONC} and generally decrease with C_i^{DIL}, but some curves exhibit a shallow maximum for certain low values of this latter quantity. More specifically, $U_{i,opt}^{CONC}$ varies between ~1.5 cm/s (for C_i^{CONC}=500 mol/m^3, C_i^{DIL}=100 mol/m^3) and ~2.3 cm/s (for C_i^{CONC}=5000 mol/m^3, C_i^{DIL}=5 mol/m^3), while $U_{i,opt}^{DIL}$ varies between ~2.2 cm/s (for C_i^{CONC}=500 mol/m^3, C_i^{DIL}=100 mol/m^3) and ~6 cm/s (for C_i^{CONC}=5000 mol/m^3, C_i^{DIL}≈15-20 mol/m^3). The optimum velocity in the diluate channel is always larger than that in the concentrate channel, a behaviour opposite to that discussed above for the optimum thickness.

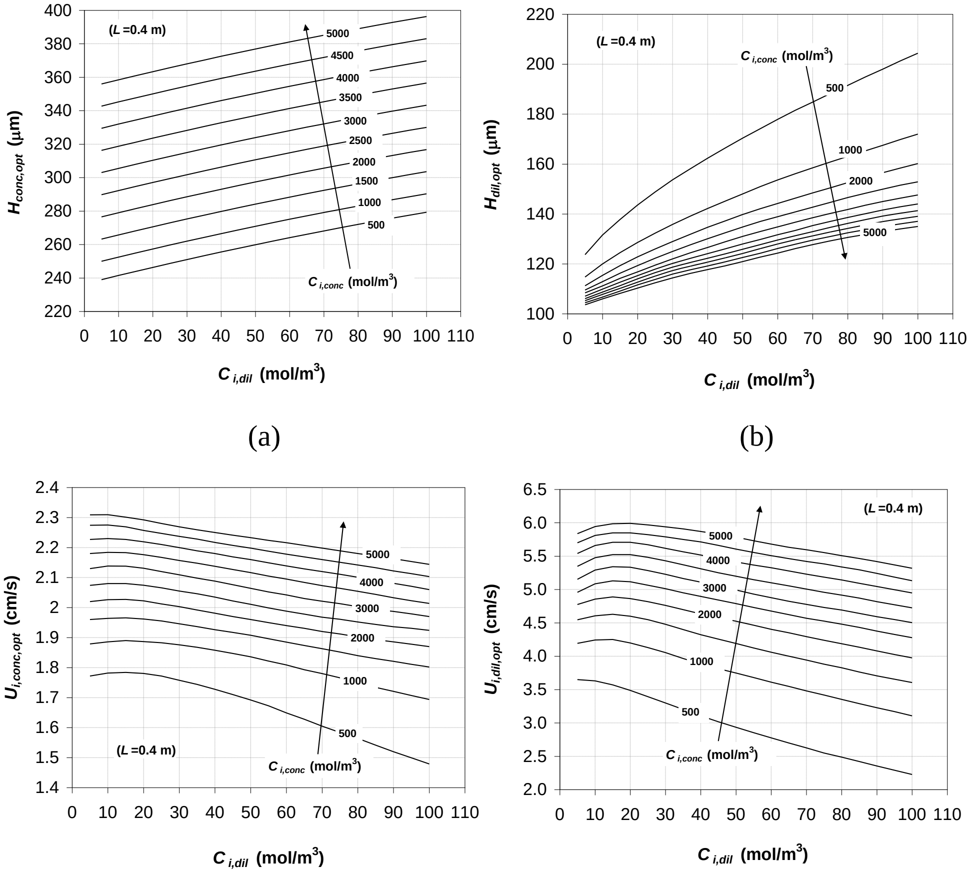

(a) (b)

(c) (d)

Figure 62. Results of the optimization study for spacerless channels in parallel flow. Graphs (a), (b), (c) and (d) show the values of H^{CONC}, H^{DIL}, U_i^{CONC}, U_i^{DIL}, respectively, providing the highest net power density NPD. All quantities are reported as functions of C_i^{DIL} for different values of C_i^{CONC} and $L=0.4$ m.

Figure 63a reports the net power density NPD_{opt} resulting from choosing the optimal values in Figure 62 for the channel thicknesses and flow velocities. NPD_{opt} increases monotonically with C_i^{CONC} but exhibits a shallow maximum as a function of C_i^{DIL} for very low values of this quantity. This is due to the fact that very low values of C_i^{DIL} act beneficially on the electromotive force E, but lead to high values of the diluate Ohmic resistance and thus of the Ohmic voltage drop η_Ω, which reduces power density. In the range considered, the highest value of NPD_{opt} (~7.7 W/m^2) is attained for the highest concentrate concentration (5000 mol/m^3, corresponding to a dense brine) and a diluate concentration of 15-20 mol/m^3 (typical river water).

By comparison, Figure 63b reports the net power density obtained by the choice of arbitrary, but typical, fixed reference values for the same parameters ($H^{CONC} = H^{DIL}$ =200 μm, $U_i^{CONC} = U_i^{DIL}$ =2 cm/s). It can be observed that in this case values of NPD (called here NPD$_{ref}$) are, in general, significantly lower; optimization leads to an increase in NPD that ranges from ~0 for the lowest C_i^{CONC} to ~25% for the highest C_i^{CONC}. Optimization also leads to a larger sensitivity of NPD to both inlet concentrations.

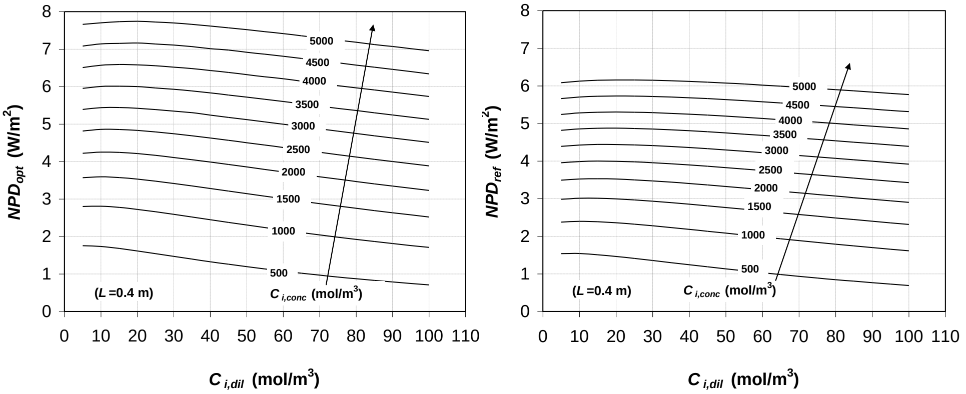

(a) (b)

Figure 63. Spacerless channels in parallel flow: net power density NPD as a function of C_i^{DIL} for different values of C_i^{CONC} and L=0.4 m. (a): optimum values of H^{CONC}, H^{DIL}, U_i^{CONC}, U_i^{DIL}, (b): reference values of the same parameters (H^{CONC}= H^{DIL}=200 μm, U_i^{CONC}=U_i^{DIL}=2 cm/s).

3.3.4 Results: spacer-filled channels in parallel flow

Figure 64 reports the same quantities as Figure 62, but for channels filled with woven spacers having a pitch-to-height ratio l/H=2 and a flow attack angle γ=45°. The flow arrangement is still parallel as in Figure 62.

The values of the control parameters H^{CONC}, H^{DIL}, U_i^{CONC}, U_i^{DIL} corresponding to the NPD maximum, graphs (a)-(d), are much different than for void channels. In particular, H_{opt}^{CONC} in graph (a) is now larger, ranging from ~350 to ~550 μm (according to C_i^{CONC} and C_i^{DIL}), and does not increase monotonically with C_i^{DIL} but exhibits a rather flat behaviour with respect to this parameter. Also H_{opt}^{DIL} in graph (b) increases significantly with respect to the spacerless case, and now ranges from ~160 to ~290 μm.

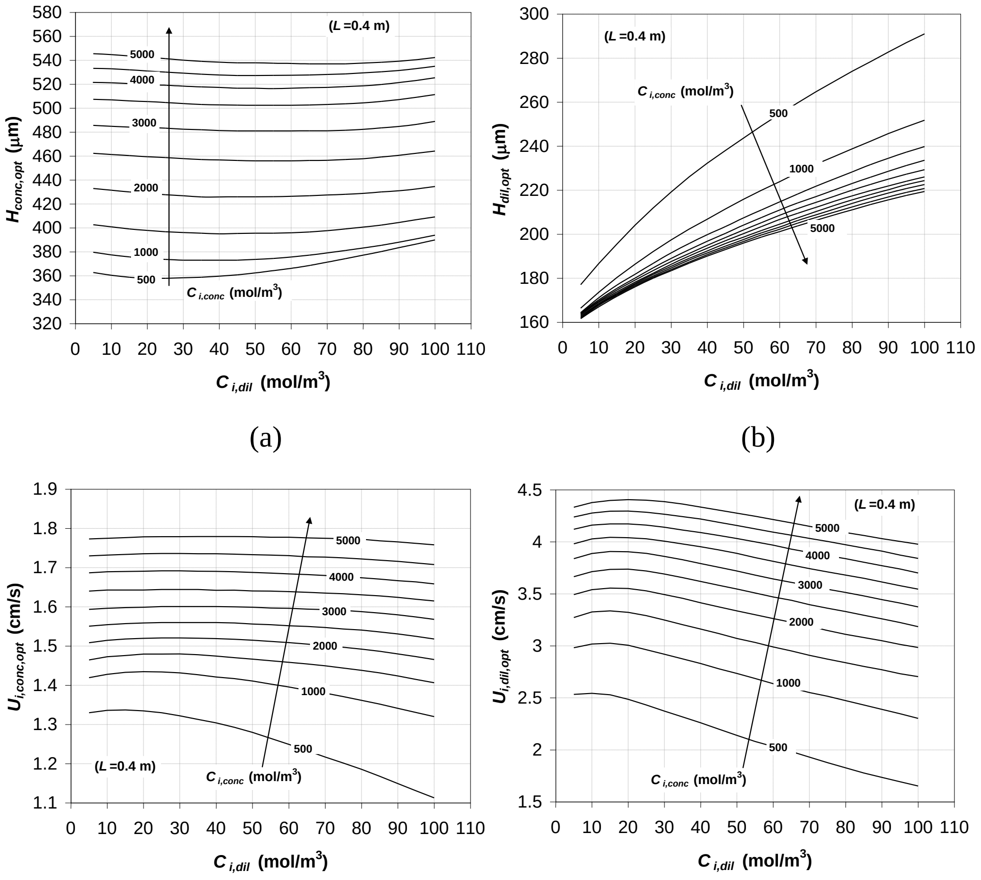

(a) (b)

(c) (d)

Figure 64. Results of the optimization study for channels filled by woven spacers (l/H=2, γ=45°) in parallel flow. Graphs (a), (b), (c) and (d) show the values of H^{CONC}, H^{DIL}, U_i^{CONC}, U_i^{DIL}, *respectively, providing the highest net power density NPD. All quantities are reported as functions of* C_i^{DIL} *for different values of* C_i^{CONC} *and L=0.4 m.*

On the contrary, optimum flow velocities are now smaller than in spacerless channels. In particular, $U_{i,opt}^{CONC}$, graph (c), ranges now between ~1.1 and ~1.8 cm/s, with a 20-25% decrease with respect to the spacerless case, and – like H_{opt}^{CONC} – is less affected by C_i^{DIL}. $U_{i,opt}^{DIL}$, graph (f), now ranges between ~1.6 and ~4.4 cm/s, ~25% less than in the spacerless case.

The reason for the increase in optimum thicknesses and the corresponding decrease in optimum velocities is that spacers cause a large increase in the friction coefficient, putting a penalty on excessively high flow speeds or excessively thin channels via an increase in in pumping power density.

Values of NPD$_{opt}$, Figure 65a, are not significantly different from those computed for void channels; the highest value of NPD$_{opt}$ rises from ~7.7 to ~8, and the overall dependence of NPD$_{opt}$ on C_i^{CONC} and C_i^{DIL} is the same. The comparison with corresponding values of NPD$_{ref}$, Figure 65b, shows that the benefits of optimization are similar to those observed for the spacerless case.

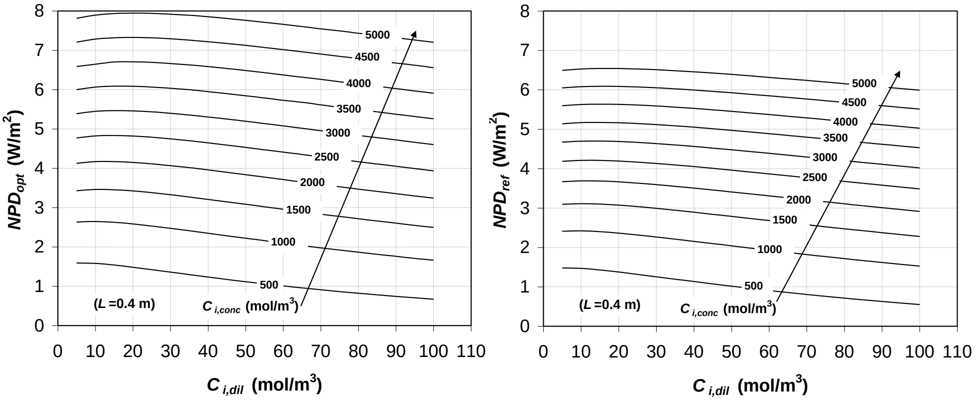

(a) (b)

Figure 65. Channels filled by woven spacers (l/H=2, γ=45°) in parallel flow: net power density NPD as a function of C_i^{DIL} for different values of C_i^{CONC} and L=0.4 m. (a): optimum values of H^{CONC}, H^{DIL}, U_i^{CONC}, U_i^{DIL}; (b): reference values of the same parameters ($H^{CONC}=H^{DIL}=200$ μm, $U_i^{CONC}=U_i^{DIL}=2$ cm/s).

For the present case of spacer-filled channels in parallel flow, which is the most likely to be encountered in practical applications, Figure 66 and Figure 67 illustrate the influence of the stack length *L*.

In particular, Figure 66 reports optimum values of channel thickness and flow velocity as functions of *L*, in the range 0.1-1 m, for different concentrate concentrations C_i^{CONC} and a fixed diluate concentration C_i^{DIL}=15 mol/m^3. The optimal channel thicknesses H^{CONC}, H^{DIL}, graphs (a) and (b), both increase with *L*; for *L*=1 m, they become as high as 550 μm and 310 μm, respectively, when the concentrate is seawater (C_i^{CONC} =500 mol/m^3), or 800 μm and 260 μm, respectively, when the concentrate is brine (C_i^{CONC} =5000 mol/m^3).

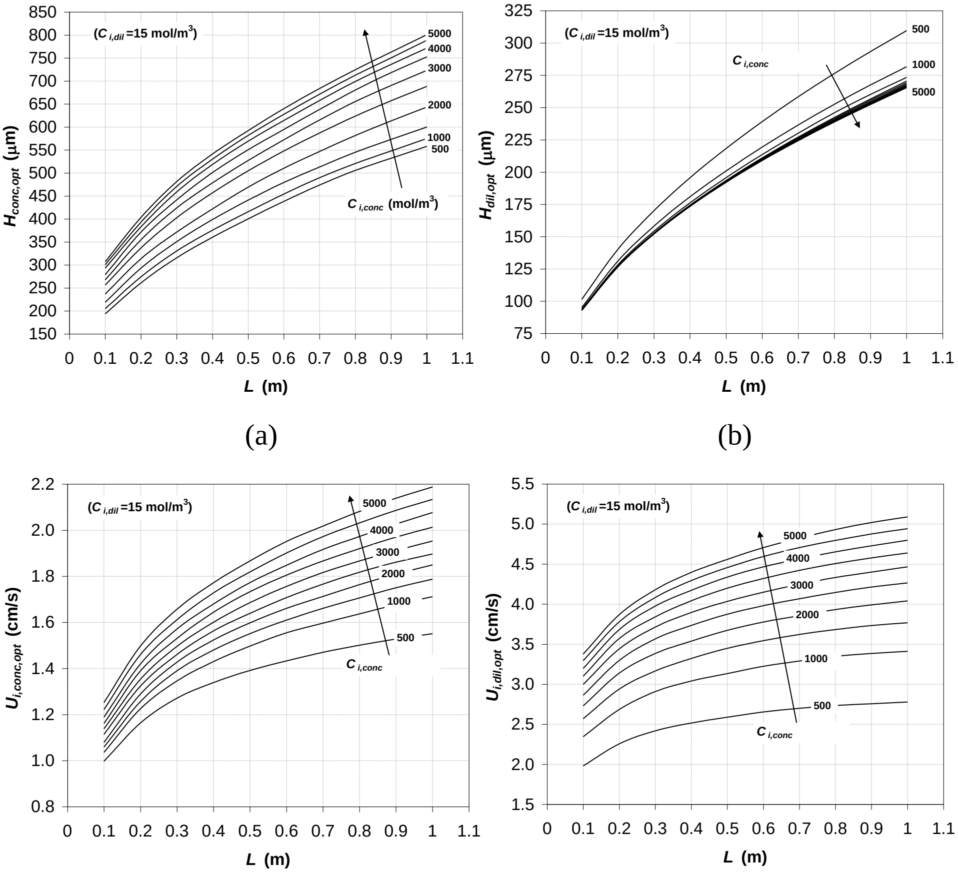

(a) (b)

(c) (d)

Figure 66. Results of the optimization study for channels filled by woven spacers (l/H=2, γ=45°) in parallel flow. Graphs (a), (b), (c) and (d) show the values of H^{CONC}, H^{DIL}, U_i^{CONC}, U_i^{DIL}, respectively, providing the highest net power density NPD. All quantities are reported as functions of the stack length L for different values of C_i^{CONC} and C_i^{DIL}=15 mol/m^3.

Note that, as already observed in discussing the results in Figure 62, H_{opt}^{CONC} increases with C_i^{CONC} while H_{opt}^{DIL} decreases. Graphs (c) and (d) show that also the optimal flow velocities both increase with L (despite the increase in frictional losses) because a high NPD is associated with a short residence time.

The results for the other configurations (void channels in parallel flow and spacer-filled channels in counter flow) are qualitatively similar.

Figure 67 compares the values of NPD corresponding to the optimum choice of the parameters H^{CONC}, H^{DIL}, U_i^{CONC}, U_i^{DIL} (NPD$_{opt}$, graph (a)) with those corresponding to fixed reference values of the same parameters (NPD$_{ref}$, graph (b)). As in Figure 66, quantities are reported as functions of the stack length L (from 0.1 to 1 m) for varying C_i^{CONC},conc and a given value (15 mol/m^3) of C_i^{DIL}.

The adverse influence of L on NPD can be observed. For example, for C_i^{CONC}=5000 mol/m^3 and the given C_i^{DIL}, a short stack with L=0.1 m yields NPD$_{opt}$≈10 W/m^2, while this quantity falls to ~6.5 W/m^2 when L=1 m. The comparison of graphs (a) and (b) shows that the benefits of optimization increase with increasing stack length; for L=1 m, the relative increase in NPD is larger than 50% for all values of C_i^{CONC}. These improvements would be even more marked at higher diluate concentrations.

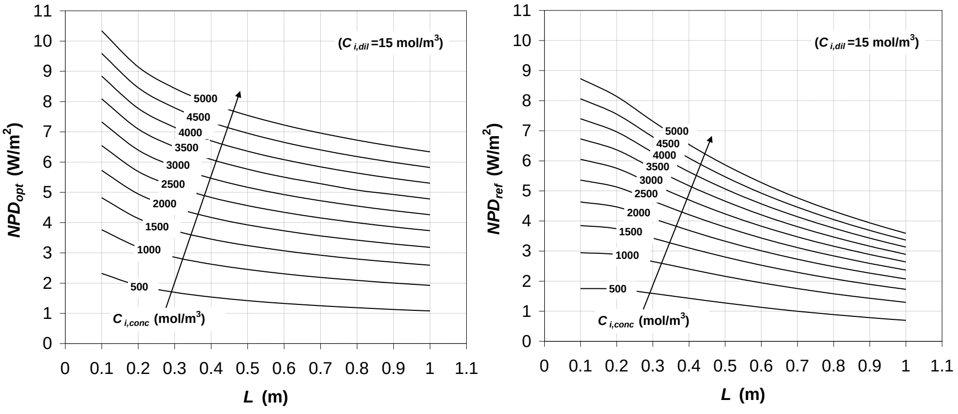

(a) (b)

Figure 67. Channels filled by woven spacers (l/H=2, γ=45°) in parallel flow: net power density NPD as a function of the stack length L for different values of C_i^{CONC} *and* C_i^{DIL}*=15 mol/m*^{3}*. (a): optimum values of* H^{CONC}, H^{DIL}, U_i^{CONC}, U_i^{DIL}*; (b): reference values of the same parameters (*H^{CONC}=H^{DIL}*=200 µm,* U_i^{CONC}=U_i^{DIL}*=2 cm/s).*

It should be observed that the parameters providing the maximum net power density do not also provide optimum values of the electrical energy extracted from a given total volume of solutions (concentrate+diluate), or net energy density (NED). Still for the case of channels filled by woven spacers and parallel flow, Figure 68 reports the quantity NED as obtained in correspondence either with the parameters H^{CONC}, H^{DIL}, U_i^{CONC}, U_i^{DIL} providing the highest NPD, graph (a) (NED$_{opt}$), or with fixed reference values of the same parameters, graph (b) (NED$_{ref}$). It can be observed that the optimization of NPD causes a reduction in NED ranging from a few percent for low values of C_i^{CONC} (e.g. 500 mol/m^3, i.e. seawater) to 40-50% for high values of C_i^{CONC} (e.g. 5000 mol/m^3, i.e. concentrated brine). This is mainly due to the lower residence times required for maximising NPD, compared to what would be needed in order to extract larger amount of energy from a specific volume of feed solutions. The couple seawater-river water (C_i^{CONC}=500 mol/m^3, C_i^{DIL}=15 mol/m^3) gave NED≈60 kJ/m^3 for all stack lengths investigated (0.1-1 m) when NPD attained its maximum of ~1.1-2.2 W/m^2 (depending on the stack length). This NED is much lower than the theoretical maximum free energy of the solutions (~880 kJ/m^3 assuming equal amounts of concentrate and diluate [28]), and also lower than that obtained in stacks which were specifically optimized for NED (~100-200 kJ/m^3 [28]).

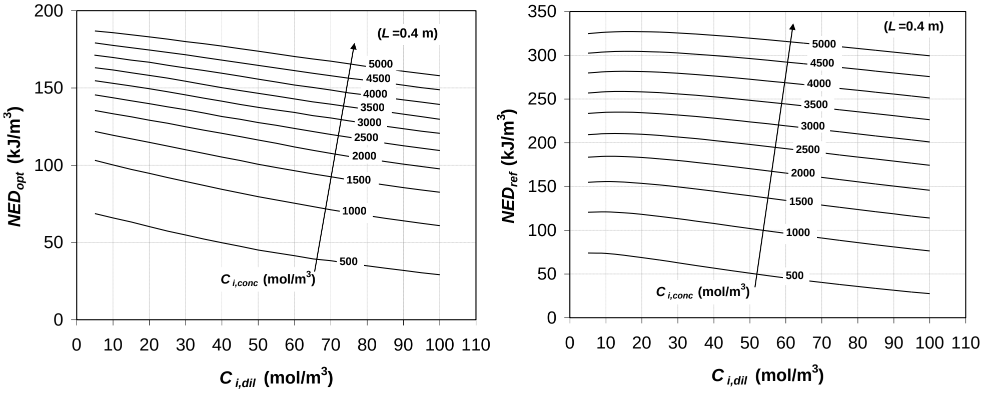

(a) (b)

Figure 68. Channels filled by woven spacers (l/H=2, γ=45°) in parallel flow: net power density NED as a function of C_i^{DIL} for different values of C_i^{CONC} and L=0.4 m. (a): values of H^{CONC}, H^{DIL}, U_i^{CONC}, U_i^{DIL} chosen to maximize NPD; (b): reference values of the same parameters (H^{CONC}=H^{DIL}=200 μm, U_i^{CONC}=U_i^{DIL}=2 cm/s).

3.3.5 Results: spacer-filled channels in counter flow

Figure 69 and Figure 70 report the same quantities as Figure 62-Figure 63 and Figure 64-Figure 65, but for woven spacer-filled channels in counter flow. By comparing Figure 69 with Figure 64, one may observe that optimum values of the parameters H^{CONC}, H^{DIL}, U_i^{CONC}, U_i^{DIL} are significantly different in counter flow than in parallel flow. In particular, switching from parallel to counter flow both H_{opt}^{CONC} and H_{opt}^{DIL} decrease by ~15-25% (according to the values of the "scenario" variables), and also optimum flow velocities decrease, although to a lesser extent (~5-15%). On the other hand, the comparison of Figure 70 with Figure 65 shows that the resulting values of NPD$_{opt}$ are very similar, with only a very small increase with respect to parallel flow. This is mainly due to the weak dependence of NPD on the optimization variables. Also for the present case of woven spacers in counter-flow, graphs of the net energy density NED corresponding to the choice of optimization variables that maximizes NPD (NED*opt*) and to fixed, reference values of the same variables (NED*ref*), show a behaviour similar to that discussed for woven spacers and parallel flow, i.e., a strong reduction of NED in correspondence with the optimization of NPD, and were not reported for brevity.

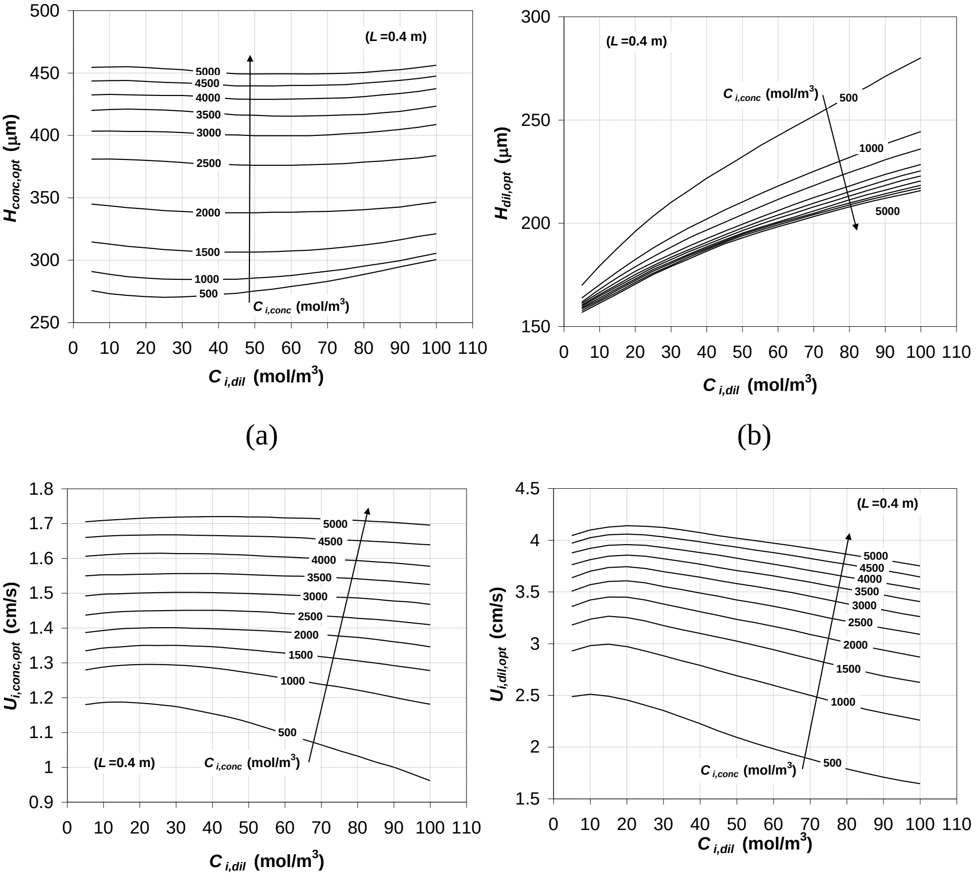

(a) (b)

(c) (d)

Figure 69. Results of the optimization study for channels filled by woven spacers (l/H=2, γ=45°) in counter flow. Graphs (a), (b), (c) and (d) show the values of H^{CONC}, H^{DIL}, U_i^{CONC}, U_i^{DIL}, respectively, providing the highest net power density NPD. All quantities are reported as functions of C_i^{DIL} for different values of C_i^{CONC} and L=0.4 m.

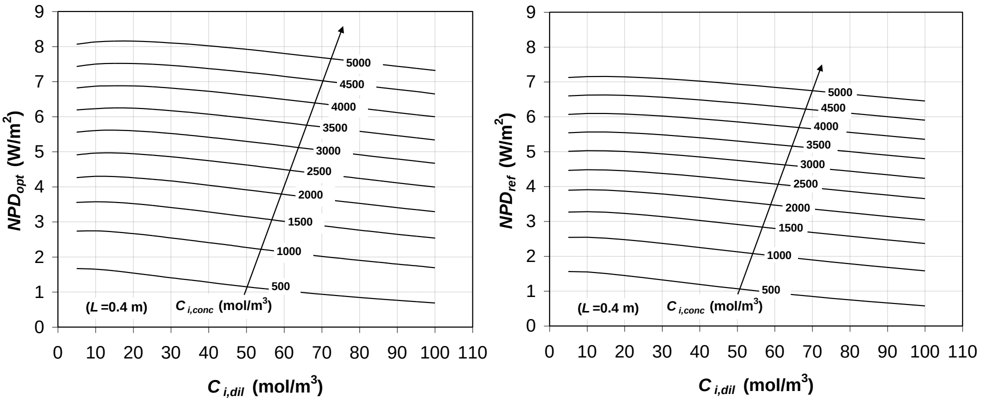

(a) (b)

Figure 70. Channels filled by woven spacers ($l/H=2$, $\gamma=45°$) in counter flow: net power density NED as a function of C_i^{DIL} for different values of C_i^{CONC} and $L=0.4$ m. (a): optimized values of H^{CONC}, H^{DIL}, U_i^{CONC}, U_i^{DIL}; (b): reference values of the same parameters ($H^{CONC}=H^{DIL}=200$ μm, $U_i^{CONC}=U_i^{DIL}=2$ cm/s).

4. ED

4.1 Model validation

The experimental set-up and method are described in Appendix C. For this preliminary validation, the membranes tested were Type 10 membranes (Fujifilm Manufacturing Europe BV, The Netherlands) and their properties are reported in Table 7. Between the membranes, woven spacers (Deukum GmbH, Germany), 155 μm thick and provided with gasket, are placed. Solutions were prepared using demineralised water and technical grade NaCl with concentrations from 0.5 to 60 g/l, encompassing the whole range of outlet concentrations expected in a real ED plant. Different inlet concentrations in the two compartments were used in order to simulate the end part of a long stack or the last stage of a multistage configuration (see Table 10). For each couple of inlet concentrations, solutions velocities in the range 0.25 – 2 cm/s were imposed and were kept equal in the concentrate and diluate compartments.

In the following, the current density *i* is computed as the experimental applied current *I*, divided by the active membrane area.

Figure 71 reports experimental results for concentrate and diluate outlet concentrations and stack voltage as functions of the current density, and a comparison with the one-dimensional stack model.

Table 10. Experimental operating conditions.

	Concentrate	**Diluate**
Inlet concentration	0.5 / 30 /60 g/l	0.5 g/l
	1 / 30 / 60 g/l	1 g/l
Velocity	0.25 / 0.5 / 1 / 1.5 / 2 cm/s	

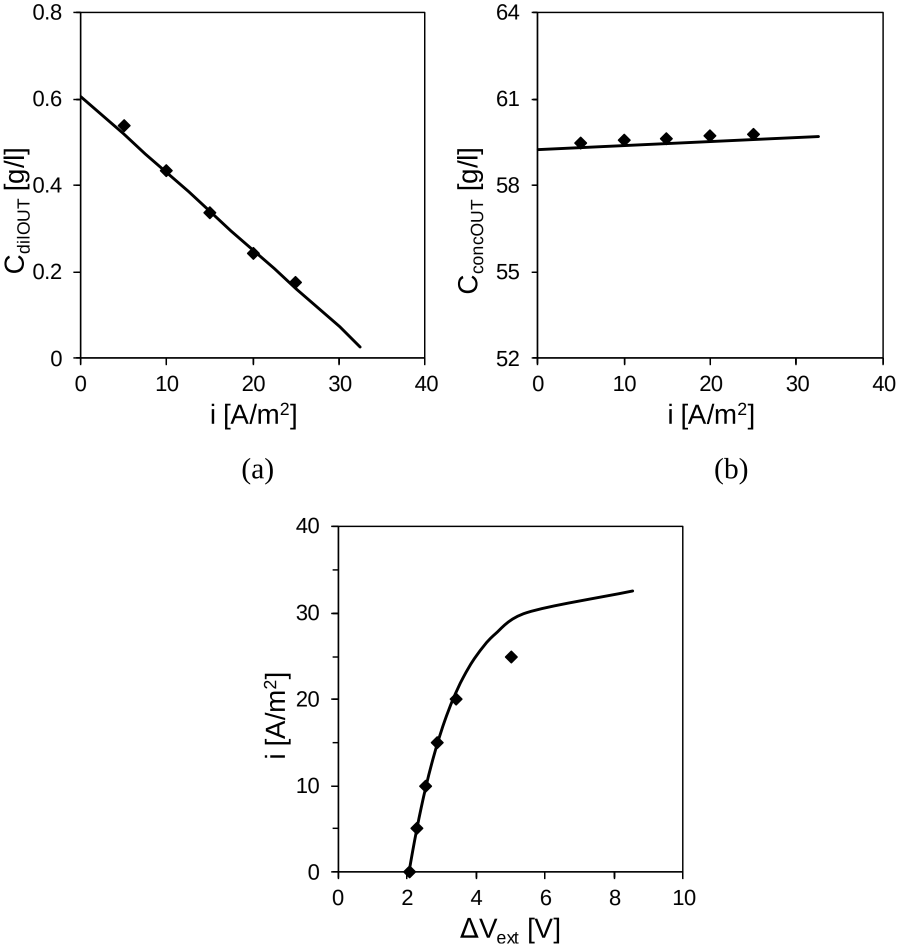

(a)

(b)

(c)

Figure 71. Diluate and concentrate outlet concentrations as functions of the current density. Current density – voltage curve. Experimental data (symbols) and simulation results (lines) are compared. Data were obtained using NaCl solutions with inlet concentrations of C^{CONC}=60 g/l in the concentrate and C^{DIL}=0.5 g/l in the diluate. The velocity was equal to 2 cm/s.

Overall, the model predictions are in good agreement with the experimental results; however, at high current density values, the current-voltage curve is not satisfactorily predicted. The region where the current density-voltage curve changes slope is called limiting region Several reasons can be invoked for this discrepancy between model predictions and experimental results. First, among the several non-ideal phenomena involved in ED, the model takes into account only salt diffusion and osmotic / electro-osmotic fluxes. Moreover, concentration polarization is computed from Sherwood numbers provided, in their turn, by CFD simulations in which the membrane surface is assumed homogenous and electroneutrality is imposed. These two assumptions lead to a *plateau* in the current-voltage curve, determining the diffusion-limited current density, and do not consider the possible establishment of electroconvective motions [49,182]. Gurreri *et al.*[69] reported a good match between the Sherwood numbers obtained from their CFD simulations, under the same assumptions, and the Sherwood numbers experimentally deduced by Li *et al.* [27,183] and Koutsou *et al.* [91]. However, these experimental results were obtained with the spacer directly in contact with the electrode and, as discussed in the following Section 4.3, this condition provides the theoretical diffusion-limited current density, which is higher than LCD in Electrodialysis.

The LCD appearance in ED needs to be deeply investigated by proper designed ED experiments from which an empirical correlation can be obtained and implemented in the model.

4.2 Critical current density

A lower threshold of the current density, which here is defined as “critical current density” (CCD), was observed in the experiments: below this limit, the outlet concentration is higher than that of the input, while, above this limit, desalination is obtained. This can be observed in Figure 72, reporting experimental diluate outlet concentrations as functions of the current density. The inlet concentrate / diluate concentrations are a) 30 g/l and 0.5 g/l; b) 60 g/l and 0.5 g/l. Five solution velocities, from 0.25 to 2 cm/s, are considered.

In Figure 72a, for current densities below ~3 A/m^2, the outlet diluate concentration is higher than 0.5 g/l. This is due to the osmotic and salt diffusion phenomena, which depend on the concentration difference between the two compartments.

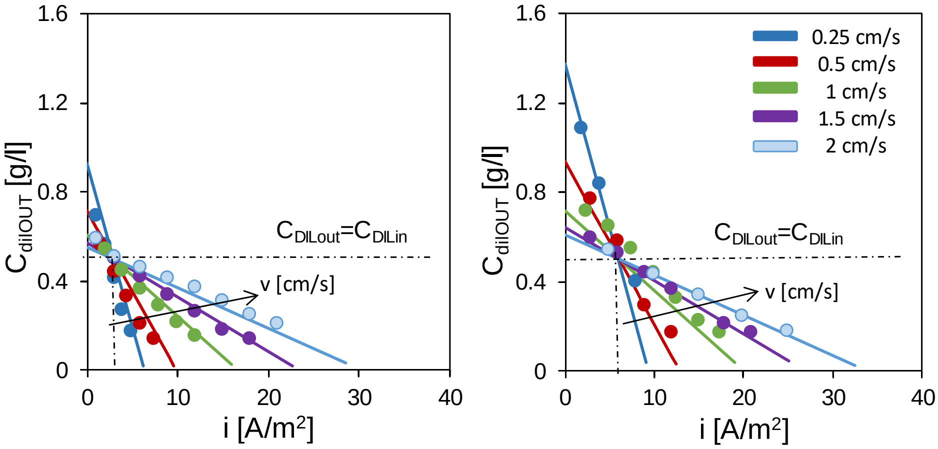

(a) (b)

Figure 72. Diluate outlet concentration vs current density. Experimental data (symbols) and simulation results (lines) are compared. Five solution velocities are examined. NaCl solutions are characterized by concentrate / diluate inlet concentrations of: a) C^{CONC} *= 30 g/l and* C^{DIL} *= 0.5 g/l; b)* C^{CONC} *= 60 g/l and* C^{DIL} *= 0.5 g/l.*

When the concentration in the concentrate doubles, also the CCD doubles. For example, when the concentrate concentration is 60 g/l (Figure 72b), the CCD increases and becomes ~6 A/m^2. The curves at different velocities intersect all in a single point, i.e. the CCD does not depend on fluid velocities. This independence arises from the fact that the above-mentioned non-ideal phenomena (osmosis, diffusion etc.), which lead to a CCD, are weakly dependent on the solutions velocity. An equivalent way of expressing this concept is that transport phenomena in the direction of the flow (advection) and in the direction orthogonal to it and through the membranes (electromigration, diffusion, osmotic fluxes) can be decoupled, as stated by Sonin and Probstein [33].

Under critical current density conditions, the total salt flux going out from the diluate channel is zero, i.e. the coulombic flux, N_S^{COUL}, is equal and opposite to the diffusive flux, N_S^{DIF}.

The diffusive flux through a membrane pair can be expressed as in Eq. (60). When a symmetric concentration profile can be assumed so that $C_{AEM}^{SOL} = C_{CEM}^{SOL}$ and the membrane properties and thickness are equal for anionic and cationic membranes, the diffusive flux can be re-written as:

$$N_S^{DIF} = 2N_{S,IEM}^{DIF} = 2\frac{D_{IEM}(C^{CONC} - C^{DIL})}{H_{IEM}} \tag{79}$$

Once the permselectivity and the salt permeability are known, by combining Eq (59) and Eq (79) the CCD can be determined as:

$$CCD = \frac{2FD_{IEM}(C^{CONC} - C^{DIL})}{H_{IEM}[Tr^{CEM} - (1 - Tr^{AEM})]} \tag{80}$$

For the membranes used in the experiments reported in this thesis, the manufacturer (Fujifilm B.V.) provided a salt diffusion permeability coefficient of $4 \cdot 10^{-12}$ m^2/s, while the permselectivity and the membrane thickness are reported in Table 7. Moreover, an experimental characterization of these membranes confirmed similar salt diffusion permeability values (see Appendix C). In the case of C^{CONC} = 30 g/l and C^{DIL} = 0.5 g/l, by applying the Eq (15), a CCD of 3.07 A/m^2 can be obtained, which is equal to that found graphically.

4.3 Limiting Current Density in ED

In regard to the concentration polarization phenomenon in ED, an example of concentration profiles in the concentrate and diluate compartments is reported in Figure 73a. These profiles arise because the kinetics of transport in solutions and in membranes are different, which leads to enrichment and depletion layers next to the membranes. This phenomenon can also be explained by considering the transport numbers, which are higher in membranes than in solutions: moving from the solution to the membrane, the migrative flux of counter-ions increases and a concentration gradient arises in the liquid phase [149].

Observing the diluate channel, the concentration at the membrane surface decreases and, according to the classical theory of concentration polarization in an electroneutral solution [138], when the electrolyte concentration at the interface approaches zero, the diffusion-limited current density is reached [184,185]. This condition corresponds to a *plateau* in the current-voltage curve (Figure 73b).

According to this theory, the first predictions of the limiting current density was proposed by Peers [136] in 1956. In the Peers equation (see Table 11) δ is the diffusion boundary layer thickness. This is often defined as the distance from the membrane to the cross point of the tangents drown to the concentration profile at the interface and in the bulk solution [46]. In the literature, the Lévêque equation [171,186] is more commonly adopted: it is derived from the Peers equation and the Graetz-Lévêque theory of developing laminar flow through spacerless channels, and it is valid for membranes characterized by a short length, i.e., $(LD)/(H^2u) < 10^{-2}$, and homogenous surface [187].

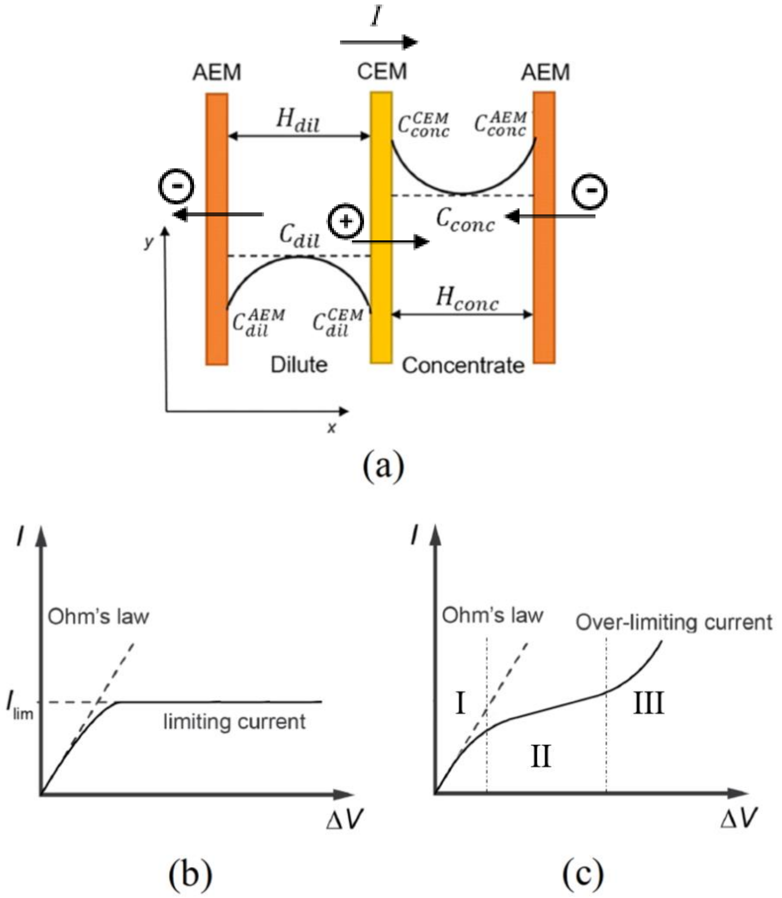

Figure 73. (a) Concentration profiles in an ED cell pair; (b) current-voltage curve according to the classical theory of concentration polarization [188]*; (c) typical current-voltage curve observed in working ED unit* [189].

Among the most recent models proposed in the literature to estimate LCD, Geraldes and Afonso [190] considered the electrodialysis of multi-ionic solutions: using a linearized form of the Nernst–Planck equation together with the electroneutrality condition at the solution/membrane interface, they deduced an explicit expression of LCD, which requires the effective diffusivity of the multi-ionic solution. Nakayama *et al*. [172] started from the Nernst-Planck equation, which they reduced to a convection-diffusion transport equation with an effective diffusion coefficient by eliminating the electrophoresis term. This equation was then applied in the boundary layer, by using the principle of similarity of the classical boundary layer theory [191], in order to obtain asymptotic results for concentrations, limiting current density and stack voltage, for long and short ED channels.

All the above models can predict the *plateau* in the current-voltage curve (Figure 73b), which can be observed only in simple electrochemical cells in which a single solution-filled channel is limited by two electrodes. In these cases, the diffusion-limited current density is univocally determined by the *plateau*. When ion-exchange membranes (IEMs) are present, as in the case of real ED stacks, there is no actual saturation of current: as illustrated in Figure 73c, the current does not exhibit a marked *plateau* but rather a region of slow increase which merges without a sharp transition with a third region, the overlimiting region [192]. The appearance of this last region was initially attributed to the loss of permselectivity and the transport of H^+ and OH^-, produced by a water splitting reaction. These phenomena, however, were later identified as often non-dominant contributions to the overlimiting current: in fact, even for currents much larger than the diffusion-limited value, charge is mainly transported by salt ions and the contribution of water splitting is minor [49]. The main reason of the overlimiting current was rather found in membrane surface non-uniformity and in electroconvection phenomena [46,182,193] (Part II, Section 4.5). The second region, still called *plateau* region, appears at much lower current values than the diffusion-limited [182]. For example, Krol *et al*. [194,195] measured the limiting current density and the transition time in a Plexiglas™ membrane cell with six separate compartments; the experimental results were lower than those calculated using theoretical expressions such as the Peers equation. The micro-scale mechanisms responsible for this behaviour are not yet fully understood; it is widely believed that some of the phenomena that cause overlimiting currents (e.g. membrane non-uniformity, electroconvection, etc.) may have a role also in determining a limiting condition. Rubinstein *et al*. [49] observed that when electroneutrality is imposed, as assumed in classical theory of concentration polarization [138], the current-voltage curve cannot exhibit the S-shape with an overlimiting region, typical of ED systems. More realistic current-voltage curves can be predicted if the electroneutrality condition is replaced by the full Poisson equation for the electrical potential [153]. Moreover, from the experiments carried out by Shaposhnik *et al*. [47], it can be observed that, when the limiting current is reached, the concentration at the membrane-solution interface is not zero but rather attains a finite minimum value.

As a consequence of this departure from the purely diffusion-controlled behaviour, the identification of a limiting current density in real ED stacks is not obvious. However, the concept of LCD is still useful for a number of reasons. First, since water splitting can lead to scaling or fouling, it is important to operate with a safe margin below the corresponding conditions. Second, since the attainment of LCD can be associated with a maximum in current efficiency (as will be discussed later), the knowledge of this quantity facilitates the efficient design of ED equipment [196]. Third, the voltage increase required to reach values of current above LCD can be dramatically high and is often not justified by a good increase in desalted water production. Therefore, a predictive method for LCD should be implemented into any simulation or design tool for ED systems [197].

As an alternative to physically-based models, purely empirical correlations for the LCD can be found in the literature, often in the form of power laws in which LCD is related to the fluid velocity and the bulk concentration in the diluate. Table 11 summarizes theoretical and empirical correlations presented in the literature.

Table 11. Summary of theoretical and empirical correlations presented in the literature.

Author (year)	**Equation**	**Ref.**
Peers (1956)	$i_{lim} = \frac{FDC}{\delta(Tr_{IEM} - Tr_{SOL})}$	[136]
Lévêque (1973)	$i_{lim} = 1.47\frac{FDC}{H(Tr_{IEM} - Tr_{SOL})}\left(\frac{H^2u}{LD}\right)^{1/3}$	[171,186]
Geraldes and Afonso (2010)	$i_{lim} = F\frac{k_{c,eff}}{D_{eff}}z_1D_1(C_{1,b} + C_{2,b} + C_{3,b})$	[190]
Nakayama *et al.* (2017)	$i_{lim} = 1.772F\bar{C}_d(0)\left(\frac{\bar{u}_d}{L}\varepsilon D_e\left(1 + \xi\frac{\bar{u}_dW}{D_e}\right)\right)^{\frac{1}{2}}$ $for \quad \frac{\bar{u}_dW^2}{\varepsilon D_e\left(1 + \xi\frac{\bar{u}_dW}{D_e}\right)L} \gg 1$	[172]
Lee *et al.* (2002, 2006)	$i_{lim} = aCu^b$	[134,198]
Tanaka (2004, 2005)	$i_{lim} = (m_1 + m_2u_{out})C_{out}^{\prime n_1 + n_2u_{out}}$	[199,200]

Lee *et al.* [134] obtained an equation for the limiting current in which the coefficients are quite constant in a relative wide concentration range of the feed solution except for very low concentrations, but they are affected by the hydrodynamic conditions, including the flow velocity [198]. Instead of using the inlet or average velocity, Tanaka [200] found a correlation in which the coefficient and the exponent are functions of the outlet velocity of the dilute solution. However, correlations are usually calibrated against experiments carried out in specific electrochemical cells, often using only one ion-exchange membrane and one solution [182,192,194,195,199,201–203]. In other cases, the LCD is measured in simplified or real ED systems [134,190,196,198,200,204].

Since the “practical limiting current density” in ED is not identifiable by a marked *plateau*, several alternative methods, many of which of graphical nature, have been proposed in the literature so far. Isaacson and Sonin [196] proposed to consider as a measure of the limiting current, the intersection between a straight line extrapolated from the linear (Ohmic) region and the tangent drawn past the turning point in the region in which the current tends to level off. In 1959, Cowan and Brown [205] were the first who plotted the apparent resistance $\Delta V/i$ against the reciprocal current density $1/i$ to identify the limiting current density. They designated as LCD the point at which the trend line with a negative slope cuts that with a positive slope. Although several methods have been proposed and many efforts have been made so far, the determination of the LCD is still ambiguous.

Figure 74a and Figure 74c show the determination of LCD in an ED unit fed with 0.5 g/l for both solutions, while Figure 74b and Figure 74d refer to the case of feeds at 60 g/l and 0.5 g/l for the concentrate and diluate, respectively. First, the method proposed by Isaacson and Sonin [196] was applied. As it can be seen from Figure 74a and Figure 74b, the slope of the right side tangent is not uniquely determined and depends on the density of the available experimental data. LCD values of ~12.3 and 17.8 A/m^2 were obtained for the two test cases (a) and (b), respectively.

Also the method proposed by Cowan and Brown [205], which identifies the LCD in the plot of the apparent resistance $\Delta V/i$ against the reciprocal current $1/i$ (Figure 74c and Figure 74d) was used. In some plots (Figure 74c), the trend line for higher $1/i$ values (low current values) was almost horizontal. The values of LCD thus obtained by the intersection of the two tangents, were ~12.8 and 16.7 A/m^2, respectively, for test cases (c) and (d); these values are, especially in case (d), different from those obtained by the Isaacson-Sonin method.

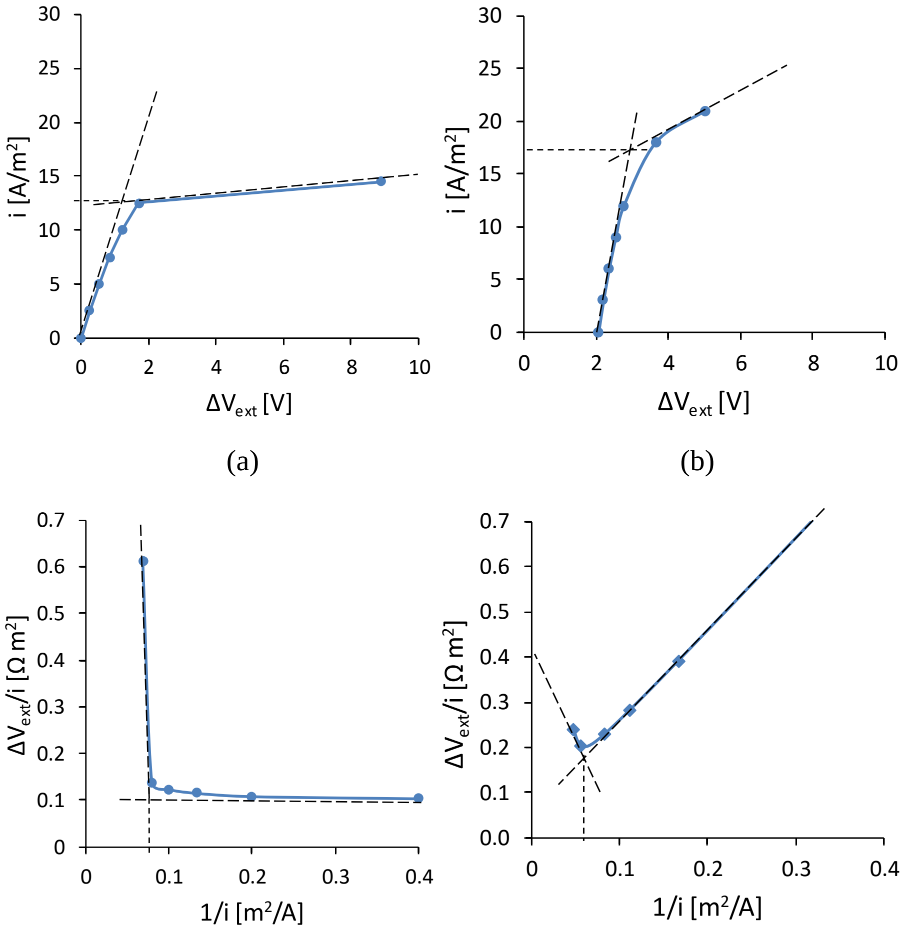

(a) (b)

(c) (d)

Figure 74. Graphs (a, b) Isaacson and Sonin method: current density vs applied voltage. Graphs (c, d) Cowan-Brown method: $\Delta V/i$ vs $1/i$. Symbols represent experimental data. These curves were obtained with NaCl solutions of: a) and c) equal concentration in both compartments, $C^{DIL} = C^{CONC} = 0.5$ g/l; b) and d) concentrate concentration $C^{CONC} = 60$ g/l and diluate concentration $C^{DIL} = 0.5$ g/l. Velocities were 1.5 cm/s in both compartments.

Mandersloot and Hicks [32], using the Cowan-Brown method, also observed quasi-horizontal regions in the $\Delta V/i$ vs. $1/i$ curve. In their experiments, they kept the concentration in the concentrate fixed while letting the diluate concentration vary, and concluded that this horizontal section appears because the membrane potential becomes negligible at high diluate concentrations. Experiments here reported suggest that the $\Delta V/i$ vs. $1/i$ curve flattens for $1/i \rightarrow \infty$ ($i \rightarrow 0$), as in Figure 74c, not when the diluate concentration is high, but rather when the difference (C^{CONC}–C^{DIL}) tends to zero, so that also the back electromotive force $\Delta V(i=0)$ (residual potential at zero current) tends to zero.

This is illustrated by the current density-voltage curve of Figure 74a, which corresponds to Figure 74c. On the contrary, when $(C^{CONC}–C^{DIL}) \neq 0$, one also has $\Delta V(i=0) \neq 0$, as shown in the current density-voltage curve of Figure 74b. In this case, in the linear region (low electrical current) the applied voltage can be approximated (neglecting the influence of concentration polarization) as $\Delta V= \Delta V(i=0)$+constant×i, and the ratio $\Delta V/i$ decreases as the current density i increases.

The methods illustrated in Figure 74 are the most used in the literature; however, as discussed above, they may lead to an ambiguous determination of the limiting current in some cases, because the choice of the “appropriate” tangent lines is difficult. Meng *et al*. [206] pointed out the uncertainties of these methods and proposed a new method, but only to determine the optimal operating current, which should be lower than the limiting current. They used the desalting efficiency η defined as the ratio $\left(C_{in}^{DIL} - C_{out}^{DIL}\right)/C_{in}^{DIL}$. As the current increases, this parameter shows a maximum, which can be identified with the optimal operating current [206].

Proposed method based on the current efficiency

As an alternative to the desalting efficiency η, the current efficiency (or current utilization) λ [207] can be used to identify an optimal operating current and it can be defined as:

$$\lambda = \frac{zF\left(Q_{in}^{DIL} C_{in}^{DIL} - Q_{out}^{DIL} C_{out}^{DIL}\right)}{I} \tag{81}$$

From the experimental values of current, flow rates and concentrations, the calculated λ was plotted against the current density as illustrated in Figure 75. For all experimental tests, a maximum of λ always occurs in such plots. Up to a certain value of the current density i, the current efficiency increases so that the $C_{out}^{DIL}(i)$ curve exhibits a negative curvature (downward concavity). The increase of λ with the current density is because the coulombic flux becomes more and more dominant with respect to diffusive and osmotic fluxes. Once the maximum is reached, other detrimental phenomena (loss of permselectivity? depletion layer and space charge region appearance? water dissociation?) should appear, making λ decreases with i. When the current efficiency attains a maximum, the $C_{out}^{DIL}(i)$ curve exhibits an inflection point (i.e., its curvature changes sign).

Kwak *et al*. [208] also observed this trend of the current efficiency and stated that the maximum *λ* corresponds to the initial stage of the overlimiting region. More appropriately, based on the results here reported, the current density corresponding to the maximum *λ* can be identified with the LCD, obtaining values of 11.6 and 19.2 A/m^2 for the cases (a) and (b), respectively. Indeed, these values are close to the above reported LCD values predicted by the Isaacson-Sonin or the Cowan-Brown (Figure 74) methods, but as an advantage, the method based on the *λ* maximum is less ambiguous and has a more practical usefulness.

The *λ* - *i* plot, proposed to determine LCD, can also provide the CCD value: it corresponds to the zero current efficiency in the *λ* - *i* plot. For example, for inlet concentrations of 30 and 0.5 g/l, in the corresponding *λ* - *i* plot of Figure 75b, *λ* is zero for a current density of ~3 A/m^2 that is the same value previously found for the CCD.

While the CCD concept has little relevance in ED fed by two solutions of equal concentrations, in the case of two feed streams at different concentrations (e.g. in a multistage or feed and bleed ED system), a proper design must ensure that the critical current density value is well exceeded by the actual current density and that a large span exists between CCD and LCD, so as to leave comfortable margins for a flexible operation of the unit.

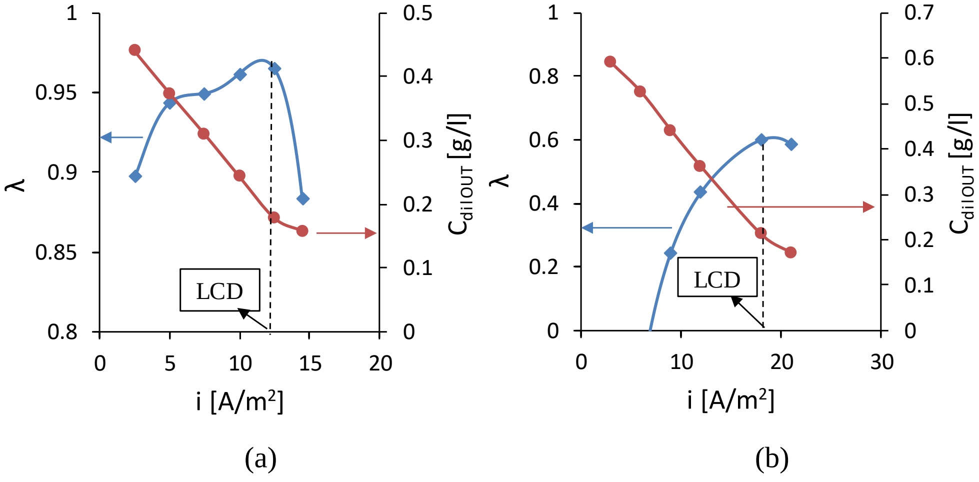

Figure 75. Current efficiency (diamonds) and outlet diluate concentration (circles) as function of current density. Symbols are experimental data (trend lines were drawn to guide the eye). Data were obtained with NaCl solutions of: a) equal concentration in both compartments, $C^{DIL} = C^{CONC} = 0.5$ g/l; b) concentrate concentration $C^{CONC} = 60$ g/l and diluate concentration $C^{DIL} = 0.5$ g/l. Velocities were 1.5 cm/s in both compartments.

4.4 ED stack performance and LCD

It was observed in Figure 71, the one-dimensional model is in good agreement with the experiments until the LCD is reached. As reported in Section 4.1, an empirical correlation for the LCD, obtained from experiments with ED unit, is needed.

The theoretical and empirical correlations presented in the literature (Table 11) show a dependence of the LCD on the diluate concentration. This fact reflects the operating conditions used in the experiments, in which often there is only one solution in an electrochemical test section [182,192,194,195,199,201–203] or, even if an ED stack is used, the same solution is fed into both the concentrate and the diluate compartments [134,190,196,198,200,204]. When the experiments are performed with the same inlet concentrations, one may conclude that LCD is only a function of the diluate concentration. However, in ED systems, different concentrations in the compartments can be found, especially near the outlet of the stack.

Figure 76 summarizes the experimental results, obtained for the operating condition reported in Table 10, by reporting LCD, as determined by using the maximum current efficiency method illustrated above, as a function of the solution velocity for different values of the concentration in the concentrate compartment.

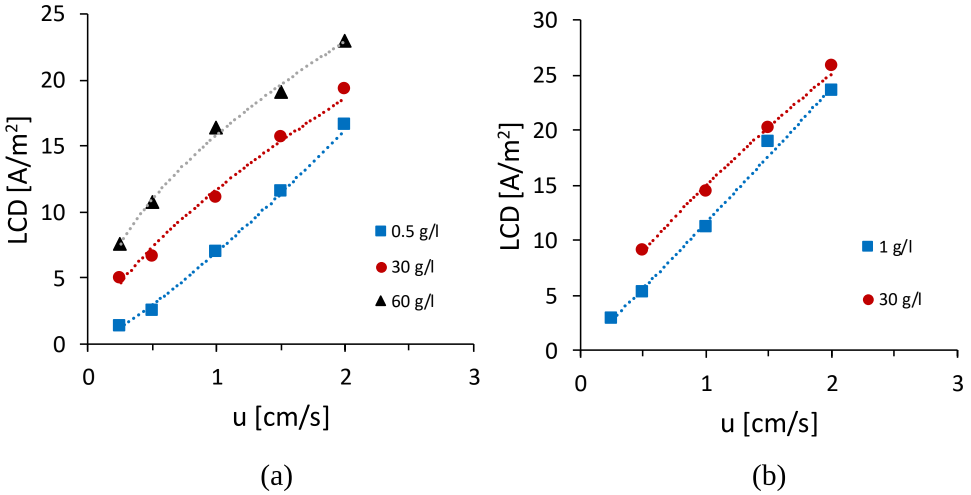

(a) (b)

Figure 76. Experimental results obtained with 155 μm spacers: LCD as a function of the solution velocity for different values of the concentration in the concentrate compartment. a) concentration in the diluate C_{dil} = 0.5 g/l; b) concentration in the diluate C_{dil} = 1 g/l. Trend lines (power laws) are added to guide the eye.

Figure 76a is for a diluate concentration of 0.5 g/l, while Figure 76b for a diluate concentration of 1 g/l. Data can be interpolated by power laws, as commonly found in the literature (see Table 11).

First, each graph confirms that, as commonly reported in the literature, LCD increases strongly with the solution velocity. Second, the comparison of the results in Figure 76a and Figure 76b, obtained with the same concentrate (30 g/l) and two different diluate concentrations (0.5 and 1 g/l, respectively), confirms that LCD increases with the diluate concentration. Furthermore, the comparison of the different curves in each graph, obtained for the same diluate concentration but different concentrations in the concentrate, shows that LCD increases significantly also with C^{CONC}. This effect, usually not considered in the literature, is probably caused by the fact that salinity in the concentrate compartment affects the diluate concentration due to non-ideal phenomena such as diffusion and osmosis. It should be noticed that the trend of LCD vs u is similar to the trend of Sh vs Re reported in Figure 35b, for woven spacer and γ=45°, when the inlet concentrations are equal. In this case, indeed, the main contribution to the LCD appearance is the concentration polarization phenomena. However, when inlet concentration difference increases, the LCD shows a weaker dependency on u, due to the higher influence of other phenomena, such as osmotic and diffusive flux, on the LCD.

From the previous results, the following correlation for the LCD was obtained:

$$LCD = a\frac{FC^{DIL}D^{DIL}}{H}\left(\frac{H^2u}{LD^{DIL}}\right)^b \tag{82}$$

where a and b are:

$$a = 0.455892 \cdot \left[0.019161\left(\frac{C^{CONC}}{C^{DIL}}\right) + 1\right] \tag{83}$$

$$b = 1.140255\left(\frac{C^{CONC}}{C^{DIL}}\right)^{-0.13983} \tag{84}$$

in which C^{CONC} and C^{DIL} are the inlet concentrations, H and u are the channel thickness and the void velocity respectively, both equal for the diluate and concentrate compartments.

The correlation type of Eq. (82) and the dimensionless group (H^2u/LD^{DIL}) are the same of the Lévêque equation [171,186]. In Figure 77, the LCD values predicted by Eq. (82) are reported and compared with the experimental results. The experimental results are well fitted by the correlation with a maximum error of ~17%.

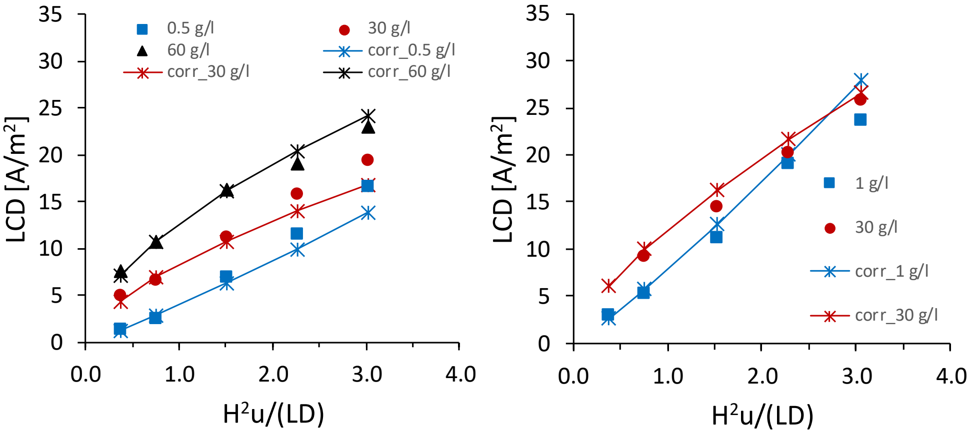

(a) (b)

Figure 77. Experimental results obtained with 155 μm spacers: LCD as a function of the parameter (H^2u/LD) for different values of the concentration in the concentrate compartment. a) concentration in the diluate C^{DIL} = 0.5 g/l; b) concentration in the diluate C^{DIL} = 1 g/l. Lines and asterisk are the LCD values obtained by the Eq. (82).

The empirical correlation was implemented in the model so that locally the current is limited to a maximum value corresponding to the limiting current predicted by the correlation. In Figure 78, the one-dimensional model with the implemented correlation is compared with the experimental results obtained with 60 g/l and 0.5 g/l as inlet concentrations in the concentrate and in the diluate respectively, and inlet velocity equal to 2 cm/s. Compared to the basic one-dimensional model that overestimated the LCD (Figure 71), now the model with the empirical correlation is able to satisfactorily predict the experimental current density – voltage curve. However, once the limiting current predicted by the correlation is reached along the entire length of the channel, a *plateau* region is predicted by the model and, as explained in Part III, Section 4.3, this is not what actually occurs in a real ED stack in which the current density always increases with the voltage and an overlimiting region is expected. Moreover, the updated model is still not able to predict the slope variation in the outlet diluate concentration curve. Despite these small drawbacks, the model with the correlation implemented is still able to provide better predictions than the basic model.

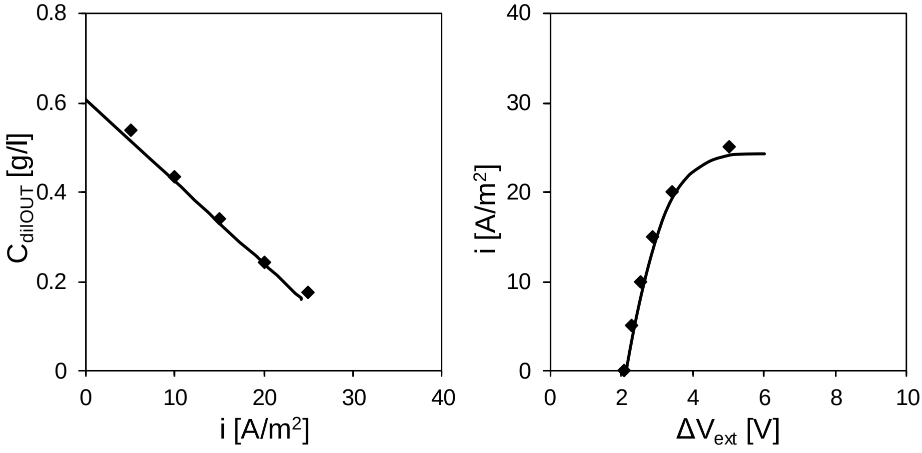

(a) (b)

Figure 78. a) Outlet Diluate concentration vs current density. b) Current density – voltage curve. Experimental data (symbols) and simulation results (lines) are compared. Simulation results were obtained using the one-dimensional model in which the empirical correlation (Eq. (82)) for LCD was implemented. Data were obtained using NaCl solutions with inlet concentrations of C^{CONC} = 60 g/l in the concentrate and C^{DIL} = 0.5 g/l in the diluate. The velocity was equal to 2 cm/s.

4.4.1 Effect of spacer thickness

Experiments were carried out also with thicker spacers, of about 280 μm (Deukum GmbH, Germany), keeping Type 10 membranes (Fujifilm B.V.) and in the same operating conditions reported in Table 10. However, only three inlet velocities were considered (0.25, 0.5 and 1 cm/s) due to a limitation in the available pumps.

In Figure 79, the experimental values of the outlet diluate concentration are reported as function of the current density. The model results are also reported as lines and they are in good agreement with the experiments until the slope change that it is not predicted by the model.

The CCD is identified in Figure 79 by the intersection of the curves and is equal to ~4.5 A/m^2. In the same conditions but with spacer thickness of 155 μm, the CCD was found equal to ~6 A/m^2 (Figure 72). The difference in the CCD values obtained with the two spacers is probably not due to the difference in channel thickness, but to a difference in salt diffusion permeability between the membranes used in the two tests. In fact, even if the type of membranes used in both experimental campaigns is the same, experimental measurements led to a value of ~$3\cdot10^{-12}$ m^2/s for the membrane used with the 280 μm spacer, while a value of ~$4\cdot10^{-12}$ m^2/s was found for the membrane used in the 155 μm spacer tests. This difference is probably due to the use of IEMs belonging to different batches.

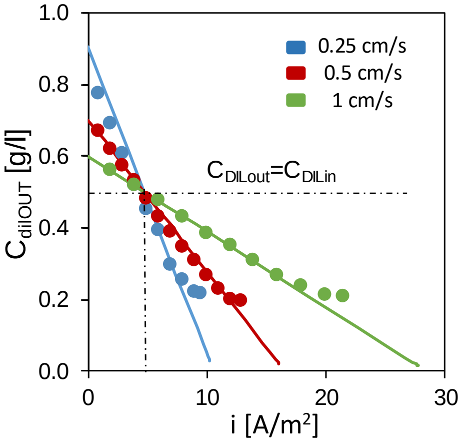

Figure 79. Diluate outlet concentration vs current density. Experimental data (symbols) with 280 μm spacers and simulation results (lines) obtained with the basic model are compared. Three solution velocities are examined. NaCl solutions are characterized by concentrate / diluate inlet concentrations of C^{CONC} = 60 g/l *and* C^{DIL} = 0.5 g/l.

Results obtained with the two spacer thickness are compared in Figure 80. The current density-voltage curves, reported in Figure 80a, show that, in the linear part of the curve, for a given current density, the voltage drop is slightly larger in the case of the 280 μm spacer. This is due to the fact that, when the channel thickness increases, the channel Ohmic resistance increases but not exactly proportionally to the thickness variation because, at a certain current density, the outlet concentration is not the same in the two cases. In Figure 80b, it is possible to observe indeed that the desalting effect is larger with 155 μm spacers, having a lower outlet diluate concentration for a given current density. This effect is due to the fact that the flow rate is lower when 155 μm spacers are adopted, thus the same coulombic flux, which is proportional to the current, leads to a lower outlet concentration. The dotted black line in Figure 80b corresponds to an outlet concentration equal to the inlet one. The corresponding current density, i.e. the CCD values, are slightly different in the two cases, as already observed in Figure 79. Observing the current efficiency curve, it can be seen that with 280 μm spacers the current efficiency is more or less always higher with respect to the 155 μm spacers. Moreover, the maximum current efficiency, which corresponds to the LCD, is observed at higher current density values when 280 μm spacers are adopted. This can be also easily noticed looking at

Figure 80a where the slope change in the current density-voltage curve is attained at higher current density values.

This result cannot be reconciled with the classic concentration polarization theory for the limiting current density, which predicts a value of i_{lim} inversely proportional to the diffusion boundary layer thickness δ [136], which can be expressed also as the ratio Sh/H [134,198].

However, the results obtained are consistent with other findings reported in the literature: for example, Zhong *et al*. [209] in 1983 studied the dependence of LCD on the channel thickness H, observing an increase with H with a maximum attained for H~1 mm and a decrease afterwards. Moreover, Tado *et al*. [210], on the basis of the Nernst-Planck equations, predicted an increase of the LCD as the channel thickness increased from 0.5 mm to 1.2 mm.

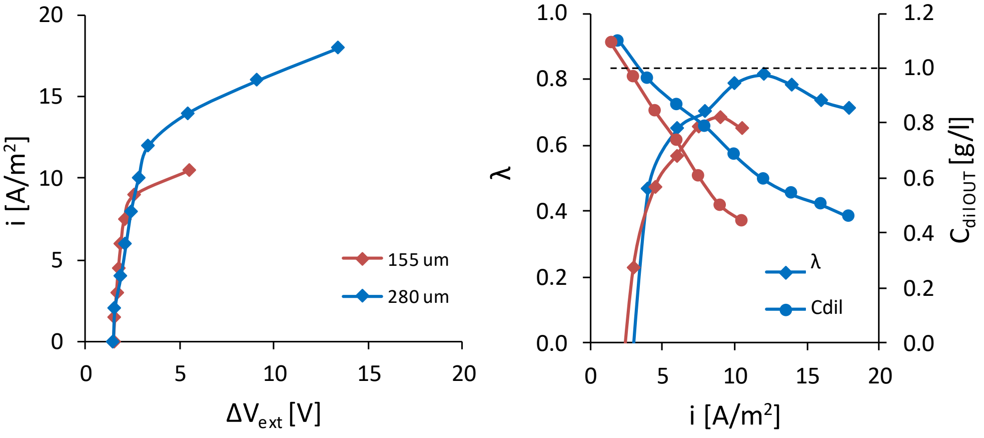

(a) (b)

Figure 80. a) Current density – voltage curve. b) Diluate outlet concentration (circles) and current efficiency (diamonds) vs current density. Experimental data obtained with spacers of 155 μm (red curves) and with spacers of 280 μm (blue curves) are compared. NaCl solutions are characterized by concentrate / diluate inlet concentrations of C^{CONC}=30 g/l and C^{DIL} =1 g/l. Inlet velocity is 0.5 cm/s for both solutions.

In Figure 81 the experimental LCD values, determined as the current density values corresponding to the maximum of the current efficiency, and obtained with 280 μm spacers, are reported. These results are well predicted by the empirical correlation reported in Eq. (82) which therefore remains valid when the channel thickness varies.

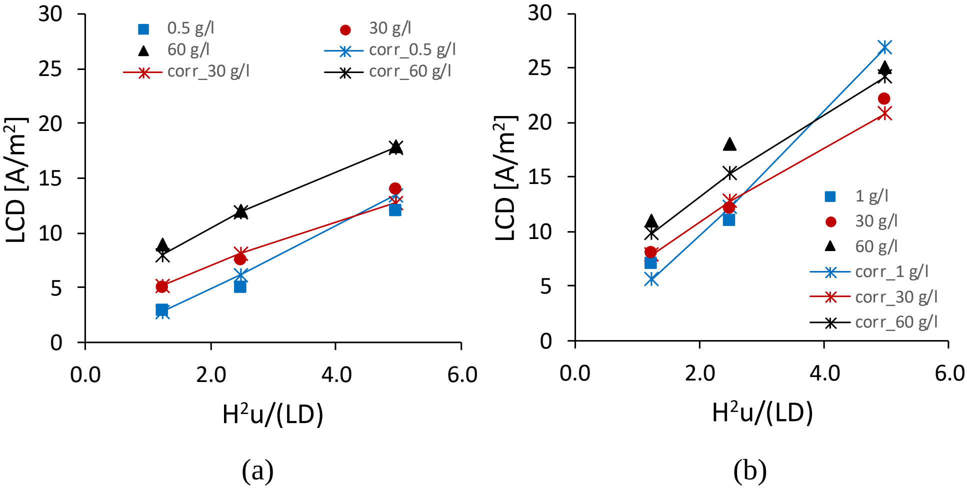

(a) (b)

Figure 81. Experimental results obtained with 280 μm spacers: LCD as a function of the parameter (H^2u/LD) for different values of the concentration in the concentrate compartment. a) concentration in the diluate C^{DIL} = 0.5 g/l; b) concentration in the diluate C^{DIL} = 1 g/l. Lines and asterisk are the LCD values obtained by the Eq. (82).

4.4.2 Effect of membrane properties

In order to study the effect of membrane properties on LCD and stack performance, experiments were carried out in the same operating conditions reported in Table 10, with spacers thick 155 µm and with Type 12 membranes (Fujifilm B.V.). Properties of these membranes are reported in Table 12.

Table 12. Properties of the FUJIFILM Type 12 ion-exchange membranes (data provided by manufacturer).

	AEM	**CEM**
Permselectivity[a] [%]	96.65	98.2
Osmotic permeability $L_{p,IEM}$ [ml/m²h·bar]	2.3	3.53
Resistance[b] [Ω cm²] (coefficient *a*) (Eq. (41))	6.31	4.1
Thickness (dry) [µm]	100	104

[a] Based on electric potential measured over the membrane between 0.05 M and 0.5 M KCl solutions at 25°C.

[b] Measured in 2 M NaCl solution at 25°C.

These membranes differ from the Type 10 especially for the osmotic permeability and for the electrical resistance. In particular, Type 12 membranes show an osmotic permeability $L_{p,IEM}$ which is ~55 – 70% lower than the value reported for Type 10 membranes (Table 7). In regard to the electrical resistance of Type 12 membranes, this is equal to two or even three times the value of Type 10 membranes.

It should be highlighted that no data about the salt diffusion permeability coefficient of Type 12 membranes were provided by the manufacturer. However, from the experimental determination of the CCD, it is possible to estimate this property as explained in Part III, Section 4.2. In Figure 82, experimental results and model prediction of the outlet diluate concentration are plotted as functions of the current density, in the case of 60 g/l and 0.5 g/l as inlet concentrations in the compartments concentrate and diluate compartments, respectively.

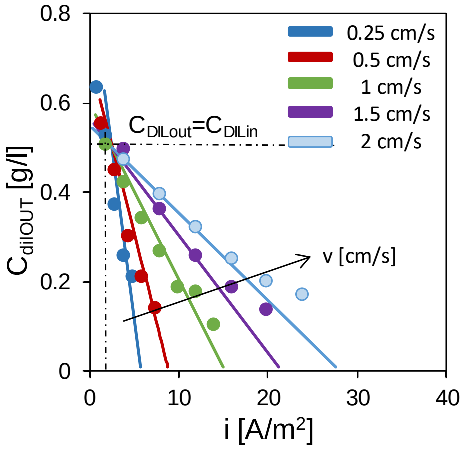

Figure 82. Diluate outlet concentration vs current density. Experimental data (symbols) with Type 12 membranes and simulation results (lines) obtained with the basic model are compared. Three solution velocities are examined. NaCl solutions are characterized by concentrate / diluate inlet concentrations of C^{CONC}*=60 g/l and* C^{DIL}*=0.5 g/l.*

As already observed in Figure 72 and in Figure 79, also in this case the model is not able to predict the slope variation in the outlet concentration curve. All the curves intersect at a point that identifies the CCD which is equal to ~2.5 A/m^2. This value is much lower than what obtained with Type 10 membranes in the same conditions (Figure 72) and corresponds to a salt diffusion permeability coefficient of ~1.6 m^2/s.

In Figure 83, experimental results obtained with Type 12 (blue curves) and Type 10 membranes (red curves), with 60 g/l and 0.5 g/l as inlet concentrations and 2 cm/s as inlet velocity, are compared.

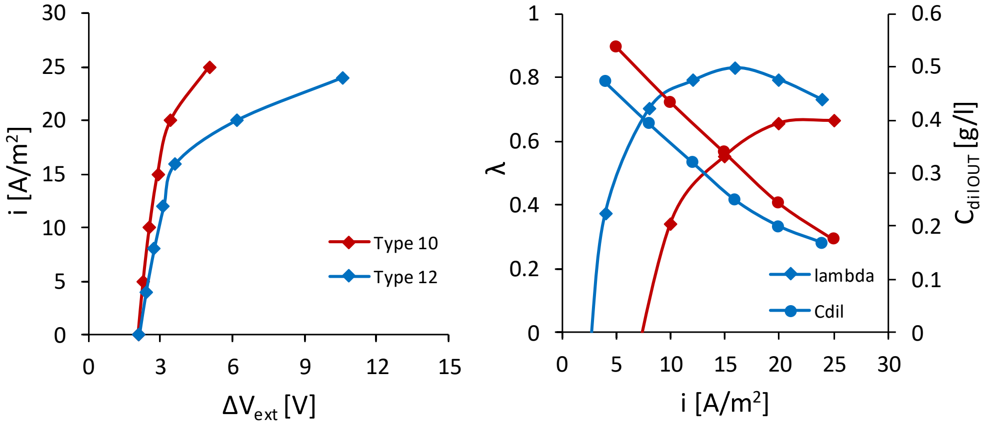

(a) (b)

Figure 83. a) Current density – voltage curve. b) Diluate outlet concentration (circles) and current efficiency (diamonds) vs current density. Experimental data obtained with Type 10 membranes (red curves) and with Type 12 membranes (blue curves) are compared. NaCl solutions are characterized by concentrate / diluate inlet concentrations of C^{CONC}=60 g/l and C^{DIL} =0.5 g/l. Inlet velocity is 2 cm/s for both solutions.

Observing Figure 83a, in the linear part of the current density-voltage curve, for a given current density, the voltage is higher when Type 12 membranes are adopted. This result was of course expected because of the higher electrical resistance of Type 12 membranes with respect to the Type 10. After the linear part, the slope variation is attained at lower current density in the case of Type 12 membranes. This result can be observed also in Figure 83b where the current efficiency is plotted against the current density. Type 12 membranes provide current efficiency values higher than Type 10 but the maximum is attained at lower current density, which corresponds to lower LCD value. It is also possible to see that the point at current efficiency zero correspond to two different CCD values, confirming that the salt diffusion permeability coefficient of Type 12 membranes is lower than Type 10.

In all the experiments performed, the LCD values obtained with Type 12 were always lower than LCD values obtained with Type 10. As a consequence, Eq. (82) with parameters *a* and *b* expressed as in Eqs. (83)-(84), cannot fit the experimental results. Keeping the same type of correlation as in Eq. (82), the following different expressions for *a* and *b* were found in order to fit the results with Type 12 membranes:

$$a = 0.479687 \cdot \left[0.006415\left(\frac{C^{CONC}}{C^{DIL}}\right) + 1\right] \tag{85}$$

$$b = 0.840545\left(\frac{C^{CONC}}{C^{DIL}}\right)^{-0.001774} \tag{86}$$

In Figure 84, the LCD values predicted by Eqs. (82)-(83)-(84) are reported and compared with the experimental results. The experimental results are well fitted by the correlation with a maximum error of ~20%.

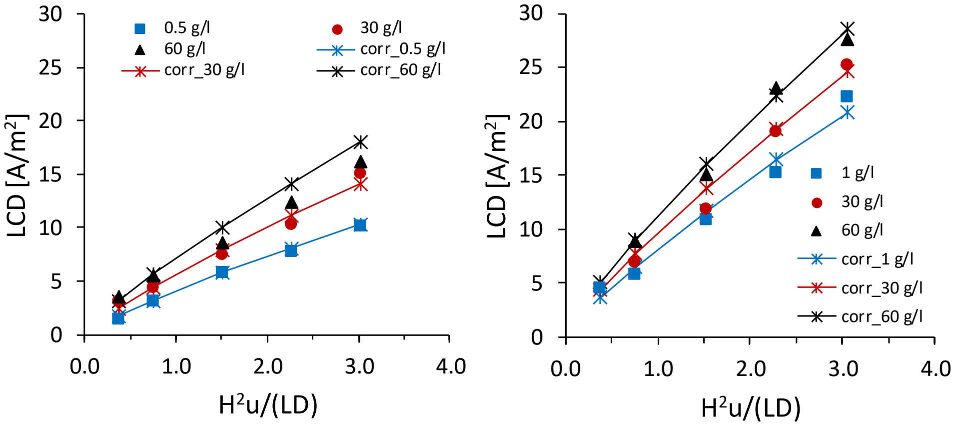

(a) (b)

Figure 84. Experimental results obtained with Type 12 membranes: LCD as a function of the parameter (H^2u/LD) for different values of the concentration in the concentrate compartment. a) concentration in the diluate C^{DIL}=0.5 g/l; b) concentration in the diluate C^{DIL}=1 g/l. Lines and asterisk are the LCD values obtained by the Eq. (82), in which the parameters a and b are defined as in Eqs. (85)-(86).

The final goal would be to obtain one correlation in which the parameters *a* and *b* depend on the membrane properties, so that the correlation is generally valid. To do this however, it is necessary to do other experimental campaigns with membranes having different properties, in order to clearly understand how each individual membrane property affects the LCD.

4.4.3 Effect of profiled membranes

Pillars profiled membranes

When profiled membranes are adopted, the stack in no more symmetric. In the case of profiled membranes with pillars (see Figure 85), each channel contains the profiles of only one membrane type, either cationic or anionic. The channel thickness is created by the height of the pillars which touch the flat side of the other membrane.

Pillars membranes with profiles of 150 μm, with p/H=6.66, were experimentally tested in a cross-flow stack (REDstack B.V.) with 10 cell pairs. The open area, i.e. the membrane area not occupied by profiles, is equal to 50%. These membranes have same properties of Type 10 membranes (Table 7) and were provided by Fujifilm B.V.

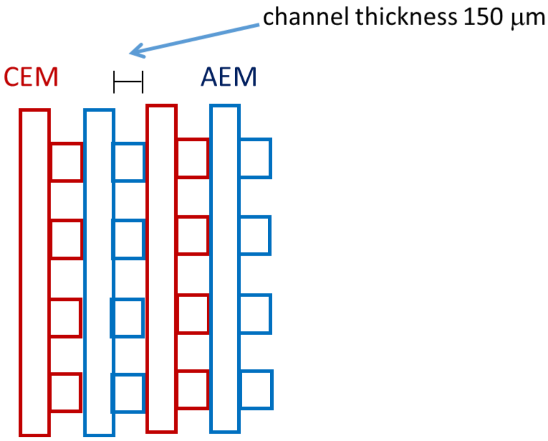

Figure 85. Schematic representation of two cell pairs with pillars profiled membranes. Cation exchange membranes are in red and anion exchange membranes in blue. The channel thickness is created by the pillars itself.

In order to study the possible asymmetric behaviour of the stack with profiled membranes, experiments were carried out changing the current direction. Concentrations of 0.5 and 1 g/l of NaCl were tested as inlet values in the diluate and in the concentrate compartments, respectively. To exclude the effect of possible flow misdistribution in the channels, the diluate and concentrate compartments were changed. Moreover, the experiments were performed in the three possible modes: ED, RED and ARED. Results are reported in Figure 86a while a zoom of the ED mode is shown in Figure 86b. In the latter, the scheme of the profiled CEM is only reported as a reference to specify the current direction. The reported values of current density were obtained as the ratio of the total current and the active membrane area, excluding the profiles.

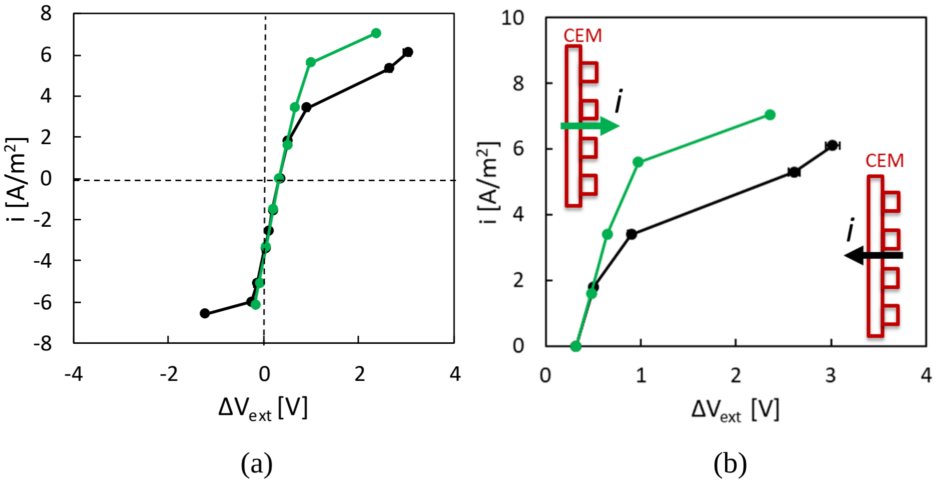

Figure 86. Experiments with pillars profiled membranes. Current density vs applied external voltage: a) results in ED, RED and ARED modes; b) zoom of the results in ED mode. NaCl solutions are characterized by concentrate / diluate inlet concentrations of C^{CONC}*=1 g/l and* C^{DIL} *=0.5 g/l. Inlet velocity is 1 cm/s for both solutions.*

The best results were obtained when, considering the cation exchange membrane, the current was directed from the membrane bulk to the profiles: in this case, indeed, the green curve shows higher LCD. It is worth to note that the black curve, corresponding to the worst configuration, shows a slope change also in ARED mode, which reminds a limiting behaviour.

In the best observed configuration, an experimental campaign was performed adopting the operating conditions reported in Table 10. Experimental results obtained with profiled membranes were compared with results obtained with Type 10 flat membranes and spacers of thickness similar to pillars profiles, i.e. 155 μm. In Figure 87 an example of this comparison is reported for the case with 30 g/l and 0.5 g/l as inlet concentrations in the diluate and in the concentrate, respectively, and 1 cm/s as inlet velocity in both compartments.

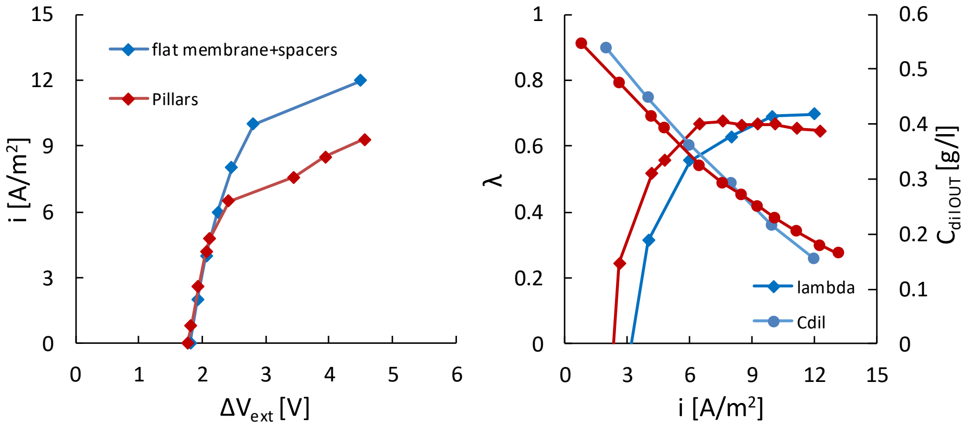

(a) (b)

Figure 87. a) Current density – voltage curve. b) Diluate outlet concentration (circles) and current efficiency (diamonds) vs current density. Experimental data obtained with pillars profiled membranes (red curves) and with flat Type 10 membranes and 155 µm spacers (blue curves) are compared. NaCl solutions are characterized by concentrate / diluate inlet concentrations of C^{CONC}*=30 g/l and* C^{DIL} *=0.5 g/l. Inlet velocity is 1 cm/s for both solutions.*

Observing the linear part of the current density – voltage curve Figure 87a, it is possible to observe that the two configurations provide the same voltage for a given current density. However, at the same current density, the desalination effect is slightly higher when pillars profiled membranes are adopted: in Figure 87b, indeed, the red curves for pillars profiled membranes show that the outlet diluate concentration is lower while the current efficiency is higher than what obtained with flat membranes and spacers (blue curves). It should be pointed out that, even if profiled and flat membranes, are provided by the manufacturer (Fujifilm B.V.) as Type 10 membranes with the same properties, looking at the zero current efficiency value, this corresponds to two different CCD values: pillars profiled membranes, in particular, show a lower CCD (~2.34 A/m^2 against ~3.2 A/m^2 for flat membranes), thus also a lower salt diffusion permeability coefficient (~$3\cdot10^{-12}$ m^2/s against ~$4\cdot10^{-12}$ m^2/s for flat membranes). However, since this discrepancy was also observed when Type 10 membranes from different batches were used, it is not possible to exclude that this can be the reason also in this case.

In regard to the LCD appearance, this is observed at lower current density values when pillars profiled membranes are adopted. This can be related to the poor mixing promotion obtained with the tested pillar configuration with respect to the woven spacers, also confirmed by the Sh values reported in Part II, Sections 4.1 and 4.2.

The basic version of the model (with no limitation for the LCD appearance), presented in Part III, Section 2, was used to simulate an ED stack with pillars profiled membranes. Model predictions and experimental results are compared in Figure 88. The model, which includes CFD results for the Sherwood number, the friction factor *f* and the expression for the Ohmic resistance of a whole cell pair presented in Part II, Sections 4 and 5, for profiled membranes presented in Part II, is in good agreement with the experiments as long as the current density is below the LCD.

To obtain an empirical correlation for the LCD when profiled membranes are adopted, a large experimental campaign is ongoing at University of Palermo, in which pillars profiled membranes with different geometric parameters (*l*/*p*, *p*/*H* and open area) are investigated.

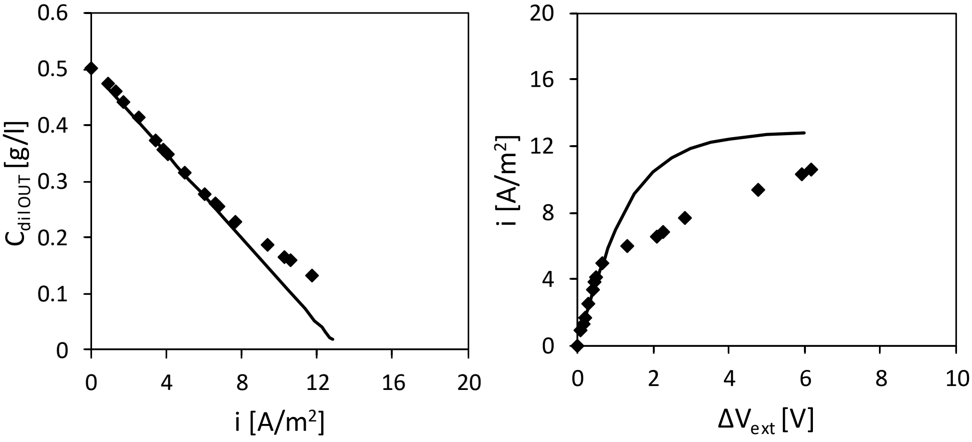

Figure 88. a) Outlet Diluate concentration vs current density. b) Current density – voltage curve. Experimental data (symbols) and simulation results (lines) obtained for pillars profiled membranes are compared. Simulation results were obtained using the basic version of the one-dimensional model without the empirical correlation for LCD. Data were obtained using NaCl solutions with inlet concentrations of $C^{CONC}=C^{DIL}=0.5$ *g/l. The velocity was equal to 1 cm/s.*

OCF profiled membranes

The stack is not symmetric even when OCF profiled membranes are adopted. This is due to the fact that membranes provided by Fujifilm B.V. were profiled only on one side: these profiles are straight filaments which have to be orthogonal to the other profiles of the opposite membrane (see Appendix C). This means that the thickness of one of the two channel is created by the sum of the height of the two orthogonal profiles while, in the other channel, a spacer is used to separate the flat sides of the membranes (Figure 89).

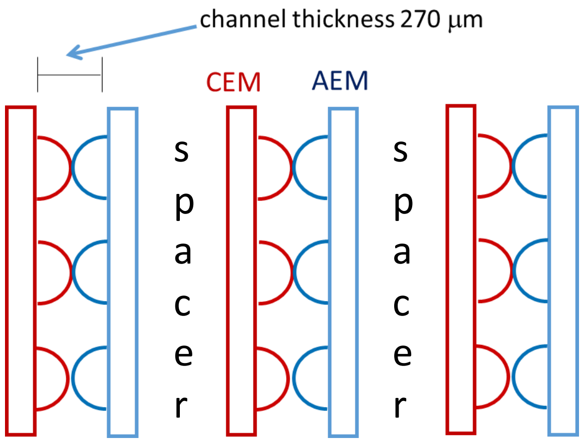

Figure 89. Schematic representation of two and a half cell pairs with OCF profiled membranes. Cation exchange membranes are in red and anion exchange membranes in blue. The channel thickness is created by the two overlapped cross filaments. In one of the two channels, a spacer is needed.

In order to study the asymmetric behaviour of the stack with OCF profiled membranes, the same type of experiments described for pillars membranes were carried out. The results reported in Figure 90 show that also in this case a better configuration exists and it coincide with the result obtained with pillars: when the current flows from the bulk of a CEM to the profile, better performance are expected.

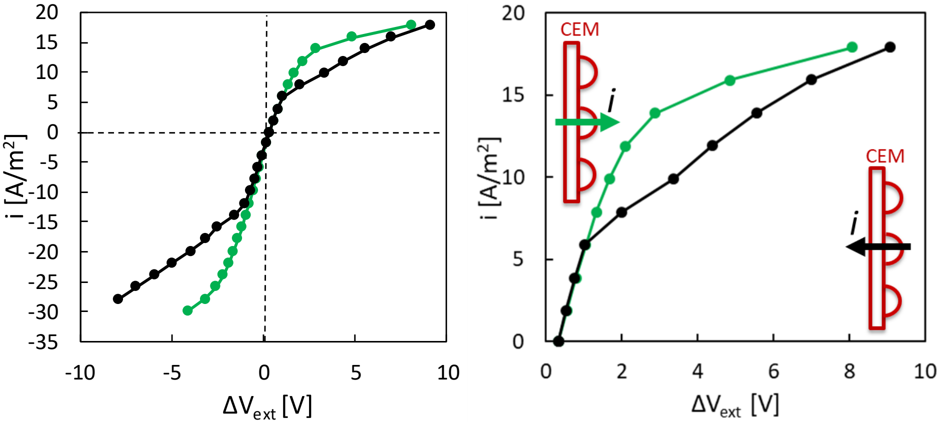

(a) (b)

Figure 90. Experiments with OCF profiled membranes. Current density vs applied external voltage: a) results in ED, RED and ARED modes; b) zoom of the results in ED mode. NaCl solutions are characterized by concentrate / diluate inlet concentrations of C^{CONC}*=1 g/l and* C^{DIL} *=0.5 g/l. Inlet velocity is 1 cm/s for both solutions.*

In these experiments, more current density steps were adopted and this allowed observing, even in the best configuration, the slope variation in ARED mode, also observed in Figure 86, for pillars membranes.

In the best observed configuration, an experimental campaign was performed adopting the operating conditions reported in Table 10 and the experimental method described in Appendix C. Experimental results obtained with OCF profiled membranes were compared with results obtained with Type 10 flat membranes and spacers of thickness similar to the channel with profiles, i.e. 280 µm. In Figure 91 an example of this comparison is reported for the case with 30 g/l and 0.5 g/l as inlet concentrations in the diluate and in the concentrate, respectively, and 1 cm/s as inlet velocity in both compartments. Observing Figure 91a, it is possible to observe that, in the first linear part of the curve, the OCF profiled membranes provide a lower voltage for a given current density. Moreover, the desalination effect is the same in the two cases. In Figure 91b, indeed, the current efficiency and the outlet diluate concentration curves obtained in the two configurations are overlapped. It should be pointed out that, in this case, the zero current efficiency value corresponds to equal CCD values and so equal salt diffusion permeability.

In regard to the LCD appearance, this is observed at higher current density values when OCF profiled membranes are adopted.

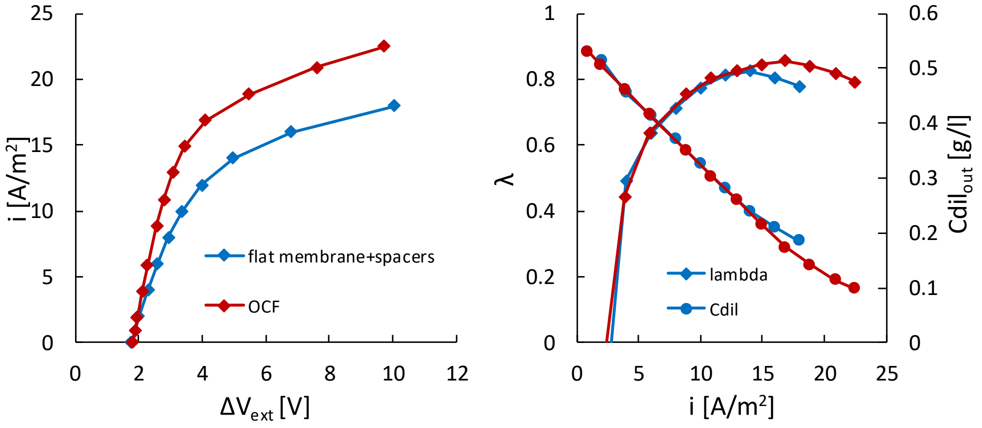

(a) (b)

Figure 91. a) Current density – voltage curve. b) Diluate outlet concentration (circles) and current efficiency (diamonds) vs current density. Experimental data obtained with OCF profiled membranes (red curves) and with flat Type 10 membranes and 270 µm spacers (blue curves) are compared. NaCl solutions are characterized by concentrate / diluate inlet concentrations of C^{CONC}*=30 g/l and* C^{DIL} *=0.5 g/l. Inlet velocity is 1 cm/s for both solutions.*

Also in the case of OCF profiled membranes, the predictions of the basic version of the model (with no limitation for the LCD appearance), presented in Part III, Section 2, were compared with experimental results (Figure 92). The model, which includes CFD results for the Sherwood number, the friction factor *f* and the expression for the Ohmic resistance of a whole cell pair presented in Part II, Sections 4 and 5, for profiled membranes presented in Part II, is in good agreement with the experiments as long as the current density is below the LCD.

To obtain an empirical correlation for the LCD when profiled membranes are adopted, a large experimental campaign is ongoing at University of Palermo, in which OCF profiled membranes with different geometric parameters (*l*/*H* and open area) are investigated.

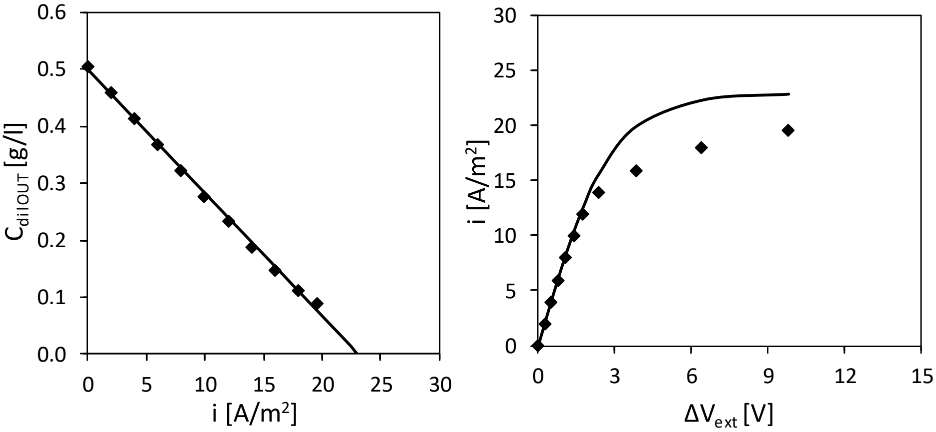

Figure 92. a) Outlet Diluate concentration vs current density. b) Current density – voltage curve. Experimental data (symbols) and simulation results (lines) obtained for OCF profiled membranes are compared. Simulation results were obtained using the basic version of the one-dimensional model without the empirical correlation for LCD. Data were obtained using NaCl solutions with inlet concentrations of C^{CONC}=C^{DIL}=0.5 g/l. The velocity was equal to 1 cm/s.

Part IV: Process modelling and characterisation of advance hybrid systems

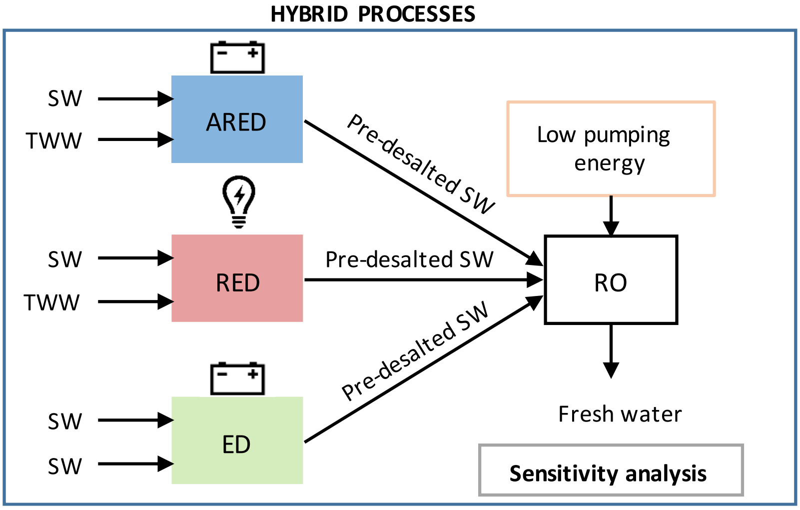

The following results have partially been published in:

La Cerva *et al.*, *Desalination*, vol. 467, 2019.

1. Literature review

(Assisted) Reverse Electrodialysis coupled with RO

In hybrid arrangements with RO, the RED process, besides reducing the energy consumption by producing green energy, can be used as a pre-treatment, reducing the feed salinity (i.e. the pressure level required for pumping in RO) or can be integrated with existing desalination plants using their outlet brine as the high salinity (typically above 50-60 g/l) feed and providing also a desalting strategy for brine disposal [211].

Li *et al*. [82] explored both concepts in different configurations of RED and RO integration by using a simple lumped parameters model. Considering spacerless channels in RED under batch operations, they first studied the effects of the external load and of the concentration and volume of the dilute solution on the energy harvested and on the outlet concentration of the saline stream. The optimized operating conditions, which maximise the specific energy harvested and minimize the discharge time, were found for a low to high salinity ratio close to 0.01, an external load equal to the initial internal resistance and a volumetric ratio of the low to the high salinity solution of 2. This optimized design for the RED process was then combined with the RO process for which ideal membranes and uniform hydraulic pressure were considered. The authors observed that the RED-RO configuration is more effective in reducing the specific energy consumption compared to the RO-RED design. Moreover, arranging the RED process as a pre-treatment, reduces the risk of scaling for RO, since some divalent ions (Ca^{2+} and Mg^{2+}) can partially be removed. Also more complex schemes were simulated, showing promising results in reducing the energy consumption. However, the authors did not investigate the full optimisation of the integrated system, which may lead to very different “optimal” operating conditions compared to what was found by optimising the stand-alone RED and RO units.

More recently, Mei *et al*. [212] experimentally observed that the power density harvested from RED process can be increased if the sink stream, at low concentration, has concentration between 0.01 and 0.02 M, typical of effluents from treated municipal wastewater, or when the high concentration stream has concentration from 0.6 to 2 M, typical of brine from RO. From these results, they proved that RED can be coupled with RO both as a pre-treatment and a post-treatment. However, they did not study the integrated system and a cost analysis is missing.

Other studies only focused on the role of RED process as a post-treatment to reduce the concentration of the brine produced in RO or other industrial processes, before discharging it, producing electric energy at the same time [10,213,214].

Another pre-desalting option is the Assisted Reverse Electrodialysis (ARED) process. In ARED an additional external voltage is applied in order to increase the stack electrical current (and consequently, the salt flux from seawater to the sink stream) above the short-circuit condition. Vanoppen *et al*. [81,177] have proposed a hybrid scheme, consisting of an ARED stage followed by a brackish water RO (BWRO). The authors carried out experiments in order to characterize the ARED stack and then, considering the ARED-RO combination, they observed that, under certain operating conditions, an energy consumption reduction is possible. The economic analysis showed that the ARED-RO coupling was competitive with the stand-alone SWRO when the price of the ion-exchange membranes (IEMs) was lower than 10 €/m^2.

Electrodialysis coupled with RO

A different integration scheme for seawater RO desalination is the coupling with an Electrodialysis (ED) unit. In this case, Electrodialysis has the theoretical advantage of requiring lower specific energy for the removal of salt from high salinity streams when only a partial desalination is performed [215,216]. With reference to this latter case, ED can be coupled to RO for pre-desalting the feed seawater, thus reducing the operating pressure of RO.

Galama *et al*. [39] studied experimentally the pre-desalination of seawater by ED. Supported by literature data on the energy consumption of BWRO systems, they found that current densities higher than 50 A/m^2 led to overall energy consumptions of the ED-BWRO lower than those of the stand-alone ED. The authors claimed the potential reduction of energy consumption also with respect to SWRO. However, no comparison with conventional stand-alone SWRO and no data supporting this conclusion were reported. Moreover, only energy costs are considered, which leads to possible misleading conclusions. McGovern *et al*. [215,216] assessed the ED desalination performance by letting the feed salinity vary and they found the partial desalination of highly concentrated brackish waters as the most cost effective application, thus envisioning a possible use in ED-BWRO coupled treatments. The performance of an ED-BWRO real plant was tested for brackish water (2000-4000 ppm) desalination in domestic applications [217], showing promising results in increasing the recovery of produced water.

To the best of our knowledge, the only cost analysis presented so far on the ED-RO coupling has been performed by Post *et al*. [6]. They considered a theoretical ED spacerless unit, with ideal membranes (perfectly ion-selective, no transport of co-ions and water) and a low membrane cost (5 €/m^2). Under these assumptions, considering a limited range of operating conditions and considering theoretical energy consumptions, the ED-BWRO configuration was shown to be competitive with respect to SWRO.

For the sake of completeness, it should be mentioned that other coupling solutions presented in the literature concern the application of RO-ED systems, i.e. hybrid processes where the RO retentate brine is fed to a following ED step (in more or less complex schemes which may involve recirculations), e.g. for valorisation of reverse osmosis brines [218–221].

The above literature review shows that schemes of hybridization in which electromembrane processes are used to valorise the brine produced in RO are very promising because they allow the diluted brine to be discharged with less environmental damages and/or they can also produce electricity. Concerning the use of electromembrane processes as pre-desalting steps for RO, a few works show the potential benefits of this integrations. However, the analysis reported are theoretical or based on simplified models, while a comparison with the standard stand-alone SWRO is not reported and cost analysis is often missing.

In this thesis, a comprehensive simulation tool was developed in order to perform a sensitivity analysis of the operation of hybrid (A)RED-RO and ED-RO schemes for seawater desalination under the constraint of a final product having a salinity lower or equal to 0.5 g/l. This salinity threshold coincides with the secondary drinking water regulation for total dissolved solids adopted by the US Environmental Protection Agency (EPA) [222]. The simulation tool was adopted to analyse the influence of operating parameters and operational strategies on the cost saving of the hybrid systems compared to stand-alone SWRO, identifying promising operational ranges and schemes.

2. RO model and validation

The model adopted for the RO process is a lumped parameter model, in which average concentrations and pressure in each RO module are considered to compute water and salt fluxes, while variations along the modules of each pressure vessel (PV) are considered. Another simplifying assumption is that the pressure drops in the permeate channel are neglected.

Under these assumptions and with reference to Figure 93, which shows an example of a typical series arrangement of RO spiral-wound modules inside a PV, the mass balance equations in the *i*-th module can be written as:

$$Q_r^i = Q_f^i - Q_p^i \tag{87}$$

$$C_r^i Q_r^i = C_f^i Q_f^i - C_p^i Q_p^i \tag{88}$$

where Q_r^i is the retentate flow rate, Q_f^i is the feed flow rate, Q_p^i is the permeate flow rate, C_r^i, C_f^i and C_p^i are the salt concentrations in the retentate, in the feed and in the permeate, respectively.

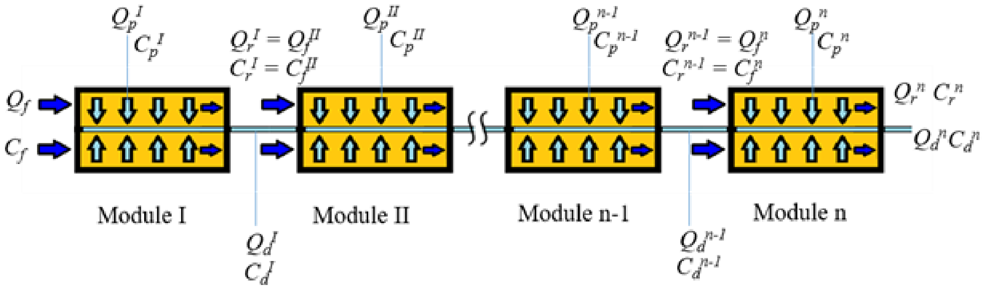

Figure 93. Sketch of an RO pressure vessel with n spiral wound membrane elements in series.

The permeate concentration (C_p^i) can be obtained from the salt molar flux (N_s^i) expression:

$$N_s^i = B\left(C_{f,avg}^i - C_p^i\right)/M_S \tag{89}$$

where *B* is the salt permeability constant, M_S is the molar mass of salt (in this case NaCl at 25 °C), while $C_{f,avg}^{i}$ and C_{p}^{i} are the average concentrations in the feed and in the permeate (expressed in g/l), respectively.

The water flux (J_{W}^{i}) and the permeate flow rate (Q_{p}^{i}) are functions of the water permeability constant, A_p, and the net driving force, according to Eq. (90):

$$Q_{p}^{i} = J_{W}^{i} S = A_p\left[P_{avg}^{i} - \left(\pi_{f}^{i} - \pi_{p}^{i}\right)\right]S \tag{90}$$

in which P_{avg}^{i} is the feed channel average pressure, π_{f}^{i} and π_{p}^{i} are the osmotic pressures of the feed (considering the average concentration in the channel) and the permeate, calculated by the Van't Hoff equation.

Since the average concentration ($C_{f,avg}^{i}$) depends on the permeate flow rate (Q_{p}^{i}) and this latter, in its turn, depends on $C_{f,avg}^{i}$ (as it affects the osmotic pressure π_{f}^{i}), an iterative calculation is necessary to solve the set of equations.

The permeate is collected in the permeate duct, where its flow rate is added to that produced in all previous modules, while the concentration is obtained by a weighted average of the outlet concentrations from the previous modules, where the weights are the relevant flow rates. At the outlet of the pressure vessel, the flow rate (Q_{d}^{n}) and the salt concentration (C_{d}^{n}) of the permeate are:

$$Q_{d}^{n} = \sum_{i=1}^{n} Q_{p}^{i} \tag{91}$$

$$C_{d}^{n} = \frac{\sum_{i=1}^{n} C_{p}^{i} Q_{p}^{i}}{Q_{p}^{n}} \tag{92}$$

The outlet pressure in the *i*-th module is calculated as the inlet pressure minus the frictional losses:

$$P_{r}^{i} = P_{f}^{i} - \Delta P^{i} \tag{93}$$

Considering only the distributed frictional losses along the module, these can be estimated by the Darcy-Weisbach equation:

$$\Delta P^{i} = f\frac{L}{d_h}\rho^{SOL}\frac{{u_{void}}^{2}}{2} \tag{94}$$

where f is the friction factor, L is the module length, d_h is the channel hydraulic diameter assumed equal to twice the channel thickness, ρ^{SOL} is the density of the solution fed into the module and u_{void} is the void velocity, i.e. the velocity which would yield the given flow rate if the channel were spacerless.

The friction factor depends on the spacer geometry and on the Reynolds number. In regard to the spacer geometry, in the feed channel of an RO module, usually overlapped spacers are adopted [47–49]. Due to the lack of detailed data on the spacer geometry adopted in the commercial RO modules considered in this work, friction factor values obtained by CFD simulations for overlapped spacers (reported in Part II, Section 5) were used. In the range of the Reynolds numbers investigated here (100-300), the friction factor for the overlapped spacer with an orientation of 45° with respect to the flow, can be estimated as $f \approx 10 \cdot (96/\mathrm{Re})$.

The RO model described was implemented in a MS Excel™ spreadsheet and solved by macros. Since a validation with experimental results was not possible, the present model was compared with the theoretical predictions of two widely used commercial codes provided by DOW Chemical Company: ROSA, a user-friendly program for the RO module design, and its evolution, the more recently developed WAVE software [50]. In all simulations one PV was considered with seven modules, all of the same type, which guarantee for all cases the achievement of the target permeate concentration (lower than 0.5 g/l). The modules were selected among three products offered by DOW Chemical, whose main features are reported in Table 13 and Table 14.

In Figure 94, the comparison between the model here presented and the commercial codes ROSA and WAVE is reported for the case of a single PV with seven SW30XHR-440i modules. The inlet flow rate was set equal to 10 m^3/h with a concentration of 32 g/l NaCl and the feed pressure was imposed equal to 40 bar. Figure 94 shows that our model predictions are in very good agreement with those of the two commercial codes, with only a small overestimation of the permeate concentration.

Table 13. Performance data of RO modules provided by DOW Chemical [49–51].

	BW30HR-440i	**SEAMAXX**	**SW30XHR-440i**
Active area [m^2]	41	41	41
Length [m]	1.016	1.016	1.016
Channel thickness [mm]	0.7112	0.7112	0.7112
Permeate Flow rate [m^3/day]	48 [a]	64.4 [b]	23 [b]
Salt Rejection [%]	99.4 [a]	99.7 [b]	99.82 [b]

[a] Values based on the following test conditions: 2,000 ppm NaCl, 15.5 bar, 25°C, pH 8 and 15% recovery.

[b] Values based on the following test conditions: 32,000 ppm NaCl, 55 bar, 25°C, pH 8 and 8% recovery.

Table 14. Membrane properties derived from the data in Table 13.

	BW30HR-440i	**SEAMAXX**	**SW30XHR-440i**
A_p [l/(m^2h bar)]	3.581	2.424	0.938
B [l/(m^2h)]	0.294	0.197	0.0458

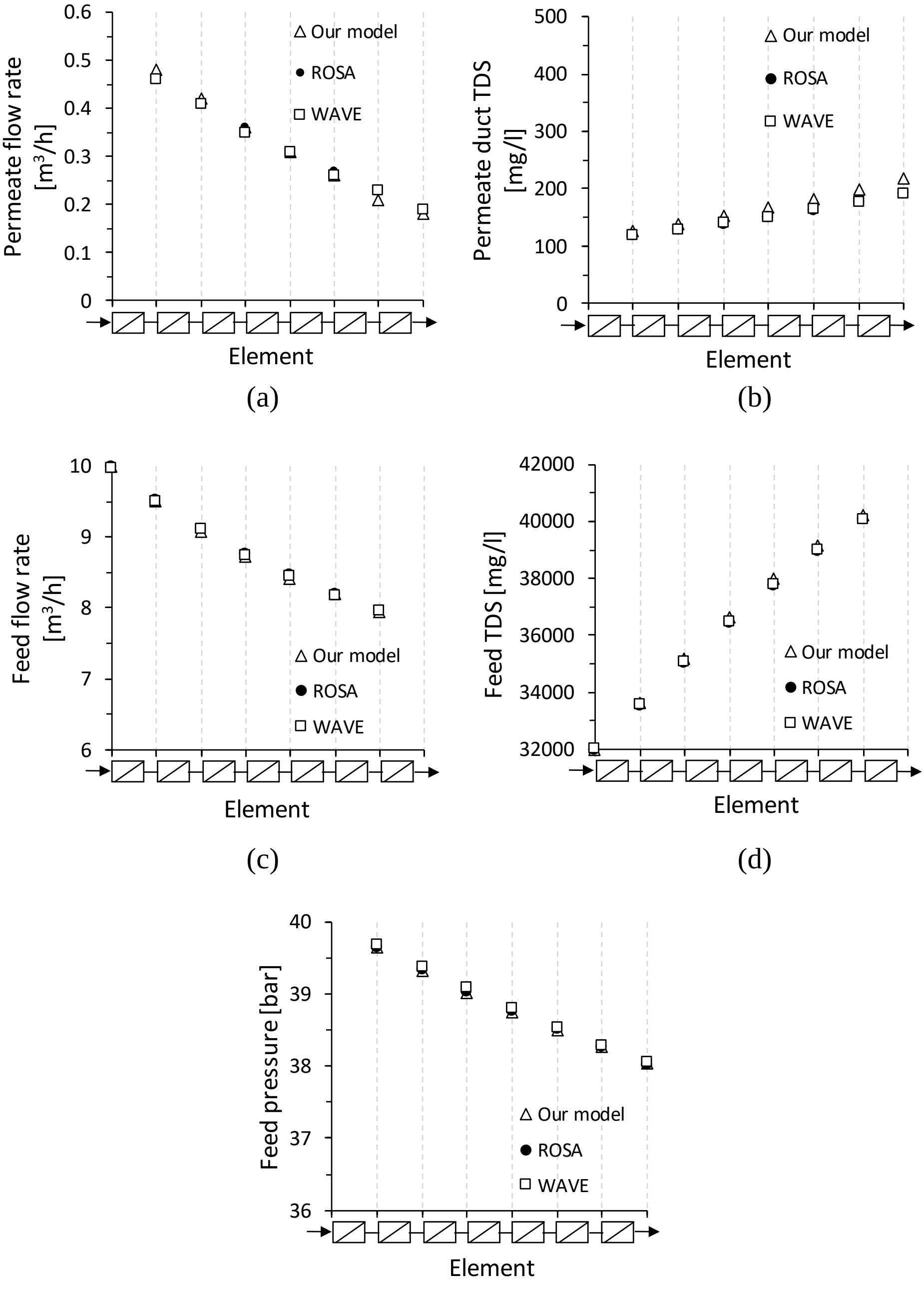

(a) (b)

(c) (d)

(e)

Figure 94. Comparison between the RO model presented in this thesis (empty triangles) and predictions of ROSA (solid circles) and WAVE (empty squares) software. Flow rates and TDS for feed and permeate duct are reported as a function of the elements. The feed pressure is also reported. Simulations were conducted with RO module SW30XHR-440i, inlet flow rate of 10 m^3/h, inlet concentration of 32 g/l NaCl and feed pressure of 40 bar.

3. Model validation

The simulation tool adopted for hybrid schemes was obtained by combining the one-dimensional model for electromembrane processes described in Part III and the model for RO presented in the previous section. Both models were implemented in Excel™.

Within the activities of the *REvivED water* project (Low energy solutions for drinking water production by a Revival of ElectroDialysis system), funded by the European Union's Horizon 2020 Research and Innovation program (Grant Agreement no. 685579), a pilot demonstration system was constructed by Trunz Water Systems AG, and installed in May 2019 in Burriana, Spain, in a wastewater treatment plant owned by FACSA, a Spanish private company. This location was chosen for the possibility to have both seawater and wastewater that is needed if the RED mode has to be tested. The pilot system is installed inside of a weather resistant container for outdoor applications (Figure 95).

The plant can produce 25 m^3/day of fresh water and consists of two 44×44 stacks (REDstack B.V.) in series, each one having 288 cell pairs with Type 10 membranes (Fujifilm B.V.) and spacers of thickness 280 μm, followed by an RO pressure vessel with 6 DOW (Filmtec) SW30-4040 modules. Seawater is pre-treated by a sand filter, a wrapped cartridge filter with a filter size of 100 μm and an ultrafiltration (UF) system with a pore size of 0.02 μm. In the case of wastewater, the pre-treatment system is similar to that one described for seawater with an activated carbon filter added after the UF. The picture in Figure 96 shows the plant inside the container.

Five different operation modes were assumed for the two stacks:

- Two stages ED, one pass;
- One stage ED, feed and bleed;
- Two stages ED, feed and bleed;
- RED-ED, one pass (both SW and TWW exiting from the first stack are fed into the second);
- RED-ED, split (only SW from the first stack is split and fed into second stack).

In all modes, a polarity and a feedwater reversals are expected in both stack every 30 minutes in order to prevent scaling and membrane fouling [223,224].

All the settings and parameters for the pre-treatment, the ED and the RO systems can be controlled by three different E-Panels. An example is reported in Figure 97.

Figure 95. Outside of the container in which the integrated (R)ED-ED-RO system is installed. Photo taken during the inauguration and the visit at the plant on May 28, 2019 in Burriana, Spain.

Figure 96. Inside the container. At the bottom left, the box containing the two stacks. Above the box, the RO pressure vessel. On the right, ultrafiltration systems.

The pilot system was tested in the "Two Stages ED, one pass" mode, in which the pre-treated seawater is fed into the first stack and then into the second one, in both diluate and concentrate compartments. The pre-desalted seawater exiting from the second stack is collected in a buffer tank and fed into the RO pressure vessel.

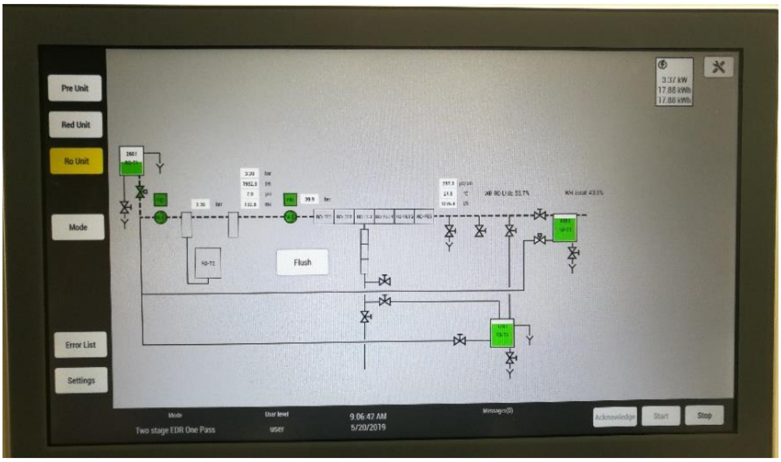

Figure 97. E-Panel for the RO system. The pressure vessel is depicted in the centre. Valves, tanks, filters and pumps are also reported. The dotted line and the pumps in green, mean that the system is running.

The first tests were performed for 1-2 hours, studying the plant response to different operating conditions. In addition, the reproducibility was analysed, showing good results. After these tests, an experiment of 8 hours was carried out in order to study the stability of the plant. This experiment was carried out by fixing the desired flow rates at the outlet of the second stack, the applied voltage in the first stack and the outlet conductivity from the second stack. In particular, the settings are the following:

- $Q_{out,II\ stack}^{DIL} = 1800\ l/h$
- $Q_{out,II\ stack}^{CONC} = 900\ l/h$
- $\Delta V_{I\ stack} = 100\ V$
- $\sigma_{out,II\ stack}^{DIL} = 26\ mS/cm$

The ratio between the flow rates in the diluate and concentrate compartments is chosen in order to have a water recovery of ~67%. The RO will produce ~1000 l/h with a final water recovery of ~37%. The decision to not control the outlet conductivity from the first stack and to apply a certain voltage is due to the observation of malfunctions and poor performance with respect to the second stack. Indeed, after the firsts short tests, a rapid increase in the electric resistance was observed in the first stack. To avoid that the voltage could increase and damage the rectifier when the outlet conductivity is controlled, an applied voltage of 100 V was safely fixed.

In Figure 98, voltage and current are reported against time in both first (graphs a and b) and second stack (graphs c and d). The fluctuations correspond to the polarity reversal. The applied voltage of 100 V in the first stack corresponds to a current of ~30 A, leading to a stack resistance of ~3 Ω.

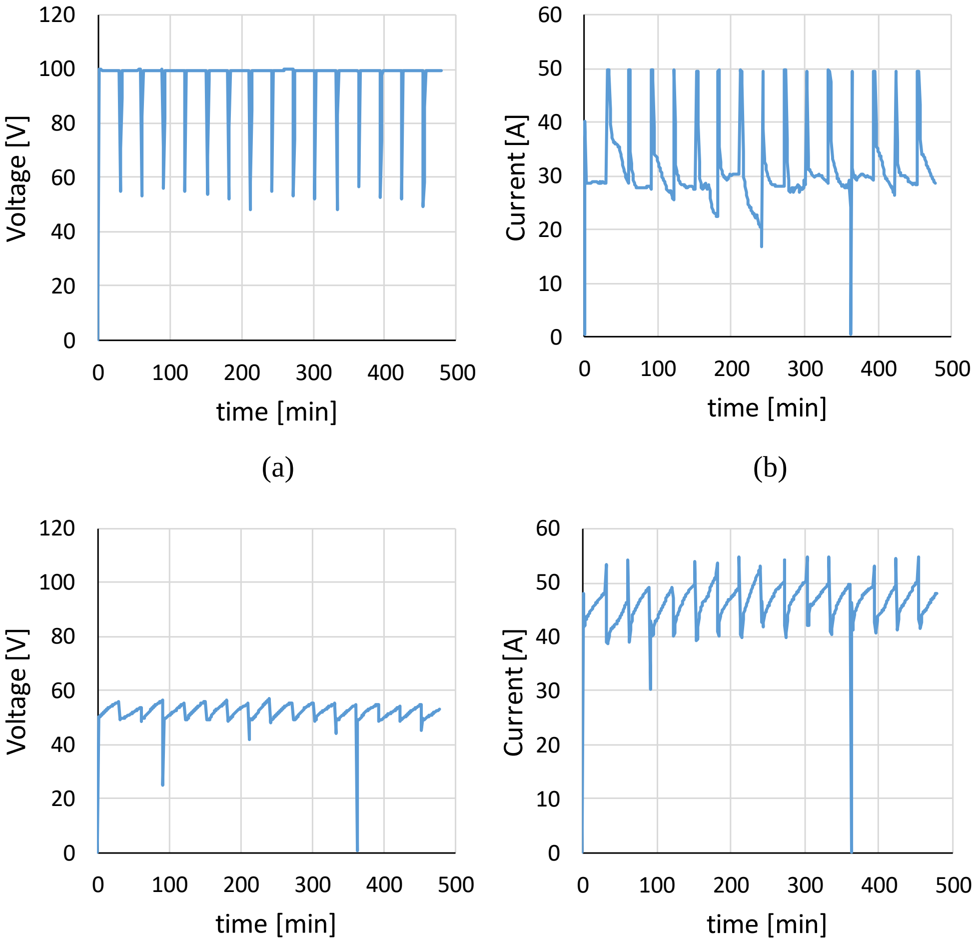

(a) (b)

(c) (d)

Figure 98. Voltage and current vs time in the first stack (a, b) and in the second one (c, d).

In the second stack, the outlet diluate conductivity is controlled to reach the set point of 26 mS/cm, which requires a current of ~48 A and a corresponding voltage of ~58 V. In the second stack, the resistance is ~1.2 Ω. This confirms the poor performance of the first stack observed after the first tests.

In Figure 99a, the inlet conductivity in the first stack is reported. This is equal to ~ 51 mS/cm for both diluate and concentrate compartment and it is constant in time. Graph (b) and (c) in Figure 99, report the outlet diluate conductivity from the first and second stack, respectively. The big fluctuations correspond to the moment in which the feed water is reversed.

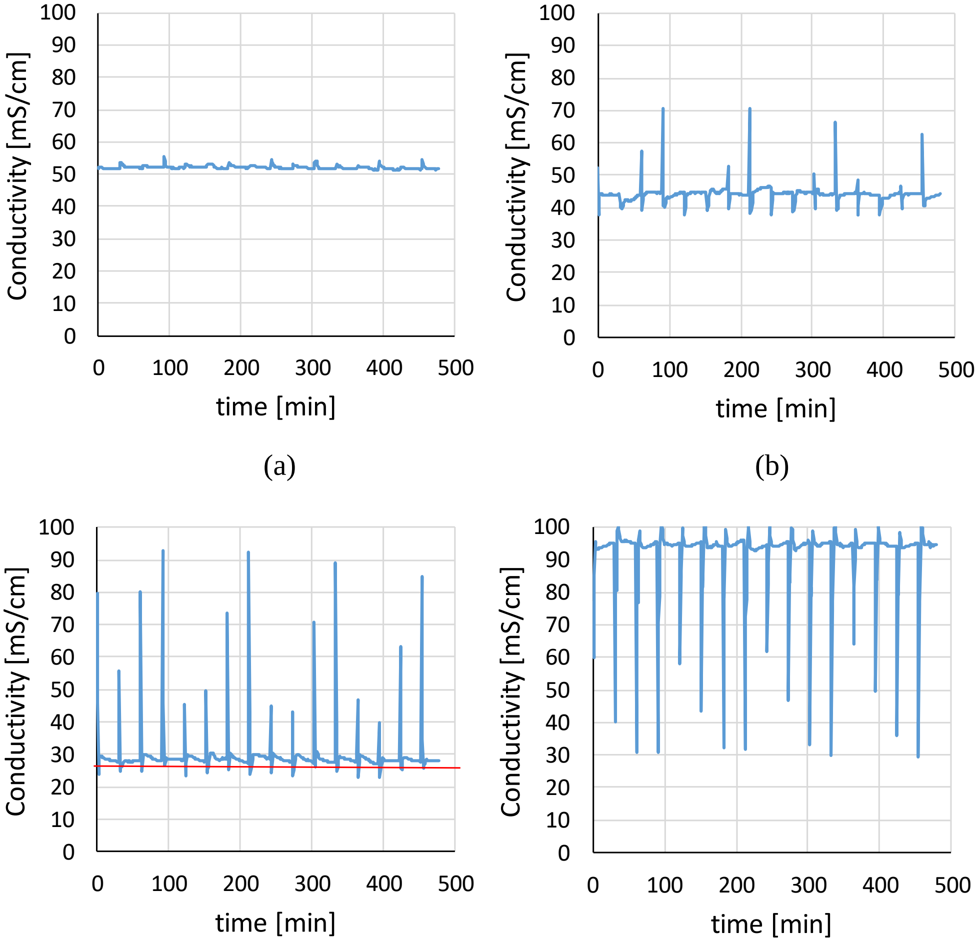

(a) (b)

(c) (d)

Figure 99. Conductivity vs time: a) inlet diluate and concentrate conductivity in the first stack; b) outlet diluate conductivity from the first stack; c) outlet diluate conductivity from the second stack; d) outlet concentrate conductivity from the second stack.

A current of 30 A in the first stack (Figure 98b) leads to an outlet diluate conductivity of ~44 mS/cm. The red line in graph (c) identifies the set point of 26 mS/cm which is not fully reached mainly because the control in conductivity has a slow response and the frequency of polarity reversal was too small. In regard to the outlet concentrate conductivity (Figure 98d), this is equal to ~95 mS/cm and shows the same fluctuations observed in graphs (b) and (c).

In Figure 100, the outlet flow rates from the diluate (graph a) and concentrate (graph b) compartments are reported as functions of time. The red lines identify the set point. Despite some fluctuations, the desired flow rates are well reached by the control program.

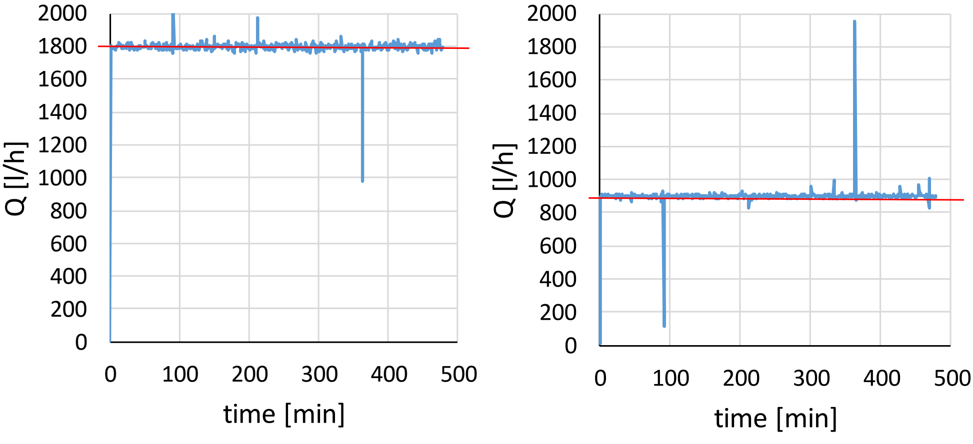

(a) (b)

Figure 100. Outlet flow rates from the second stack as functions of time: a) diluate flow rate; b) concentrate flow rate.

The experimental results obtained from this experiment were used to validate the simulation tool for integrated systems. The electromembrane and the RO models are both valid for monovalent ions, i.e. for binary salts such as NaCl. The experiment was performed with real seawater so other salts are present even if in lower concentrations than NaCl. To run the simulation, the experimental conductivity values were assumed to be equal to concentrations of only NaCl.

The simulation was run at fixed current, equal to the experimental one. In Figure 101, experimental values of voltage are reported and compared with model predictions. The voltage predicted by the model in the first stack is much lower than what observed in the experiment while there is a good agreement in the second stack. This big difference between the model and the experiment in the first stack is essentially due to malfunctions in the first stack.

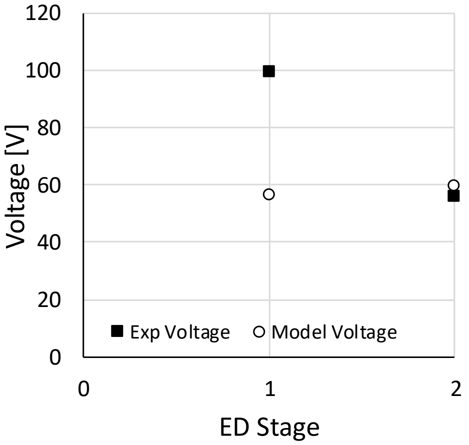

Figure 101. Voltage in the first and second stack. Experimental results are compared with model predictions (empty symbols).

Experimental values of flow rate (graph a) and conductivity (graph b) are compared with model predictions in Figure 102. The experimental values are considered as average values over time while the model provides stationary results. As it can be observed, the model is in good agreement with experiment and the small difference in conductivity values is mainly due to the fact that multivalent ions are not considered in the model.

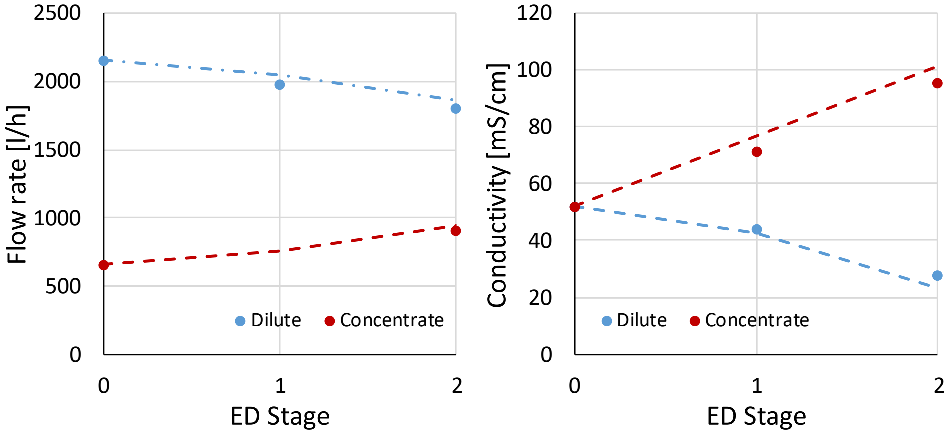

(a) (b)

Figure 102. a) Flow rates and b) conductivity in the first and second stack. Experimental results (symbols) are compared with model predictions (dotted lines).

In regard to the RO, the same experimental pressure value was fixed in the model to run the simulation. The results from the model are compared with the experimental values in Table 15.

Table 15. Experimental results and model prediction of outlet conductivity and permeate flow rate after the RO process.

	Pressure [bar]	**Outlet permeate conductivity [µS/cm]**	**Outlet permeate flow rate [l/h]**
Experiment	36.99	437.47	1019.05
Model	36.99	468.17	1168.5

The model overestimates the outlet conductivity by ~7% and the permeate flow rate by ~15%, proving to be in satisfactory agreement with the experiments.

To conclude, the simulation tool for hybrid schemes can be considered validated and in the following section will be used to perform sensitivity and economic analysis.

4. Sensitivity analysis

4.1 (A)RED-RO and ED-RO integrated process schemes

Simulations were performed fixing feed seawater concentration of 30 g/l NaCl and a flow rate of 346 m^3/day related to the velocity and number of cell pairs of the pre-desalting units (see Table 16). A concentration target equal or lower than 0.5 g/l NaCl for the final permeate produced was fixed for all simulations. The electrochemical pre-treatment of the (A)RED-RO coupled system was fed with a low salinity stream (e.g. treated wastewater) at 1 g/l NaCl. For (A)RED and ED processes, co-current stacks of 0.5 × 0.5 m^2 were simulated. The membrane properties reported in Table 2 were adopted in all the simulations.

Table 16. Features of the electromembrane plant (ARED, RED or ED).

	N° of cell pairs	**Inlet fluid velocity [cm/s]**	**Residence time [s]**
Case A	2500	2	25
Case B	5000	1	50

A spacer thickness of 160 μm was considered for the diluate and concentrate compartments. As a reference case (referred to as Case_A, see Table 16), an electromembrane plant with 2500 cell pairs and an inlet fluid velocity of 2 cm/s, corresponding to a residence time of 25 s, was considered. A second configuration with 5000 cell pairs (referred to as Case_B), with an inlet fluid velocity of 1 cm/s (corresponding to a residence time of 50 s) was also simulated. A flow ratio of 1 was fixed for the two streams entering the pre-treatment unit.

The areal blank resistance, related to the electrode compartments, was set equal to $2{\cdot}10^{-3}\ \Omega\ m^2$. The efficiencies of the pump and of the Energy Recovery Device (ERD) were both assumed equal to 0.75 for the integrated process scheme.

A sensitivity analysis was performed by changing the external voltage in the (A)RED and ED processes. The maximum value of voltage under RED conditions was that maximising the power provided. The same absolute value (with negative sign) was set as the maximum voltage for the ARED process while 7 intermediate values were set, including the Open Circuit condition (ΔV=0), as indicated in Table 17.

Under ED conditions, the maximum external voltage corresponds to a current density around ~90% of the limiting current density (LCD). The limiting current was estimated by the empirical correlation (Eqs. (82)-(84)) reported in Part III, Section 4.4. The feed pressure in the RO stage was suitably modified in order to reach the concentration target and, at the same time, maximise the water recovery.

In regard to the RO step, in all simulations one PV with seven modules, all of the same type, was considered. The chosen module must guarantee for all cases the achievement of the target permeate concentration (lower than 0.5 g/l). The modules were selected among three products offered by DOW Chemical, whose main features are reported are reported in Table 13 and Table 14.

In the hybrid systems, the RO modules were assumed to be SEAMAXX for RO feed concentrations (i.e., pre-desalted water concentrations) above 15 g/l NaCl and BW30HR-440i for RO feed concentrations below this threshold. Preliminary comparative simulations confirmed that, below 15 g/l, BWRO modules were (as expected) more energy-effective than SWRO ones. Single-pass RO was assumed here in all cases; however, it should be observed that a two-pass treatment would probably be adopted in BWRO when working with real solutions, in order to reduce the content in Boron and other dissolved solids in the final permeate.

Table 17. Values of external voltage in the electromembrane pre-treatment chosen for the sensitivity analysis.

RED	$\Delta V^* = \Delta V \rightarrow \mathrm{NPD}_{max}$ in RED
	$\Delta V = \Delta V^*/2$
	$\Delta V = \Delta V^*/3$
	$\Delta V = \Delta V^*/5$
Short circuit RED	$\Delta V = 0$
ARED	$\Delta V = -\Delta V^*/5$
	$\Delta V = -\Delta V^*/3$
	$\Delta V = -\Delta V^*/2$
	$\Delta V = -\Delta V^*$
ED	$\Delta V^{**} = \Delta V \rightarrow$ 90% LCD
	$\Delta V = \Delta V^{**}/2$
	$\Delta V = \Delta V^{**}/3$
	$\Delta V = \Delta V^{**}/5$

In order to properly evaluate the performance of the hybrid systems, a comparison with a stand-alone SWRO was performed. For each simulated case, the same RO feed flow rate as in the hybrid case was fixed, but keeping a concentration of 30 g/l NaCl. Operating feed pressure was made vary in order to respect the constraint of permeate concentration (< 0.5 g/l NaCl) and to obtain the same permeate flow rate of the corresponding case with the hybrid system. Even in the stand-alone SWRO, one PV with seven modules was assumed. The SW30XHR-440i module was selected for the stand-alone SWRO, as it is the only one (among those listed in Table 13 and Table 14) able to operate under all the conditions investigated, without incurring in alarms or exceeding the operating limits (specified in the data sheets or obtained from the ROSA and WAVE software). For the stand-alone SWRO, an efficiency of 0.9 was assumed for the energy recovery device.

4.2 Analysed performance indicators

One of the performance indicators adopted is the net specific energy consumption, i.e. the total energy consumed (by the hybrid process or the stand-alone SWRO) divided by the flow rate of the permeate produced. For comparison purposes, another indicator, the Cost Saving (*CS*) coefficient, has been defined as:

$$CS = \frac{UPC_{SWRO} - UPC_{hybrid}}{UPC_{SWRO}} \cdot 100\% \tag{95}$$

where UPC_{SWRO} and UPC_{hybrid} are the Unit Product Costs (*UPC*) related to the stand-alone SWRO and to the hybrid plant respectively. *UPC* is the sum of the capital cost depreciated over the plant life (*CapC*) and the operating cost (*OpC*) and it can be calculated as:

$$UPC = CapC + OpC\ [€/m^3] \tag{96}$$

where

$$CapC = \frac{\frac{Capital\ cost\ [€]}{Plant\ lifetime\ [y]}}{Plant\ capacity\ \left[{}^{m^3}/_{h}\right] \times Working\ hours\ per\ year \left[{}^{h}/_{y}\right]} \tag{97}$$

and

$$OpC = \frac{Annual\ operating\ cost\ \left[{}^{€}/_{y}\right]}{Plant\ capacity\ \left[{}^{m^3}/_{h}\right] \times Working\ hours\ per\ year \left[{}^{h}/_{y}\right]} \tag{98}$$

Capital costs (*CapC*) associated with RO have been assumed not to change passing from one configuration to the other, including the change in RO module type (Table 13 and Table 14). This RO *CapC* can be neglected for comparison purposes. For (A)RED and ED, *CapC* were calculated as proportional to the membrane area and considering a Lang factor of 2, as quantified in Table 18. Thus, in terms of membrane costs, a perspective analysis was performed in a range of costs from 5 to 20 €/m^2. These costs are aligned with the literature and, as the RO membrane costs decreased from 1 to 2 orders of magnitude in a few decades due to technology development, likewise these IEM costs are reasonably expected in a near future due to technological improvements and to the increasing spreading of ion-exchange membrane processes [6,81,225–227].

Operating costs (*OpC*) were expressed as proportional to the net energy consumption, i.e. the algebraic sum of all the energy contributions of the ED/(A)RED process, considered positive (as shown in Figure 49c) in the case of energy consumed (ARED, ED and RO) and negative in the case of energy produced (RED), plus the energy consumed in the RO stage.

It is worth noting that the calculated *UPC* does not include the capital costs (and operating costs, other than energy consumption) for the RO unit, thus it cannot be seen as the actual cost of product, but as a parameter useful for comparison purposes.

In regard to the pre-treatments, it was assumed that seawater entering the pre-desalting units of a hybrid system was subjected to the same pre-treatment steps as in stand-alone SWRO plants. Thus the pre-treatments costs were neglected for comparison purposes.

Table 18. Assumptions for the economic analysis.

	Scenarios							
	Reference	**2**	**3**	**4**	**5**	**6**	**7**	**8**
Energy cost [€/kWh]	0.15	0.15	0.15	0.3	0.3	0.3	0.08	0.08
RED/ED plant [€/m^2]	20	10	40	20	10	40	20	10
RED/ED plant lifetime	10 years							
Working hours per year	8000 h/year							

It is worth noting that ED and RED processes do not need an intensive pre-treatment of feed water, for which 100 μm filtration or sand filtration are enough to significantly reduce fouling on membrane surfaces [6,228]. Moreover, in the case of RED fed with TWW and heavily contaminated industrial brines, experimental campaigns indicated that the RED process is quite robust and simple periodic switching of feed waters [224,229] or acid/alkaline treatment applied with low frequency (once per week) [214,230] can significantly reduce fouling, biofouling and clogging phenomena. Thus, given the much higher sensitivity of RO to fouling and scaling phenomena, a much less important effect on ED/RED would be expected when feeding it with pre-treated seawater.

Eight different cost scenarios were studied: the first one was taken as a reference case; the others were obtained by considering a higher and a lower value for the energy and the RED/ED plant costs. The scenario with the highest RED/ED plant cost and the lowest energy cost was not considered as it is clearly the least favourably placed for the hybrid system.

From this sensitivity analysis, scenarios in which the hybrid systems are advantageous with respect to the conventional stand-alone SWRO will be identified.

4.3 Results and Discussion: (A)RED-RO

The first analysis illustrates the operating and performance parameters for the hybrid system (A)RED-RO. In Figure 103a, the power (provided or required) and the current in the (A)RED process are reported as functions of the external voltage. Note that the power contains also the pumping power, associated with pressure losses in the channels. The salt concentration of the pre-desalted stream from the (A)RED process is reported in Figure 103b.

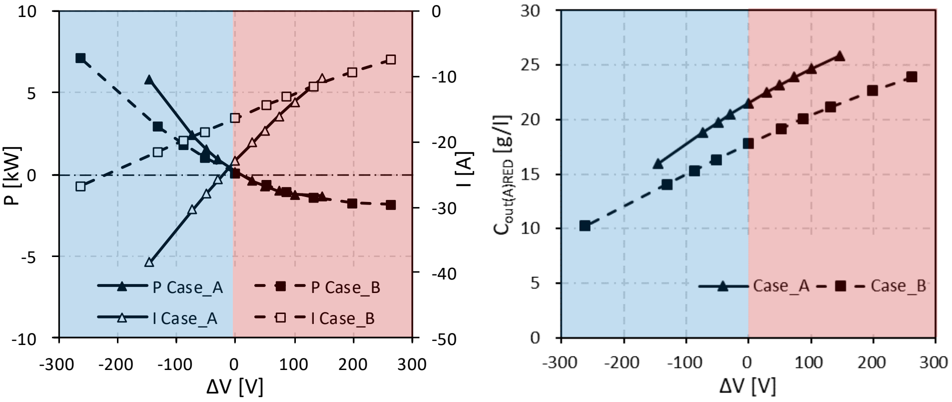

(a) (b)

Figure 103. Plots of (a) power and current, (b) outlet concentration of pre-desalted stream from the (A)RED process as a function of the external voltage. Positive voltages are for RED; ΔV=0 is the short-circuit RED; negative voltages are for ARED.

The desalination rate reached by the electromembrane pre-treatment increases when going from right to left in the chart, i.e. as the electrical current increases in absolute value. Therefore, the ARED pre-treatment provides a more desalted feed to the RO stage compared to the RED process, with a minimum value (in the range here investigated) of ~9 g/l NaCl. Moreover, the desalting degree is lower (i.e. the concentration is higher) in the electromembrane plant with a lower number of cell pairs (Case_A). In fact, for a given external voltage value, Case_A and Case_B are in two different operating conditions and, in particular, Case_B works close to the short-circuit condition (Figure 103a), so that the desalination degree is higher than in Case_A. In addition, the lower amount of ions transported in Case_A is further induced by a lower residence time. Under ARED conditions, Case_A and Case_B would be ideally equivalent, i.e. in Case_A, the current is higher, while the residence time is lower. However, non-ideal fluxes (osmotic transport and salt diffusion) contributing to dilute the seawater stream have less effect when the residence time is shorter, thus increasing the outlet concentration from the stack in Case_A. It is worth noting that, due to concentrations lower than 15 g/l NaCl achieved at high voltages ($\Delta V = -\Delta V^*/2 \approx -130$ V and $\Delta V = -\Delta V^* \approx -260$ V), the ARED plant configuration of Case_B is coupled to the RO module for brackish water.

Figure 104 reports the inlet feed pressure in RO, the outlet permeate concentration and the permeate flow rate as functions of the external voltage. The pressure required in the RO unit is in the range from ~35 bar to ~19 bar (while pressure higher than 50 bar are needed in the stand-alone SWRO). Fixing the same product flow rate for the stand-alone SWRO and for the hybrid process, the permeate salt concentration is higher in the two-stage coupled scheme despite the lower inlet concentration in the RO unit. This can be explained looking at the higher salt permeability of the RO modules selected for the coupled scheme compared to the SWRO modules (see Table 14).

As the electrical current increases (in absolute value), the reduction of concentration obtained in the pre-treatment (Figure 103b) is reflected in that obtained downstream the RO unit (Figure 104b), and results in a lower feed pressure in the RO unit (Figure 104a) and in an increase of flow rate (Figure 104c).

In particular, passing from the highest to the lowest external voltage, the permeate salt concentration decreases from ~0.38 g/l to ~0.2 g/l NaCl, and the flow rate increases from ~120 m^3/day to ~140 m^3/day, with overall recovery from 34% to 41%. In the case of stand-alone SWRO, the salt concentration in the treated water is almost constant and stands at lower values (~0.1 g/l NaCl). Since the voltage slightly influences the permeate flow rate in the hybrid system, each simulation of the stand-alone SWRO process has been performed by adjusting the permeate flow rate to that of the corresponding hybrid process in order to allow a direct comparison.

In regard to specific energy consumptions and costs, in Figure 105 the (A)RED-RO hybrid system is compared with the stand-alone SWRO for both Case_A (graphs (a) and (b)) and Case_B (graphs (c) and (d)). Graphs (a) and (c) of Figure 105 show that, in both Case_A and Case-B, the specific energy consumption of the hybrid process is lower than that of the stand-alone SWRO (which is almost constant, around 1.8 kWh/m^3) in a wide range of voltage, especially for the RED-RO scheme, where the pre-desalting step produces energy and causes a small reduction of energy consumed in the RO.

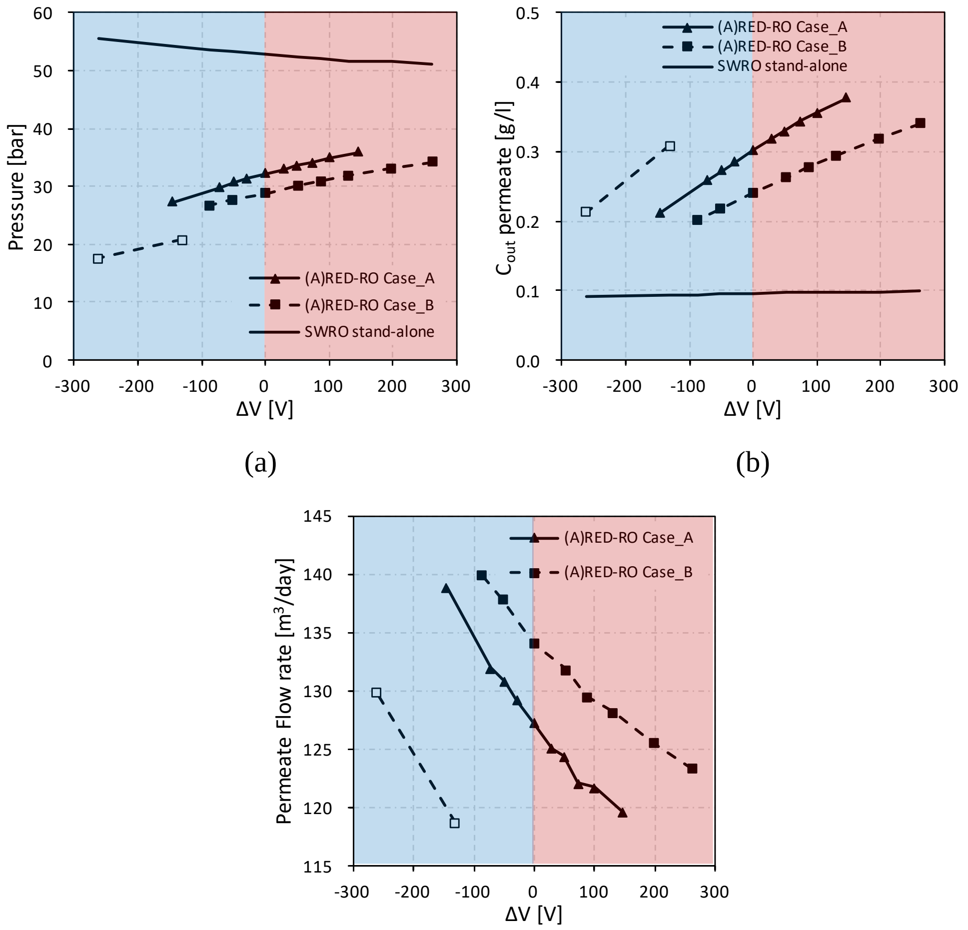

(a)

(b)

(c)

Figure 104. Plots of (a) the feed pressure in RO, (b) outlet permeate concentration and (c) permeate flow rate for the (A)RED-RO integrated process and for the stand-alone SWRO as a function of the external voltage. In Case_B, for two values of the external voltage in the ARED process, the BW30HR-440i RO module was used (empty symbols). The permeate flow rates for the stand-alone SWRO are not reported as they coincide with each single case. Positive voltages are for RED; ΔV=0 is the short-circuit RED; negative voltages are for ARED.

The minimum energy consumption of the RED-RO coupling is ~1.24 kWh/m^3 in Case_A and ~1.04 kWh/m^3 in Case_B, occurring between conditions of maximum power ($\Delta V = \Delta V^*$, the highest value of voltage considered here) and the short-circuit (ΔV = 0), i.e. $\Delta V = \Delta V^*/2$. In the ARED-RO process, the pre-desalting consumes energy, but further reduces the energy demand of the RO step, resulting in a total energy consumption lower than that of the stand-alone SWRO.

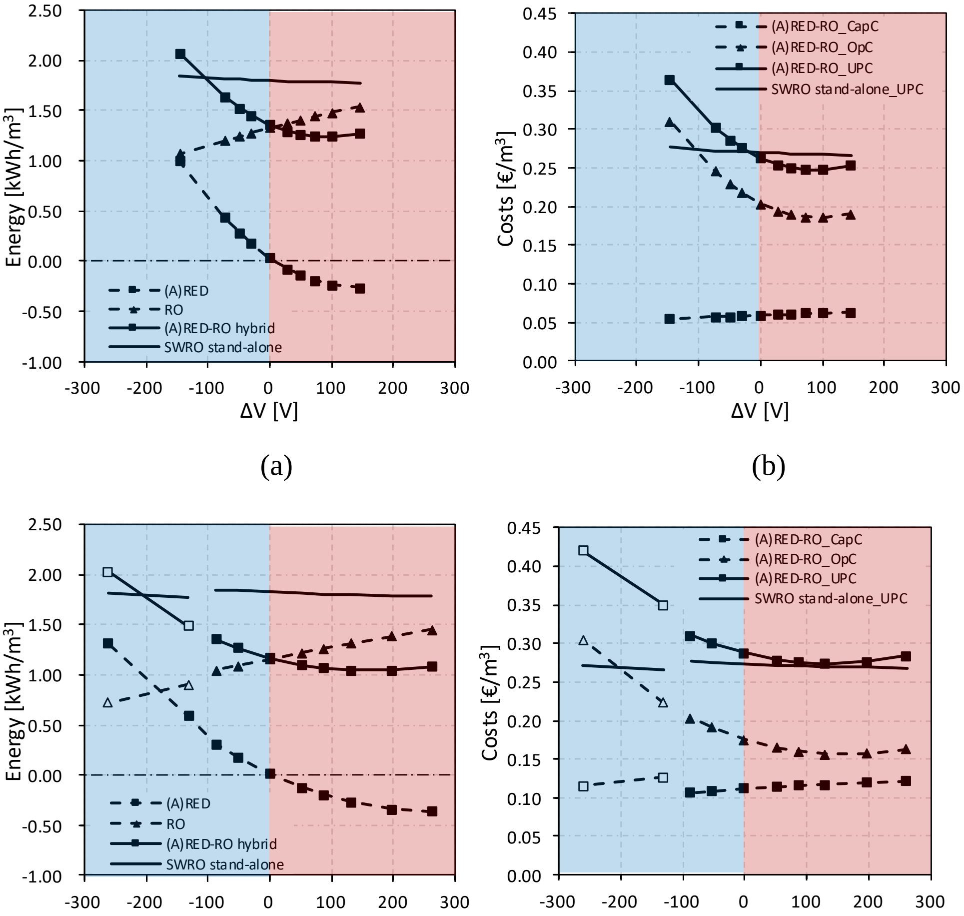

(a) (b)

(c) (d)

Figure 105. Trends of the energy consumption (positive) or production (negative) per unit volume of permeate produced (left column) and costs (right column) comparison as a function of the external voltage. Graphs (a) and (b) are for the Case_A and graphs (c) and (d) are for the Case_B. In Case_B, for two values of the external voltage in the ARED process, the BW30HR-440i RO module was used (empty symbols). Positive voltages are for RED; ΔV=0 is the short-circuit RED; negative voltages are for ARED. These results were obtained in the reference scenario.

The values of total energy consumption are directly reflected in the lower operating costs *OpC*, as shown in graphs (b) and (d) of Figure 105. However, the capital costs *CapC* (assumed proportional to the installed IEM area) make the total costs go up. Note that the slight increase of the *CapC* as the voltage increases, is due to the lower flow rate of permeate produced.

Looking at the final unit product cost *UPC*, the range of external voltage where the hybrid system is more cost effective (UPC_{hybrid} equal or lower than the UPC_{SWRO}) is narrower than the range in which an energy saving is obtained. In Case_B, even if the *OpC* is lower than in Case_A, the *CapC* contribution is responsible for a UPC_{hybrid} always higher than the UPC_{SWRO}, making this case not competitive.

The competitiveness of the two cases with respect to the stand-alone SWRO, can be easily highlighted by using the cost saving *CS* coefficient (Eq. (95)) reported in Figure 106 as a function of the external voltage. For any absolute value of the voltage, the RED-RO coupling is cheaper than the ARED-RO one, thanks to the energy produced by the RED process, along with the energy saved in the following RO step.

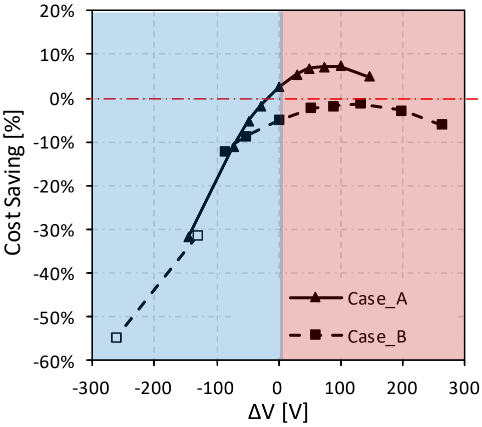

Figure 106. Trend of the Cost Saving of the (A)RED-RO hybrid system as a function of the external voltage. In Case_B, for two values of the external voltage in the ARED process, the BW30HR-440i RO module was used (empty symbols). Positive voltages are for RED; $\Delta V=0$ is the short-circuit RED; negative voltages are for ARED. These results were obtained in the reference cost scenario.

The cost saving exhibits a maximum under the RED process at an intermediate condition between the maximum power and the short-circuit ($\Delta V = \Delta V^*/2$) which corresponds to the minimum energy consumption in the hybrid system. In this voltage range, the electromembrane plant configuration of Case_A provides higher cost savings due to the lower *CapC*. Under the conditions simulated and the reference cost scenario, the maximum cost reduction is ~7.5% (with respect to the stand-alone SWRO process). As observed above in discussing Figure 105, Case_B is not competitive with respect to Case_A because, in a wide range of voltages, it produces or consumes almost the same power than Case_A (Figure 103a) but with a double required membrane area, so that the related *CapC* gives a heavy contribution to the final unit product cost *UPC*.

Basically, combinations of operating conditions leading to RO feed concentrations below 15 g/l, for which a single-pass treatment with BWRO modules was assumed, turn out to perform worse than stand-alone SWRO. Of course, the performance would be even worse if a multi-pass treatment were adopted. For the same reason, it is unnecessary to investigate the possible effects of a more drastic pre-desalting treatment, e.g. by multi-stage ED or (A)RED.

The cost saving may significantly change with the cost of energy and of (A)RED plant. Figure 107 reports the results relevant to the eight different cost scenarios (declared in Table 18) for Case_A only.

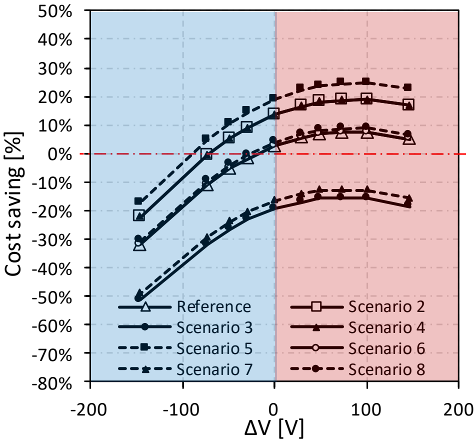

Figure 107. Trend of the Cost Saving as a function of the external voltage for eight costs scenarios. Positive voltages are for RED; ΔV=0 is the short-circuit RED; negative voltages are for ARED. These results were obtained for Case_A.

In scenario 5, with low (A)RED plant cost and high energy cost, the highest values of cost saving are obtained, with a maximum of ~25%, and positive values of *CS* in almost the whole range of voltage. Scenarios 2 and 4 give the same results and provide cost saving values slightly lower than scenario 5. The reference scenario but also scenarios 6 and 8, in which the costs are for both (A)RED plant and energy the highest and lowest respectively, still provide positive cost saving values but in a narrower range of voltage. In these cases, the maximum cost saving is ~7.5%. Cases in which the energy cost decreases but the (A)RED plant cost is kept as in the reference scenario, or also the cases in which the (A)RED plant cost increases and the reference energy cost is kept constant, as in scenarios 3 and 7, favour the competitiveness of the stand-alone SWRO desalination for any voltage applied.

4.4 Results and Discussion: ED-RO

In the case of the ED-RO hybrid system, the pre-desalting is achieved by applying ED to the feed seawater, thus removing some of the salt before the stream enters the RO unit. Power required and electrical currents for this case are reported in Figure 108a, while the salt concentration of the pre-desalted stream is reported in Figure 108b, both as a function of the external voltage. As the applied voltage increases, the electrical current increases, thus boosting the pre-desalting, achieving a minimum concentration of ~9 g/l NaCl.

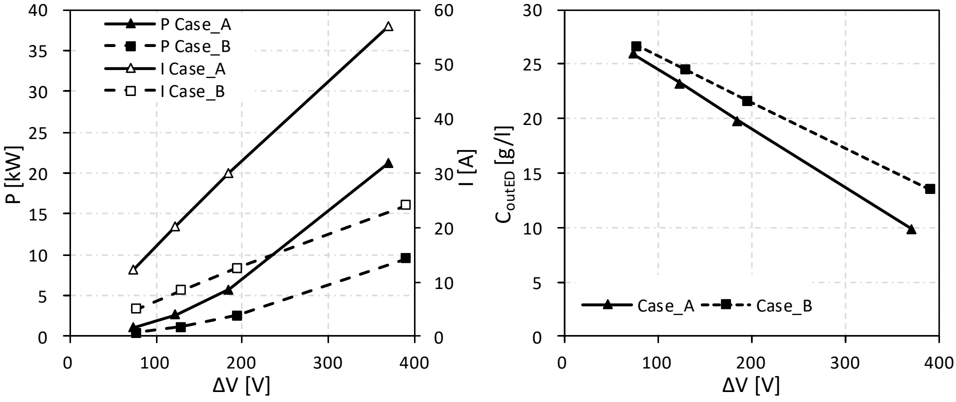

(a) (b)

Figure 108. Plots of (a) power and current, (b) outlet concentration of pre-desalted stream from the ED process as a function of the external voltage.

As in the case of the ARED treatment, Case_A and Case_B differ only due to the effect of non-ideal phenomena, such as water flux and salt flux through the IEMs. However, in ED these fluxes reduce the current efficiency and, thus, pre-desalting effect. Since the amount of water and salt transported by osmosis and diffusion, respectively, is larger when the residence time is higher, the plant of Case_B attains a lower level of pre-desalting compared to Case_A. With the values of voltage chosen for the simulations (Table 17), the concentration at the outlet of ED falls in a range similar to that of the (A)RED pre-treatment (Figure 103b). When the highest values of voltage (*ΔV* = *ΔV***≈ 370-390 V, corresponding to a current density equal to 90% of the limiting one) are simulated, the low concentrations attained by ED require the use of brackish water RO module.

Figure 109 reports the feed pressure in RO (a), the outlet permeate concentration (b) and the permeate flow rate (c) obtained by the different schemes (both stand-alone SWRO and ED-RO) as a function of the external voltage. The pressure required in the RO step of the hybrid system varies from ~37 bar to ~17 bar, while pressures higher than 50 bar are needed in the stand-alone SWRO.

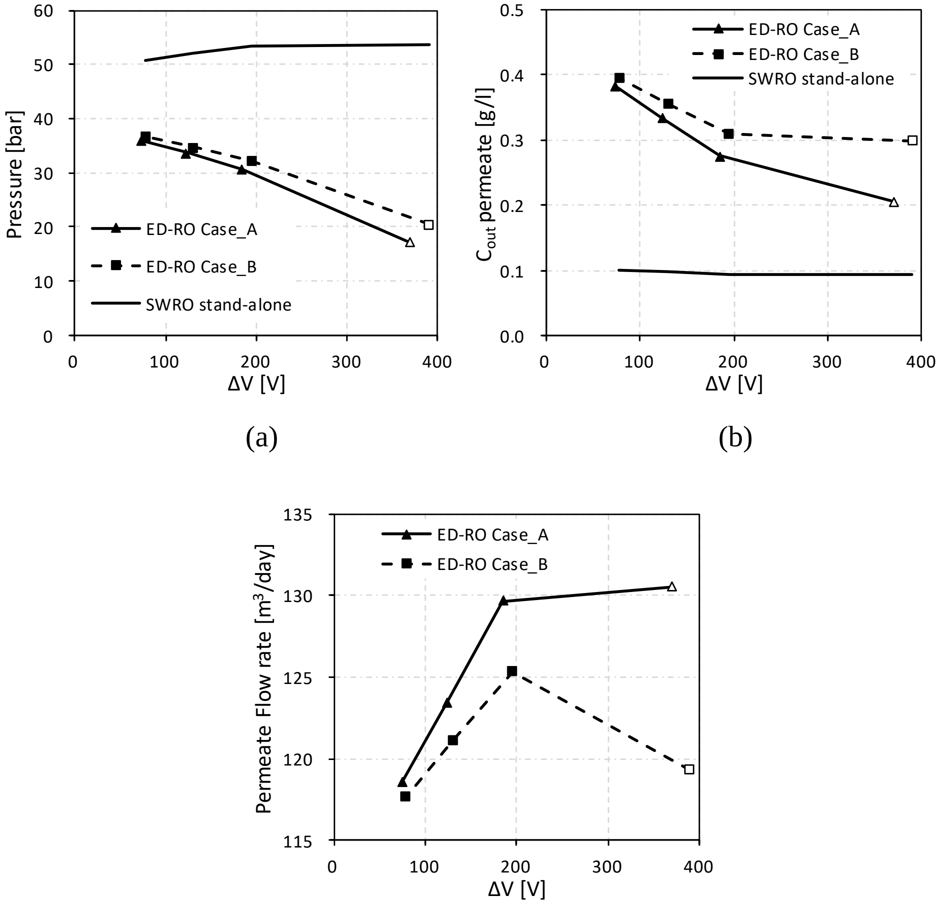

(a)

(b)

(c)

Figure 109. Plots of (a) feed pressure in RO, (b) outlet permeate concentration and (c) permeate flow rate for the ED-RO integrated process and for the stand-alone SWRO as a function of the external voltage. For the highest voltage applied in the ED process, the BW30HR-440i RO module was used

(empty symbols). The permeate flow rates for the stand-alone SWRO are not reported as they coincide with each single case.

Under the assumption of equal permeate flow rate, the salt concentration in the permeate is almost constant for stand-alone SWRO at 0.1 g/l NaCl and is higher in the case of the ED-RO coupling. This concentration decreases as the voltage increases, and also the flow rate increases. However, in Case_B and at the highest voltage simulated, i.e. $\Delta V = \Delta V^{**}$, these trends are inverted, due to the different performance of the brackish water RO module. The permeate concentration varies from ~0.39 to ~0.21 g/l NaCl. The range of the permeate flow rate is narrower than in the (A)RED-RO coupling (~119-131 m^3/day against 120-140 m^3/day, see Figure 104 for comparison). The overall water recovery is also lower, ranging from 34% to 36%.

Details on specific energy consumptions and costs of the ED-RO desalination process are shown in Figure 110.

The energy consumed by the stand-alone SWRO treatment is ~1.75 kWh/m^3 while that consumed by the ED-RO scheme is equal or larger and increases as the voltage increases. As a matter of fact, the energy demand of the ED pre-treatment exceeds the energy saving in the following RO stage, and this occurs at a larger extent as the voltage increases. Translating these results in terms of *OpC* and calculating *CapC* (~0.06 €/m^3 and ~0.12 €/m^3 for Case_A and Case_B respectively), it follows that the total costs considered for the ED-RO process are higher than for the stand-alone SWRO.

These results can be also expressed in terms of cost saving which assumes high negative values as reported in Figure 111. This means that the conditions simulated (plant configuration and operating conditions) are not favourable for the ED-RO coupled scheme in the reference cost scenario, while the stand-alone SWRO and (A)RED-RO (Figure 106) are economically better choices.

Of course, the same remarks made in Section 4.3, concerning the adoption of a multi-stage treatment in (A)RED-BWRO apply also to the present condition of ED-RO.

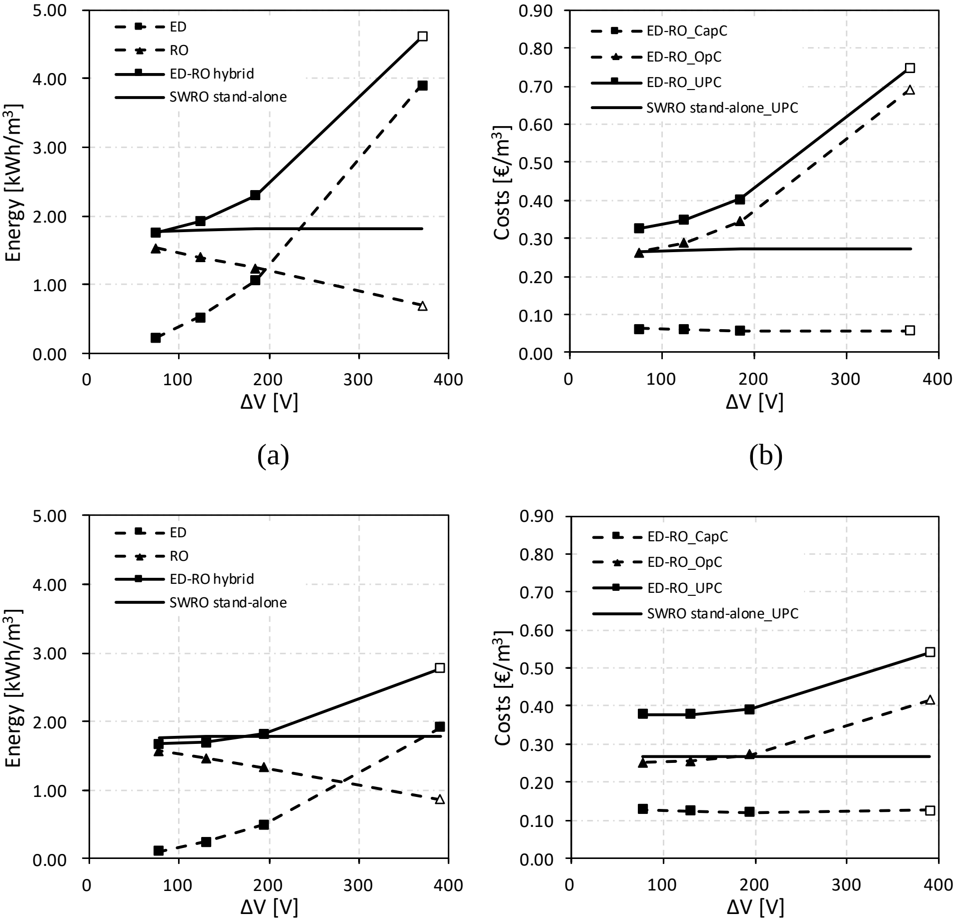

(a) (b)

(c) (d)

Figure 110. Trends of the energy consumption per unit volume of permeate produced (left column) and costs (right column) comparison as a function of the external voltage. Graphs (a) and (b) are for the Case_A and graphs (c) and (d) are for the Case_B. For the highest voltage applied in the ED process, the BW30HR-440i RO module was used (empty symbols). These results were obtained in the reference scenario.

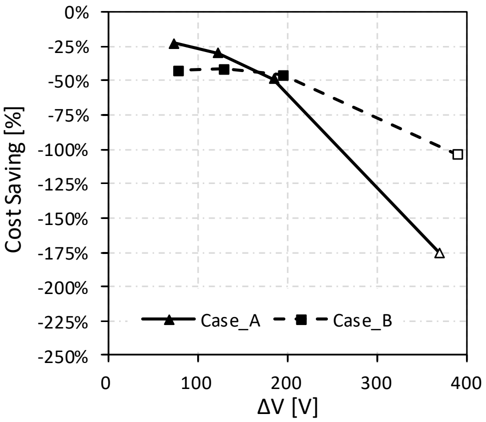

Figure 111. Trend of the Cost Saving of the ED-RO hybrid system as a function of the external voltage. For the highest external voltage in the ED process, the BW30HR-440i RO module was used (empty symbols). These results were obtained in the reference cost scenario.

In Figure 111, it can be also observed that up to a voltage of ~180 V (ΔV**/2) the operation by the plant with less cell pairs, i.e. Case_A, is less expensive, while the opposite occurs at higher voltages. At high voltages, the *UPC* in Case_A is heavily affected by the high *OpC* which decreases rapidly when the voltage decreases. In Case_B, the energy consumption and also the *OpC* are less influenced by the voltage and so at low voltages, the *UPC* is affected by the high *CapC*, which is twice the one of Case_A. For these reason, at low voltages, Case_A shows a cost saving higher than Case_B.

The comparison of eight different cost scenarios is reported in Figure 112 for Case_A. Even in the most optimistic cost scenario associated to a reduced price of ED plant and an increased cost of energy (Scenario 5, Table 18), ED-RO coupling is not economically competitive, despite the cost saving is improved (but still negative).

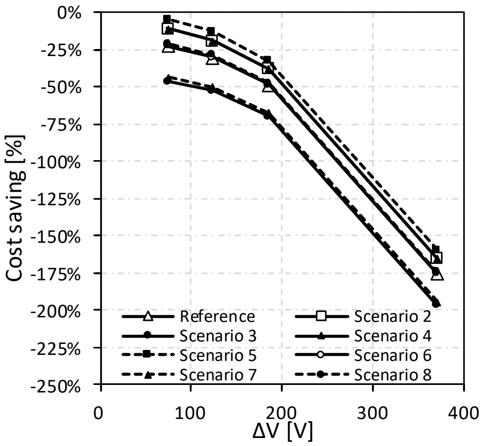

Figure 112. Trend of the Cost Saving as a function of the external voltage for eight costs scenarios. For the highest voltage applied in the ED process, the BW30HR-440i RO module was used (empty symbols). These results were obtained for Case_A.

This behaviour makes the ED-RO process much less interesting than (A)RED-RO, which instead can reduce the desalination cost with respect to the stand-alone SWRO. On the other hand, if the cost of energy was lower or the ED plant cost was higher (pessimistic scenarios 3 and 7), the ED-RO would be even more expensive.

4.5 High performing IEMs

In the previous analysis, the effect of the RED/ED plant cost (proportional to the membrane area) on the cost saving, i.e. on the competitiveness with respect to the stand-alone SWRO was investigated. In this section, the effect of using high performing IEMs on the system performances was studied. In regard to possible membrane properties improvements, the commercial Fujifilm Type 10 membranes considered in this thesis (Table 7) have already a very high permselectivity but they still have a fairly high electric resistance. Considering that the literature reports about membranes with resistances well below 1 Ω cm^2 [226], in order to do a perspective analysis, “high performing” IEMs with electrical resistance equal to a quarter of that of the Fujifilm Type 10 membranes were considered (Table 7) [231].

Figure 113a and Figure 113b report the cost saving obtained with the Fujifilm Type 10 membranes and with the high performing IEMs for the (A)RED-RO and the ED-RO hybrid systems respectively. These results were obtained considering only the configuration plant of Case_A, in the reference and best (RED/ED plant cost of 10 €/m^2, energy cost of 0.3 €/kWh) cost scenarios. Considering the reference cost scenario (black curves), in the (A)RED-RO hybrid system with high performing IEMs, the maximum cost saving is attained at an external voltage value closer to the short-circuit condition and is of ~16%, i.e. twice the value obtained with Fujifilm Type 10 membranes. It can be also observed that the cost saving with high performing IEMs is not always higher than with Fujifilm Type 10 membranes (Figure 113a) due to the RO stage performance: in ARED conditions at high voltages ($\Delta V = -\Delta V^*/2 \approx -65$ V and $\Delta V = -\Delta V^* \approx -130$ V), the cost saving sharply decreases because of the low performance of the BW30HR-440i module that needs to be coupled with the ARED plant when concentrations lower than 15 g/l NaCl are achieved.

When high performing IEMs are adopted in the ED-RO hybrid system (Figure 113b), a slight increase in the cost saving can be observed, but it always has negative values. It can therefore be noted that, despite the best performance of the membranes, the ED-RO system remains uncompetitive with respect to the stand-alone SWRO. Finally, looking at the best cost scenarios (red curves), further advantages are recorded for the (A)RED-RO case with high performing IEMs, with a maximum cost saving of ~33%, while in the ED-RO case a nil cost saving is obtained at low voltages.

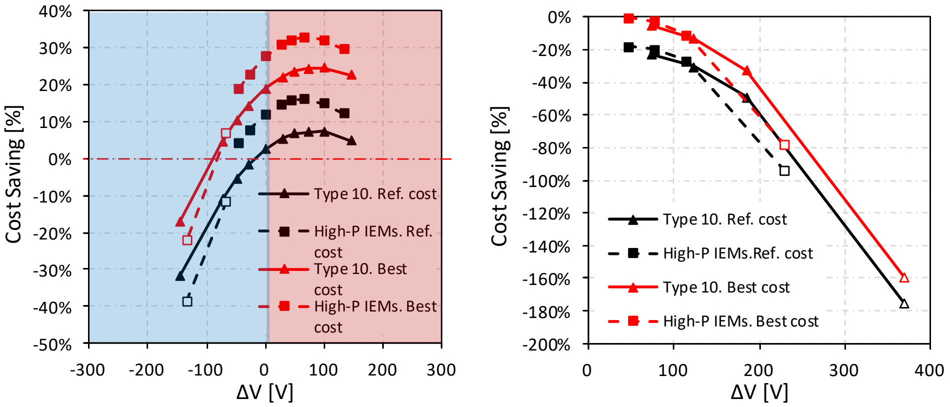

(a) (b)

Figure 113. Influence of using reference Fujifilm Type 10 IEMs or high performing IEMs on the cost saving of the (A)RED_RO (a) and of the ED-RO (b) hybrid systems as a function of the external voltage. The empty symbols refer to cases in which the BW30HR-440i module was used. These results were obtained for Case_A, in the reference (black curves) and best (red curves) cost scenarios.

Conclusions

Following the structure of the thesis, the main conclusions will be reported below for each of the three Parts of this work.

Part II – CFD in membrane processes

The Unit Cell approach adopted in all simulations was reported. Several experimental and computational studies have shown that fully developed conditions are usually attained within a few cells from the inlet, so that the relatively cheap unit cell approach is amply sufficient for comparative studies and preliminary design purposes, while the more demanding developing flow approach should be adopted only when entry or side-end effects are specifically addressed.

A number of issues arising in the study of fluid flow and heat/mass transfer in membrane processes involving flat, spacer-filled, channels (either plane or spirally wound) were clarified. In regard to the choice of the scales for data reduction and for the definition of dimensionless numbers, this remains, of course, a matter of subjective preference, but the use of the hydraulic diameter of the “void” channel, $2H$, as the length scale and of the corresponding “void” velocity, u_{void}, as the velocity scale offers definite advantages. In particular, it allows a more correct performance comparison between different spacers (including the “null” case of a spacerless channel), whereas other choices of scales, e.g. the hydraulic diameter of the spacer-filled channel d_h and the “interstitial” velocity u_m, may yield misleading results.

In regard to the definition of local heat or mass transfer coefficients, the definition based on the local heat / mass flux and on the difference between the local temperature or concentration at the wall and the corresponding bulk values remains the most commonly adopted. However, these quantities may become singular or negative at some points of the wall in complex geometries. For this and other reasons, the definition of the average coefficients as surface averages (definition 1) should be avoided, and the alternative averages $h^{(2)} = \{q''_w\}/(T_b - \{T_w\})$; $k^{(2)} = \{j_w\}/(C_b - \{C_w\})$ (definition 2), which do not suffer from singularities, are preferable both in computational and in experimental work.

In regard to the comparison between one-side and two-side heat or mass transfer, this choice has a dramatic impact on the corresponding coefficients: these may be up to 30% higher in a two-side configuration, yielding correspondingly higher heat or mass fluxes per unit membrane area. Experimental or computational results obtained for one-side transfer should not be extended to two-side transfer, because not only the values of the average Nusselt / Sherwood numbers, but also their dependence on Re and other parameters, may differ significantly, and the relative performance ranking of different configurations may be altered.

In regard to the choice of temperature or concentration boundary conditions at the walls representing the fluid-membrane interfaces in CFD simulations, it was shown that it may have a significant impact on the computed Nusselt or Sherwood numbers, especially in laminar flow. Therefore, experimental data ought to be compared only with CFD results based on a realistic description of the actual boundary conditions, rather than with idealized cases based on uniform temperature / concentration (Dirichlet) or uniform heat / mass flux (Neumann) conditions. For design purposes, it is preferable to use convection coefficients based on generalized (Robin) boundary conditions with realistic values of the heat / mass transfer resistance at the wall.

In regard to the complex dependence of heat / mass transfer and pressure drop upon the physical and geometrical parameters that characterize the spacer-filled channels, an analysis was presented for overlapped spacers with orthogonal filaments. The Nusselt and Sherwood number $\mathrm{Nu}^{(2)}$ and $\mathrm{Sh}^{(2)}$ on either side varied in a complex way with the Reynolds number, exhibiting in some cases a *plateau* in an interval of Re (for example, this was between Re≈100 and Re≈300 for l/H=2.5 and γ=20°); the friction coefficient f decreased monotonically with Re but did not follow a simple power-law dependence. When the spacer aspect ratio l/H was made to vary, for sufficiently high Reynolds number $\mathrm{Nu}^{(2)}$ and $\mathrm{Sh}^{(2)}$ exhibited a maximum at some value of l/H depending on Re and γ (for example, the maximum was at l/H≈3.5 for Re=300 and γ=45°), while f decreased monotonically with l/H. Finally, $\mathrm{Nu}^{(2)}$ and $\mathrm{Sh}^{(2)}$ varied in a complex way with the flow attack angle, exhibiting in some cases multiple maxima and minima even in the basic interval γ=0-π/4; similar variations were also exhibited by the friction coefficient f. Notably, the three parameters Re, l/H and γ were found to interact heavily, making a separate-effect analysis impossible. For any optimization study seeking the maximum of some objective function as the parameters are made to vary in a wide range of values, interpolation from an adequately large database of Nusselt / Sherwood numbers and friction coefficients is probably to be preferred to the use of correlations which, instead, can be used if small variation ranges are considered.

Considering more in detail Membrane Distillation, other issues typical of this process were investigated. In regard to the influence of thermal conduction in the spacer, numerical simulations performed by including this phenomenon in the computational model showed that even low-conductivity polymeric spacers (λ_{spa}≈0.15 $Wm^{-1}K^{-1}$) may be responsible for up to 10% of the total heat transferred from the fluid to the membrane. Therefore, the comparison of experimental results with CFD simulations neglecting spacer conduction is questionable. Results also show that significant increments of heat flow would occur by using relatively high-conductivity spacers (e.g. λ_{spa}=2-10 $Wm^{-1}K^{-1}$), making this possibility at least worth investigating in detail.

In regard to turbulence, models suitable for low-Reynolds number turbulent flows of the kind expected in membrane distillation were identified. The attention was focussed on each model’s performance in terms of heat transfer, meaning both the distribution of the heat transfer coefficient h over a thermally active wall and the surface-averaged value $\{h\}$ of this quantity. Experimental h maps, obtained by Liquid Crystal Thermography in scale models of membrane distillation modules, were used as a benchmark. Computational results were obtained by using the unit cell approach in conjunction with alternative turbulence models. The comparison showed that, on the whole, both distributions and surface-averaged values $\{h\}$ were better predicted by ω-based models resolving the near-wall layer than by k-based models using wall functions, which, in most cases, gave either strong underpredictions or comparably strong overpredictions. Among ω-based models, the SST k-ω model provided the most satisfactory overall agreement of $\{h\}$ with experimental results in the range examined (max. 14% underprediction for moderate Re and γ=45°, max. 13% overprediction for high Re and γ=0° or 90°).

In regard to overall results of the Nusselt number, since in MD the main parameters can vary in a large range of values (especially Re) and it was also demonstrated that simple correlations cannot be obtained in this case due the complex influence of the parameters, a large database for overlapped spacers was built. Results were obtained for six values of l/H, in the whole range of γ and for Re up to ~2600.

Considering now phenomena related to electromembrane processes, CFD was used to simulate mass transfer, Ohmic resistances and electroconvection.

Results for the Sherwood number were reported for Re≤70 because this is the range of the highest interest for electromembrane processes. Overlapped spacers showed a large influence of the flow attack angle and a Sherwood number which did not monotonically increase with Re. Instead, this behaviour was observed with woven spacers, which provided very high values of Sh (up to ~300 at Re≈70). OCF profiled membranes showed a behaviour similar to the overlapped spacers but with higher Sh values (~50 at Re≈40 and γ=45° with respect to ~22 for overlapped spacers). Pillars profiled membranes, even at γ=45°, offer two different Sherwood values depending on whether the membrane side considered bears or not the protrusions. In this last case, a *plateau* was observed at Re>~35, with Sh attaining a constant value of about 16.

In all cases, correlations for Sh as a function of Re were obtained and were used in the model, presented in Part III, aimed at predicting concentration polarization phenomena.

CFD was also used to study the Ohmic behaviour of a cell pair provided either by spacer or by profiled membranes. Numerical simulations, in which the Laplace equation was solved, were performed assuming uniform conductivities for channels and membranes (function of the inlet diluate concentration). In the case of spacers, it was observed that the approximation of four electrical resistances (2 membranes, 2 channels) in series provides a good accuracy if the channel resistance (thickness divided by solution conductivity) is divided by the spacer porosity. In the case of profiled membranes, two approximated equations for the electrical resistance of the whole cell pair were proposed for OCF and pillars membranes, respectively. In all cases a fair accuracy was observed with a discrepancies not higher than ~14%.

The Nernst Planck-Poisson-Navier Stokes equations were numerically solved in 2-D and 3-D domains by a finite volume code to simulate electroconvection near an ion selective surface. An extremely fast dynamics was predicted, statistically stationary conditions being attained after a few ms. The main features of electroconvection were satisfactorily reproduced. The simulations were highly demanding, requiring very short time steps ($\Delta t \approx 10^{-8} \sim 10^{-7}$ s) and a very fine grid in the near-wall region ($\Delta y_{min} \approx 10^{-10} \sim 10^{-9}$ m) to resolve the electric double layer and the extended space charge region. 3-D test cases using ~3×10^6 grid points required ~two months of CPU time on a 128-core cluster to simulate 1 ms of real time.

In each simulation, performed to study heat or mass transfer, continuity and momentum equations were always solved. From their solution, the friction factor f was obtained and reported normalized by (96/Re), i.e. the friction factor of an empty channel (in laminar regime). It was observed that pillars profiled membranes provide the lowest enhance of pressure drops, with f only 2 times higher than in a spacerless channel. On the opposite, the highest pressure drops are observed for woven spacers, being f from 14 to 20 times higher than (96/Re). Overlapped spacers and OCF profiled membranes show similar results in the range of Re investigated.

Part III – Process modelling and characterisation of electromembrane systems

A quantitative appreciation of the relative importance of fluid dynamics-dependent quantities in affecting performance parameters (e.g. the maximum obtainable net power density in RED or the minimum energy consumption in ED) can only come from a proper coupling of CFD with a complete, albeit simple, model of electromembrane processes. This coupled strategy, based on combining the one-dimensional modelling of an electromembrane stack with a fully three-dimensional CFD modelling of the electrolyte channels, including complex configurations (spacers or profiled membranes), was presented. A unified model for three possible electromembrane processes (e.g. ED, RED and ARED) was presented and validated in all single operation mode.

In RED mode, results were compared with literature data obtained in laboratory-scale stacks and a satisfactory overall agreement was observed. Under the conditions considered for these comparisons (short stacks, low current densities and thin channels provided with spacers) the terms computed by finite-volume simulations (Sherwood numbers, friction coefficients) were found to play a relatively secondary role. However, the passage to long stacks of industrial interest (e.g. 1 m) will make an accurate estimate of friction coefficients crucial for the assessment of the net power density. Similarly, polarization losses in RED may become more important in the future, as membranes offering lower Ohmic resistances are developed.

The one-dimensional model was coupled with an optimization algorithm to determine the conditions, in RED mode, for maximum net power density (NPD) in the parameter space H^{CONC}, H^{DIL}, U^{CONC}, U^{DIL} for different combinations of the remaining (“scenario”) variables.

The optimum thickness of the concentrate channels was found to increase with the concentrate solution concentration and with the stack length, while being less sensitive to the dilute solution concentration. The optimum thickness of the diluate channels was found to decrease with the concentrate concentration while increasing with the diluate concentration and with the stack length. The optimum velocities both in the concentrate and in the diluate channels were found to increase markedly with the concentrate concentration and with the stack length and to exhibit a generally decreasing trend with the diluate concentration, with some local maxima for low values of this quantity (~10-20 mol/m^3). The optimum thickness of the concentrate channels was found to be from two to three times higher than that of the diluate channels, while the optimum velocity in the concentrate channels was found to be two-three times lower than that in the diluate ones. The resulting optimum NPD was found to increase monotonically with the concentrate concentration, to exhibit shallow maxima for diluate concentrations of 10-20 mol/m^3, and to decrease with the stack length.

Interestingly, in correspondence with maximum NPD conditions, the flow rates in the concentrate and in the diluate were found to be about the same under all conditions investigated, their ratio (concentrate/diluate) ranging from ~0.85 to ~1.3 in most cases.

The comparison of spacerless and spacer-filled channels showed that these latter do not significantly affect NPD, but cause drastic changes in the optimum values of the control parameters: namely, a strong increase in the optimum thickness of both concentrate and diluate channels, and a comparable decrease in the optimum velocities of both channels. The comparison of parallel- and counter-flow showed that in counter-flow the maximum NPD increases only slightly, but the optimum thicknesses and – to a lesser extent – the optimum flow velocities in both channels decrease significantly.

Needless to say, the above results were based on some, rather arbitrary, assumptions, the most relevant being the independence of membrane permselectivities upon the solution concentrations, the neglect of the possible effects of divalent ions and the modelling of off-channel pressure losses by means of constant hydraulic loss coefficients. In future works, these assumptions can be replaced by more realistic models. Another possible extension of this study would be the optimization of a suitable target function, combining net power density, net energy density and plant cost, rather than of the single quantity NPD.

The one-dimensional model in ED mode was compared with experimental results obtained in a cross-flow ED stack in different operating conditions. Firstly, from these experiments, in the case of different inlet concentration for dilute and concentrate solutions, the existence of a minimum value of current density required to desalinate a feed stream against a back-diffusion flux was observed. Interestingly, this critical current density does not depend on the fluid velocity, but depends on the concentration difference between the concentrate and the diluate.

The model was found in good agreement with experiments as long as the current density was below the limiting current density (LCD). In order to investigated the LCD appearance in ED and its dependence on operating conditions, stack configuration, and membrane properties, several experiments were carried out. From a first experimental campaign, performed with Type 10 membranes (Fujifilm B.V.) and 155 μm spacers (Deukum GmbH), it was observed that LCD is influenced by the solutions' velocities but also by both streams' concentrations: indeed, non-ideal phenomena such as diffusion and osmosis, which mainly depend on concentration in the concentrate, affects the diluate concentration and, consequently, also LCD.

A new method that can provide both the limiting current density (LCD) and the critical current density (CCD) was proposed. According to this method, both values are determined by plotting the current efficiency λ against the current density, where LCD is the current density at which the maximum λ occurs, while CCD corresponds to $\lambda=0$.

From these first results, an empirical correlation for LCD was obtained, provided LCD from each experiment according to the current efficiency method.

In order to study the effect of the channel thickness, experiments were performed with 280 μm spacers (Deukum GmbH), keeping the same membranes. For any given inlet velocity and concentration, maximum current efficiency and the corresponding LCD values were found both higher than in the case of 155 μm spacer. These results are not easily reconciled with the classic concentration polarization theory for the limiting current density, which predicts i_{lim} monotonically decreasing with H. However, they are consistent with other findings reported in the literature [209]. The LCD values obtained with a thicker spacer, were very well predicted by the proposed correlation obtained for a 155 μm spacer.

The effect of the membrane properties was experimentally investigated by testing Type 12 membranes (Fujifilm B.V.), which are characterized by a lower water permeability and a higher electrical resistance with respect to the Type 10. Spacers of 155 μm were adopted. In the same operating conditions, the LCD is reached at lower current densities in a stack with Type 12 membranes, compared to a stack with Type 10. It follows that the proposed LCD correlation was not able to fit these experimental results and a modified correlation, valid for Type 12 membranes, was reported. However, more investigations are needed to understand how each membrane property affects the LCD and to obtain a unique correlation, generically valid.

Finally, the effect of profiled membranes on ED stack performance and LCD appearance was investigated. OCF and pillars profiled membranes provided by Fujifilm B.V. were tested. Since the stack equipped with profiled membranes is not symmetric, the effect of the current direction was studied. An asymmetrical behaviour was observed, with higher LCD and better performance when, considering a cation exchange membrane, the current goes from the membrane bulk to the profile. In this configuration, experiments performed with pillars showed a higher desalination effect at low current but also a lower LCD with respect to a stack equipped with flat membranes and spacers. Better results, instead, were obtained with OCF profiled membranes which provide higher LCD values and lower energy consumptions compared to flat membranes and spacers.

Part IV – Process modelling and characterisation of advanced hybrid systems

A simulation tool for hybrid systems was presented: here the one-dimensional model for electromembrane processes is coupled with a lumped parameter model for Reverse Osmosis. The hybrid model was validated by comparison with experimental results obtained at the pilot prototype installed at Burriana (Spain) within the activities of the *REvivED water* EU project. Typical time dependent results of the experiments were reported and discussed. The average results were then compared with steady-state predictions of the hybrid model. A good agreement was observed with only an overestimation of the outlet conductivity by ~7% and the permeate flow rate by ~15%.

The performance and the costs savings of two coupled processes, (A)RED-RO ((assisted) reverse electrodialysis–reverse osmosis) and ED-RO (electrodialysis–reverse osmosis), were assessed by the validated simulation tool. A sensitivity analysis was performed by changing some design parameters and operating conditions, and considering different cost scenarios.

The (A)RED-RO requires an energy consumption lower than the stand-alone SWRO for a wide range of external voltage in the electromembrane pre-desalting step. A maximum cost saving of ~7.5% can be attained when (i) the external voltage is half that giving the maximum power and (ii) the RED cell pairs are less (2500 rather than 5000), thus reducing *CapC*, in the “reference” cost scenario. In an optimistic cost scenario with low RED/ED plant costs, proportional to the IEMs costs (10 €/m2), and high energy cost (0.3 €/kWh) the maximum cost saving can be enhanced to ~24.6%. Therefore, (A)RED-RO coupling is promising, especially in the perspective of a reduced cost of IEMs.

In ED-RO coupling, the energy consumption of the ED pre-treatment exceeds the energy saving of the following RO stage in most cases. Therefore, the cost saving values are negative in all cases (i.e. the cost of desalination by ED-RO is larger than SWRO). It follows that, under the conditions simulated here, ED-RO coupling is not as attractive as (A)RED-RO.

In a perspective analysis with high performing IEMs, the (A)RED-RO system allowed a doubled cost saving (~16%) compared to the reference cost scenario with Fujifilm Type 10 membranes. Even with high performing IEMs, the ED-RO system, despite an increase in the cost saving values, was not competitive with respect to the stand-alone SWRO.

Nevertheless, the optimization of plant and operating conditions, along with the IEMs cost abatement, leave room for improvement in the more competitive (A)RED-RO coupling and also ED-RO coupling. Moreover, other scenarios arising from different hybridization schemes can be devised. All this may open the way for the implementation of cost effective conceptual designs for novel systems of seawater desalination.

Appendix A: Analytical solutions in a plane channel

Although, in the present thesis, the attention is focused on complex, spacer-filled channels (which can only be studied by means of fully three-dimensional numerical simulations), in order to appreciate the influence of thermal boundary conditions on heat transfer it is instructive to consider a simpler, essentially one-dimensional, problem (plane Poiseuille flow) since it leads to ordinary differential equations which can be solved to a very high accuracy. The mathematical treatment and the results obtained can easily be adapted also to mass transfer with obvious changes.

Consider the steady, hydrodynamically and thermally fully developed flow of a constant-property fluid in a plane channel of half-thickness δ_c. Let x be the streamwise direction and y the cross stream one, with y=0 at the midplane, and let $u(y)$ be the velocity along x, U its average, $T(x, y)$ the temperature and $\lambda_f/(\rho\cdot c_p)$ the thermal diffusivity.

Consider first the case of symmetric two-side cooling, which can be characterized by a symmetry condition at the midplane and a general (3rd type) boundary conditions at one wall:

$$\left[\frac{\partial T}{\partial y}\right]_0 = 0; \quad -\lambda_f \left[\frac{\partial T}{\partial y}\right]_{\delta_c} = \frac{1}{r_T}\left[T(x,\delta_c) - T_\infty\right] \tag{A. 1}$$

T_∞ being a uniform external temperature and r_T an interposed thermal resistance. Let $\vartheta = T - T_\infty$ and

$$\vartheta_b = \frac{1}{2\delta\rho U}\int_{-\delta_c}^{\delta_c} \vartheta u dy \tag{A. 2}$$

its bulk value. The following dimensionless variables can be introduced

$$\eta \equiv \frac{y}{\delta_c}; \quad \xi \equiv \frac{x}{\delta_c}; \quad \tilde{u} \equiv \frac{u}{U}; \quad Pe_{\delta_c} \equiv \frac{\rho c_p U \delta_c}{\lambda_f} \tag{A. 3}$$

The Poiseuille velocity distribution and the energy balance equation can be written

$$\tilde{u} = \frac{3}{2}(1 - \eta^2) \tag{A. 4}$$

$$\frac{\partial^2 \vartheta}{\partial \eta^2} = Pe_{\delta_c} \tilde{u} \frac{\partial \vartheta}{\partial \xi} \tag{A. 5}$$

The assumption of thermally fully developed flow implies

$$\vartheta = \vartheta_b(x) \cdot \varphi(y) \tag{A. 6}$$

so that Eq. (A. 5) can be written

$$\frac{1}{\varphi \tilde{u}} \frac{\partial^2 \varphi}{\partial \eta^2} = Pe_{\delta_c} \frac{\partial \vartheta}{\partial \xi} \tag{A. 7}$$

Following the method of separation of variables, Eq. (A. 7) splits into the two distinct equations

$$\frac{1}{\varphi \tilde{u}} \frac{\partial^2 \varphi}{\partial \eta^2} = -B^2 \tag{A. 8}$$

$$Pe_{\delta_c} \frac{\partial \vartheta}{\partial \xi} = -B^2 \tag{A. 9}$$

in which the constant $-B^2$ must be negative because, for example, $\vartheta_b>0$ implies $d\vartheta_b /d\xi < 0$ (cooled fluid). By substituting the velocity profile of Eq. (A. 4) into Eq. (A. 8) one obtains

$$\frac{d^2 \varphi}{d \eta^2} + \frac{3}{2} B^2 (1 - \eta^2) \varphi = 0 \tag{A. 10}$$

This is a non-integrable ODE with non-constant coefficients which can easily be solved numerically. The boundary conditions for φ are derived from Eqs. (A. 4) and (A. 6):

$$\left[\frac{\partial \varphi}{\partial \eta}\right]_0 = 0; \quad \varphi(1) = B^2 R_T \tag{A. 11}$$

in which $R_T=r_T\lambda_f/\delta_c$ (dimensionless thermal resistance). The following condition must also be satisfied:

$$\left[\frac{\partial\varphi}{\partial\eta}\right]_1 = -B^2 \tag{A. 12}$$

which is derived from the enthalpy balance:

$$-\lambda\left[\frac{\partial\vartheta}{\partial y}\right]_{\delta_c} = -\delta_c\rho c_p U\frac{d\vartheta_b}{dx} \tag{A. 13}$$

Conceptually, Eq. (A. 10) for $\varphi(\eta)$, with B.C.'s (A. 11), must be solved numerically for each generic B^2, and B^2 has to be varied so as to satisfy Eq. (A. 12). A simple iterative procedure was implemented in Fortran to perform this calculation. After convergence, the heat transfer coefficient is

$$h = \frac{q_w^{"}}{\vartheta_b} = -\frac{\lambda_f}{\delta_c\vartheta_b}\left[\frac{d\vartheta}{d\eta}\right]_\delta \tag{A. 14}$$

which can be made dimensionless as a Nusselt number Nu=h $(4\delta_c/\lambda_f)$ (based on the channel hydraulic diameter 4 δ_c). From the above equations and definitions, it follows that

$$Nu = \frac{4}{R_T}\frac{\varphi(1)}{1-\varphi(1)} \tag{A. 15}$$

Note that a different value of Nu and a different profile $\varphi(\eta)$ are computed for each choice of the dimensionless thermal resistance R_T. Note also that the Dirichlet and Neumann conditions are obtained as limiting cases for $R_T=0$ and $R_T\rightarrow\infty$, respectively. The function Nu(R_T) is represented in Figure A.1 by the “Two-side” line.

Consider now the case of one-side cooling, i.e. cooling from one wall with the opposite wall adiabatic. The thermal boundary conditions (A. 1) are replaced by

$$\left[\frac{\partial T}{\partial y}\right]_{-\delta_c} = 0;\quad -\lambda_f\left[\frac{\partial T}{\partial y}\right]_{\delta_c} = \frac{1}{r_T}\left[T(x,\delta_c) - T_\infty\right] \tag{A. 16}$$

and their dimensionless counterparts (A. 11) are replaced by

$$\left[\frac{\partial\varphi}{\partial\eta}\right]_{-1} = 0; \quad \varphi(1) = 2B^2R_T \tag{A. 17}$$

while all other equations and definitions remain unchanged. The solution for Nu is reported in Figure A.1 as the “One-side” line. Note the lower levels of Nu with respect to the “Two-side” case.

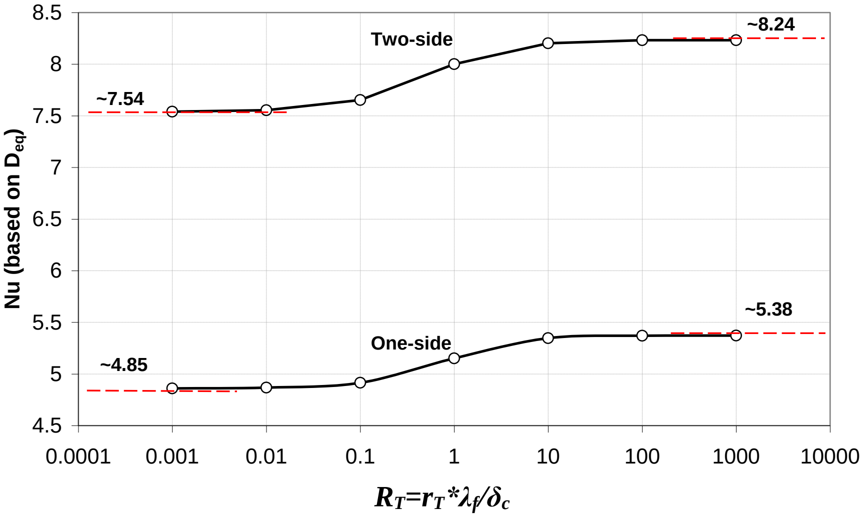

Figure A.1. Nusselt number in a plane channel as a function of the dimensionless thermal resistance R_T.

Appendix B: Experimental technique and results in MD

The measurement of wall temperatures was performed by Thermochromic Liquid Crystals (TLC). Their use is well documented in the scientific literature both for the measurement of surface temperature distributions [232–234] or for the joint visualization of flow and temperature fields [235,236]. Details of the test section and of the image processing procedure are described in [100,107], and only a short description of the experimental method will be provided here.

The test section, Figure B. 1, consisted of a hot and a cold channel whose outer walls were 20 mm thick Plexiglas® slabs, separated by a 1 mm thick transparent polycarbonate (PC) layer. Hot water was forced to flow through one of the channels, filled with the spacer to be tested whose thickness established the channel height H. A sheet of Hallcrest® thermochromic liquid crystals, ~0.12 mm thick, was interposed between the spacer and the polycarbonate layer, with its visible surface touching this latter; a very thin layer of transparent silicone grease was used to provide adhesion and thermal contact between the TLC sheet and the PC layer. Cold water was forced in parallel flow on the opposite side of the polycarbonate layer, i.e. within the cold channel, which was left void (i.e., without a spacer) and whose height was 3 mm.

Experimental tests were carried out in a scaled-up spacer-channel configuration characterized by H=1 cm, l=2 cm [100].

The TLC colour distribution was recorded by a digital camera through the outer wall of the cold channel, the cold water, the polycarbonate layer, and the transparent polyester foil which makes up most of the TLC sheet's thickness. Images, acquired in RAW format, were converted into TIFF and then split into HSV (Hue, Saturation, Value) components. Only the Hue component was used to extract the temperature distribution.

The thermochromic response of the TLC sheet was characterized by an in-situ calibration, performed by the isothermal method [100,107]. A 6th degree polynomial was used to fit the data within the experimentally investigated range.

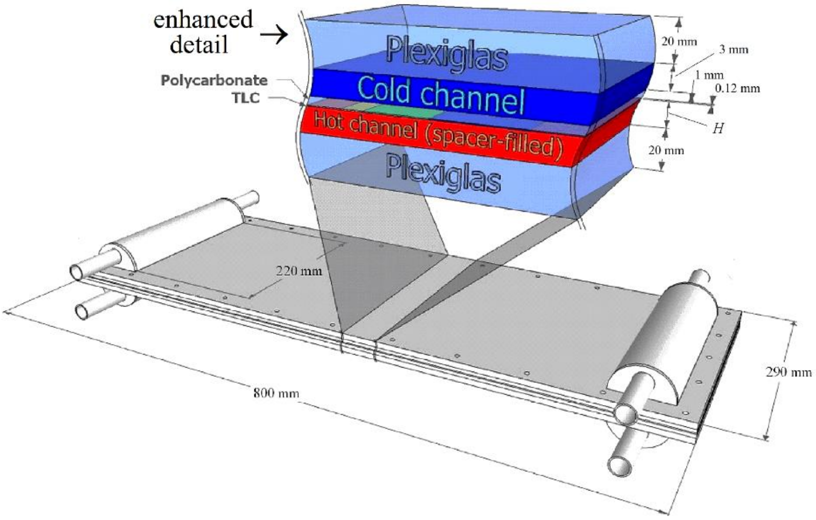

Figure B. 1. Representation of the test section with an enhanced detail of the different layers.

The temperature profile across the different layers of the test section is schematically shown in Figure B. 2. With reference to this sketch, an analysis of the heat transfer process under the assumption of one-dimensional transport gives the local hot-side heat transfer coefficient h as a function of the locally measured temperature T_w of the TLC sheet once the bulk temperatures T_b, T_c of the hot and cold fluids and the cold-side heat transfer coefficient h_c are known:

$$h = \frac{1}{r_T} \cdot \frac{T_w - T_c}{T_b - T_w} \qquad \text{(B. 1)}$$

in which r_T is an overall thermal resistance made up of the conductive thermal resistances s/λ_f of the thermochromic liquid crystal film (TLC) and of the polycarbonate layer (PC), in series with the convective thermal resistance $1/h_c$ associated with the cold channel:

$$r_T = \frac{s_{TLC}}{\lambda_{TLC}} + \frac{s_{PC}}{\lambda_{PC}} + \frac{1}{h_c} \qquad \text{(B. 2)}$$

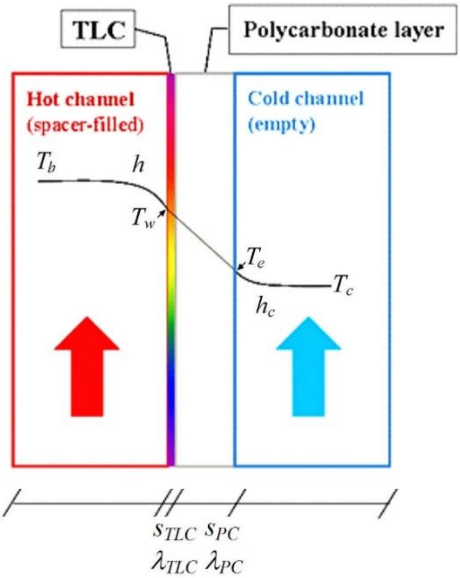

Figure B. 2. Sketch of the temperature profile across the test section.

T_b and T_c were measured by Pt100 RTDs at the inlet and outlet of the hot and cold channels and a linear variation of these quantities along the flow direction was assumed. The coefficient h_c was estimated by the Dittus-Bölter correlation ($\mathrm{Nu}=0.023\ \mathrm{Re}^{0.8}\ \mathrm{Pr}^{0.4}$) written for turbulent flow in the cold channel.

Liquid Crystal Thermography is mainly a whole-field temperature visualization technique; however, in several papers [100,107,232,233] it was demonstrated that, if properly calibrated and correctly applied, it can also provide quantitative measurements of heat transfer coefficients. Of course, a careful uncertainty analysis is necessary because the accuracy of experimental h values can affect the choice of turbulence models and wall functions [237].

For overlapped spacers with $l/H=2$, experimental results were obtained in the Reynolds number range 100~2000. The visual observation of the test section showed that the alternate pattern of hot and cold wall regions (as indicated by the TLC colour) remained steady only up to Re≈400. At higher Reynolds numbers, the TLC colour pattern exhibited time-dependent irregular oscillations with small amplitude and characteristic frequencies of a few Hz. Note that neither the amplitude nor the frequency of these irregularities are immediately related with the amplitude and frequency of turbulent temperature fluctuations proper, because of the damping role played by the thermal inertia of the TLC foil itself and of the polycarbonate sheet immediately in contact with it.

The images of a single unit cell were processed time-averaging the wall temperature distributions pertaining to 10 instants taken at intervals of about 10 s, long enough for the correlations between individual distributions to vanish. Results were found to be practically indistinguishable from those obtained by ensemble-averaging as explained above. Note that averaging will reduce the uncertainties discussed above, although a precise estimate of this reduction would require a knowledge of the relative contribution of random and systematic errors to the overall uncertainty.

Figure B. 3 reports experimental time-averaged distributions of the local heat transfer coefficient *h* on the top (thermally active) wall for the three orientations γ=0° (a), 45° (b) and 90° (c) and for moderate Reynolds numbers, ranging between ~600 and ~750. To the right of each graph the Reynolds number Re, the surface-averaged value of *h*, $\{h\}$, and the flow direction are shown. For readability, two different colour scales are used, one for γ=0° and one for γ=45° and 90°.

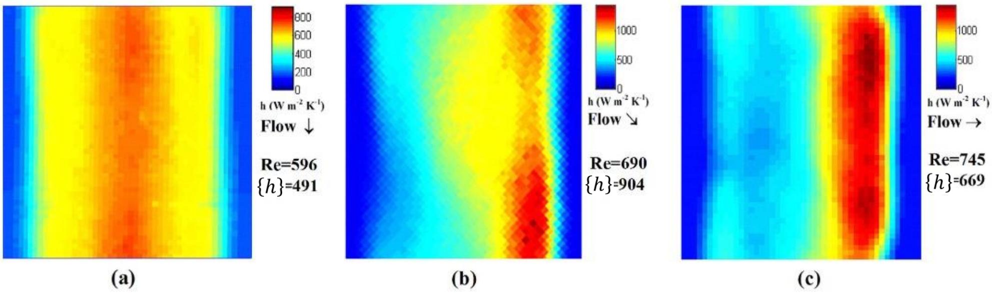

Figure B. 3. Experimental distribution of the local heat transfer coefficient h on the top (thermally active) wall for Re≈600-750 and different flow attack angles. (a) γ=0°, Re=596; (b) γ=45°, Re=690; (c) γ=90°, Re=745. The direction of the flow and the surface-averaged values of h, $\{h\}$, are reported.

The orientation γ=0° (a) yields the most uniform distribution of *h* but rather low values of this quantity. The orientation γ=90° (c) yields high values of *h* immediately upstream of each transverse rod, but low values downstream, and a surface-averaged value of *h* which is only slightly higher than that obtained for 0° (if the difference in Reynolds number is taken into account). The orientation γ=45° (b) provides the highest average *h* and a forward-skewed distribution similar to that observed for γ=90°.

Figure B. 4 reports corresponding distributions obtained for high Re (1820-1850). As in the lower Re cases, different colour scales are used. Remarks similar to the above ones apply. The highest values of $\{h\}$ are still provided by the orientation γ=45° (b). The orientation γ=90° (c) yields a marked spanwise non-uniformity in the distribution of *h*, with a relative minimum at the centre of the region located immediately upstream of the transverse rod.

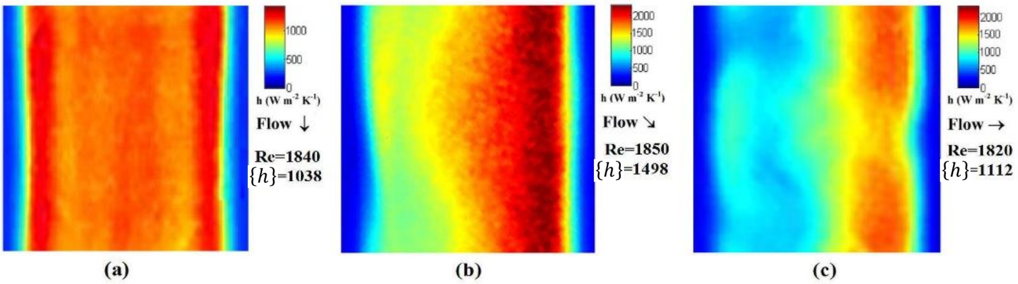

Figure B. 4. Experimental distribution of the local heat transfer coefficient h on the top (thermally active) wall for Re≈1820-1850 and different flow attack angles. (a) γ=0°, Re=1840; (b) γ=45°, Re=1850; (c) γ=90°, Re=1820. The direction of the flow and the surface-averaged values of h, {h}, are reported.

Appendix C: Database for overlapped spacers

Considering the overlapped spacer configuration with an intrinsic angle between the filaments α=90°, with non-conductive spacers and two-side heat transfer, the following results for the Nusselt number and the friction factor were obtained. A third type boundary condition was imposed at both top and bottom walls, with an external temperature T_{ext}=19°C and an external thermal resistance $r_{T,ext}=\delta_c/\lambda_f$ (i.e. according the notation in Appendix A, $R_T= r_{T,ext}\lambda_f/\delta_c=1$). No slip conditions were imposed at both walls and on the filaments' surface.

More than ~1300 simulations were performed considering the flow attack angle γ in the range 0°÷45° and six values for the ratio l/H (1.5; 2; 3.3; 4; 5; 6)

In all the simulations, the Reynolds number based on the friction velocity Re_τ was imposed from which the pressure gradient in the main flow direction was derived. The corresponding Reynolds number was then computed by the numerical solver. All the results were interpolated and plotted as function of the Reynolds number in the range 10÷2560. This range of course includes laminar and turbulent regimes. Laminar simulations were extended up to Re≈1000, while simulations with SST k-ω turbulence model were carried out starting from Re≈200, so that in the intermediate range Re=200-1000 results from both approaches were obtained. In principle, the SST k-ω turbulence model is capable of predicting laminar flow at low Re, so that the results should merge with the laminar ones. However, this does not always occur: in the overlap range, for example, the friction factor from SST k-ω is lower than that calculated by laminar simulations. A careful examination of the laminar results reveals that they exhibit fluctuations and unsteadiness above Re≈300, which can explain the higher values of the friction factor. Therefore, for Re>~300 the results of the SST k-ω turbulence model were considered, while laminar results were chosen for lower Re.

In the following figures (Figure C. 1 − Figure C. 6), one for each value of l/H, results of f, $\mathrm{Nu}^{(2)}_{\mathrm{inf}}$ and $\mathrm{Nu}^{(2)}_{\mathrm{sup}}$ are reported as functions of Re for different values of γ. For l/H=1.5 and l/H=2, the plot of the friction factor clearly shows the transition to turbulent regime with the typical jump reported in the Moody diagram in transitional flows. It is important to highlight that this transition occurs at Re well above the value (300) used as a threshold between laminar and SST results, and therefore it is not associated with the change in the model used.

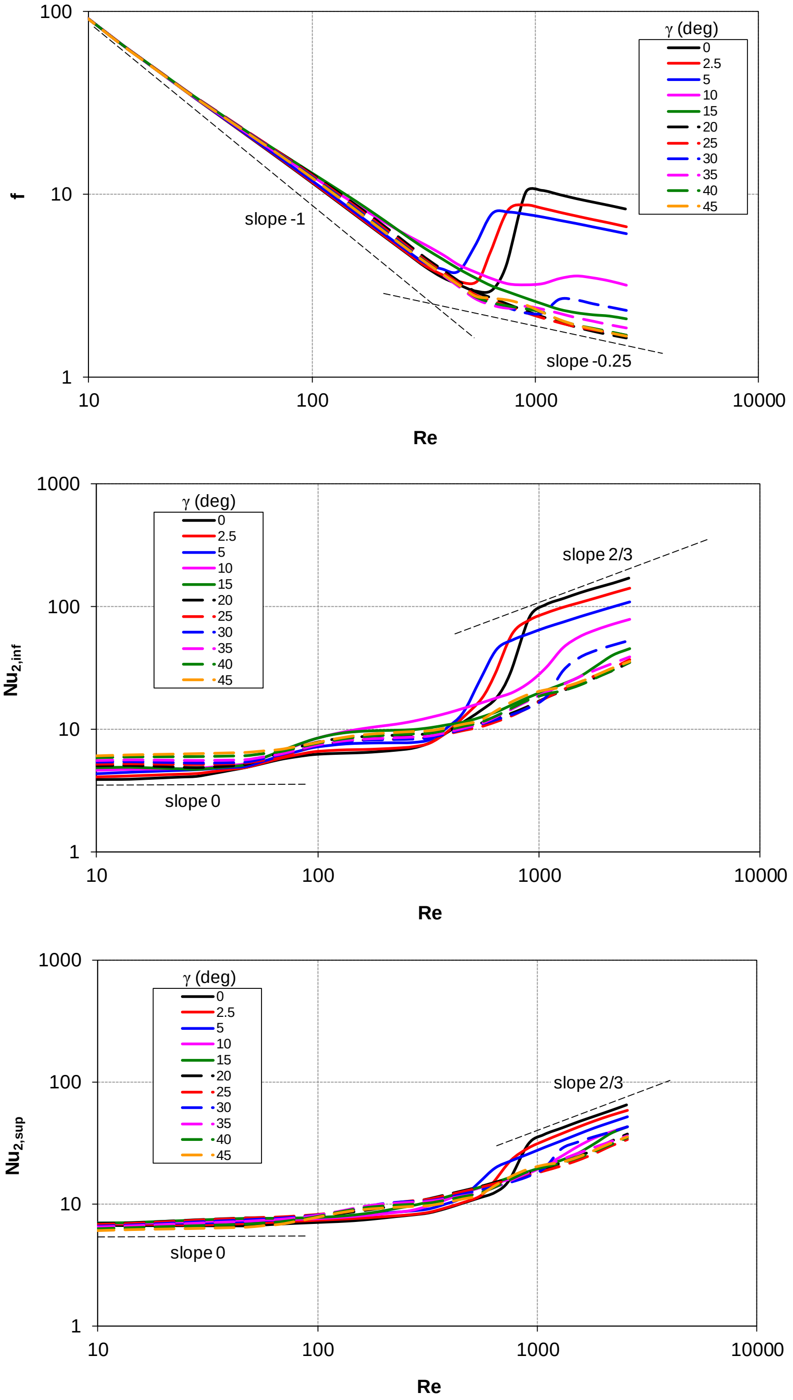

Figure C. 1. From the top: f, $Nu^{(2)}_{inf}$, $Nu^{(2)}_{sup}$. Results obtained for l/H=1.5, in the range of Re from 10 to 2560, and γ from 0° to 45°.

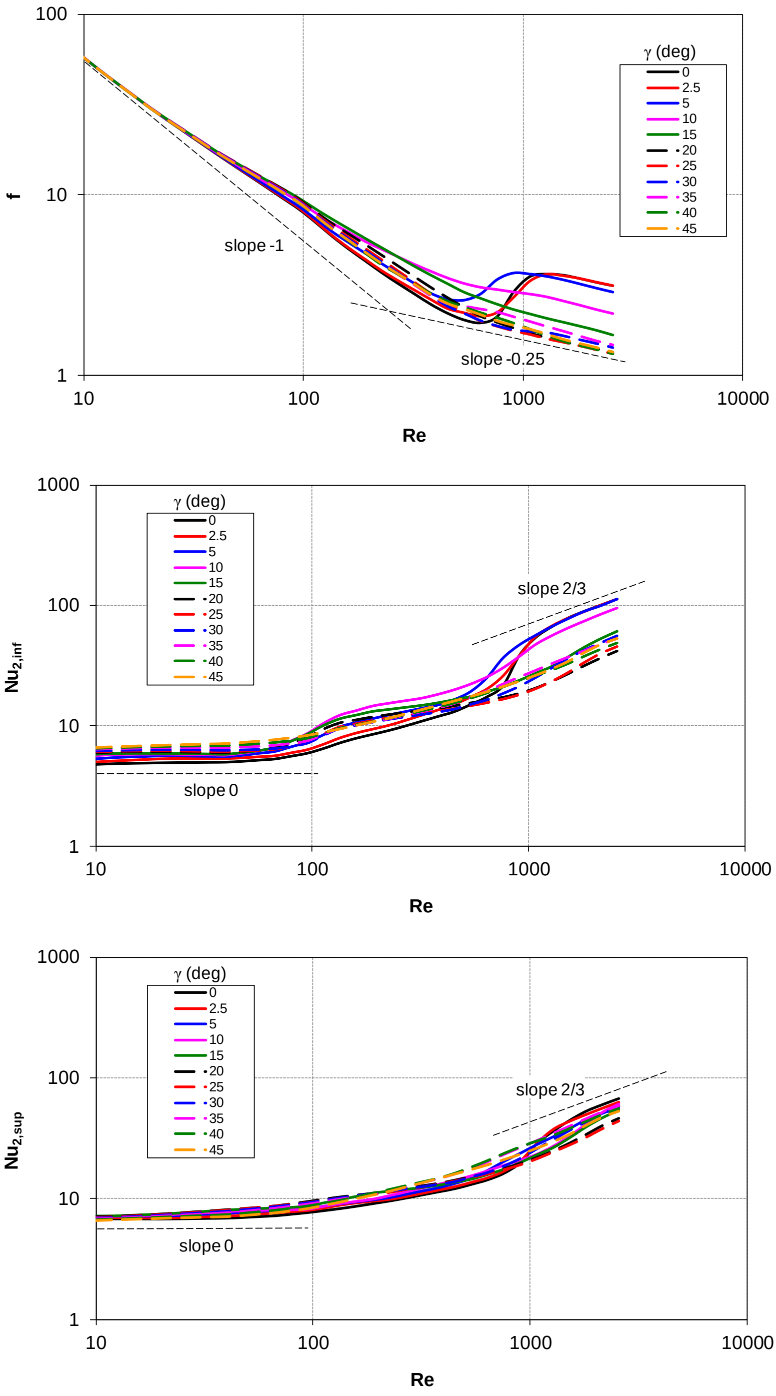

Figure C. 2. From the top: f, $Nu^{(2)}_{inf}$, $Nu^{(2)}_{sup}$. Results obtained for l/H=2, in the range of Re from 10 to 2560, and γ from 0° to 45°.

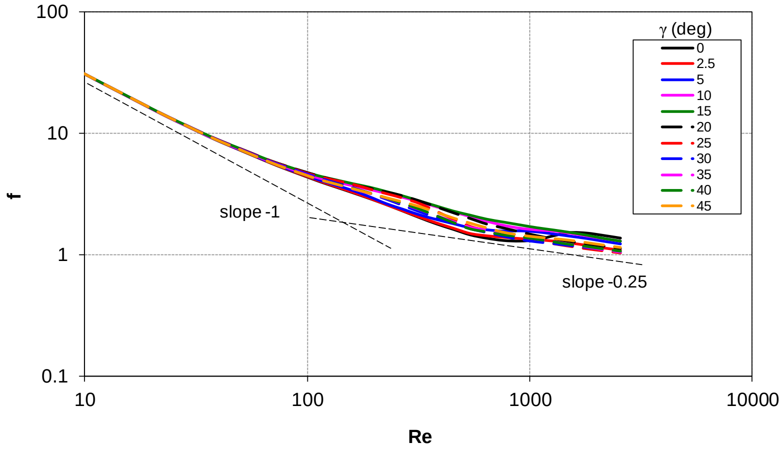

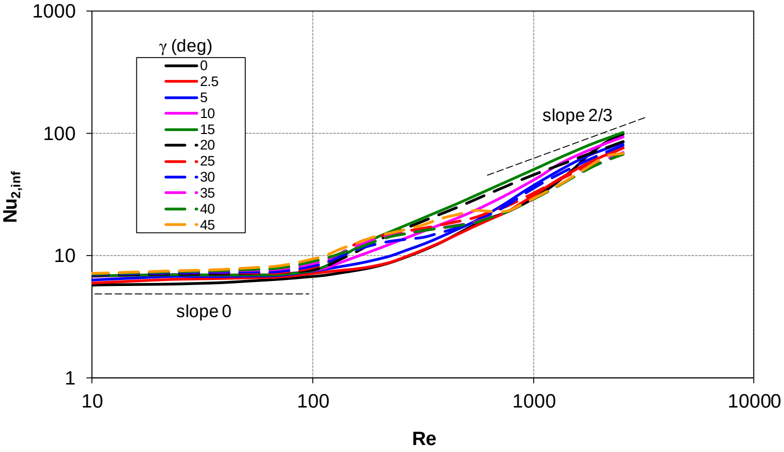

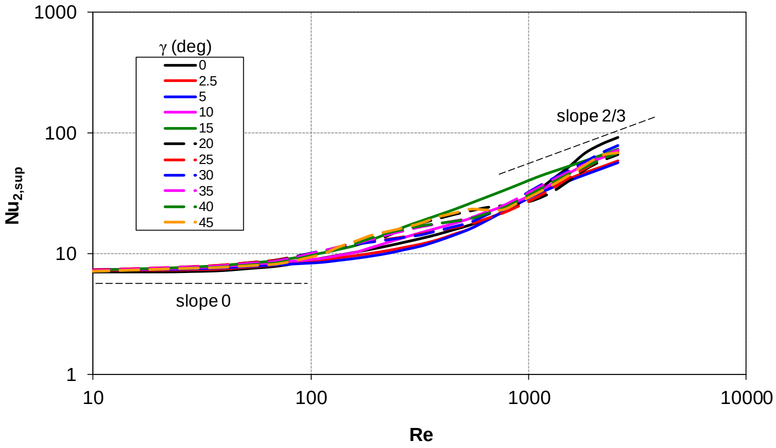

Figure C. 3. From the top: f, $Nu^{(2)}_{inf}$, $Nu^{(2)}_{sup}$. Results obtained for l/H=3.3, in the range of Re from 10 to 2560, and γ from 0° to 45°.

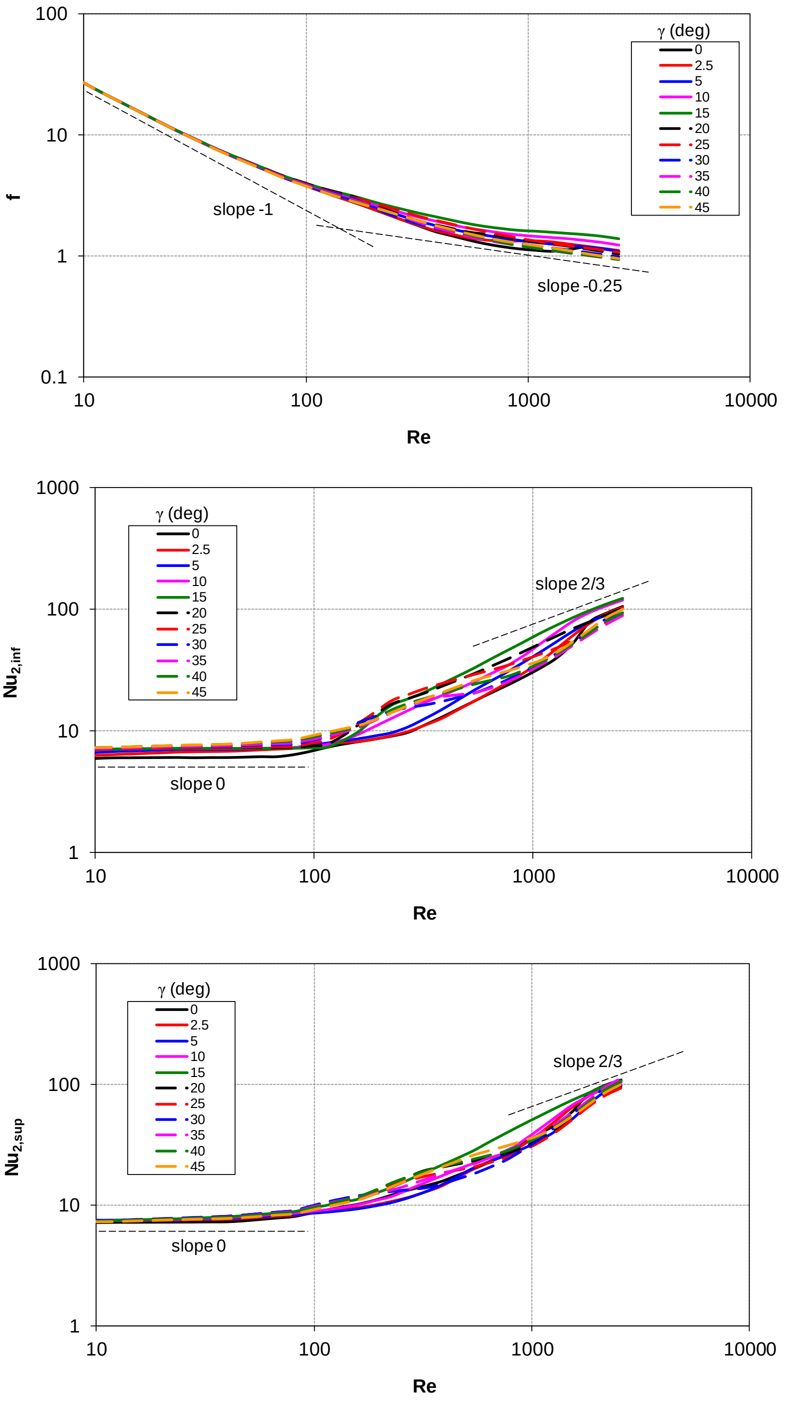

Figure C. 4. From the top: f, Nu$^{(2)}_{inf}$, Nu$^{(2)}_{sup}$. Results obtained for l/H=4, in the range of Re from 10 to 2560, and γ from 0° to 45°.

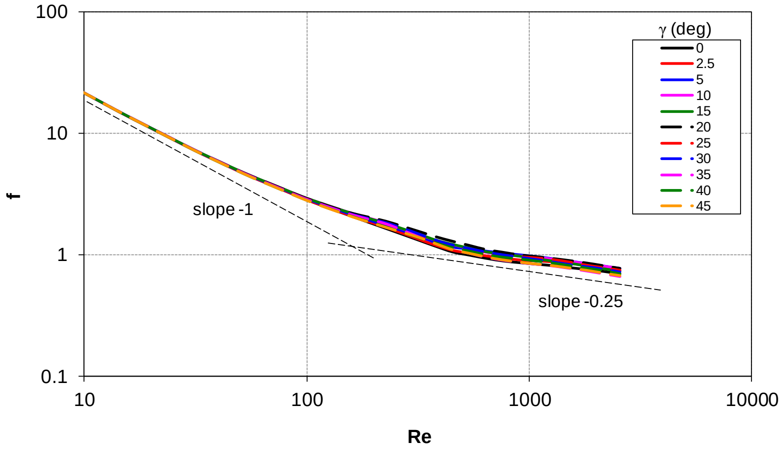

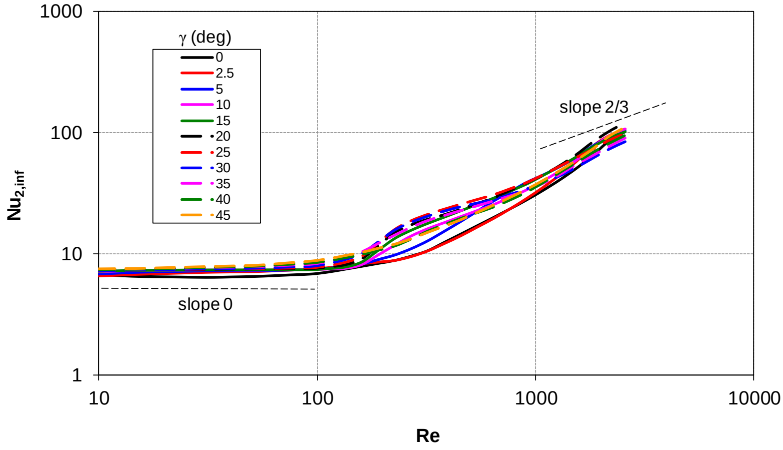

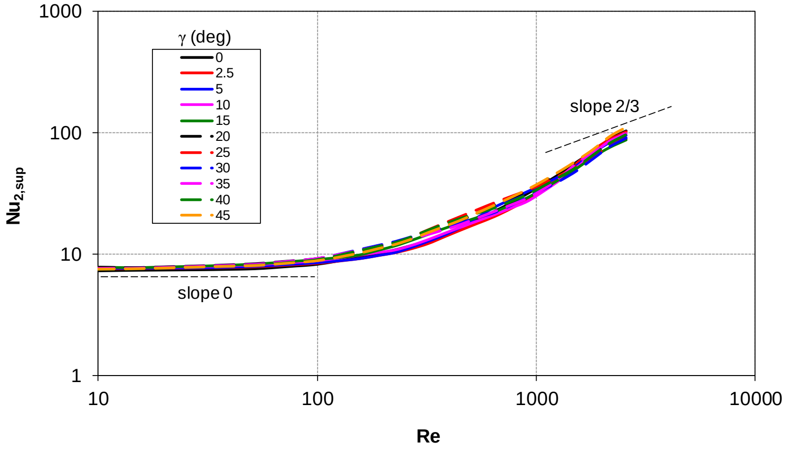

Figure C. 5. From the top: f, $Nu^{(2)}_{inf}$, $Nu^{(2)}_{sup}$. *Results obtained for l/H=5, in the range of Re from 10 to 2560, and γ from 0° to 45°.*

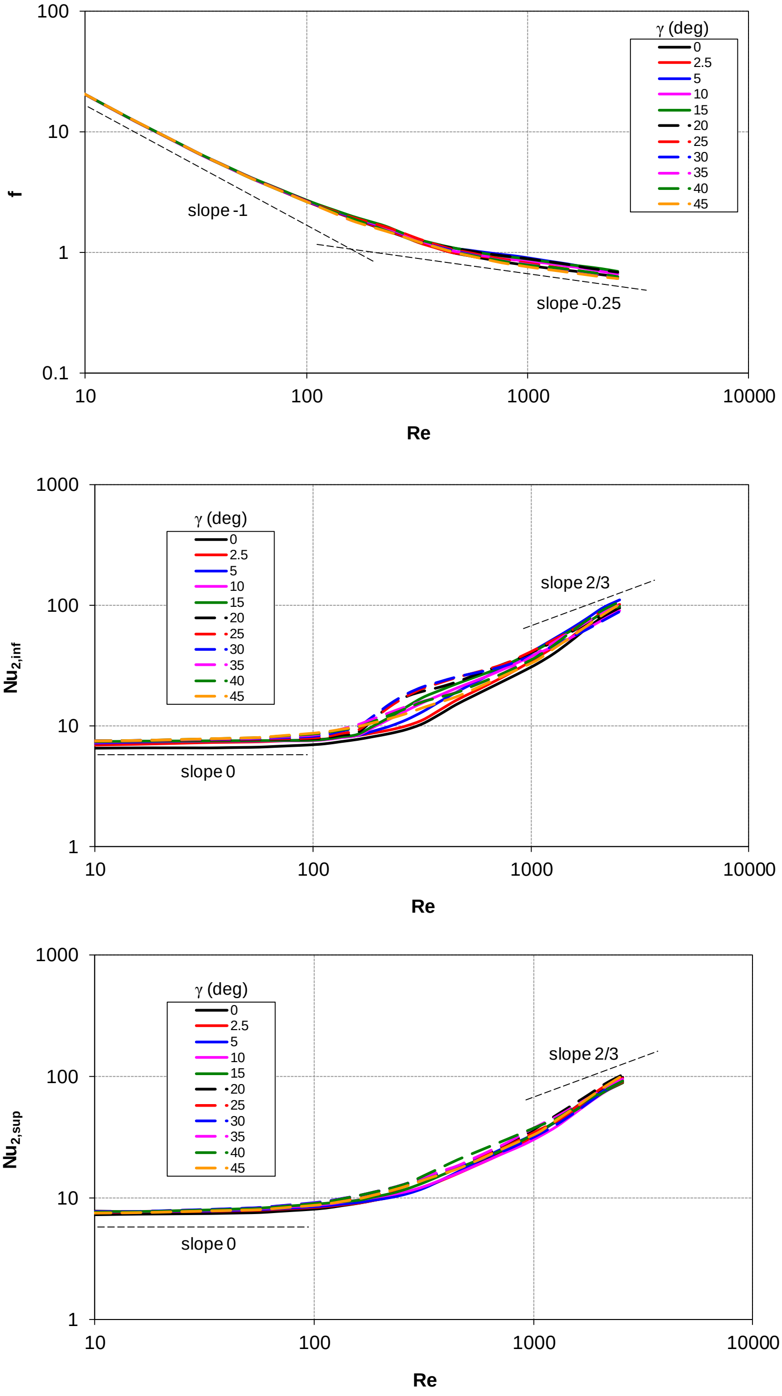

Figure C. 6. From the top: f, Nu$^{(2)}_{inf}$, Nu$^{(2)}_{sup}$. Results obtained for l/H=6, in the range of Re from 10 to 2560, and γ from 0° to 45°.

This clear transition to turbulent regime can be observed also in the Nusselt number at l/H=1.5 and l/H=2. At higher values of the pitch to height ratio, the transition is not clearly visible as a jump in Nu or f values but rather as a slope variation.

Moreover, the influence of the flow attack angle γ becomes less and less important when l/H increases. Especially in the friction factor plots it can be observed that all the curves at different γ values collapse in one.

Appendix D: Experimental method in electromembrane processes

ED/(A)RED unit

The experiments presented in this thesis were carried out by using a cross-flow stack (REDstack B.V., The Netherlands). The electrodes, shown in Figure D. 1, have an active area of 0.01 m^2. They are made of titanium with an iridium-MMO (mixed metal oxide) coating and are fixed on a polymethylmethacrylate (PMMA) support, in which the channels for the electrode rinse solution are also drilled.

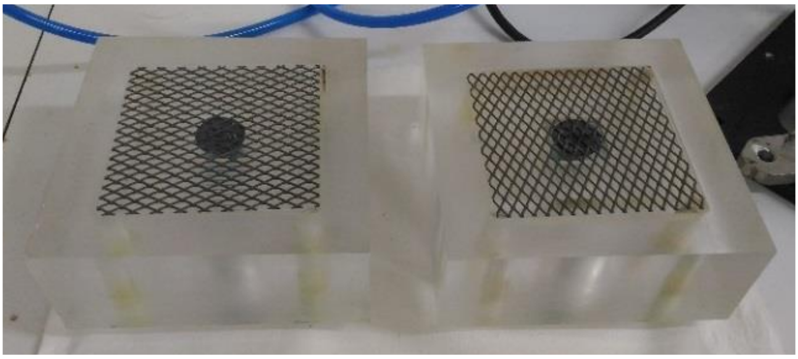

Figure D. 1. End plates and electrodes.

The first element positioned on the electrode (both on anode and cathode) is a spacer with a thickness of 480 μm, placed to create the channel for the electrode solution. The spacer is surrounded by a gasket which ensures the sealing of the electrode compartment. Both elements are shown in Figure D. 2.

To prevent the electrode solution from entering the first cell pair, an additional cationic membrane is interposed between the first cell pair and the channel of the electrode solution. At this point, the cell pairs are assembled by alternating a CEM, and an AEM. The flat membranes tested were Type 10 and Type 12 provided by Fujifilm B.V. Their properties are reported in Table 7 and Table 12, respectively. Pillars profiled membranes and OCF profiled membranes were also provided by Fujifilm B.V. and their properties are the same of flat Type 10.

In a conventional stack with spacers, woven spacers (Deukum, GmbH) of 155 μm or 280 μm were interposed between CEM and AEM. Both spacers had a pitch to height ratio l/H=2 and a porosity of 75%. In the case of pillars profiled membranes

(Figure D. 3), the space between two membranes was created by the pillars themselves.

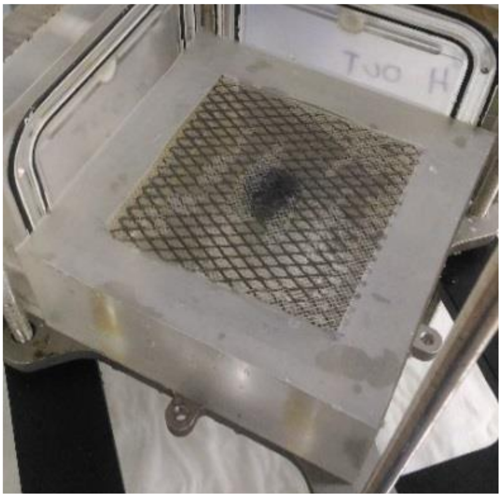

Figure D. 2. Electrode rinse solution channel.

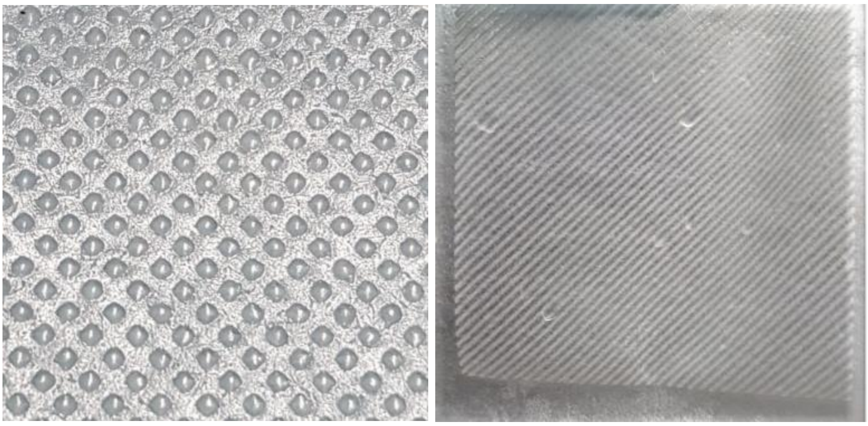

(a) (b)

Figure D. 3. Pictures of (a) pillars and (b) OCF profiled membranes. Top view.

In the case of OCF profiled membranes (Figure D. 3), once the CEM was placed with the profiles on top, the AEM was placed with its profiles touching orthogonally the CEM profiles. Having both profiles in one channel, in the other channel a spacer of 280 μm was positioned. All the experiments were performed with 10 cell pairs.

An example of spacer of 280 μm and the assembled stack are reported in Figure D. 4.

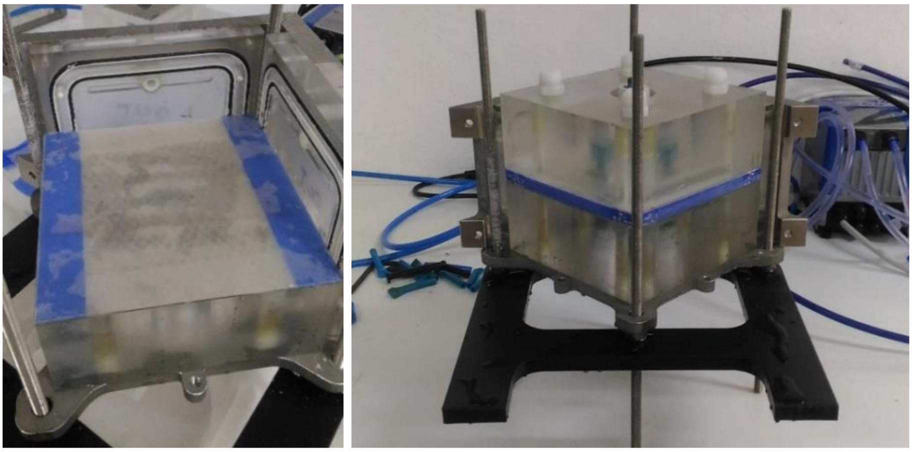

Figure D. 4. Assembly steps of the stack equipped with spacers.

The two PMMA plates between which the cell pairs are positioned, are enclosed by four plates which act as manifolds for the distribution/collection of the solutions to/from the channels, as shown in Figure D. 5.

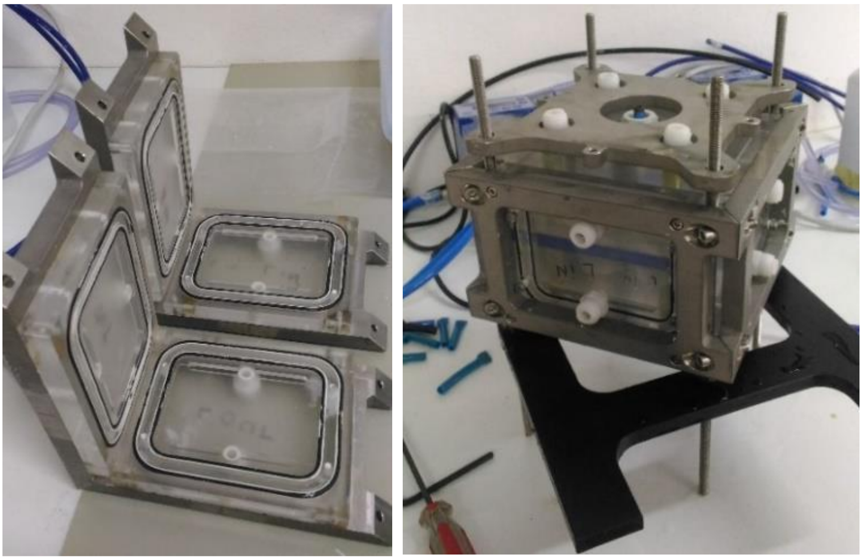

Figure D. 5. Manifolds.

Experimental set-up and method for IEMs characterization tests

During the ED or (A)RED operations, a difference in concentrations is established between the two solutions, which causes a diffusive flux of salt from the more concentrate to the dilute solution, and an osmotic flow of water in the opposite direction. Therefore, among the fundamental properties required to describe an IEM, there are the salt permeability due to diffusion and the water permeability due to osmosis. In particular, these properties are needed for the calculation of the total flows of water and salt in the one-dimensional model presented in Part III, Section 2. In this regard, tests were carried out to evaluate both properties and compare them with those provided by the manufacturer.

In these tests, the stack described above was used, assembled with 10 cell pairs. No power supply was used. Even if no electrochemical reactions occur in this type of experiment, the electrode rinse solution was pumped into the electrode compartment, in order to establish the same pressure conditions that occur during ED/(A)RED tests. Salt solutions were prepared using demineralized water and NaCl, with concentrations from 0.5 to 60 g/l, using the conditions shown in Table D. 1.

Table D. 1. Operating conditions in the IEMs characterization tests.

	Concentrate [g/l]	**Diluate [g/l]**
Test 1	30	0.5
Test 2	30	10
Test 3	60	0.5

The solutions were pumped into the stack with a flow rate of 42 ml/min. To assess weight variations due to water and salt flows, each solution, within a laboratory beaker, was placed on a precision balance and recirculated in the stack. A schematic representation of the experimental set up is shown in Figure D. 6. The initial volume of the solution was known (500 ml), as well as the weight, different for each salt concentration. Each test lasted one hour, during which the weight variations and the conductivity of both solutions were recorded every 5 minutes. At the end of the test, the volume of solutions was measured again.

The data obtained were elaborated to calculate the water and salt fluxes and, consequently, the salt diffusion permeability coefficient and the osmotic permeability of the membranes.

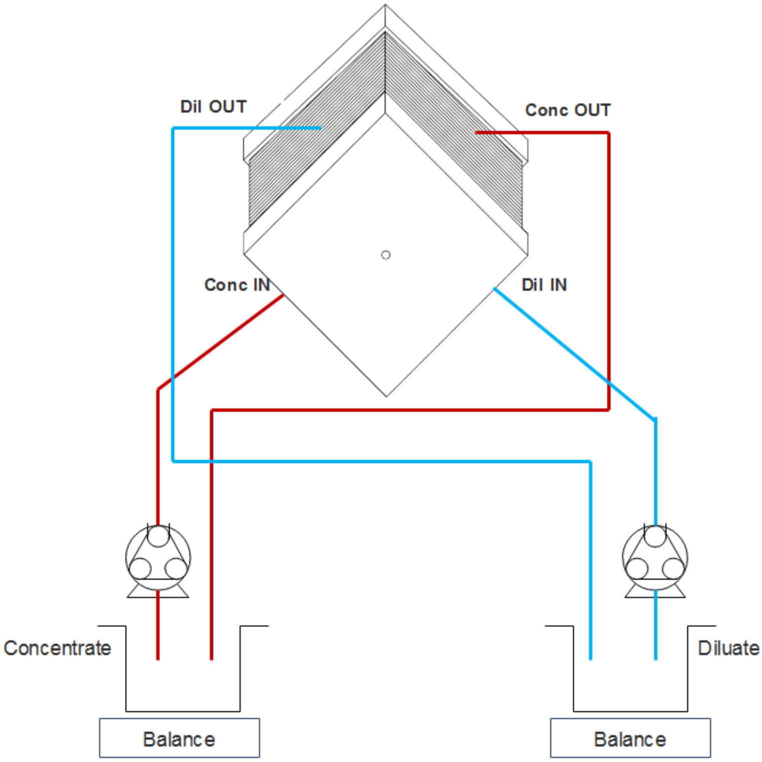

Figure D. 6. Experimental set-up for IEMs characterization tests.

Results of the IEMs characterization tests

The variations in solution mass and conductivity, due to the diffusive and osmotic water fluxes, were recorded every 5 minutes. Knowing the initial and final mass and the initial and final volume of the two solutions, density was calculated and it was assumed a linear variation during the test. To convert conductivity to concentration, Islam's correlation was used.

During each experiment, the volume in the concentrate solution increases, due to the osmotic flux of water directed from the more diluted to the more concentrated solution, while the salt concentration decreases because the salt moves in the opposite direction.

Therefore, starting from the experimental data, i.e. the concentrations and the mass variation Δm, the quantities of interest were obtained as follows.

The salt mass in the dilute solution at the *i*-th time instant is calculated as:

$$g_{S,i}^{DIL} = C_i^{DIL} V_i^{DIL} \tag{D. 1}$$

where C_i^{DIL} is the diluate concentration and V_i^{DIL} is the diluate volume. Therefore, the salt mass flow into the diluate (per cell pair) at the generic time step is:

$$G_{S,i}^{DIL} = \frac{g_{S,i}^{DIL} - g_{S,i-1}^{DIL}}{t_i - t_{i-1}} \cdot \frac{1}{n_{cp}} \tag{D. 2}$$

where (t_i-t_{i-1}) is the time step between each measurement and n_{cp} is the number of cell pairs in the stack. At this point, the salt diffusion permeability coefficient (average between the two membranes) is calculated as follows:

$$D_{IEM,i} = \frac{G_{S,i}^{DIL}}{2\left(C_{i/2}^{CONC} - C_{i/2}^{DIL}\right)S} \cdot H_{IEM} \tag{D. 3}$$

in which S is the stack active area, H_{IEM} is the membrane thickness (supposed the same for the two membranes) and $C_{i/2}^{SOL}$ is the mean concentration between instants t_{i-1} and t_i. The final value adopted for D_{IEM} is the average of those calculated for each time step.

Regarding the determination of the osmotic permeability, it is necessary to calculate the water mass in the concentrate solution as:

$$g_{W,i}^{CONC} = g_{TOT,i}^{CONC} - g_{S,i}^{CONC} \tag{D. 4}$$

where $g_{TOT,i}^{CONC}$ is the total mass of the concentrate solution and $g_{S,i}^{CONC}$ is the salt mass in concentrate solution, calculated by using Eq. (D. 1).

The water mass flow rate per cell pair is obtained as:

$$G_{W,i}^{CONC} = \frac{g_{W,i-1}^{CONC} - g_{W,i}^{CONC}}{t_{i-1} - t_i} \cdot \frac{1}{n_{cp}} \tag{D. 5}$$

thus, the osmotic permeability (average between the two membranes) is:

$$L_{p,IEM,i} = \frac{G_{W,i}^{CONC}}{2\left(\pi_{i/2}^{CONC} - \pi_{i/2}^{DIL}\right)S} \tag{D. 6}$$

where $\pi_{i/2}^{SOL}$ is the mean osmotic pressures between instants t_{i-1} and t_i, calculated by means of Pitzer's model.

The final value adopted for $L_{p,IEM}$ is the average of those calculated for each time step. Results are shown, for each couple of concentrations tested, in Table D. 2.

Table D. 2. Results of salt diffusion permeability and water permeability coefficients for Type 10 membranes (Fujifilm B.V.)

	D_{IEM} **[m²/s]**	$L_{p,IEM}$ **[ml/m²h bar]**
Test 1	$2.55\cdot10^{-12}$	5.6
Test 2	$2.39\cdot10^{-12}$	5.2
Test 3	$3.83\cdot10^{-12}$	6

Experimental set-up and method for ED/ARED tests

The electrode rinse solution used was a 0.3 M $K_3Fe(CN)_6$; 0.3 M $K_4Fe(CN)_6\cdot3H_2O$; 0.25 M NaCl solution. It was pumped into the stack by a peristaltic pump (Masterflex Cole-Palmer) with a flow rate of 180 ml/min. A similar pump is used for the feed solutions, for which a one-pass flow arrangement was used. Pressure transducers (Endress+Hauser Cerabar M) were installed at the inlet of each stream, and conductivity was measured at the inlet and the outlet by a portable conductivity-meter (WTW 340i).

For all measurements, the procedural prescriptions recommended in reference [238] for electrodialysis experiments were followed. A potentiostat/galvanostat was used (Ivium Technologies, The Netherlands) to increase the current pulse-wise: each current pulse duration (typically 300 s) was at least eight times the residence time of feed water in the system to ensure steady-state conditions, and it was preceded and followed by a short period of open circuit (open circuit voltage, OCV) [65]. For each current pulse, the stationary voltage value or its mean value in the presence of oscillations, was taken in order to build the current-voltage curve.

In ARED experiments, a stabilized power supply (Elektro-Automatic GmbH, Germany) was adopted.

A schematic representation of the experimental set-up, equal for both ED and ARED experiments, is reported in Figure D. 7.

During each step in which the current was kept constant, a sample of each solution at the outlet was taken to measure the conductivity, from which a corresponding concentration value was obtained. Conductivity was measured also at the inlet of the ED stack before starting each test.

Moreover, before starting each experimental campaign (i.e., each set of tests conducted before disassembling the stack), the stack was checked for external and internal leakages. During the test for internal leakages, a single channel was fed, for example the diluate, and the flow rate exiting the other channel (in this example, the concentrate) was verified to be below the measurability threshold. In this way, sealing defects and lesions in membranes or gaskets are excluded.

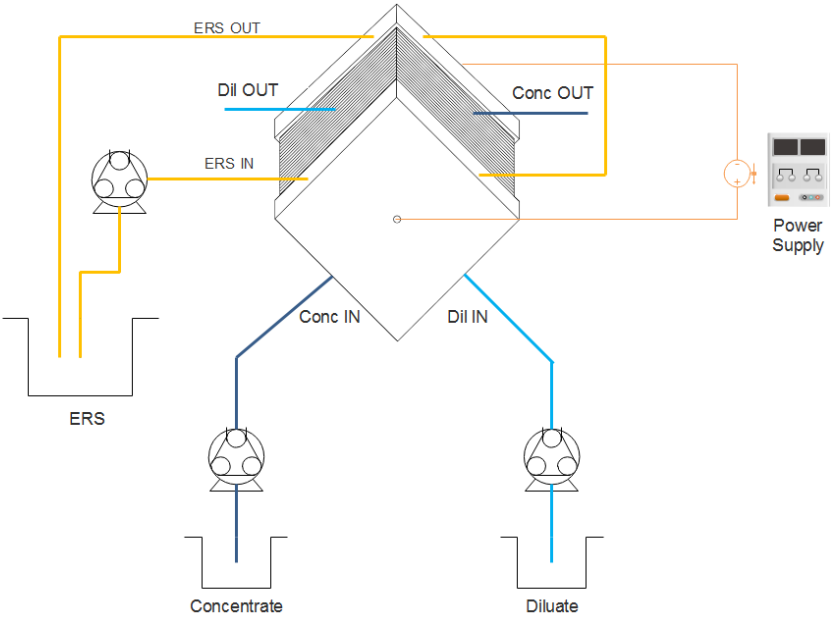

Figure D. 7. Experimental set-up for ED/ARED tests.

References

1. Onsekizoglu, P. Membrane Distillation: Principle, Advances, Limitations and Future Prospects in Food Industry. *Distillation - Advances from Modeling to Applications* **2012**, 233–266.

2. IEA 2018 World Energy Outlook - Executive Summary. *Oecd/Iea* **2018**, 11.

3. Jia, Z.; Wang, B.; Song, S.; Fan, Y. Blue energy: Current technologies for sustainable power generation from water salinity gradient. *Renewable and Sustainable Energy Reviews* **2014**, *31*, 91–100.

4. Yip, N.Y.; Vermaas, D.A.; Nijmeijer, K.; Elimelech, M. Thermodynamic, energy efficiency, and power density analysis of reverse electrodialysis power generation with natural salinity gradients. *Environmental Science and Technology* **2014**, *48*, 4925–4936.

5. Tran, M.; Koncagul, E.; Connor, R. *Rapporto 2016 delle Nazioni Unite sullo sviluppo delle risorse idriche mondiali: ACQUA E LAVORO Fatti e cifre*; 2016;

6. Post, J.W.; Huiting, H.; Cornelissen, E.R.; Hamelers, H.V.M. Pre-desalination with electro-membranes for SWRO. *Desalination and Water Treatment* **2011**, *31*, 296–304.

7. Wang, P.; Chung, T.S. Recent advances in membrane distillation processes: Membrane development, configuration design and application exploring. *Journal of Membrane Science* **2015**, *474*, 39–56.

8. Gude, V.G. Desalination and sustainability - An appraisal and current perspective. *Water Research* **2016**, *89*, 87–106.

9. Zarzo, D.; Prats, D. Desalination and energy consumption. What can we expect in the near future? *Desalination* **2018**, *427*, 1–9.

10. Lee, S.; Choi, J.; Park, Y.G.; Shon, H.; Ahn, C.H.; Kim, S.H. Hybrid desalination processes for beneficial use of reverse osmosis brine: Current status and future prospects. *Desalination* **2018**, *454*, 104–111.

11. Subramani, A.; Badruzzaman, M.; Oppenheimer, J.; Jacangelo, J.G. Energy minimization strategies and renewable energy utilization for desalination: A review. *Water Research* **2011**, *45*, 1907–1920.

12. Voutchkov, N. Energy use for membrane seawater desalination - current status and trends. *Desalination* **2017**, *431*, 2–14.

13. Drioli, E.; Ali, A.; Macedonio, F. Membrane distillation: Recent developments and perspectives. *Desalination* **2015**, *356*, 56–84.

14. Xu, K.; Qu, D.; Zheng, M.; Guo, X.; Wang, C. Water Reduction and Nutrient Reconcentration of Hydrolyzed Urine via Direct-Contact Membrane

Distillation: Ammonia Loss and Its Control. *Journal of Environmental Engineering (United States)* **2019**, *145*, 1–8.

15. Bhattacharjee, C.; Saxena, V.K.; Dutta, S. Fruit juice processing using membrane technology: A review. *Innovative Food Science and Emerging Technologies* **2017**, *43*, 136–153.
16. González-Bravo, R.; Elsayed, N.A.; Ponce-Ortega, J.M.; Nápoles-Rivera, F.; El-Halwagi, M.M. Optimal design of thermal membrane distillation systems with heat integration with process plants. *Applied Thermal Engineering* **2015**, *75*, 154–166.
17. Subramani, A.; Jacangelo, J.G. Emerging desalination technologies for water treatment: A critical review. *Water Research* **2015**, *75*, 164–187.
18. Camacho, L.M.; Dumée, L.; Zhang, J.; Li, J. de; Duke, M.; Gomez, J.; Gray, S. Advances in membrane distillation for water desalination and purification applications. *Water (Switzerland)* **2013**, *5*, 94–196.
19. Kim, H.C.; Shin, J.; Won, S.; Lee, J.Y.; Maeng, S.K.; Song, K.G. Membrane distillation combined with an anaerobic moving bed biofilm reactor for treating municipal wastewater. *Water Research* **2015**, *71*, 97–106.
20. Yan, Z.; Yang, H.; Qu, F.; Yu, H.; Liang, H.; Li, G.; Ma, J. Reverse osmosis brine treatment using direct contact membrane distillation: Effects of feed temperature and velocity. *Desalination* **2017**, *423*, 149–156.
21. Sanmartino, J.A.; Khayet, M.; García-Payo, M.C.; El-Bakouri, H.; Riaza, A. Treatment of reverse osmosis brine by direct contact membrane distillation: Chemical pretreatment approach. *Desalination* **2017**, *420*, 79–90.
22. Mediras – Membrane Distillation in Remote Areas Available online: https://www.mediras.eu/ (accessed on Nov 9, 2019).
23. Fritzmann, C.; Löwengerg, J.; Wintgens, T.; Melin, T. State-of-the-art of reverse osmosis desalination. *Desalination* **2007**, *216*, 1–76.
24. Ghaffour, N.; Lattemann, S.; Missimer, T.; Ng, K.C.; Sinha, S.; Amy, G. Renewable energy-driven innovative energy-efficient desalination technologies. *Applied Energy* **2014**, *136*, 1155–1165.
25. Martínez-Díez, L.; Vázquez-González, M.I. Temperature and concentration polarization in membrane distillation of aqueous salt solutions. *Journal of Membrane Science* **1999**, *156*, 265–273.
26. Strathmann, H. Electromembrane Processes: Basic Aspects and Applications. *Comprehensive Membrane Science and Engineering* **2010**, *2*, 391–429.
27. Li, F.; Meindersma, W.; De Haan, A.B.; Reith, T. Optimization of commercial net spacers in spiral wound membrane modules. *Journal of Membrane Science* **2002**, *208*, 289–302.

28. Veerman, J.; Saakes, M.; Metz, S.J.; Harmsen, G.J. Reverse electrodialysis: Performance of a stack with 50 cells on the mixing of sea and river water. *Journal of Membrane Science* **2009**, *327*, 136–144.

29. Choi, I.; Han, J.Y.; Yoo, S.J.; Henkensmeier, D.; Kim, J.Y.; Lee, S.Y.; Han, J.; Nam, S.W.; Kim, H.J.; Jang, J.H. Experimental investigation of operating parameters in power generation by lab-scale reverse electro-dialysis (RED). *Bulletin of the Korean Chemical Society* **2016**, *37*, 1010–1019.

30. Tedesco, M.; Cipollina, A.; Tamburini, A.; Micale, G. Towards 1 kW power production in a reverse electrodialysis pilot plant with saline waters and concentrated brines. *Journal of Membrane Science* **2017**, *522*, 226–236.

31. Strathmann, H. *Ion-Exchange Membrane Separation Processes*; First ed.; Elsevier: Amsterdam, 2004; ISBN 044450236X.

32. Mandersloot, W.G.B.; Hicks, R.E. Concertration polarization on ion exchange resin membranes in electrodialytic demineralization. *Industrial and Engineering Chemistry Process Design and Development* **1965**, *4*, 304–308.

33. Sonin, A.A.; Probstein, R.F. A Hydrodynamic theory of desalination by Electrodialysis. *Desalination* **1968**, *5*, 293–329.

34. Solt, G. Early days in electrodialysis. *Desalination* **1995**, *100*, 15–19.

35. Wilson, J.R. *Demineralization by electrodialysis*; Butterworths Scientific Publications, 1960;

36. Jaroszek, H.; Dydo, P. Ion-exchange membranes in chemical synthesis – a review. *Open Chemistry* **2016**, *14*, 1–19.

37. Campione, A.; Gurreri, L.; Ciofalo, M.; Micale, G.; Tamburini, A.; Cipollina, A. Electrodialysis for water desalination: A critical assessment of recent developments on process fundamentals, models and applications. *Desalination* **2018**, *434*, 121–160.

38. Strathmann, H. Electrodialysis, a mature technology with a multitude of new applications. *Desalination* **2010**, *264*, 268–288.

39. Galama, A.H.; Saakes, M.; Bruning, H.; Rijnaarts, H.H.M.; Post, J.W. Seawater predesalination with electrodialysis. *Desalination* **2014**, *342*, 61–69.

40. REvivED water – Low energy solutions for drinking water production by a REvival of ElectroDialysis systems Available online: https://www.revivedwater.eu/ (accessed on Nov 9, 2019).

41. Nagarale, R.K.; Gohil, G.S.; Shahi, V.K. Recent developments on ion-exchange membranes and electro-membrane processes. *Advances in Colloid and Interface Science* **2006**, *119*, 97–130.

42. Tedesco, M.; Hamelers, H.V.M.; Biesheuvel, P.M. Nernst-Planck transport

theory for (reverse) electrodialysis: I. Effect of co-ion transport through the membranes. *Journal of Membrane Science* **2016**, *510*, 370–381.

43. Tedesco, M.; Hamelers, H.V.M.; Biesheuvel, P.M. Nernst-Planck transport theory for (reverse) electrodialysis: II. Effect of water transport through ion-exchange membranes. *Journal of Membrane Science* **2017**, *531*, 172–182.

44. Koros, W.J..; MA, Y.H..; Shimidzu, T. TERMINOLOGY FOR MEMBRANES AND MEMBRANE PROCESSES. *International Union of Pure & Applied Chemistry* **1996**, *68*, 1479–1489.

45. Gherasim, C.-V.; Křivčík, J.; Mikulášek, P. Investigation of batch electrodialysis process for removal of lead ions from aqueous solutions. *Chemical Engineering Journal* **2014**, *256*, 324–334.

46. Nikonenko, V. V.; Kovalenko, A. V.; Urtenov, M.K.; Pismenskaya, N.D.; Han, J.; Sistat, P.; Pourcelly, G. Desalination at overlimiting currents: State-of-the-art and perspectives. *Desalination* **2014**, *342*, 85–106.

47. Shaposhnik, V.A.; Vasil’eva, V.I.; Reshetnikova, E. V Concentration Polarization of Ion-Exchange Membranes in Electrodialysis: An Interferometric Study. *Russian Journal of Electrochemistry* **2000**, *36*, 773–777.

48. Shaposhnik, V.A.; Vasil’eva, V.I.; Grigorchuk, O. V. The interferometric investigations of electromembrane processes. *Advances in Colloid and Interface Science* **2008**, *139*, 74–82.

49. Rubinstein, I.; Shtilman, L. Voltage against Current Curves of Cation Exchange Membranes. *Journal of the Chemical Society, Faraday Transactions 2: Molecular and Chemical Physics* **1978**, 231–246.

50. Scialdone, O.; Guarisco, C.; Grispo, S.; D’Angelo, A.; Galia, A. Investigation of electrode material – Redox couple systems for reverse electrodialysis processes. Part I: Iron redox couples. *Journal of Electroanalytical Chemistry* **2012**, *681*, 66–75.

51. Scialdone, O.; Albanese, A.; D’Angelo, A.; Galia, A.; Guarisco, C. Investigation of electrode material – redox couple systems for reverse electrodialysis processes. Part II: Experiments in a stack with 10–50 cell pairs. *Journal of Electroanalytical Chemistry* **2013**, *704*, 1–9.

52. Pattle, R.E. Production of electric power by mixing fresh and salt water in the hydroelectric pile. *Nature* 1954, *174*, 660.

53. Daniilidis, A.; Vermaas, D.A.; Herber, R.; Nijmeijer, K. Experimentally obtainable energy from mixing river water, seawater or brines with reverse electrodialysis. *Renewable Energy* **2014**, *64*, 123–131.

54. REAPower – Reverse Electrodialysis Alternative Power Production Available online: http://www.reapower.eu/ (accessed on Nov 9, 2019).

55. Tedesco, M.; Scalici, C.; Vaccari, D.; Cipollina, A.; Tamburini, A.; Micale, G. Performance of the first reverse electrodialysis pilot plant for power production from saline waters and concentrated brines. *Journal of Membrane Science* **2016**, *500*, 33–45.

56. RED Heat to Power – Generating electricity from low-grade heat at higher efficiencies and lower costs Available online: http://www.red-heat-to-power.eu/ (accessed on Nov 9, 2019).

57. Cipollina, A.; Micale, G. *Sustainable Energy from Salinity Gradients*; Elsevier, 2016; ISBN 9780857095459.

58. Vermaas, D.A.; Guler, E.; Saakes, M.; Nijmeijer, K. Theoretical power density from salinity gradients using reverse electrodialysis. *Energy Procedia* **2012**, *20*, 170–184.

59. Tedesco, M.; Cipollina, A.; Tamburini, A.; Bogle, I.D.L.; Micale, G. A simulation tool for analysis and design of reverse electrodialysis using concentrated brines. *Chemical Engineering Research and Design* **2015**, *93*, 441–456.

60. Vermaas, D.A.; Saakes, M.; Nijmeijer, K. Doubled power density from salinity gradients at reduced intermembrane distance. *Environmental Science and Technology* **2011**, *45*, 7089–7095.

61. Post, J.W.; Hamelers, H.V.M.; Buisman, C.J.N. Energy recovery from controlled mixing salt and fresh water with a reverse electrodialysis system. *Environmental Science and Technology* **2008**, *42*, 5785–5790.

62. Długołęcki, P.; Gambier, A.; Nijmeijer, K.; Wessling, M. Practical potential of reverse electrodialysis as process for sustainable energy generation. *Environmental Science and Technology* **2009**, *43*, 6888–6894.

63. Pawlowski, S.; Sistat, P.; Crespo, J.G.; Velizarov, S. Mass transfer in reverse electrodialysis: Flow entrance effects and diffusion boundary layer thickness. *Journal of Membrane Science* **2014**, *471*, 72–83.

64. Vermaas, D.A.; Saakes, M.; Nijmeijer, K. Power generation using profiled membranes in reverse electrodialysis. *Journal of Membrane Science* **2011**, *385–386*, 234–242.

65. Vermaas, D.A.; Saakes, M.; Nijmeijer, K. Enhanced mixing in the diffusive boundary layer for energy generation in reverse electrodialysis. *Journal of Membrane Science* **2014**, *453*, 312–319.

66. Veerman, J.; Saakes, M.; Metz, S.J.; Harmsen, G.J. Electrical power from sea and river water by reverse electrodialysis: A first step from the laboratory to a real power plant. *Environmental Science and Technology* **2010**, *44*, 9207–9212.

67. Pawlowski, S.; Crespo, J.G.; Velizarov, S. Pressure drop in reverse

electrodialysis: Experimental and modeling studies for stacks with variable number of cell pairs. *Journal of Membrane Science* **2014**, *462*, 96–111.

68. Gurreri, L.; Tamburini, A.; Cipollina, A.; Micale, G.; Ciofalo, M. CFD prediction of concentration polarization phenomena in spacer-filled channels for reverse electrodialysis. *Journal of Membrane Science* **2014**, *468*, 133–148.

69. Gurreri, L.; Tamburini, A.; Cipollina, A.; Micale, G.; Ciofalo, M. Flow and mass transfer in spacer-filled channels for reverse electrodialysis: a CFD parametrical study. *Journal of Membrane Science* **2016**, *497*, 300–317.

70. Gurreri, L.; Ciofalo, M.; Cipollina, A.; Tamburini, A.; Van Baak, W.; Micale, G. CFD modelling of profiled-membrane channels for reverse electrodialysis. *Desalination and Water Treatment* **2014**, *3994*, 1–20.

71. Długołecki, P.; Ogonowski, P.; Metz, S.J.; Saakes, M.; Nijmeijer, K.; Wessling, M. On the resistances of membrane, diffusion boundary layer and double layer in ion exchange membrane transport. *Journal of Membrane Science* **2010**, *349*, 369–379.

72. Shenvi, S.S.; Isloor, A.M.; Ismail, A.F. A review on RO membrane technology: Developments and challenges. *Desalination* **2015**, *368*, 10–26.

73. Henthorne, L.; Boysen, B. State-of-the-art of reverse osmosis desalination pretreatment. *Desalination* **2015**, *356*, 129–139.

74. Stover, R.L. Seawater reverse osmosis with isobaric energy recovery devices. *Desalination* **2007**, *203*, 168–175.

75. Amy, G.; Ghaffour, N.; Li, Z.; Francis, L.; Linares, R.V.; Missimer, T.; Lattemann, S. Membrane-based seawater desalination: Present and future prospects. *Desalination* **2017**, *401*, 16–21.

76. Peñate, B.; García-Rodríguez, L. Current trends and future prospects in the design of seawater reverse osmosis desalination technology. *Desalination* **2012**, *284*, 1–8.

77. Kim, J.; Park, M.; Snyder, S.A.; Kim, J.H. Reverse osmosis (RO) and pressure retarded osmosis (PRO) hybrid processes: Model-based scenario study. *Desalination* **2013**, *322*, 121–130.

78. Wan, C.F.; Chung, T.S. Techno-economic evaluation of various RO+PRO and RO+FO integrated processes. *Applied Energy* **2018**, *212*, 1038–1050.

79. Blandin, G.; Verliefde, A.R.D.; Tang, C.Y.; Le-Clech, P. Opportunities to reach economic sustainability in forward osmosis-reverse osmosis hybrids for seawater desalination. *Desalination* **2015**, *363*, 26–36.

80. Vanoppen, M.; Blandin, G.; Derese, S.; Le Clech, P.; Post, J.; Verliefde, A.R.D. *Salinity gradient power and desalination*; Elsevier Ltd., 2016; ISBN

9780081003237.

81. Vanoppen, M.; Criel, E.; Andersen, S.; Prévoteau, A.; Verliefde, A.R.D. Assisted Reverse Electrodialysis: a novel technique to decrease Reverse Osmosis energy demand. *AMTA/AWWA Membrane Technology Conference, Papers* **2016**, *32*, 1–12.

82. Li, W.; Krantz, W.B.; Cornelissen, E.R.; Post, J.W.; Verliefde, A.R.D.; Tang, C.Y. A novel hybrid process of reverse electrodialysis and reverse osmosis for low energy seawater desalination and brine management. *Applied Energy* **2013**, *104*, 592–602.

83. La Cerva, M.; Cipollina, A.; Ciofalo, M.; Albeirutty, M.; Turkmen, N.; Bouguecha, S.; Micale, G. CFD Investigation of Spacer-Filled Channels for Membrane Distillation. *Membranes* **2019**, *9*, 91.

84. Cao, Z.; Wiley, D.E.; Fane, A.G. CFD simulations of net-type turbulence promoters in a narrow channel. *Journal of Membrane Science* **2001**, *185*, 157–176.

85. Qureshi, M.; Shakaib, M. CFD Study for Temperature and Concentration Profiles in Membrane Channels. In Proceedings of the Proceedings of International Conference on Energy and Sustainability; Karachi, Pakistan, 2013.

86. Schock, G.; Miquel, A. Mass transfer and pressure loss in spiral wound modules. *Desalination* **1987**, *64*, 339–352.

87. Shakaib, M.; Hasani, S.M.F.; Ahmed, I.; Yunus, R.M. A CFD study on the effect of spacer orientation on temperature polarization in membrane distillation modules. *Desalination* **2012**, *284*, 332–340.

88. Phattaranawik, J.; Jiraratananon, R.; Fane, A.G. Effects of net-type spacers on heat and mass transfer in direct contact membrane distillation and comparison with ultrafiltration studies. *Journal of Membrane Science* **2003**, *217*, 193–206.

89. Karode, S.K.; Kumar, A. Flow visualization through spacer filled channels by computational fluid dynamics I. Pressure drop and shear rate calculations for flat sheet geometry. *Journal of Membrane Science* **2001**, *193*, 69–84.

90. Da Costa, A.R.; Fane, A.G.; Wiley, D.E. Spacer characterization and pressure drop modelling in spacer-filled channels for ultrafiltration. *Journal of Membrane Science* **1994**, *87*, 79–98.

91. Koutsou, C.P.; Yiantsios, S.G.; Karabelas, A.J. Direct numerical simulation of flow in spacer-filled channels: Effect of spacer geometrical characteristics. *Journal of Membrane Science* **2007**, *291*, 53–69.

92. Koutsou, C.P.; Yiantsios, S.G.; Karabelas, A.J. A numerical and experimental study of mass transfer in spacer-filled channels: Effects of spacer geometrical

characteristics and Schmidt number. *Journal of Membrane Science* **2009**, *326*, 234–251.

93. Koutsou, C.P.; Karabelas, A.J. A novel retentate spacer geometry for improved spiral wound membrane (SWM) module performance. *Journal of Membrane Science* **2015**, *488*, 129–142.

94. Cipollina, A.; Di Miceli, A.; Koschikowski, J.; Micale, G.; Rizzuti, L. CFD simulation of a membrane distillation module channel. *Desalination and Water Treatment* **2009**, *6*, 177–183.

95. Cipollina, A.; Micale, G.; Rizzuti, L. Membrane distillation heat transfer enhancement by CFD analysis of internal module geometry. *Desalination and Water Treatment* **2011**, *25*, 195–209.

96. Al-sharif, S.; Albeirutty, M.; Cipollina, A.; Micale, G. Modelling flow and heat transfer in spacer-filled membrane distillation channels using open source CFD code. *Desalination* **2013**, *311*, 103–112.

97. Mojab, S.M.; Pollard, A.; Pharoah, J.G.; Beale, S.B.; Hanff, E.S. Unsteady laminar to turbulent flow in a spacer-filled channel. *Flow, Turbulence and Combustion* **2014**, *92*, 563–577.

98. Saeed, A.; Vuthaluru, R.; Vuthaluru, H.B. Investigations into the effects of mass transport and flow dynamics of spacer filled membrane modules using CFD. *Chemical Engineering Research and Design* **2015**, *93*, 79–99.

99. Bucs, S.S.; Valladares Linares, R.; Marston, J.O.; Radu, A.I.; Vrouwenvelder, J.S.; Picioreanu, C. Experimental and numerical characterization of the water flow in spacer-filled channels of spiral-wound membranes. *Water Research* **2015**, *87*, 299–310.

100. Tamburini, A.; Renda, M.; Cipollina, A.; Micale, G.; Ciofalo, M. Investigation of heat transfer in spacer-filled channels by experiments and direct numerical simulations. *International Journal of Heat and Mass Transfer* **2016**, *93*, 1190–1205.

101. Schwinge, J.; Neal, P.R.; Wiley, D.E.; Fletcher, D.F.; Fane, A.G. Spiral wound modules and spacers: Review and analysis. *Journal of Membrane Science* **2004**, *242*, 129–153.

102. Ghidossi, R.; Veyret, D.; Moulin, P. Computational fluid dynamics applied to membranes: State of the art and opportunities. *Chemical Engineering and Processing: Process Intensification* **2006**, *45*, 437–454.

103. Hitsov, I.; Maere, T.; De Sitter, K.; Dotremont, C.; Nopens, I. Modelling approaches in membrane distillation: A critical review. *Separation and Purification Technology* **2015**, *142*, 48–64.

104. Karabelas, A.J.; Kostoglou, M.; Koutsou, C.P. Modeling of spiral wound membrane desalination modules and plants - review and research priorities.

Desalination **2015**, *356*, 165–186.

105. Fimbres-Weihs, G.A.; Wiley, D.E. Review of 3D CFD modeling of flow and mass transfer in narrow spacer-filled channels in membrane modules. *Chemical Engineering and Processing: Process Intensification* **2010**, *49*, 759–781.

106. Tamburini, A.; Cipollina, A.; Al-Sharif, S.; Albeirutty, M.; Gurreri, L.; Micale, G.; Ciofalo, M. Assessment of temperature polarization in membrane distillation channels by liquid crystal thermography. *... and Water Treatment* **2014**, 37–41.

107. Tamburini, A.; Pitò, P.; Cipollina, A.; Micale, G.; Ciofalo, M. A Thermochromic Liquid Crystals Image Analysis technique to investigate temperature polarization in spacer-filled channels for Membrane Distillation. *Journal of Membrane Science* **2013**, *447*, 260–273.

108. Ali, A.; Macedonio, F.; Drioli, E.; Aljlil, S.; Alharbi, O.A. Experimental and theoretical evaluation of temperature polarization phenomenon in direct contact membrane distillation. *Chemical Engineering Research and Design* **2013**, *91*, 1966–1977.

109. Khayet, M.; Cojocaru, C.; Baroudi, A. Modeling and optimization of sweeping gas membrane distillation. *Desalination* **2012**, *287*, 159–166.

110. Chang, H.; Chang, C.L.; Hung, C.Y.; Cheng, T.W.; Ho, C.D. Optimization Study of Small-Scale Solar Membrane Distillation Desalination Systems (s-SMDDS). *International Journal of Environmental Research and Public Health* **2014**, *11*, 12064–12087.

111. Cipollina, A.; Sparti, M.G. Di; Tamburini, A.; Micale, G. Development of a Membrane Distillation module for solar energy seawater desalination. *Chemical Engineering Research and Design* **2012**, *90*, 2101–2121.

112. Francis, L.; Ghaffour, N.; Alsaadi, A.S.; Nunes, S.P.; Amy, G.L. Performance evaluation of the DCMD desalination process under bench scale and large scale module operating conditions. *Journal of Membrane Science* **2014**, *455*, 103–112.

113. Heinzl, W.; Büttner, S.; Lange, G. Industrialized modules for MED Desalination with polymer surfaces. *Desalination and Water Treatment* **2012**, *42*, 177–180.

114. BAoBaB – Blue Acid/Base Battery: Storage and recovery of renewable electrical energy by reversible salt water dissociation Available online: http://www.baobabproject.eu/ (accessed on Nov 9, 2019).

115. Winter, D.; Koschikowski, J.; Wieghaus, M. Desalination using membrane distillation: Experimental studies on full scale spiral wound modules. *Journal of Membrane Science* **2011**, *375*, 104–112.

116. Summers, E.K.; Arafat, H.A.; Lienhard V, J.H. Energy efficiency comparison of single-stage membrane distillation (MD) desalination cycles in different configurations. *Desalination* **2012**, *290*, 54–66.

117. Wardeh, S.; Morvan, H.P. CFD simulations of flow and concentration polarization in spacer-filled channels for application to water desalination. *Chemical Engineering Research and Design* **2008**, *86*, 1107–1116.

118. Ponzio, F.N.; Tamburini, A.; Cipollina, A.; Micale, G.; Ciofalo, M. Experimental and computational investigation of heat transfer in channels filled by woven spacers. *International Journal of Heat and Mass Transfer* **2017**, *104*, 163–177.

119. Launder, B.E.; Spalding, D.B. The numerical computation of turbulent flows. *Computer methods in applied mechanics and engineering* **1974**, *3*, 269–289.

120. Yakhot, V.; Orszag, S.A.; Thangam, S.; Gatski, T.B.; Speziale, C.G. Development of turbulence models for shear flows by a double expansion technique. *Physics of Fluids A* **1992**, *4*, 1510–1520.

121. Wilcox, D.C. Reassessment of the scale-determining equation for advanced turbulence models. *AIAA Journal* **1988**, *26*, 1299–1310.

122. Menter, F.R. Two-equation eddy-viscosity turbulence models for engineering applications. *AIAA Journal* **1994**, *32*, 1598–1605.

123. Menter, F.R.; Kuntz, M.; Langtry, R. Ten Years of Industrial Experience with the SST Turbulence Model. *Turbulence, Heat and Mass Transfer* **2003**, *4*, 625–632.

124. Launder, B.E.; Reece, G.J.; Rodi, W. Progress in the development of a Reynolds-stress turbulence closure. *Journal of Fluid Mechanics* **1975**, *68*, 537–566.

125. Speziale, C.G.; Sarkar, S.; Gatski, T.B. Modelling the pressure-strain correlation of turbulence : An invariant dynamical systems approach. *Journal of Fluid Mechanics* **1991**, *227*, 245–272.

126. Gnielinski, V. G1 Durchströmte Rohre. In *VDI-Wärmeatlas*; Springer Berlin Heidelberg: Berlin, Heidelberg, 2013; pp. 785–792 ISBN 978-3-642-19981-3.

127. Lee, P.S.; Garimella, S. V.; Liu, D. Investigation of heat transfer in rectangular microchannels. *International Journal of Heat and Mass Transfer* **2005**, *48*, 1688–1704.

128. Shakaib, M.; Hasani, S.M.F.; Mahmood, M. CFD modeling for flow and mass transfer in spacer-obstructed membrane feed channels. *Journal of Membrane Science* **2009**, *326*, 270–284.

129. Islam, S.S.; Gupta, R.L.; Ismail, K. Extension of the Falkenhagen-Leist–

Kelbg Equation to the Electrical Conductance of Concentrated Aqueous Electrolytes. *Journal of Chemical and Engineering Data* **1991**, *36*, 102–104.

130. Tedesco, M.; Cipollina, A.; Tamburini, A.; van Baak, W.; Micale, G. Modelling the Reverse ElectroDialysis process with seawater and concentrated brines. *Desalination and Water Treatment* **2012**, *49*, 1–21.

131. Pawlowski, S.; Rijnaarts, T.; Saakes, M.; Nijmeijer, K.; Crespo, J.G.; Velizarov, S. Improved fluid mixing and power density in reverse electrodialysis stacks with chevron-profiled membranes. *Journal of Membrane Science* **2017**, *531*, 111–121.

132. Tanaka, Y. Ion-exchange membrane electrodialysis program and its application to multi-stage continuous saline water desalination. *Desalination* **2012**, *301*, 10–25.

133. Wagholikar, V.V.; Zhuang, H.; Jiao, Y.; Moe, N.E.; Ramanan, H.; Goh, L.M.; Barber, J.; Lee, K.S.; Lee, H.P.; Fuh, J.Y.H. Modeling cell pair resistance and spacer shadow factors in electro-separation processes. *Journal of Membrane Science* **2017**, *543*, 151–162.

134. Lee, H.J.; Sarfert, F.; Strathmann, H.; Moon, S.H. Designing of an electrodialysis desalination plant. *Desalination* **2002**, *142*, 267–286.

135. Galama, A.H.; Hoog, N.A.; Yntema, D.R. Method for determining ion exchange membrane resistance for electrodialysis systems. *Desalination* **2016**, *380*, 1–11.

136. A. M. Peers General Discussion. *Discussion of Faraday Society* **1956**, *21*, 124.

137. Spiegler, K.S. Polarization at ion exchange membrane-solution interfaces. *Desalination* **1971**, *9*, 367–385.

138. Levich, B.Y.B. The theory of concentration polarisation. *Discussion of Faraday Society* **1947**, *1*, 37–49.

139. Frilette, V.J. Electrogravitational Transport at Synthetic Ion Exchange Membrane Surfaces. *The Journal of Physical Chemistry* **1957**, *61*, 168–174.

140. Rubinstein, I.; Zaltzman, B. Electro-osmotically induced convection at a permselective membrane. *Physical Review E - Statistical Physics, Plasmas, Fluids, and Related Interdisciplinary Topics* **2000**, *62*, 2238–2251.

141. Lerman, I.; Rubinstein, I.; Zaltzman, B. Absence of bulk electroconvective instability in concentration polarization. *Physical Review E - Statistical, Nonlinear, and Soft Matter Physics* **2005**, *71*, 1–9.

142. Zaltzman, B.; Rubinstein, I. Electro-osmotic slip and electroconvective instability. *Journal of Fluid Mechanics* **2007**, *579*, 173–226.

143. Rubinstein, I.; Zaltzman, B. Extended space charge in concentration

polarization. *Advances in Colloid and Interface Science* **2010**, *159*, 117–129.

144. de Valenca, J.C. *Overlimiting current properties at ion exchange membranes*; 2017; ISBN 9789036543149.

145. Ibanez, R.; Stamatialis, D.F.; Wessling, M. Role of membrane surface in concentration polarization at cation exchange membranes. *Journal of Membrane Science* **2004**, *239*, 119–128.

146. Volodina, E.; Pismenskaya, N.; Nikonenko, V.; Larchet, C.; Pourcelly, G. Ion transfer across ion-exchange membranes with homogeneous and heterogeneous surfaces. *Journal of Colloid and Interface Science* **2005**, *285*, 247–258.

147. Balster, J.; Yildirim, M.H.; Stamatialis, D.F.; Ibanez, R.; Lammertink, R.G.H.; Jordan, V.; Wessling, M. Morphology and microtopology of cation-exchange polymers and the origin of the overlimiting current. *Journal of Physical Chemistry B* **2007**, *111*, 2152–2165.

148. Davidson, S.M.; Wessling, M.; Mani, A. On the Dynamical Regimes of Pattern-Accelerated Electroconvection. *Scientific Reports* **2016**, *6*, 1–10.

149. Nikonenko, V. V.; Pismenskaya, N.D.; Belova, E.I.; Sistat, P.; Huguet, P.; Pourcelly, G.; Larchet, C. Intensive current transfer in membrane systems: Modelling, mechanisms and application in electrodialysis. *Advances in Colloid and Interface Science* **2010**, *160*, 101–123.

150. Roghmans, F.; Evdochenko, E.; Stockmeier, F.; Schneider, S.; Smailji, A.; Tiwari, R.; Mikosch, A.; Karatay, E.; Kühne, A.; Walther, A.; et al. 2D Patterned Ion-Exchange Membranes Induce Electroconvection. *Advanced Materials Interfaces* **2019**, *6*, 1–11.

151. Wessling, M.; Morcillo, L.G.; Abdu, S. Nanometer-thick lateral polyelectrolyte micropatterns induce macrosopic electro-osmotic chaotic fluid instabilities. *Scientific Reports* **2014**, *4*, 1–5.

152. Kwak, R.; Pham, V.S.; Lim, K.M.; Han, J. Shear flow of an electrically charged fluid by ion concentration polarization: Scaling laws for electroconvective vortices. *Physical Review Letters* **2013**, *110*.

153. Urtenov, M.K.; Uzdenova, A.M.; Kovalenko, A. V.; Nikonenko, V. V.; Pismenskaya, N.D.; Vasil'eva, V.I.; Sistat, P.; Pourcelly, G. Basic mathematical model of overlimiting transfer enhanced by electroconvection in flow-through electrodialysis membrane cells. *Journal of Membrane Science* **2013**, *447*, 190–202.

154. Uzdenova, A. 2D mathematical modelling of overlimiting transfer enhanced by electroconvection in flow-through electrodialysis membrane cells in galvanodynamic mode. *Membranes* **2019**, *9*.

155. Druzgalski, C. Direct numerical simulation of electroconvective chaos near

an ion-selective membrane. **2013**, *110804*, 1–17.

156. Karatay, E.; Druzgalski, C.L.; Mani, A. Simulation of chaotic electrokinetic transport: Performance of commercial software versus custom-built direct numerical simulation codes. *Journal of Colloid and Interface Science* **2015**, *446*, 67–76.

157. Demekhin, E.A.; Nikitin, N. V.; Shelistov, V.S. Three-dimensional coherent structures of electrokinetic instability. *Physical Review E - Statistical, Nonlinear, and Soft Matter Physics* **2014**, *90*, 1–9.

158. Luo, K.; Wu, J.; Yi, H.-L.L.; Tan, H.-P.P. Three-dimensional finite amplitude electroconvection in dielectric liquids. *Physics of Fluids* **2018**, *30*, 23602.

159. Woldemariam, D.; Kullab, A.; Fortkamp, U.; Magner, J.; Royen, H.; Martin, A. Membrane distillation pilot plant trials with pharmaceutical residues and energy demand analysis. *Chemical Engineering Journal* **2016**, *306*, 471–483.

160. La Cerva, M.; Liberto, M. Di; Gurreri, L.; Tamburini, A.; Cipollina, A.; Micale, G.; Ciofalo, M. Coupling CFD with a one-dimensional model to predict the performance of reverse electrodialysis stacks. *Journal of Membrane Science* **2017**, *541*, 595–610.

161. Campione, A.; Cipollina, A.; Bogle, I.D.L.; Gurreri, L.; Tamburini, A.; Tedesco, M.; Micale, G. A hierarchical model for novel schemes of electrodialysis desalination. *Desalination* **2019**, *465*, 79–93.

162. Battaglia, G.; Gurreri, L.; Airòfarulla, G.; Cipollina, A.; Pirrotta, A.; Micale, G.; Ciofalo, M. Membrane deformation and its effects on flow and mass transfer in the electromembrane processes. *International Journal of Molecular Sciences* **2019**, *20*, 11–15.

163. Battaglia, G.; Gurreri, L.; Farulla, G.A.; Cipollina, A.; Pirrotta, A.; Micale, G.; Ciofalo, M. Pressure-induced deformation of pillar-type profiled membranes and its effects on flow and mass transfer. *Computation* **2019**, *7*, 1–14.

164. Battaglia, G.; Gurreri, L.; Cipollina, A.; Pirrotta, A.; Velizarov, S.; Ciofalo, M.; Micale, G. Fluid–Structure Interaction and Flow Redistribution in Membrane-Bounded Channels. *Energies* **2019**, *12*, 4259.

165. Zourmand, Z.; Faridirad, F.; Kasiri, N.; Mohammadi, T. Mass transfer modeling of desalination through an electrodialysis cell. *Desalination* **2015**, *359*, 41–51.

166. Tadimeti, J.G.D.; Kurian, V.; Chandra, A.; Chattopadhyay, S. Corrugated membrane surfaces for effective ion transport in electrodialysis. *Journal of Membrane Science* **2016**, *499*, 418–428.

167. Gurreri, L.; Battaglia, G.; Tamburini, A.; Cipollina, A.; Micale, G.; Ciofalo, M. Multi-physical modelling of reverse electrodialysis. *Desalination* **2017**,

423, 52–64.

168. Tamburini, A.; La Barbera, G.; Cipollina, A.; Micale, G.; Ciofalo, M. CFD prediction of scalar transport in thin channels for reverse electrodialysis. *Desalination and Water Treatment* **2014**, *3994*, 1–22.
169. Campione, A.; Cipollina, A.; Toet, E.; Gurreri, L.; Bogle, I.D.L.; Micale, G. Water desalination by capacitive electrodialysis: Experiments and modelling. *Desalination* **2020**, *473*, 114150.
170. Pawlowski, S.; Geraldes, V.; Crespo, J.G.; Velizarov, S. Computational fluid dynamics (CFD) assisted analysis of profiled membranes performance in reverse electrodialysis. *Journal of Membrane Science* **2016**, *502*, 179–190.
171. Newman, J.; Thomas-Alyea, K.E. *Electrochemical Systems*; Third edit.; John Wiley & Sons, Inc.: Hoboken, 2004; ISBN ISBN: 978-0-471-47756-3.
172. Nakayama, A.; Sano, Y.; Bai, X.; Tado, K. A boundary layer analysis for determination of the limiting current density in an electrodialysis desalination. *Desalination* **2017**, *404*, 41–49.
173. Green, D.W.; Perry, R.H. *Perry's Chemical Engineers' Handbook*; eighth.; McGraw-Hill: New York, 2007;
174. Pitzer, K.S.; Mayorga, G. Thermodynamics of electrolytes. II. Activity and osmotic coefficients for 2-2 electrolytes. *Journal of Solution Chemistry* **1974**, *3*, 539–546.
175. Vitagliano, V.; Lyons, P. a Diffusion coefficients for aqueous solutions of sodium chloride and barium chloride. *Journal of the American Chemical Society* **1956**, *76*, 1549–1552.
176. Veerman, J.; de Jong, R.M.; Saakes, M.; Metz, S.J.; Harmsen, G.J. Reverse electrodialysis: Comparison of six commercial membrane pairs on the thermodynamic efficiency and power density. *Journal of Membrane Science* **2009**, *343*, 7–15.
177. Vanoppen, M.; Criel, E.; Walpot, G.; Vermaas, D.A.; Verliefde, A. Assisted reverse electrodialysis—principles, mechanisms, and potential. *npj Clean Water* **2018**, *1*, 9.
178. Veerman, J.; Saakes, M.; Metz, S.J.; Harmsen, G.J. Reverse electrodialysis: A validated process model for design and optimization. *Chemical Engineering Journal* **2011**, *166*, 256–268.
179. Vallejo-Castaño, S.; Sánchez-Sáenz, C.I. Design and optimization of a reverse electrodialysis stack for energy generation through salinity gradients. *Dyna* **2017**, *84*, 84–91.
180. Long, R.; Li, B.; Liu, Z.; Liu, W. Reverse electrodialysis: Modelling and performance analysis based on multi-objective optimization. *Energy* **2018**,

151, 1–10.

181. Long, R.; Li, B.; Liu, Z.; Liu, W. Performance analysis of reverse electrodialysis stacks: Channel geometry and flow rate optimization. *Energy* **2018**, *158*, 427–436.

182. Rubinstein, I.; Staude, E.; Kedem, O. Role of the membrane surface in concentration polarization at ion-exchange membrane. *Desalination* **1988**, *69*, 101–114.

183. Li, F.; Meindersma, W.; De Haan, A.B.; Reith, T. Experimental validation of CFD mass transfer simulations in flat channels with non-woven net spacers. *Journal of Membrane Science* **2004**, *232*, 19–30.

184. Taky, M.; Pourcelly, G.; Gavach, C. Polarization phenomena at the interfaces between an electrolyte solution and an ion exchange membrane. Part II. Ion transfer with an anion exchange membrane. *Journal of Electroanalytical Chemistry* **1992**, *336*, 195–212.

185. Taky, M.; Pourcelly, G.; Lebon, F.; Gavach, C. Polarization phenomena at the interfaces between an electrolyte solution and an ion exchange membrane. Part I. Ion transfer with a cation exchange membrane. *Journal of Electroanalytical Chemistry* **1992**, *336*, 195–212.

186. Pis’menskaya, N.D.; Nikonenko, V. V.; Mel’nik, N. a.; Pourcelli, G.; Larchet, G. Effect of the ion-exchange-membrane/solution interfacial characteristics on the mass transfer at severe current regimes. *Russian Journal of Electrochemistry* **2012**, *48*, 610–628.

187. Belova, E.I.; Lopatkova, G.Y.; Pismenskaya, N.D.; Nikonenko, V. V.; Larchet, C.; Pourcelly, G. Effect of anion-exchange membrane surface properties on mechanisms of overlimiting mass transfer. *Journal of Physical Chemistry B* **2006**, *110*, 13458–13469.

188. Sonin, A.A.; Isaacson, M.S. Optimization of flow design in forced flow electrochemical systems, with special application to electrodialysis. *Industrial and Engineering Chemistry: Process and Design Development* **1974**, *13*, 241–248.

189. Rubinstein, I. Electroconvection at an electrically inhomogeneous permselective interface. *Physics of Fluids A: Fluid Dynamics* **1991**, *3*, 2301–2309.

190. Geraldes, V.; Afonso, M.D. Limiting current density in the electrodialysis of multi-ionic solutions. *Journal of Membrane Science* **2010**, *360*, 499–508.

191. Schlichting, H.; Gersten, K. Boundary-Layer Theory. **2017**.

192. Maletzki, F.; Rösler, H.W.; Staude, E. Ion transfer across electrodialysis membranes in the overlimiting current range: stationary voltage current characteristics and current noise power spectra under different conditions of

free convection. *Journal of Membrane Science* **1992**, *71*, 105–116.

193. Nikonenko, V. V.; Mareev, S.A.; Pis'menskaya, N.D.; Uzdenova, A.M.; Kovalenko, A. V.; Urtenov, M.K.; Pourcelly, G. Effect of electroconvection and its use in intensifying the mass transfer in electrodialysis (Review). *Russian Journal of Electrochemistry* **2017**, *53*, 1122–1144.

194. Krol, J.J.; Wessling, M.; Strathmann, H. Chronopotentiometry and overlimiting ion transport through monopolar ion exchange membranes. *Journal of Membrane Science* **1999**, *162*, 155–164.

195. Krol, J.J.; Wessling, M.; Strathmann, H. Concentration polarization with monopolar ion exchange membranes: Current-voltage curves and water dissociation. *Journal of Membrane Science* **1999**, *162*, 145–154.

196. Isaacson, M.S.; Sonin, A.A. Sherwood Number and Friction Factor Correlations for Electrodialysis Systems, with Application to Process Optimization. *Industrial & Engineering Chemistry Process Design and Development* **1976**, *15*, 313–321.

197. Nikonenko, V. V.; Istoshin, A.G.; Urtenov, M.K.; Zabolotsky, V.I.; Larchet, C.; Benzaria, J. Analysis of electrodialysis water desalination costs by convective-diffusion model. *Desalination* **1999**, *126*, 207–211.

198. Lee, H.J.; Strathmann, H.; Moon, S.H. Determination of the limiting current density in electrodialysis desalination as an empirical function of linear velocity. *Desalination* **2006**, *190*, 43–50.

199. Tanaka, Y. Concentration polarization in ion-exchange membrane electrodialysis: The events arising in an unforced flowing solution in a desalting cell. *Journal of Membrane Science* **2003**, *216*, 149–164.

200. Tanaka, Y. Limiting current density of an ion-exchange membrane and of an electrodialyzer. *Journal of Membrane Science* **2005**, *266*, 6–17.

201. Zerdoumi, R.; Oulmi, K.; Benslimane, S. Electrochemical characterization of the CMX cation exchange membrane in buffered solutions: Effect on concentration polarization and counterions transport properties. *Desalination* **2014**, *340*, 42–48.

202. Długołecki, P.; Anet, B.; Metz, S.J.; Nijmeijer, K.; Wessling, M. Transport limitations in ion exchange membranes at low salt concentrations. *Journal of Membrane Science* **2010**, *346*, 163–171.

203. Choi, J.-H.; Kim, S.-H.; Moon, S.-H. Heterogeneity of Ion-Exchange Membranes: The Effects of Membrane Heterogeneity on Transport Properties. *Journal of colloid and interface science* **2001**, *241*, 120–126.

204. Balster, J.; Pünt, I.; Stamatialis, D.F.; Wessling, M. Multi-layer spacer geometries with improved mass transport. *Journal of Membrane Science* **2006**, *282*, 351–361.

205. Cowan, D.A.; Brown, J.H. Effect of Turbulence on Limiting Current in Electrodialysis Cells. *Industrial and Engineering Chemistry* **1959**, *51*, 1445–1448.

206. Meng, H.; Deng, D.; Chen, S.; Zhang, G. A new method to determine the optimal operating current (Ilim′) in the electrodialysis process. *Desalination* **2005**, *181*, 101–108.

207. Shaffer, L.H.; Mintz, M.S. Electrodialysis. In *Principles of Desalination*; Academic Press Inc.: New York, 1980 ISBN 9780128017647.

208. Kwak, R.; Guan, G.; Peng, W.K.; Han, J. Microscale electrodialysis: Concentration profiling and vortex visualization. *Desalination* **2013**, *308*, 138–146.

209. Zhong, X.W.; Zhang, W.R.; Hu, Z.Y.; Li, H.C. Effect of characterizations of spacer in electrodialysis cells on mass transfer. *Desalination* **1983**, *46*, 243–252.

210. Tado, K.; Sakai, F.; Sano, Y.; Nakayama, A. An analysis on ion transport process in electrodialysis desalination. *Desalination* **2016**, *378*, 60–66.

211. Ali, A.; Drioli, E.; Macedonio, F. Membrane Engineering for Sustainable Development: A Perspective. *Applied Sciences* **2017**, *7*, 1026.

212. Mei, Y.; Tang, C.Y. Co-locating reverse electrodialysis with reverse osmosis desalination: Synergies and implications. *Journal of Membrane Science* **2017**, *539*, 305–312.

213. Kwon, K.; Han, J.; Park, B.H.; Shin, Y.; Kim, D. Brine recovery using reverse electrodialysis in membrane-based desalination processes. *Desalination* **2015**, *362*, 1–10.

214. Luque Di Salvo, J.; Cosenza, A.; Tamburini, A.; Micale, G.; Cipollina, A. Long-run operation of a reverse electrodialysis system fed with wastewaters. *Journal of Environmental Management* **2018**, *217*, 871–887.

215. McGovern, R.K.; Zubair, S.M.; Lienhard V, J.H. The cost effectiveness of electrodialysis for diverse salinity applications. *Desalination* **2014**, *348*, 57–65.

216. McGovern, R.K.; Weiner, A.M.; Sun, L.; Chambers, C.G.; Zubair, S.M.; Lienhard V, J.H. On the cost of electrodialysis for the desalination of high salinity feeds. *Applied Energy* **2014**, *136*, 649–661.

217. Thampy, S.; Desale, G.R.; Shahi, V.K.; Makwana, B.S.; Ghosh, P.K. Development of hybrid electrodialysis-reverse osmosis domestic desalination unit for high recovery of product water. *Desalination* **2011**, *282*, 104–108.

218. Reig, M.; Casas, S.; Aladjem, C.; Valderrama, C.; Gibert, O.; Valero, F.; Centeno, C.M.; Larrotcha, E.; Cortina, J.L. Concentration of NaCl from

seawater reverse osmosis brines for the chlor-alkali industry by electrodialysis. *Desalination* **2014**, *342*, 107–117.

219. Reahl, E.R. Reclaiming reverse osmosis blowdown with electrodialysis reversal. *Desalination* **1990**, *78*, 77–89.

220. Oren, Y.; Korngold, E.; Daltrophe, N.; Messalem, R.; Volkman, Y.; Aronov, L.; Weismann, M.; Bouriakov, N.; Glueckstern, P.; Gilron, J. Pilot studies on high recovery BWRO-EDR for near zero liquid discharge approach. *Desalination* **2010**, *261*, 321–330.

221. McGovern, R.K.; Zubair, S.M.; Lienhard V, J.H. The benefits of hybridising electrodialysis with reverse osmosis. *Journal of Membrane Science* **2014**, *469*, 326–335.

222. Environmental Protection Agency 2018 Edition of the Drinking Water Standards and Health Advisories. *United States Environmental Protection Agency* **2018**, 2–6.

223. Strathmann, H. Assessment of Electrodialysis Water Desalination Process Costs. *Proceedings of the International Conference on Desalination Costing, Lemassol, Cyprus, December 6-8, 2004* **2004**, 32–54.

224. Vermaas, D.A.; Kunteng, D.; Veerman, J.; Saakes, M.; Nijmeijer, K. Periodic feedwater reversal and air sparging as antifouling strategies in reverse electrodialysis. *Environmental Science and Technology* **2014**, *48*, 3065–3073.

225. Hong, J.G.; Zhang, B.; Glabman, S.; Uzal, N.; Dou, X.; Zhang, H.; Wei, X.; Chen, Y. Potential ion exchange membranes and system performance in reverse electrodialysis for power generation: A review. *Journal of Membrane Science* **2015**, *486*, 71–88.

226. Tufa, R.A.; Pawlowski, S.; Veerman, J.; Bouzek, K.; Fontananova, E.; di Profio, G.; Velizarov, S.; Goulão Crespo, J.; Nijmeijer, K.; Curcio, E. Progress and prospects in reverse electrodialysis for salinity gradient energy conversion and storage. *Applied Energy* **2018**, *225*, 290–331.

227. Daniilidis, A.; Herber, R.; Vermaas, D.A. Upscale potential and financial feasibility of a reverse electrodialysis power plant. *Applied Energy* **2014**, *119*, 257–265.

228. Vanoppen, M.; van Vooren, T.; Gutierrez, L.; Roman, M.; Croué, L.J.P.; Verbeken, K.; Philips, J.; Verliefde, A.R.D. Secondary treated domestic wastewater in reverse electrodialysis: What is the best pre-treatment? *Separation and Purification Technology* **2019**, *218*, 25–42.

229. Vermaas, D.A.; Kunteng, D.; Saakes, M.; Nijmeijer, K. Fouling in reverse electrodialysis under natural conditions. *Water Research* **2013**, *47*, 1289–1298.

230. Di Salvo, J.; Cosenza, A.; Cipollina, A.; Tamburini, A.; Micale, G. Experimental Analysis of a Continuously Operated Reverse Electrodialysis Unit Fed with Wastewaters. *Chemical Engineering Transactions* **2017**, *60*, 307–312.

231. Micari, M.; Cipollina, A.; Giacalone, F.; Kosmadakis, G.; Papapetrou, M.; Zaragoza, G.; Micale, G.; Tamburini, A. Towards the first proof of the concept of a Reverse ElectroDialysis - Membrane Distillation Heat Engine. *Desalination* **2019**, *453*, 77–88.

232. Stasiek, J.; Collins, M.W.; Ciofalo, M.; Chew, P.E. Investigation of flow and heat transfer in corrugated passages. *Int. J. Heat Transfer* **1996**, *39*, 149–164.

233. Ciofalo, M.; Di Piazza, I.; Stasiek, J.A. Investigation of flow and heat transfer in corrugated-undulated plate heat exchangers. *Heat and Mass Transfer/Waerme- und Stoffuebertragung* **2000**, *36*, 449–462.

234. Kakade, V.U.; Lock, G.D.; Wilson, M.; Owen, J.M.; Mayhew, J.E. Accurate heat transfer measurements using thermochromic liquid crystal. Part 2: Application to a rotating disc. *International Journal of Heat and Fluid Flow* **2009**, *30*, 950–959.

235. Hiller, W.J.; Koch, S.; Kowalewski, T.A. Three-dimensional structures in laminar natural convection in a cubic enclosure. *Experimental Thermal and Fluid Science* **1989**, *2*, 34–44.

236. Ciofalo, M.; Signorino, M.; Simiano, M. Tomographie particle-image velocimetry and thermography in Rayleigh-Bénard convection using suspended thermochromic liquid crystals and digital image processing. *Experiments in Fluids* **2003**, *34*, 156–172.

237. Chen, H.T.; Tseng, H.C.; Jhu, S.W.; Chang, J.R. Numerical and experimental study of mixed convection heat transfer and fluid flow characteristics of plate-fin heat sinks. *International Journal of Heat and Mass Transfer* **2017**, *111*, 1050–1062.

238. Laktionov, E. V.; Pismenskaya, N.D.; Nikonenko, V. V.; Zabolotsky, V.I. Method of electrodialysis stack testing with the feed solution concentration regulation. *Desalination* **2003**, *151*, 101–116.